The reconstruction of the 2.41 Ga Hotazel BIF paleo-depositional environment and mechanism of iron and manganese cycling in a stratified basin.

Sten G.J. Jacobs

Utrecht, March 2019

Abstract

The Hotazel formation is the uppermost part of the Paleoproterozoic Transvaal Supergroup and is characteristic for having three distinct Mn-oxide layers interbedded with banded iron formations (BIFs). The depositional age of the Hotazel Fm. is estimated at 2.41 Ga, right at the onset of the Great Oxidation Event (GOE) which represents the transition from an anoxic ocean and atmosphere to a full oxidative cycle in the oceans at around 2.22 Ga. The Hotazel formation's stratigraphy shows an antithetic thickness relationship between the BIF and the Mn-oxide lithology's of which the primary controls remain somewhat unknown. Determining what controls this relationship is of major importance and could imply that under the right conditions, compositionally different styles of chemical sedimentation can be produced at the same time. Optical microscopy, X-ray diffraction, XRF, LA-ICP-MS and carbon isotope measurements were carried out on two different drill-cores showing this antithetic relationship a) to construct a clear correlation between the two different sections and b) to obtain in much detail the mineralogical and chemical composition, redox conditions and the paleo-depositional environment of the first BIF in the Hotazel Fm. Trace element data presented an increase in HFSE towards the base of both sections, related to allochthonous input in the water column. The REE + Y distribution showed depleted LREE, positive La, Gd and Y anomalies and no negative Ce anomaly in both sections. Apart from the absence of a negative Ce anomaly, indicating an anoxic marine environment, the water column resembled that of modern (and ancient) seawater. The carbon isotopes are largely depleted ($\delta^{13}C$ of -20.66 to -11.35 ‰) and showed a gradual increase towards the top of the MP-BIF section and a rather sharp increase towards the top of the G7BF related to differences in subsidence rate. The G7BF section is correlated to be the stratigraphic equivalent of the top 13 meters of the MP-BIF section, indicating that precipitation rates were nearly equal during time of deposition. This would subsequently imply that the bottom of the MP-BIF section had been deposited during the same time interval as the Mn-oxide intercalation of the G7BF, showing that different types of chemical sediments, under the right condition, can indeed precipitate simultaneously at laterally different parts of the basin.

First Supervisor: prof. dr. P.R.D. (Paul) Mason, Utrecht University, The Netherlands
Second Supervisor: dr. H. (Harilaos) Tsikos, Rhodes University, South Africa

1. Introduction

Banded iron formations (BIFs) are sedimentary rocks, often thinly bedded or laminated with an anomalously high content of iron (Klein, 2005; after James, 1954). Most BIFs were deposited during the Neoarchean and the Paleoproterozoic (2.7 – 2.2 Ga) and their deposition has often been linked to localized oxygen production under an anoxic atmosphere. The best-preserved successions are remarkably uniform, composed generally of fine-grained quartz (in the form of chert), magnetite, hematite together with a variable amounts of Fe-rich silicate minerals (e.g., stilpnomelane, minnesotaite, greenalite, and riebeckite) and carbonate minerals (siderite, ankerite, calcite, and dolomite). BIFs usually form in near-shore shelf environments along passive margins of cratons or in platforms over extended periods of time (Trendall, 2002). Therefore they are typically interbedded with, or grade into, carbonates and black shales. The input of aqueous iron into the seawater originates from enhanced magmatic activity at mid oceanic ridges (Isley, 1995). Plumes then transported the Fe (II) into the upper water column and laterally to the continental margin, where precipitation of BIFs occurred. The mechanisms responsible for the precipitation of aqueous ferrous iron into BIF minerals have been a broad topic of discussion.
The three main ideas of oxidizing mechanisms are:
- Abiotic photochemical oxidation (Cairns-Smith, 1978), which is an abiotic pathway to oxidize ferrous iron. During the Archean, UV-radiation could reach iron-rich seawater due to the absence of an ozone-layer. The intense UV-radiation could result in the oxidation of ferrous iron and subsequently the production of H_2 from dissolved hydrogen in the water column.
-Anoxygenic photosynthesis (Kappler et al., 2005) is a process where light couples the iron and carbon cycles. Photoferrotrophs use ferrous iron as an electron donor, which produces ferric iron instead of oxygen and transforms CO_2 into organic matter.
-The last mechanism is oxidation by oxygenic photosynthesis (Cloud, 1965) associated with cyanobacteria, which convert water and CO_2 into organic matter and free oxygen and can directly oxidize Fe (II).

The Hotazel formation is the uppermost part of the Paleoproterozoic (2.65-2.05 Ga) Transvaal Supergroup, located in South Africa and is characteristic for having 3 distinct Mn-rich (20-48 wt%) intercalations interbedded with BIFs. This implies that manganese could be a significant proxy for biogeochemical redox cycling and atmosphere-ocean evolution during BIF deposition. The increased values of Mn in the Hotazel formation were initially thought to be caused by an increase in Mn input due to enhanced hydrothermal activity or by accumulation in the basin. However no other elements show a strong increase in concentration contradicting the argument of enhanced hydrothermal activity (Oonk et al., 2018). Tsikos et al. (2010) made a model summarizing their interpretation on the paleo-depositional environment of the Hotazel formation (Figure 1). Initial deposition took place in a stratified basin enriched in dissolved Fe(II) with an Fe/Mn ratio reflecting that of an average oceanic crust (50/1), and a near-zero δ^{57}Fe composition recording the long term input of iron from hydrothermal activity or fluvial input. In this setting the stratigraphically lower Kuruman, Griquatown BIFs would have been deposited. BIFs have a preferential sequestration of Fe over Mn (Tsikos et al., 2010), slowly enriching the seawater in Mn concentration over a long period of time. Oxidation of iron would have been either aerobic or anaerobic, while Mn re-cycling in the water would have occurred through reduction of dissolved Mn (III) by co-existing Fe (II): $MnOOH + Fe^{2+} \rightarrow FeOOH + Mn^{2+}$. This may have been an important factor for the low concentration of manganese observed in Paleoproterozoic BIFs worldwide (Klein, 2005). Rayleigh fractionation of oxide-dominated BIFs would have resulted in a terminal depositional basin for the Hotazel formation, which would be characterized by an enrichment in aqueous manganese in the bottom, anoxic waters. In these anoxic to sub-oxic aqueous environment manganese concentrations can build up significantly, e.g. in the Orca Basin, where Mn^{2+} concentrations reach > 400µM (Van Cappellen et al,. 1998), resulting in a massive amount of dissolved Mn in the stratified basin during time of the Hotazel deposition. The low iron isotope signatures of the Mn-rich layers of the Hotazel formation suggest that bacterial manganese reduction is more favourable over iron cycling via DIR and thus precipitation of Mn-rich layers will occur. Tsikos and Moore (1997) proposed the superposition of transgression-regression cycles to explain the cyclicity of the Mn-rich intercalations with the BIF. However, this theory is only circumstantial, cannot be fully proved and need to be tested and refined further.

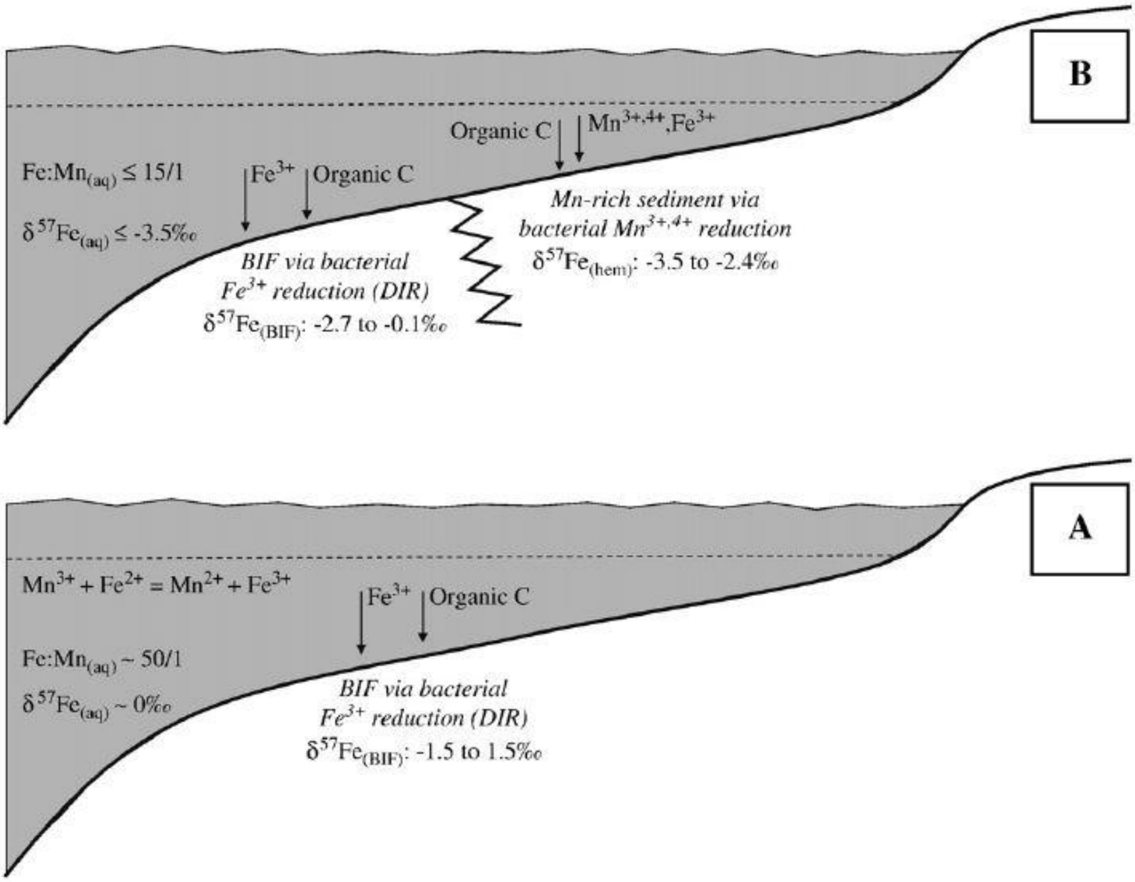

Figure 1: Diagrams illustrating key chemical and isotopic parameters of (A) an initial stratified basin for the deposition of the Kuruman/Griquatown and Brockman BIFs in the Transvaal-Hamersley Supergroups; and (B) an evolved stratified basin conductive to the deposition of a Hotazel-like BIF-Mn sequence. From Tsikos et al. (2010).

The depositional age of the Hotazel formation is estimated to be 2413 +- 15 Ma, right at the onset of the Great Oxidation Event (GOE) (Gumsley et al., 2017). The GOE represents a shift from an anoxic ocean and atmosphere with O_2 levels of 0.001% to a full oxidative cycle in the oceans at around 2.22 Ga (Holland, 2002) (Figure 2). Prior to the GOE oxygen levels were not significant enough, although Ohmoto et al. (2006) argued that the oceans and atmosphere were oxic from 3.80 Ga onward. However much stronger evidence based on the loss of mass independent fractionation of sulphur isotopes (MIF-S) suggest that O_2 concentrations in the atmosphere rose to 10^{-2} PAL (Present day Atmospheric Level) at 2.32 Ga (Bekker et al., 2004). The GOE would have had major influence on the oxidation of Fe and Mn in shallow oceans or stratified basins, as free oxygen could now be used as an oxidizer.

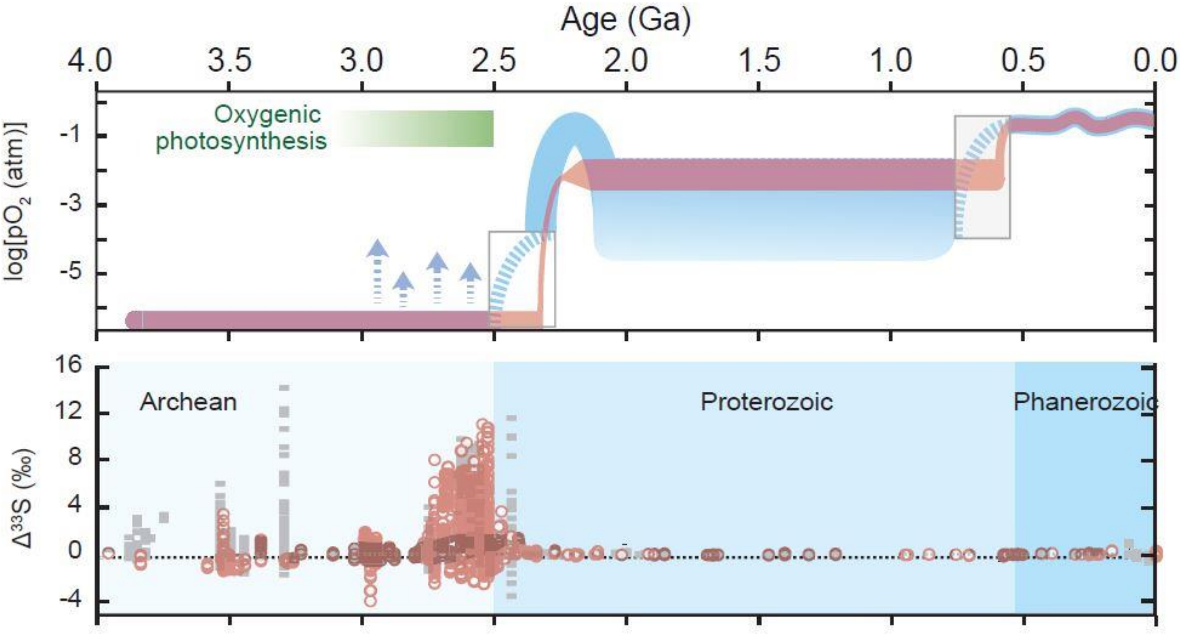

Figure 2: Temporal evolutions of various phenomena. Top) Atmospheric oxygen content as log-function of present day atmospheric levels (PAL). Bottom) Disappearance of mass-independent fractionation (as Δ^{33} S) at the GOE. From Lyons, et al. (2014)

Kirschvink et al. (2011) compared the Hotazel formation with the Firstbrook member of the Huronian Supergroup, Canada. The Firstbrook member shows enriched Mn concentrations directly after the Gowdana diamictite deposited during the Huronian glaciation event. This stratigraphic sequence shows large similarities with that of the Hotazel formation, since the Hotazel formation is deposited after the Makganyene diamictite in the Transvaal supergroup. This relation between Mn enrichment after a global glaciation is notable and could provide information on the depositional environment of the Hotazel formation and the precipitation mechanisms of manganese.

Kirschvink et al. (2000) proposed that such a large amount of Mn precipitation could have occurred as a consequence of the accumulation of dissolved Mn in the ice-covered oceans during the Paleoproterozoic Snowball glaciation and/or the subsequent Mn oxidation due to high levels of cyanobacteria in the aftermath of the snowball earth glaciation. The atmospheric O_2 levels required for the precipitation of Mn are estimated to be more than 10^{-2} PAL. When such high levels are reached, the marine surface zone of ~200m should oxidize assuming that the water column was in equilibrium with the Earth's atmosphere (e.g., Holland, 1984; Klemm, 2000). If the

Gowdana formation of the Huronian supergroup correlates with the Makganyene Formation in the Transvaal supergroup the major precipitation event of Mn and Fe was a widespread phenomenon in the shallow-marine environments in the aftermath of the global Snowball glaciation. Then the atmospheric O_2 would have remained at intermediate levels (~10^{-5}–10^{-2} PAL) before the Paleoproterozoic Snowball glaciation, and the highly oxygenated atmosphere and shallow-marine environments would have appeared immediately after the Paleoproterozoic Snowball Earth for the first time in Earth's history, right at the time of the Hotazel formation's deposition. However, Lantink et al. (2018) showed through Fe isotope data that the base of the Hotazel formation is still pre-GOE. The lack of a negative Ce anomaly in her data, indicating a marine anoxia during time of deposition, confirmed this statement. This study will elaborate on the ocean's oxygenic state during time of deposition, higher up the stratigraphy of the Hotazel formation and possibly further constrain the timing of the GOE.

The Hotazel formation contains a notable thickness variation throughout the stratigraphy. Tsikos and Moore (1997) first observed the antithetic thickness relationship between the BIF and the Mn-oxide layers. However, the primary controls of this thickness variation remained somewhat unknown, yet this relationship has enormous implications for the understanding of BIF environments in general. For this research 2 drill cores of 11 and 26 meters in thickness from the middle portion of the Hotazel formation have been sampled in the Kalahari Manganese field, South Africa and were brought back to Utrecht University to be analysed. We assume that the precipitation rate during BIF and Mn deposition in the Hotazel formation is the same across the basin. The very homogeneous mineralogical and geochemical composition of the rocks across space suggest that this assumption is reasonable. Looking at the stratigraphy of both the drill-cores and the assumption that precipitation rates were the same across space, there must have been periods in time when Mn was precipitating in one part of the basin while BIF was being deposited in another part not far away. This would imply that a given environment under the right conditions can produce compositionally different styles of chemical sedimentation at the same time.

To verify this hypothesis we take the interface between the Ongeluk formation and the overlying sediments and assume it represents time = 0 in the depositional history of the Hotazel. The black shale which has been discovered in every drill-core in the broader area of interest, is then assumed to be the chronostratigraphic marker at time = 1. Thus the enclosed sediments precipitated over the same time interval. By applying chemical stratigraphy, including C isotope data across the two selected drill-cores which shows this antithetic relationship, a chemical correlation will be made to see how both cores correspond with each other. An explanation on whether or not the smaller core is a condensed version of the larger drill-core or part of a specific stratigraphic interval needs to be established. This will also shed light on the nature of lateral variations in sedimentation rate of the BIF in the basin. Trace element and REE data will then provide further insight on the redox conditions, hydrothermal activity, detrital input and the paleo-deposition environment of the Hotazel Formation.

2. Regional Geology

2.1 Transvaal Supergroup

The Hotazel formation is part of the Neoarchean to early Proterozoic Transvaal Supergroup, located in South Africa (Figure 3). The Transvaal supergroup is typically divided into two stratigraphic distinct groups. The Ghaap group, which consist of a 1.6 km thick succession of dolomitic carbonates of the Campbellrand Formation at the base and several hundreds of meters thick BIF of the Asbestos hills and Koegas subgroups respectively at the top. The estimated age of deposition of the Ghaap group is 2.64-2.45 Ga (Beukes and Gutzmer, 2008). The Postmanburg group is the stratigraphically higher part of the Transvaal supergroup. The base consist of 100 meter glacial diamictites of the Makganyene Formation, which represents the Huronian Snowball Earth event (Kirschvink et al., 2000). This is overlain by a 600 meter thick package of basaltic andesite known as the Ongeluk Formation. These represent extrusive pillow lava's and massive flows (Cornell et al., 1996) and are subsequently overlain by the Hotazel Formation, which will be the focus of this study. The Hotazel formation is a 150 m thick chemical sediment that consist mainly of magnetite and carbonate-rich BIF which are interbedded by three distinct Mn-ore layers (Figure 4). The top of the Postmanburg group consist of 100 meter thick carbonate package called the Mooidraai formation, which is interpreted as a shallow marine platform succession (Swart, 2012).

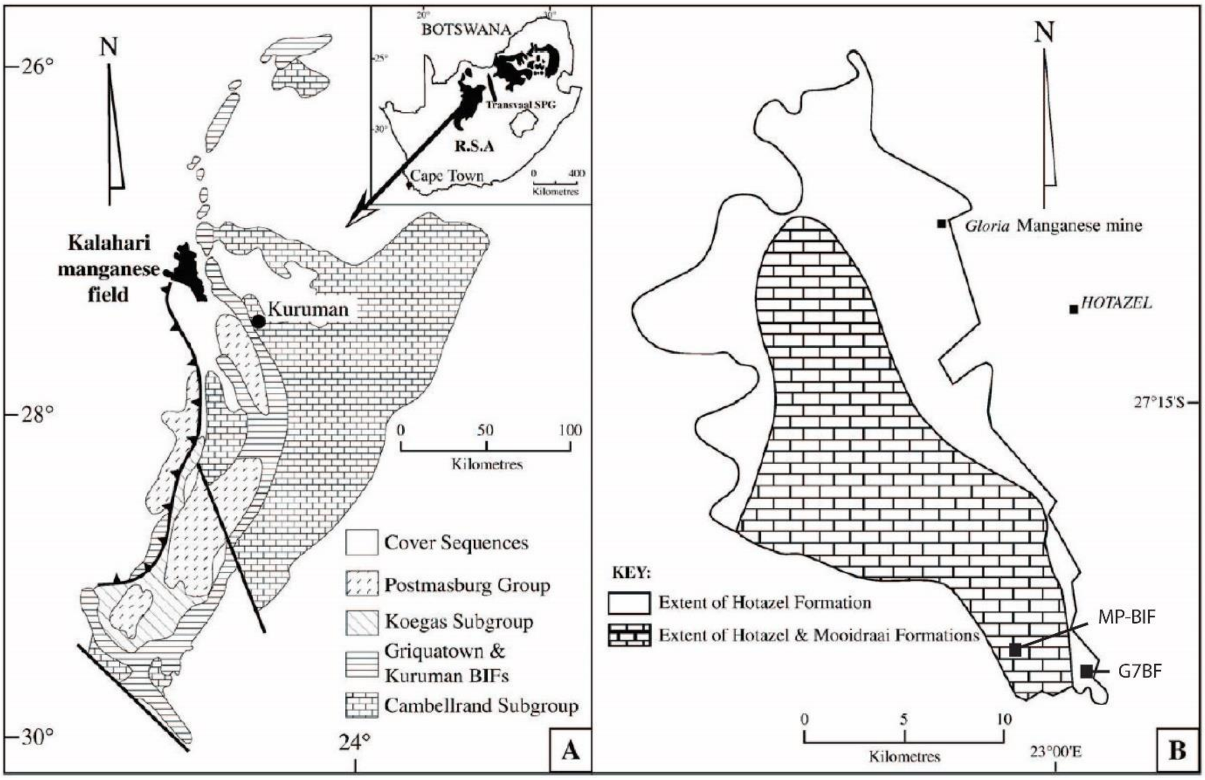

Figure 3: (A) Geographical distribution of the Transvaal Supergroup, South Africa and a simplified regional geological map of the Griqualand West Basin. (B) Geological map of the Kalahari manganese field, including the locality of the G7BF and MP-BIF drill-cores. Modified from Tsikos et al. (2010)

2.2 Hotazel Formation

The three manganese-rich layers consist mostly of braunite, a Mn silicate, hematite and a considerable amount of kutnahorite, a Mn carbonate. The thickness varies from 15-45 meter in the lowermost Mn-unit to 3-10 meters in the middle and upper unit. The BIFs in between the Mn-rich layers consist mostly of mm- to cm- scale laminated mineral assemblages of quartz (in the form of chert), magnetite and hematite. Carbonate-rich minerals e.g. ankerite and siderite form the next most abundant mineral assemblage followed by a relative low amount of iron rich silicates e.g. greenalite, stipnomelite, riebeckite and minnesotalite. The contacts between the Mn-rich layers and the BIF are gradual and is characterized by a hematite lutite lithology (Tsikos et al., 2003). A black shale is deposited stratigraphically above the middle BIF and is the only lithology lacking high concentrations of Fe and Mn. The alternation between the BIF and Mn has a highly cyclic character of which the driving mechanism is not yet fully understood. The Hotazel formation is buried underneath approximately 40 meters of tertiary sands in a 400 km^2 wide area known as the Kalahari manganese field. The chemical sediments are affected by a shallow metamorphic grade due to burial (max 200 °C) (Gutzmer and Beukes, 1996). Due to thrusting, the stratigraphy of the Hotazel formation is often duplicated.

2.3 Age constraints

The age of the Hotazel formation has been a broad topic of discussion and was originally estimated at 2.2 Ga (Cornell et al., 1996). However, the 2.22 Ga age assumed for the Ongeluk formation requires an erosional unconformity of approximately 200 Ma, which has been challenged by Moore et al. (2001). Also, the 2.394 Ga age of the Mooidraai formation would be invalidated, since it is a stratigraphically higher unit than the Ongeluk and Hotazel formations. Recent studies of Gumsley et al. (2017) provided new U-Pb age constraints for the Ongeluk formation, estimating the age at 2.426 Ga. The age of the Hotazel formation will then range from 2.42 – 2.39 Ga, right at the onset of the GOE. The regional stratigraphy of the Transvaal Supergroup including the age of each individual formation can be seen in Figure 5.

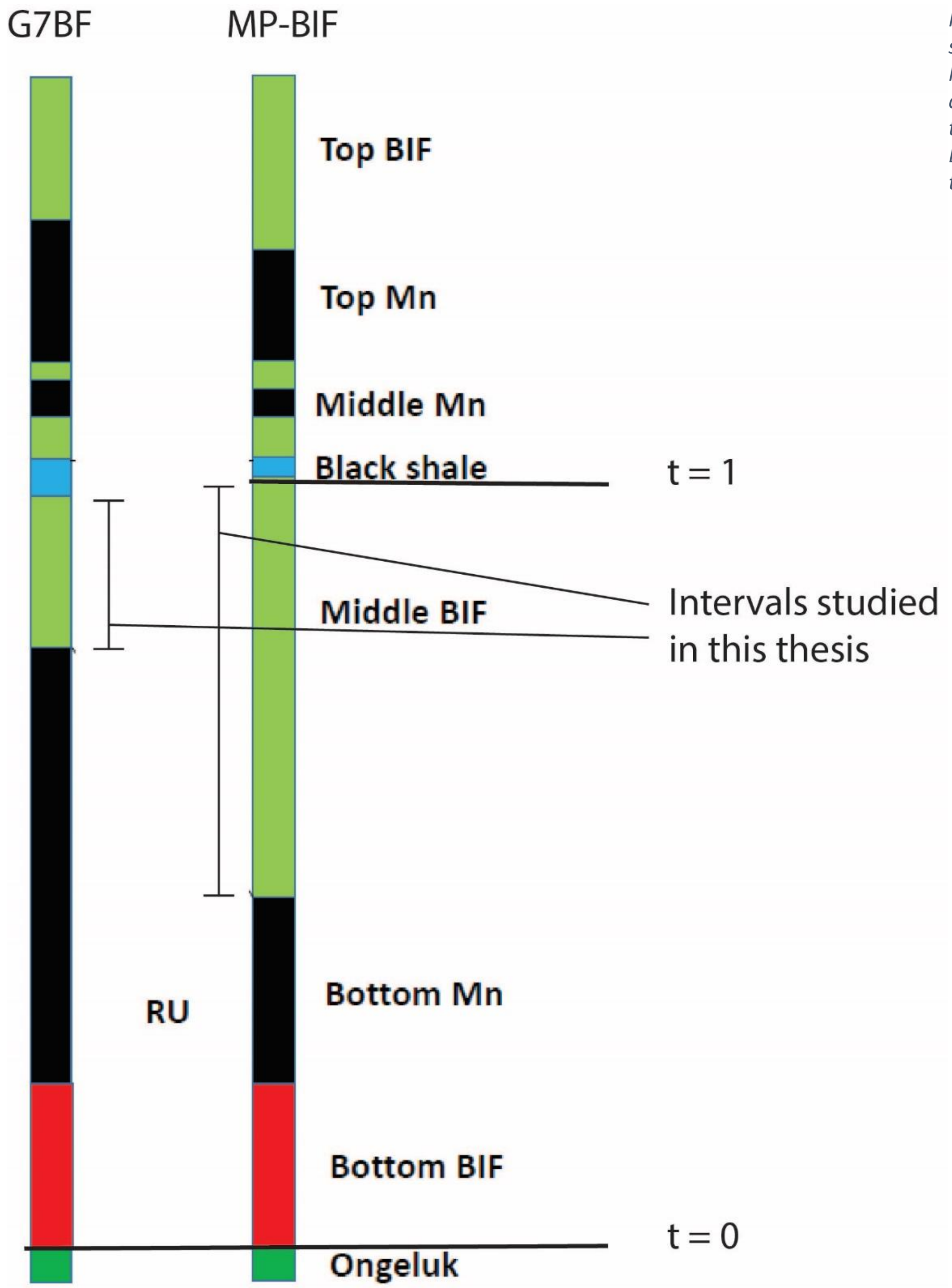

Figure 4: Simplified stratigraphic log of the Hotazel formation's drill-cores. Left the G7BF, right the MP-BIF. The middle BIF intervals are studied in this thesis.

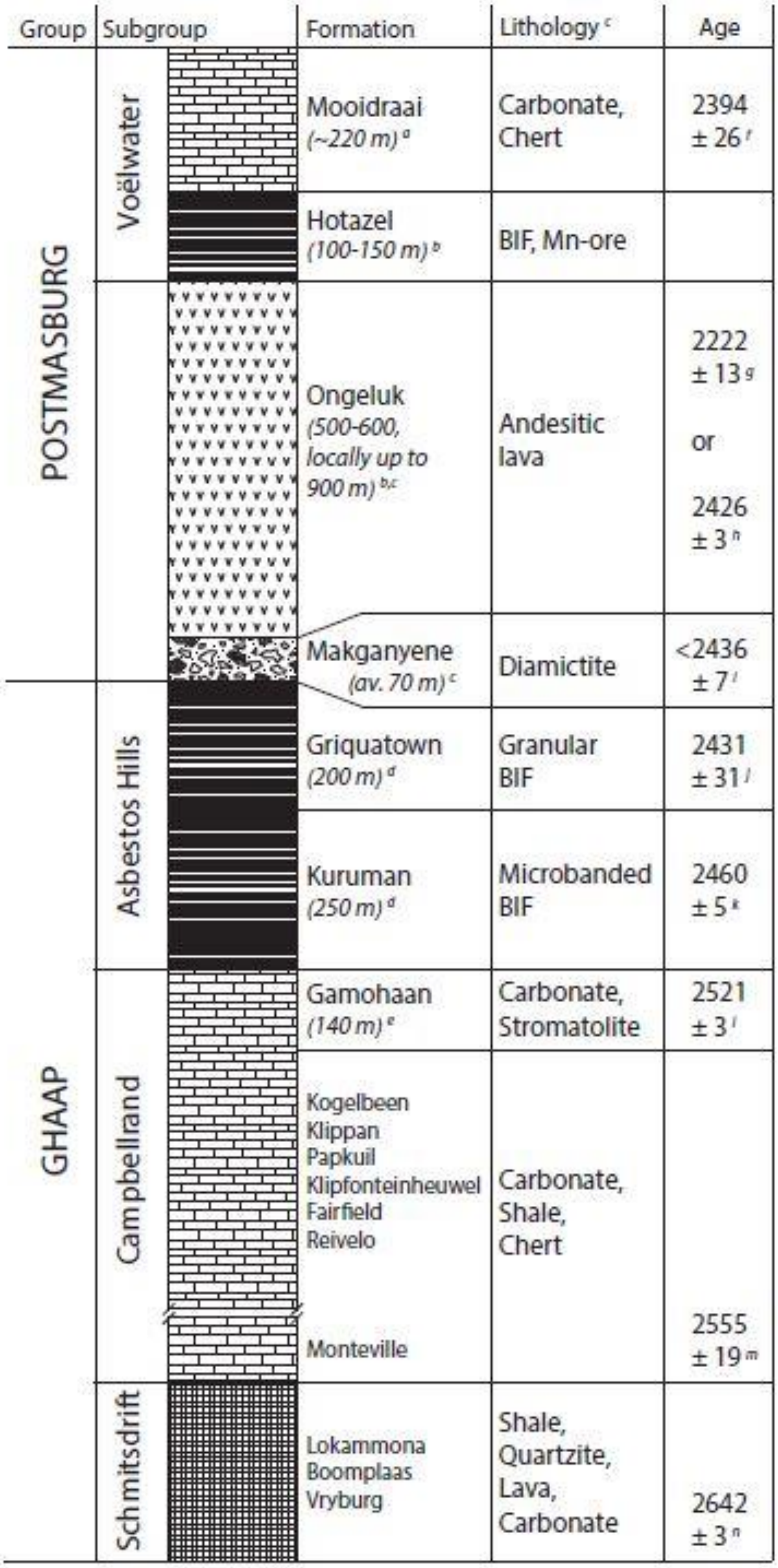

Group	Subgroup	Formation	Lithology[c]	Age
POSTMASBURG	Voëlwater	Mooidraai (~220 m)[a]	Carbonate, Chert	2394 ± 26[f]
		Hotazel (100-150 m)[b]	BIF, Mn-ore	
		Ongeluk (500-600, locally up to 900 m)[b,c]	Andesitic lava	2222 ± 13[g] or 2426 ± 3[h]
		Makganyene (av. 70 m)[c]	Diamictite	<2436 ± 7[i]
GHAAP	Asbestos Hills	Griquatown (200 m)[d]	Granular BIF	2431 ± 31[j]
		Kuruman (250 m)[d]	Microbanded BIF	2460 ± 5[k]
	Campbellrand	Gamohaan (140 m)[e]	Carbonate, Stromatolite	2521 ± 3[l]
		Kogelbeen Klippan Papkuil Klipfonteinheuwel Fairfield Reivelo Monteville	Carbonate, Shale, Chert	2555 ± 19[m]
	Schmitsdrift	Lokammona Boomplaas Vryburg	Shale, Quartzite, Lava, Carbonate	2642 ± 3[n]

Figure 5: Regional stratigraphy of the Transvaal Supergroup. From Oonk et al., (2018)
Thickness and age from:
a: Kunzmann et al., 2014
b: Tsikos et al., 2003
c: Poltreau et al., 2006
d: Oonk et al., 2018
e: Sumner 1997
f: Bau et al., 1999
g: Cornell et al., 1996
h: Gumsley et al., 2017
i: Moore et al., 2012
j: Trendall et al., 1990
k: Pickard, 2003
l: Sumner and Bowring, 1996
m: Altermann and Nelson, 1998
n: Walraven and Martini, 1995

3. Methods

3.1 Drill-core description

The BIFs were sampled from 2 drill-cores: G7BF and MP-BIF (for sample locations and core logs see Regional Geology). 22 Samples from the G7BF core and 53 samples from the MP-BIF core were cut every ~0.5 m core depth and consisted of 10 -25 cm quarter-core fragments. This was done to capture in as much detail as possible the variations of the BIFs from 2 different drill-cores and to increase the amount of data used for the chemical-stratigraphic correlation. The cores were transported to Utrecht University, where they were photographed and visually described (see Appendix). The sample numbers for each sample and its corresponding core depth (m) can be found in Table 1.

3.2 Optical microscopy

In total 26 polished thin sections were prepared of 30-µm thick slices of rock oriented perpendicularly to the orientation of the lamination. The thin sections were evenly distributed throughout the stratigraphy of both the drill-cores. Major mineral phases and petrographic textures were characterized using the optical microscope under plane polarised light (PPL) and cross-polarised transmitted light (XPL). Photomicrographs were occasionally made with a Leica MC170 HD microscope camera.

3.3 X-Ray Fluorescence

The remnants of the drill-cores were crushed and powdered using a tungsten carbide Herzog HP-MA. The Herzog HP-MA caused a contamination of both W and Co to the powdered samples. Since the contamination was dependent on the hardness of the sample, which was highly variable throughout the stratigraphy, a correction could not be made. Major element analyses of the bulk powdered sample was resolved using the Thermo ARL 9400 sequential XRF, the LOI was measured using the Leco TGA701, both at Utrecht University.

The high amount of Fe present in the samples caused interference during XRF analyses. A simple uniform correction was applied for all the Fe_2O_3 values so that the total weight amount would be ~100%.

3.4 LA-ICP-MS

Laser ablation inductively coupled plasma mass spectrometry (LA-ICP-MS) was used to obtain the trace elements, including rare earth element composition. Laser ablation was performed with a 193 nm wavelength COMpex 102 ArF excimer laser ablation system connected to an Element 2 sector field ICP-MS. The ICP-MS was operated in low resolution mode, and the laser with an energy density of 11 J/cm2 and a pulse repetition rate of 10 Hz. The laser crater diameter was the largest possible at 120 um, to give a high analytical precision. Every sample was analysed in triplex and then averaged to obtain an optimal value for each specific element and to even out any miscalculations. Ni and Mo were only measured one time as these elements were initially not present in the method used for the ICP-MS. The glass beads used for the laser ablation analysis were made by mixing 0.6 gram of sample powder and 6 gram of flux (66% Lithium Tetraborate, 34% Lithium Metaborate and 0.5% Lithium Iodide), where fusion occurred at 1200 °C. The flux was slightly contaminated with lanthanum and cerium. The contamination was corrected by measuring 3 unique glass beads made of pure iron powder and flux, each with a different ratio. Since no contamination was present in the pure iron powder, all of the measured La and Ce values were related to the contaminant in the flux and were subtracted from the original LA-ICP-MS data. The remaining REE measurements were below the detection limit and thus did not cause any contamination (see Appendix).

The reduction of the laser ablation data was performed using the software GLITTER. Calibration of the samples was performed regularly against NIST 612 glass, while BCR-2G was used as a reference standard. These results were usually within 10% of the published reference values of the GeoReM database (the measured BCR-2G values, the GeoReM standard and the sample deviations are given in the appendix). The REE+Y patterns were normalized to Post-Archean Australian Shale (PAAS) using the values of Taylor and McLennan (1985).

3.5 Carbon isotope measurements

Carbon isotope analysis of the bulk rock samples was performed using the methods of Craig (1953) and Craig (1957). Dependent on the C abundance, 60-90 mg of sample powder together with ~ 2 ml of concentrated H_3PO_4 (102 %) was carefully placed in a sealed pyrex Y tubes and made vacuum. The samples were then thermally equilibrated in an oil bath at 115 °C and then reacted for > 1 hour. The reacted gas was captured into a vacuum pump and condensed in a reactant glass tube using liquid N_2. The carbon isotope ratios were then measured using a THERMO MAT 253 Mass Spectrometer.

3.6 X-Ray Diffraction

X-Ray Diffraction (XRD) analyses were carried out on a selected amount of samples, spread out evenly throughout the stratigraphy, to obtain insight into the minerology of the BIFs. XRD is a qualitative method and thus only presents information on whether or not a mineral phase is present or not, so the total amounts cannot be acquired. Approximately 1 gram of sample powder was placed on a glass slide and analyzed using the Bruker-AXS D8 advance powder X-ray diffractometer configured with LYNXEYE detector and DAVINCI design. Ceramic 2,2 kW Cu $K\alpha_{1,2}$ tube, λ=1,54060 Å radiation was applied and operated at 40 kV/40mA.

The XRD exposes the powdered samples to X-rays at different angels (θ). The radiation will be diffracted by the crystals in the sample, when Bragg’s law is satisfied: $2d(sin\theta) = \lambda$. Differences in crystallography of the mineral phases will result in unique diffraction patterns. The angle (θ) of the diffracted radiation was measured and the characteristic crystal lattice interplanar spacing d could then be calculated and further analyzed. The 2θ plots were analyzed and interpreted using the Diffrac plus BASIC Evaluation package EVA software. The intensity peaks in the 2θ scan were analyzed and the corresponding minerals phases were selected using the program’s mineral database.

Table 1: Sample number for every sample used in this thesis with its corresponding depth (m) for both the G7BF and MP-BIF sections.

Sample Nr.	*Depth (m)*
G7BF-01	90,81
G7BF-02	91,28
G7BF-03	91,65
G7BF-04	92,1
G7BF-05	92,48
G7BF-06	92,94
G7BF-07	93,34
G7BF-08	93,88
G7BF-09	94,35
G7BF-10	94,73
G7BF-11	95,11
G7BF-12	95,73
G7BF-13	96,23
G7BF-14	96,73
G7BF-15	97,15
G7BF-16	97,54
G7BF-17	98,02
G7BF-18	98,6
G7BF-19	99,02
G7BF-20	99,42
G7BF-21	100,18
G7BF-22	100,56

Sample Nr.	*Depth (m)*
MP-BIF-01	396,45
MP-BIF-02	396,67
MP-BIF-03	397,19
MP-BIF-04	397,85
MP-BIF-05	398,4
MP-BIF-06	398,74
MP-BIF-07	399,22
MP-BIF-08	399,72
MP-BIF-09	400,21
MP-BIF-10	400,67
MP-BIF-11	401,24
MP-BIF-12	401,68
MP-BIF-13	402,04
MP-BIF-14	402,56
MP-BIF-15	403,06
MP-BIF-16	403,55
MP-BIF-17	404,04
MP-BIF-18	404,55
MP-BIF-19	405
MP-BIF-20	405,48
MP-BIF-21	405,92
MP-BIF-22	406,37
MP-BIF-23	406,79
MP-BIF-24	407,28
MP-BIF-25	407,8
MP-BIF-26	408,32
MP-BIF-27	408,7

Sample Nr.	*Depth (m)*
MP-BIF-28	409,22
MP-BIF-29	409,73
MP-BIF-30	410,21
MP-BIF-31	410,55
MP-BIF-32	411,2
MP-BIF-33	411,45
MP-BIF-34	411,96
MP-BIF-35	412,47
MP-BIF-36	412,99
MP-BIF-37	413,49
MP-BIF-38	413,98
MP-BIF-39	414,53
MP-BIF-40	414,93
MP-BIF-41	415,51
MP-BIF-42	415,87
MP-BIF-43	416,3
MP-BIF-44	416,82
MP-BIF-45	417,29
MP-BIF-46	417,86
MP-BIF-47	418,43
MP-BIF-48	418,9
MP-BIF-49	419,41
MP-BIF-50	419,85
MP-BIF-51	420,3
MP-BIF-52	420,41
MP-BIF-53	420,92

4. Results

4.1 Hotazel BIF Mineral assemblages

Table 2 shows which mineral phases have been identified in some selected samples. All samples consist mostly of quartz, presumably in the form of chert. Magnetite is the second most observed mineral phase, present in all samples apart from G7BF-14. The carbonates consist of siderite, ankerite and on occasion calcite as well. The calcite is mostly present in the G7BF core, just once in the MP-BIF. The presence of calcite is not necessarily primary and could also occur in secondary veins. However, the calcite veins visible in the quarter-core pieces were cut out to avoid contamination of secondary precipitates. Another major difference between the two sections is that siderite is present in the entire MP-BIF section, while it is nearly absent in the G7BF. Hematite can be found in the top 5 meters of the G7BF core, as well as the bottom 5 meters of the MP-BIF core. Hematite and magnetite are the only two iron oxides in this BIF succession. The iron silicates consist mostly of minnesotalite; greenalite is also present throughout the entire G7BF stratigraphy but the amount of counts measured with the XRD remained very low. Minnesotalite becomes present in the stratigraphy from G7BF-14 onwards towards the top of this section. Whereas it is present in almost the entire MP-BIF section. The remaining iron silicates e.g. stilpnomelane and riebeckite do not occur in any of the samples. The interpreted XRD results can be found in the Appendix.

Sample no. G7BF	Ch	Mag	Hem	Ank	Sid	Cal	Gre	Minn
1	X	X	X	X				
6	X	X	X	X			X	X
9	X	X	X	X		X	X	X
11	X	X		X		X	X	X
13	X	X		X		X	X	X
14	X			X		X	X	X
19	X	X			X		X	
21	X	X		X		X	X	
22	X	X		X			X	

Sample no. MP-BIF	Ch	Mag	Hem	Ank	Sid	Cal	Gre	Minn
2	X	X	X	X			X	X
8	X	X		X	X		X	X
15	X	X			X	X		X
22	X	X		X	X			X
33	X	X			X		X	X
40	X	X		X	X		X	X
42	X	X	X	X	X		X	X
46	X	X	X	X	X		X	X
49	X	X	X		X		X	X
52	X	X	X		X		X	X

Table 2: Mineral assemblages for representative samples of the Hotazel BIF, detected by the XRD. Abbreviations: Ch = Chert-Quartz; Mag = Magnetite; Hem = Hematite; Ank = Ankerite; Sid = Siderite; Cal = Calcite; Gre = Greenalite and Minn = Minnesotalite.

4.2 Petrographic observations.

The optical microscope is excellent for distinguishing carbonates, silicates and oxides within the banded iron formation and for observing general textures of the rock. The exact minerology however cannot be fully constrained without the use of an electron microprobe (EMP). The XRD results were used to confirm the presence of each individual mineral phase. The iron-oxides consist of magnetite ($Fe^{2+}Fe^{3+}{}_2O_4$) and hematite (Fe_2O_3), mostly present in larger euhedral grains (Figure 8A-D). BIF-hosted magnetite is usually also depleted in trace elements (Nadoll et al., 2014; Chung et al., 2015; Alibert, 2016). The carbonate minerals present in BIFs predominantly consist of ankerite ($Ca,Fe(CO_3)_2$), siderite ($FeCO_3$) and Calcite ($CaCO_3$). These mineral phases are easily recognizable by their high birefringence in XPL. The crystal grainsize varies from large rhombohedral grains to a microcline matrix, often together in one band (Figure 7E,F). The most common silicate mineral is quartz, in the form of chert, and is usually present as the matrix in the BIF. There are usually 4 iron-silicates present in BIFs (Klein, 2005): Greenalite [$(Fe^{2+},Fe^{3+})_{2\text{-}3}Si_2O_5(OH)_4$], Minnesotalite [$(Fe^{2+},Mg)_3Si_4O_{10}(OH)_2$], Stilpnomelane [$K(Fe^{2+},Mg,Fe^{3+})_8(Si,Al)_{12}(O,OH)_{27} \times n(H_2O)$] and Riebeckite [$Na_2(Fe^{2+}{}_3Fe^{3+}{}_2)Si_8O_{22}(OH)_2$]. Riebeckite is the only mineral in BIFs to accommodate Na, while stilpnomelane is the only mineral phase in BIFs to accommodate K. The XRD results indicated no presence of riebeckite or stilpnomelane so their occurrence is unlikely. Greenalite and minnesotalite constitute the silicate mineral phases and occur as a very fine grained matrix, together with chert. The lamination in mineralogical composition of the BIF usually spans from 400µm to 1mm thick (Figure 7A-D). Soft sediment deformation structures are present in the upper part of the stratigraphy as well (Figure 6), which was previously observed by Tsikos (1994).

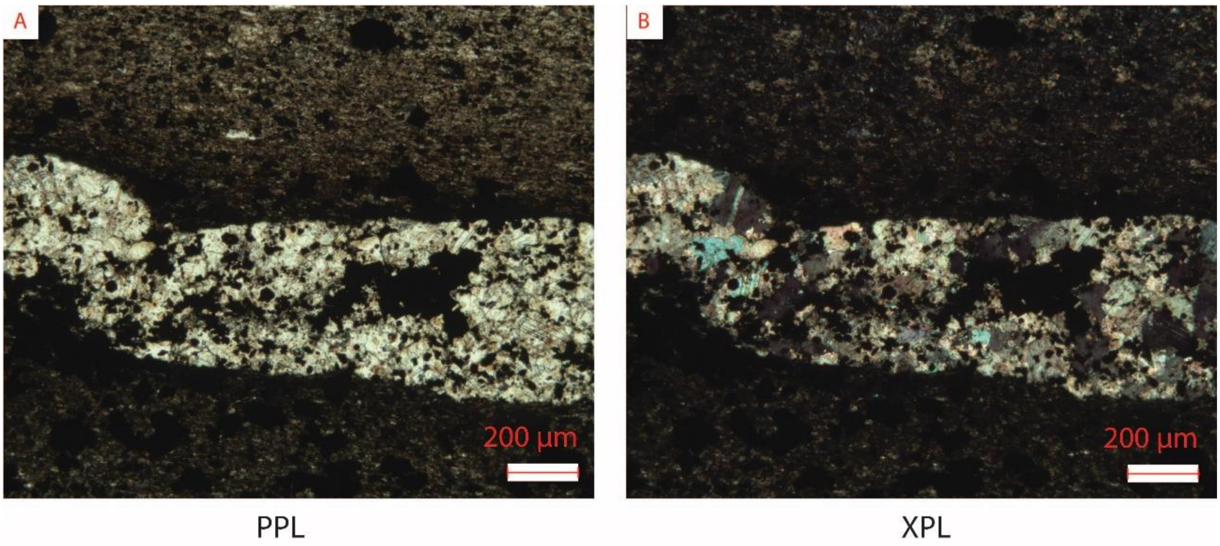

Figure 6: Soft sediment deformation structures between a carbonate-rich band and a silica-rich matrix observed in the G7BF-01 sample.

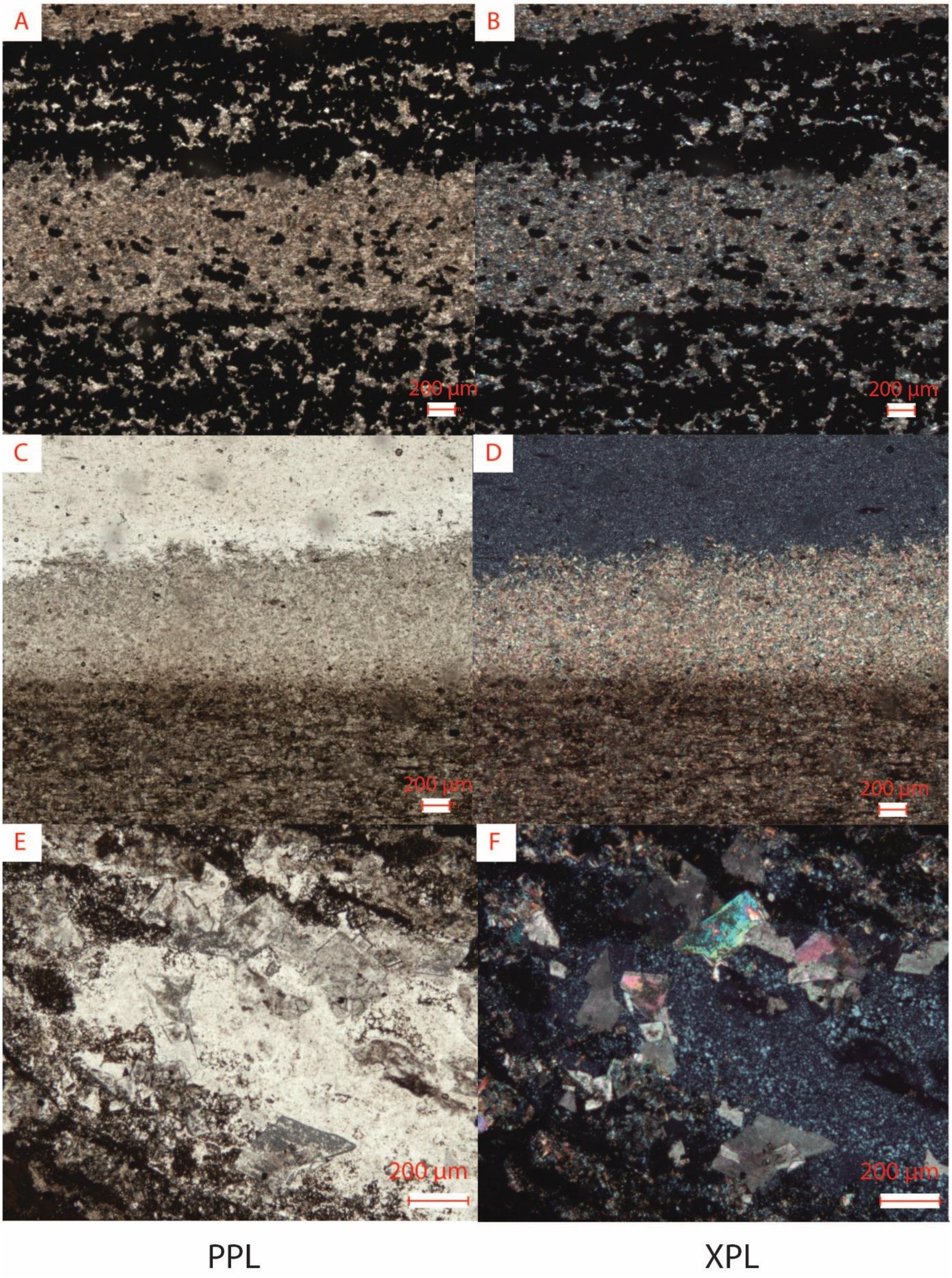

Figure 7: Microscope images of the G7BF section of the Hotazel BIF. A & B: mm scale banding between Oxide and Carbonate mineral phases (GFBF-04), C & D: sequence of 3 laminated bands of iron-oxide minerals in a chert matrix, a band of small-grainsize carbonates and an iron-silicate (presumably minnesotalite) from bottom to top (G7BF-11), E & F: rhombohedral calcite grains in a microcline matrix (G7BF-14).

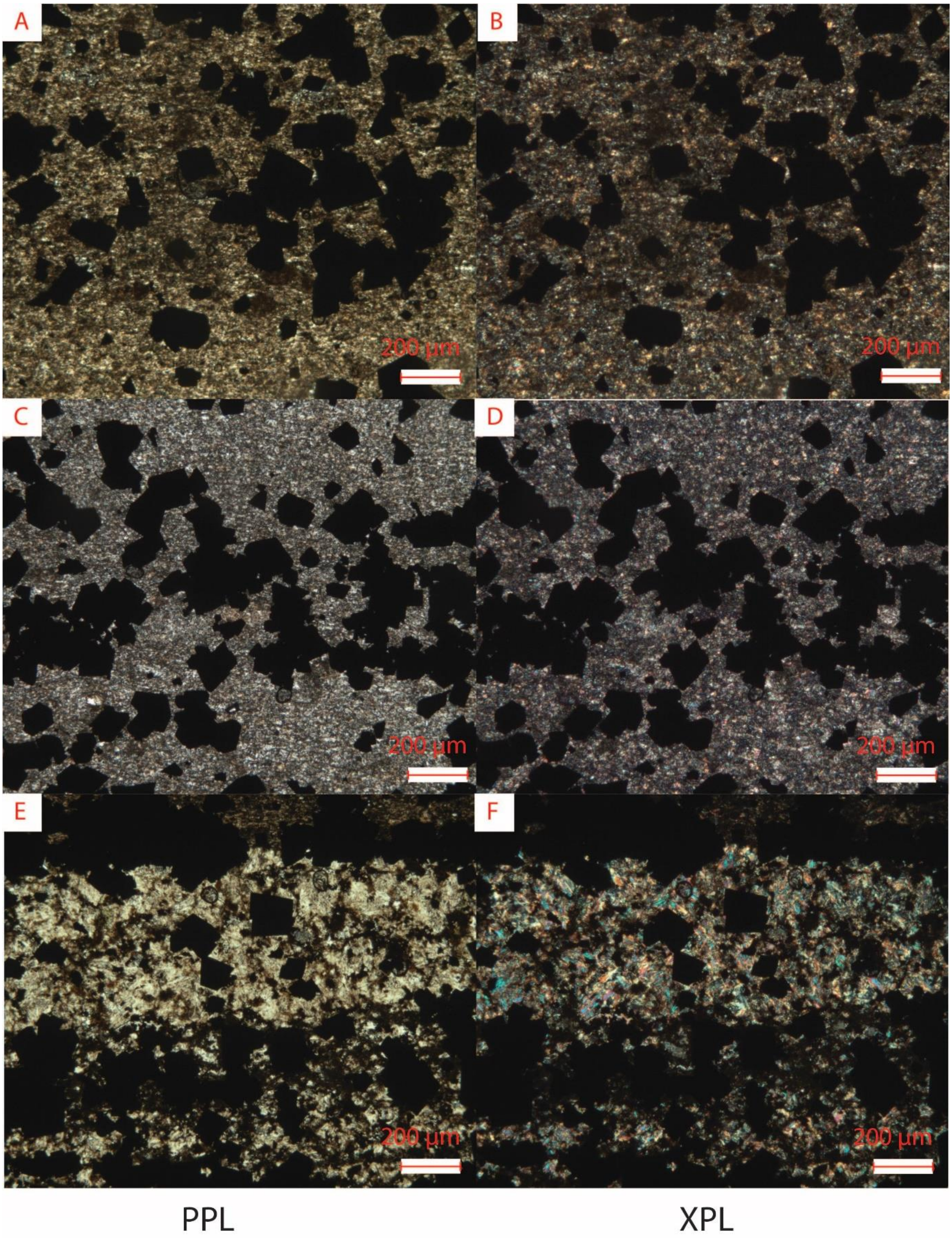

Figure 8: Microscope images of the MP-BIF section of the Hotazel BIF. A & B: Euhedral Magnetite / Hematite grains in a chert-rich matrix (MP-BIF-08), C & D: Euhedral Magnetite / Hematite grains in a carbonate matrix (MP-BIF-22), E & F: mm scale laminated oxides and small-grainsized carbonates (MP-BIF-44).

4.3 Major element geochemistry

The XRF data containing the weight percentage for each major element oxide are plotted in Figure 9 and 10. The SiO_2 concentrations in the G7BF and the MP-BIF cores range from 30.1-61.6 wt% and 22.5-61.2 wt% respectively. The average SiO_2 concentration of the G7BF samples is 45.4 wt% and is higher than that of the MP-BIF, which is 40.8 wt%. Also, there is an overall decrease in value towards the base of the MP-BIF. SiO_2 anti-correlates with Fe_2O_3 in both sections. The Fe_2O_3 concentrations range from 26.0 – 61.4 wt% and 16.0-67.1 wt% for the G7BF and MP-BIF cores respectively. On average the Fe_2O_3 concentration of the G7BF samples is 38.9 wt%, which is much lower than the 45.6 wt% of the MP-BIF. The top meter of the G7BF core is anomalously rich in silica and depleted in iron. The CaO concentrations are much lower than those of SiO_2 and Fe_2O_3 and range from 1.1-13.7 wt% in the G7BF core and from 0.3-10.5 wt% in the MP-BIF. While the CaO concentrations increase towards the base of the G7BF core, there is a gradual increase towards the top of the MP-BIF core. The MnO concentration gradually increases from 0.3 wt% at the top towards 1.4 wt% at the base in the G7BF core. This increase is also notable in the MP-BIF core, where MnO concentrations increase from 0.5 wt% at the top towards 2.1 wt% at the base. This is consistent with the stratigraphical increase in concentration towards the Mn-rich intercalation stratigraphically below this BIF. However, there is a notable difference in average MnO (wt%) concentration observed between the 2 sections. (1.04 wt% in the MP-BIF; 0.62 wt% in the G7BF). The MgO concentration also shows a gradual increase towards the base of both cores ranging in values from 0.5 towards 4.6 wt%. The Al_2O_3 concentrations increase towards the base of both cores ranging from 0.01 – 0.1 wt%. The concentrations for P_2O_5, K_2O, Na_2O and TiO_2 were all below 0.5 wt%, often even below the detection limit and will not be further discussed.

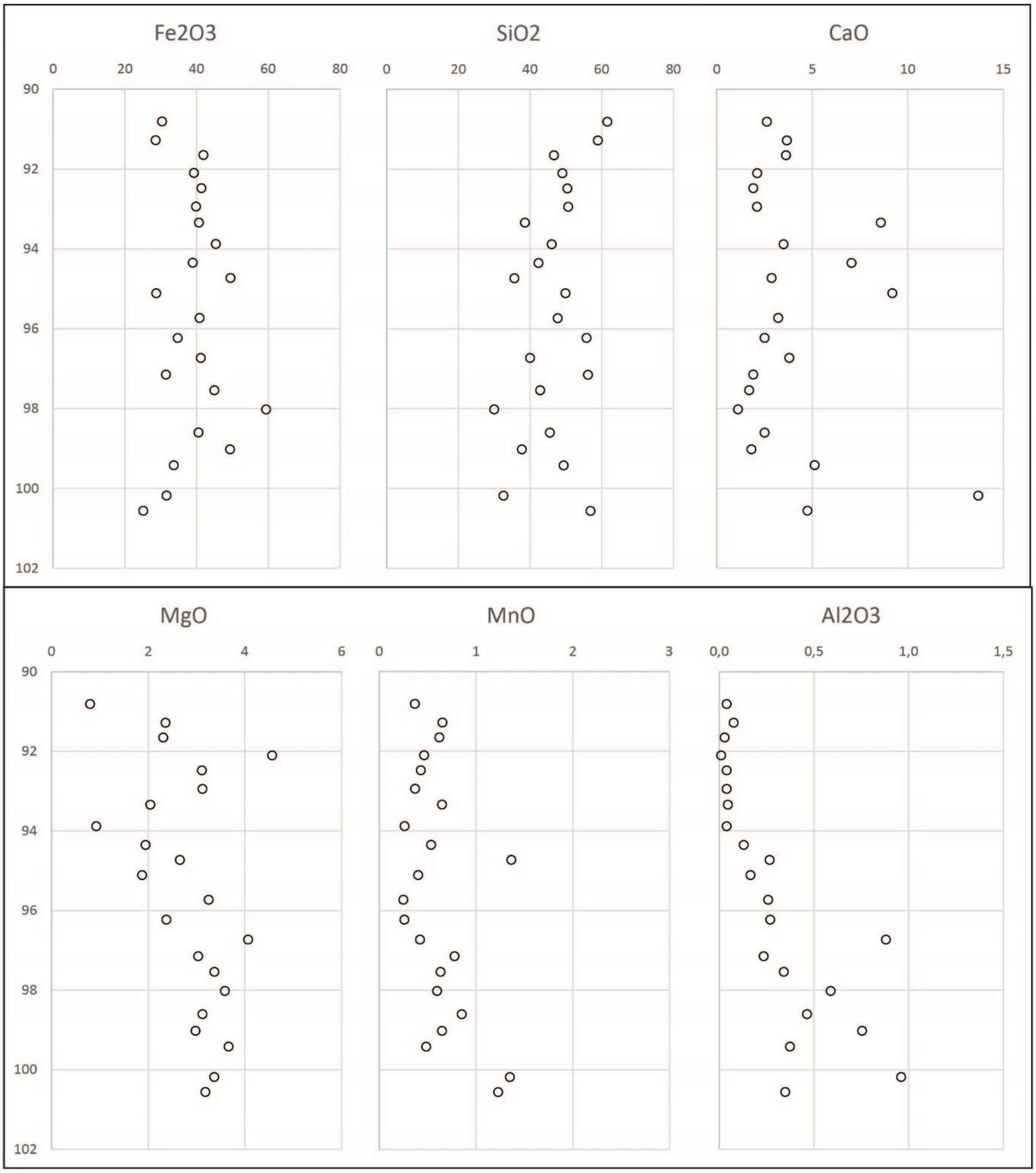

Figure 9: Major element oxides in (wt%) plotted over depth (in meters) for the G7BF section.

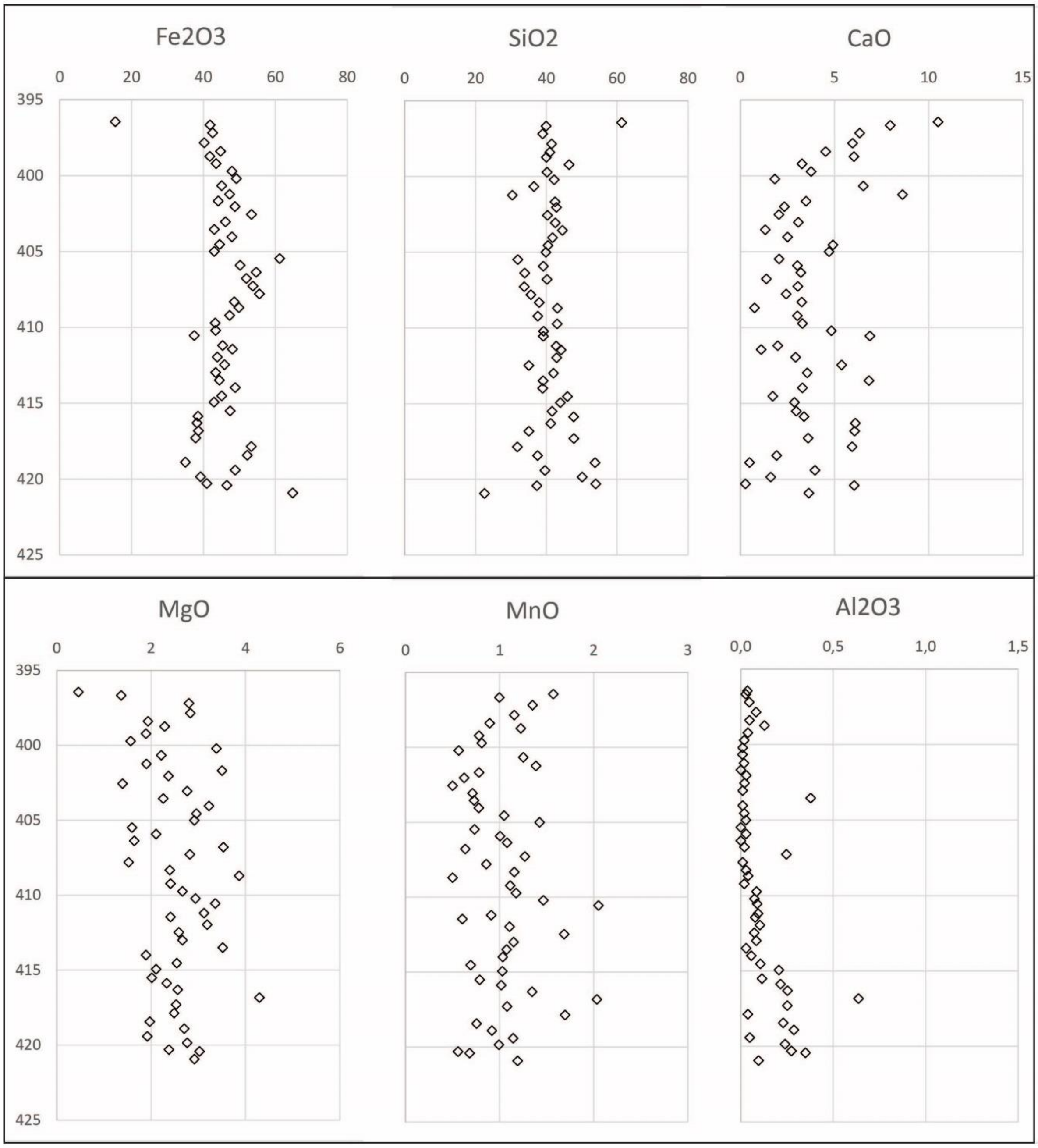

Figure 10: Major element oxides in (wt%) plotted over depth (in meters) for the MP-BIF section.

Most of the Mn is incorporated into the carbonate fraction of the BIF (Johnson et al., 2013). When plotting MnO over CaO it becomes apparent that the carbonates become more manganese rich towards the base of both cores (Figure 11).

The Fe/Mn ratio of the MP-BIF core ranges between 8.8 and 95.6 with an average of 44.7. In the G7BF core the Fe/Mn ratio values lie between 155.2 – 18.4 with an average over 65.8 (Figure 12). Overall the middle parts of both cores show the largest values, with a decrease towards the base and top of the section. There is a more notable decrease towards the base of the G7BF core, with values of 18.4 – 21.0 in the bottom 1st meter of this section. Here starts the transition towards the Mn-lutite and is therefore in agreement with Tsikos et al. (2010), which noted that the Mn-ores have a Fe/Mn ratio of ~ 15-20 and the BIF section has a Fe/Mn ratio of ~50.

Figure 11: MnO/CaO ratio plotted over depth (m) for the G7BF section (left) and the MP-BIF section (right). There is a stratigraphic increase of MnO/CaO towards the base of both sections observable in the plots.

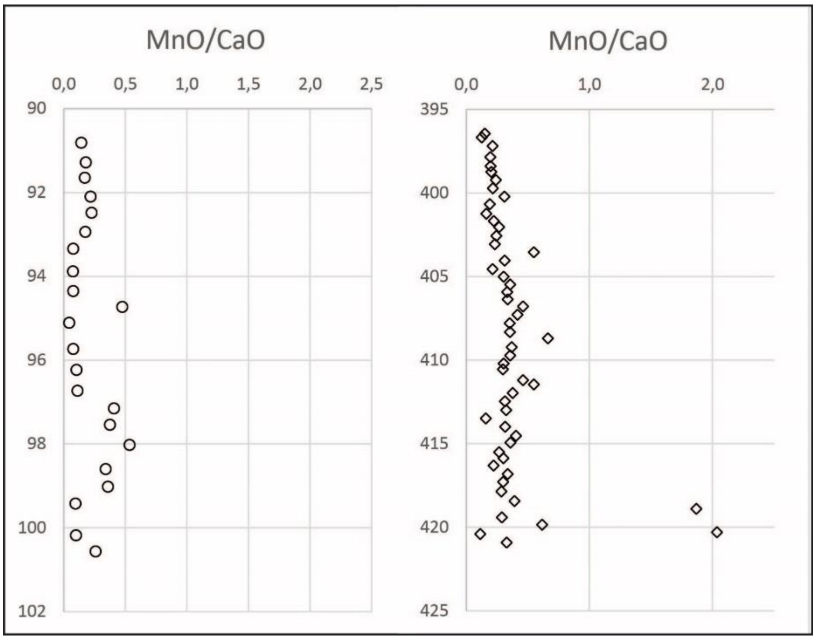

Figure 12: Fe/Mn ratio plotted over depth (m) for the G7BF section (left) and the MP-BIF section (right). See text for discussion.

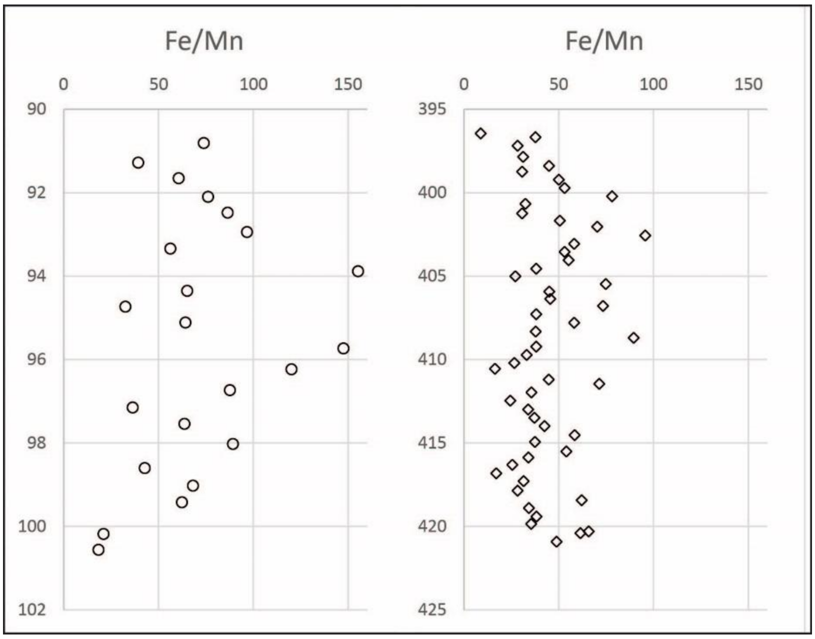

4.4 Trace element geochemistry

Figures 13 and 14 show the trace element data plotted against core depth (m) for the G7BF and MP-BIF sections respectively. Measured values of the immobile high field strength elements (HFSE) Al, Sc, Ti, Zr, Th and Pb all increase substantially towards the base of the succession. These elements reflect the presence of allochthonous detritus or volcanic-ash in the sediments. The trend can be seen in both the MP-BIF core and the G7BF core, with the increase being even greater in the latter. The succession of the MP-BIF core shows a smaller but noticeable increase in these HFSE towards the middle part of the core as well, with a peak value at 407 m depth. The total abundance of these elements however remain very low, with Al (50-5000 ppm), Ti (16-394 ppm), Sc (1,4-6,8 ppm), Zr (2,2-22 ppm), Th (0,1-2,4 ppm) and Pb (0.7-5.9 ppm). The transition metals V, Mo and Cr show a similar pattern and all increase in value towards the base of each core. Cu and Zn remains fairly constant throughout both of the cores with average values of 9 and 25 ppm respectively. The Large Ion Lithophile Elements (LILE) Sr, Rb and Ba do not show a clear stratigraphic trend. Ba remains relatively constant while Sr and Rb fluctuate somewhat throughout the sections. The G7BF and MP-BIF sections often share a similar abundance per element in ppm and major differences do not occur. Note that the error margins are small, which in terms indicates a high accuracy of the measurements and the LA-ICP-MS analyses in total.

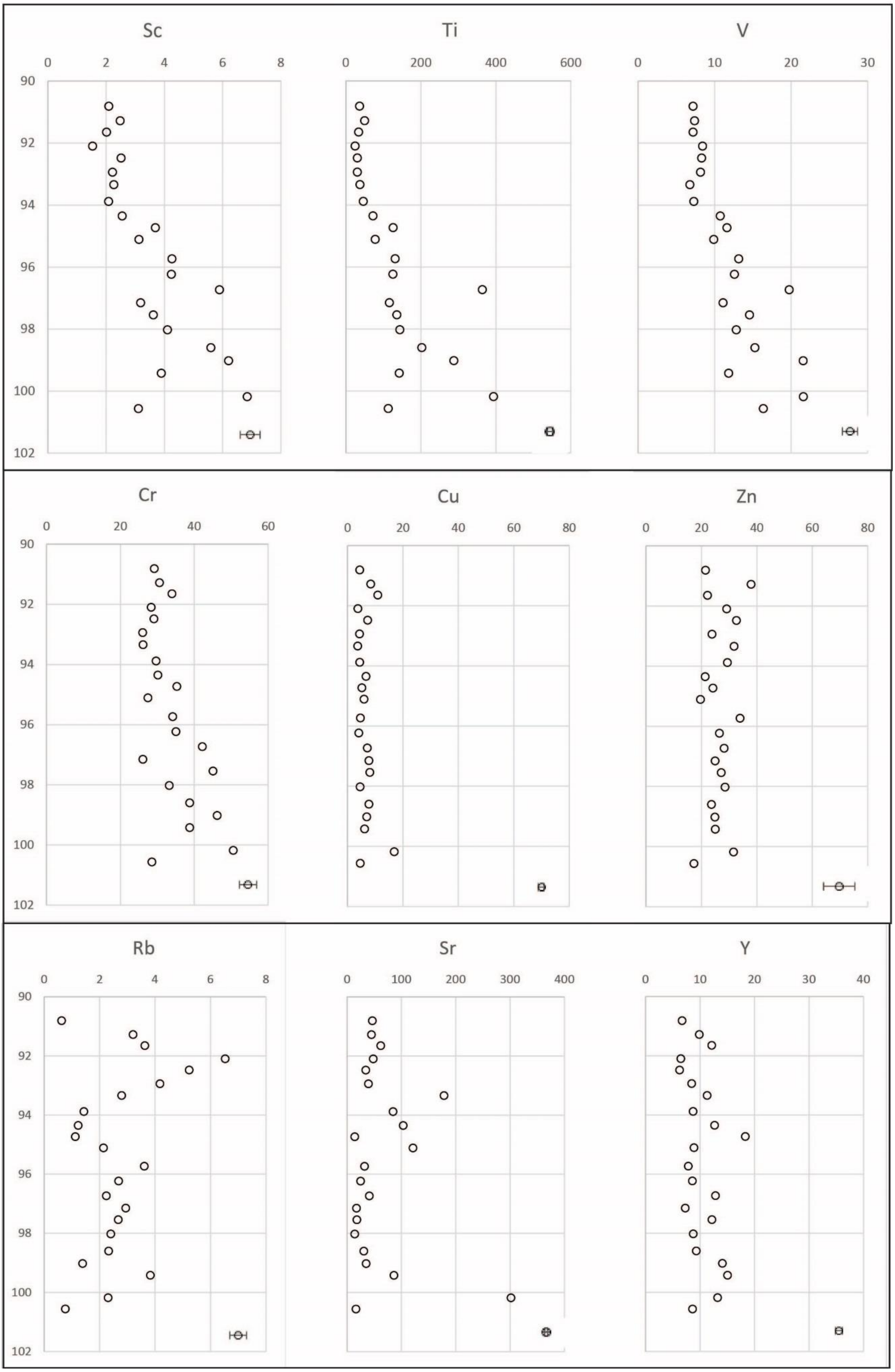

Figure 13: Trace element abundances of the G7BF section (in ppm) plotted over depth (m). All trace elements are measured using the LA-ICP-MS. Error bars are added in the lower-right corner of each plot. (See text for discussion)

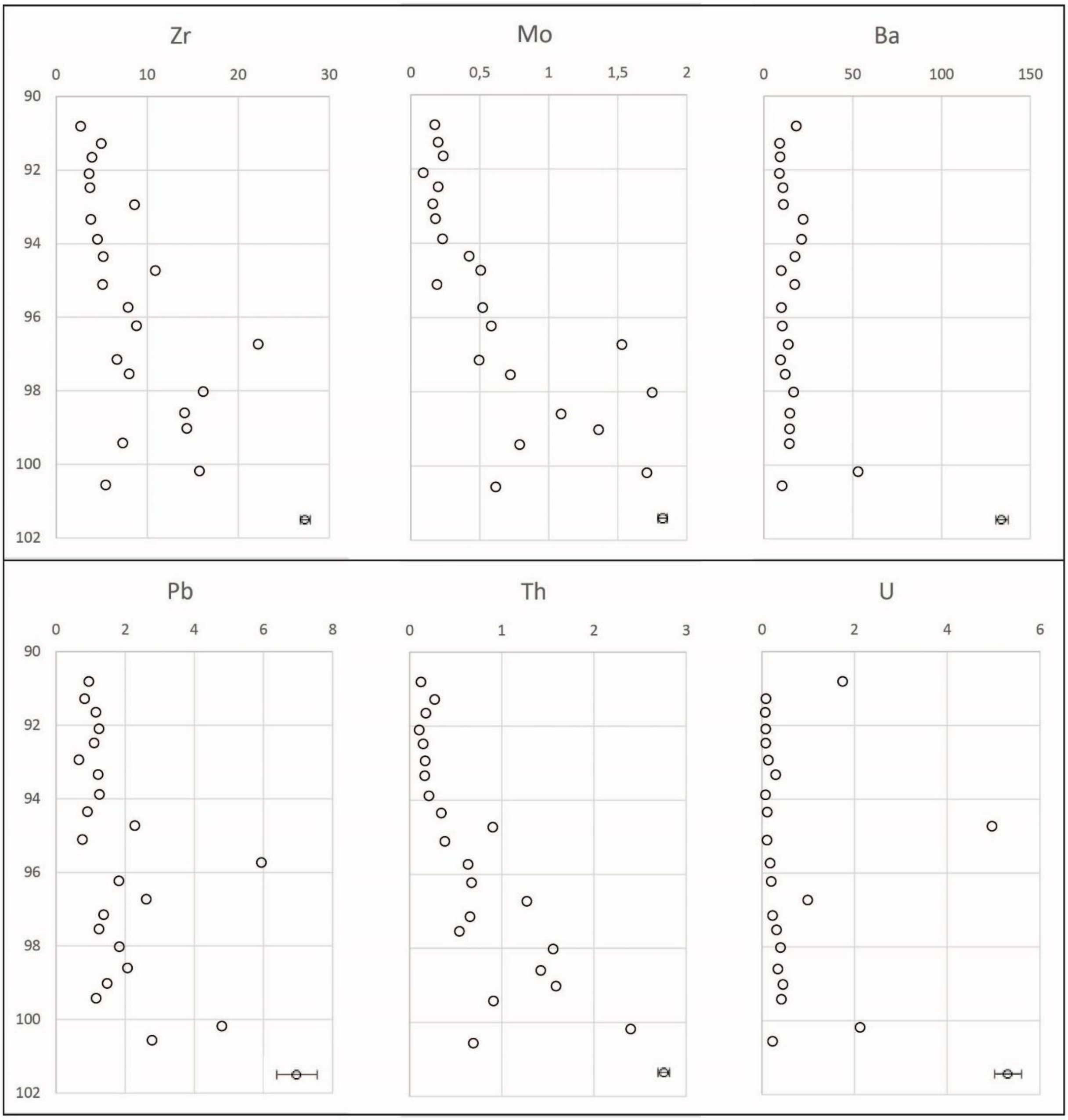

Figure 13: (Continued)

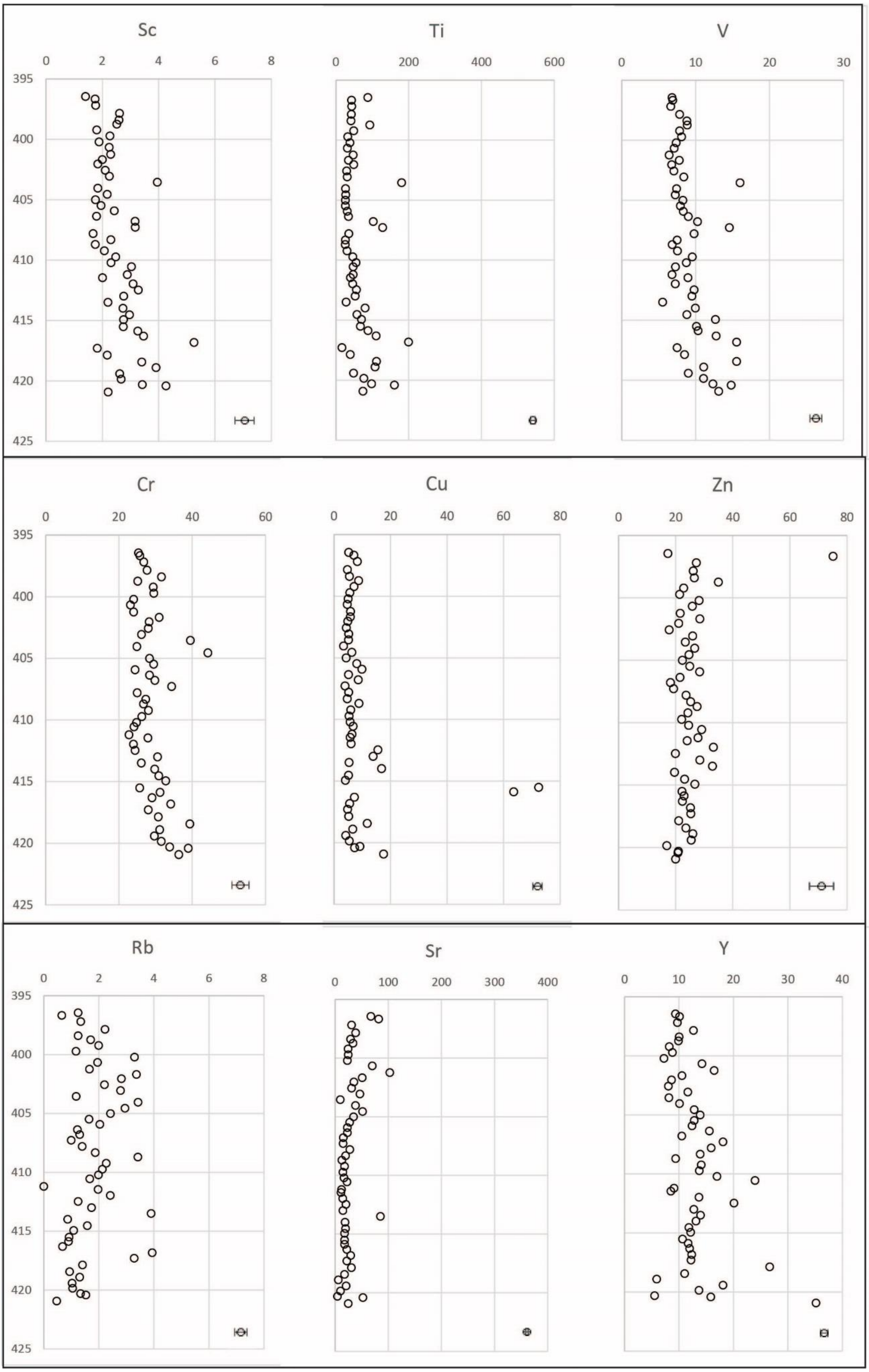

Figure 14: Trace element abundances of the MP-BIF section (in ppm) plotted over depth (m). All trace elements are measured using the LA-ICP-MS. Error bars are added in the lower-right corner of each plot. (See text for discussion)

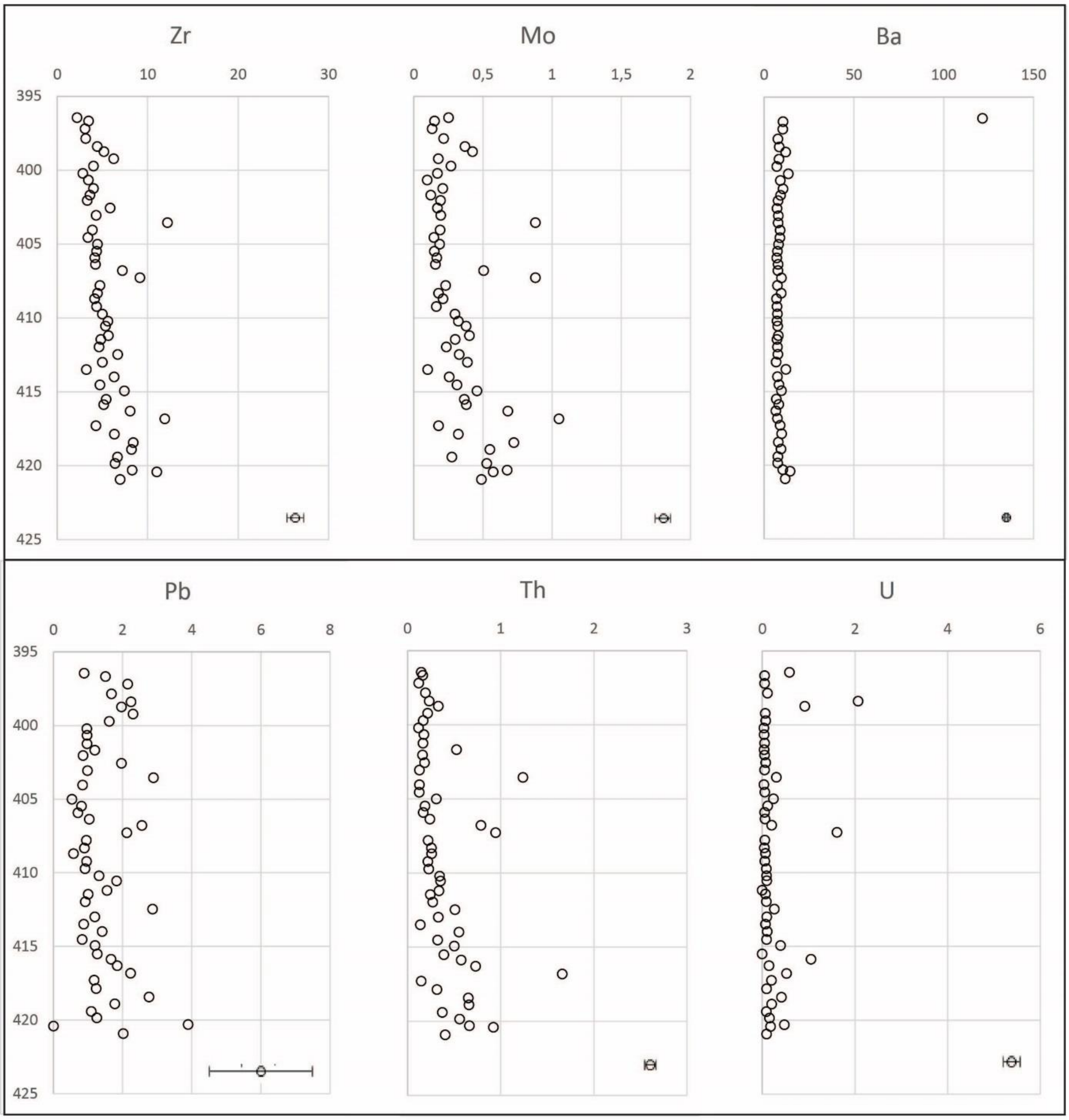

Figure 14: (Continued)

4.5 Rare-earth element and Y distribution.

The lanthanide series element abundances are often consistent with relative atomic mass in geochemical systems. This is due to the gradual decrease of ionic radii from Lanthanum (1.16 Å) towards Lutetium (0.977 Å). Anomalies present within the lanthanide series can be determined by dividing the measured abundance of an element by one extrapolated from the neighbouring REEs: $[REE_n/REE_n^*] = REE_n/(\frac{1}{2}REE_{n-1}+\frac{1}{2}REE_{n+1})$, where REE_n are reported as the normalized elemental abundance and n=1, 2, 3, is the REE in the order of the lanthanide series (Bolhar et al., 2004). Some deviations from this method are needed when an element has only one neighbour or if a neighbouring element behaves anomalously as well. Both La and Ce can be anomalous and since La has no other neighbour, La and Ce anomalies are expressed graphically by plotting Ce/ Ce* vs. Pr/Pr* (Bau and Dulski, 1996). Both Eu and Gd can be anomalous in BIF, so their anomalies are calculated using Sm and Tb: $[Eu/Eu^*] = Eu/(\frac{2}{3}Sm + \frac{1}{3}Tb)$ and $[Gd/Gd^*] = Eu/(\frac{1}{3}Sm + \frac{2}{3}Tb)$. Ce and Eu are the only REE that are redox-sensitive because they have an additional oxidation state next to the standard trivalent one. BIFs often have positive La, Eu, Gd and Y anomalies and are depleted in LREE relative to HREE.

Figure 15 shows the REE + Y distribution of the MP-BIF and the G7BF sections, each showing the minimum, maximum and average value of the entire section. The REE + Y data for modern seawater has been added for comparison with values taken from Bau et al. (1996). Modern seawater shows HREE enrichment relative to LREE, a distinct negative Ce anomaly and positive La, Gd and Y anomalies. The REE + Y signal of modern seawater is very similar to those of the MP-BIF and G7BF cores. Both cores show a positive La, Gd and Y anomaly and are enriched in HREE relative to LREE. However, the distinct negative Ce anomaly in modern seawater in not present in any of the two sections. The slope of REE + Y plot is constrained by the (Yb/Ce)N and the average values are 3.7 and 2.4 for the MP-BIF and G7BF cores respectively. There is a notable peak at 98 meters depth of the G7BF section and a gradual decrease towards the top. The MP-BIF section has 2 peaks at ~410 and ~420 meters depth with values up to 14-15 (Figure 16A). There is no correlation between (Yb/Ce)N and Zr in both sections (Figure 16B). On average the REE + Y distribution of the G7BF section is very similar to that of the MP-BIF. The Y/Ho and positive Gd anomaly however, are larger in the MP-BIF section.

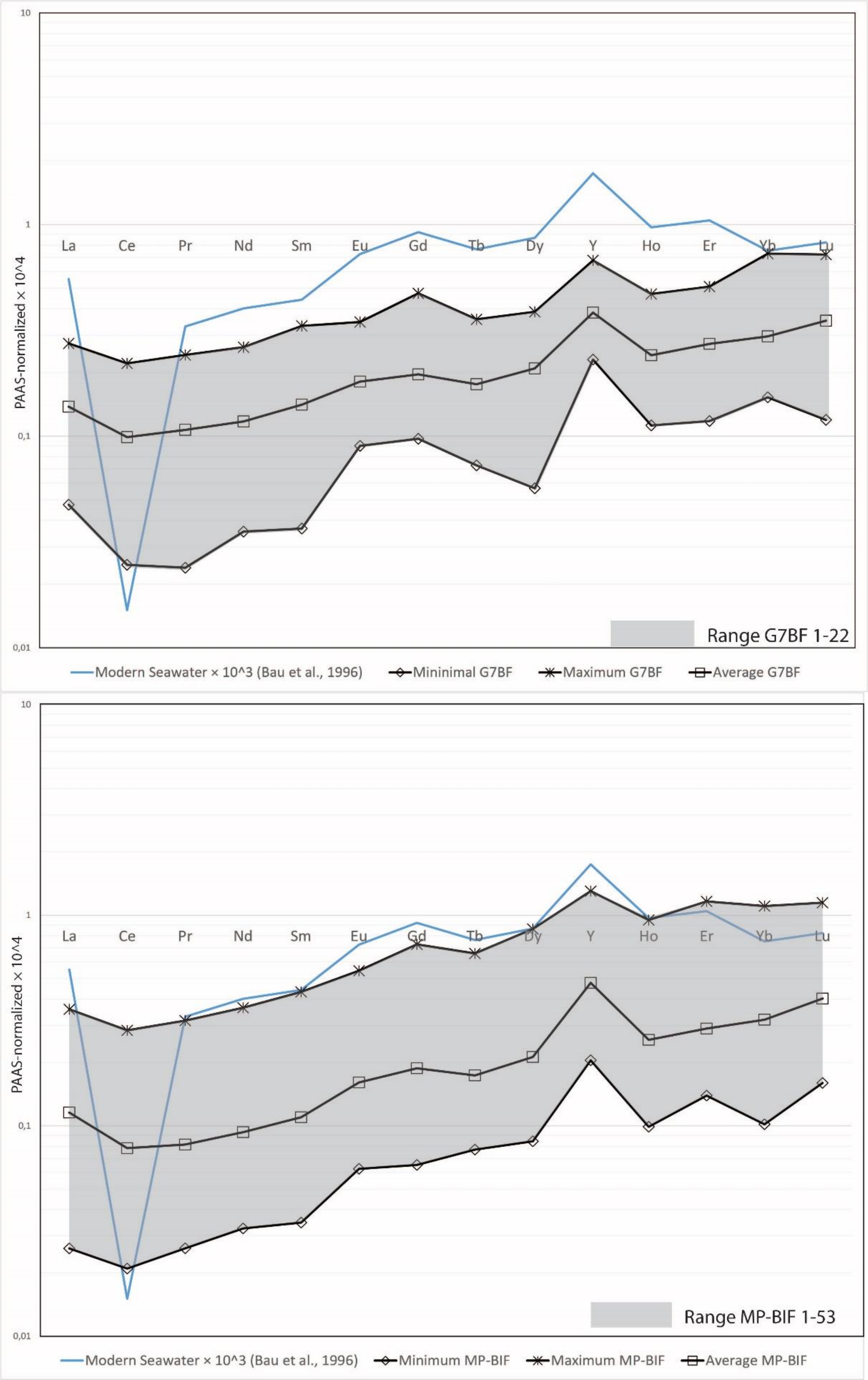

*Figure 15: Plots of rare-earth element + Y data normalised to post Archean Australian shale (PAAS). REE + Y concentration (ppm) of the Minimum, Maximum and Average values for the G7BF section (**Top)** and the MP-BIF section (**Bottom**). Both sections compared with Modern seawater values from Bau et al., (1996). The REE + Y plots show a positive La, Gd and Y anomaly, are depleted in LREE and show no distinct negative Ce anomaly. Apart from this negative Ce anomaly, which is present in modern seawater, the REE + Y distribution is very similar to those of modern sweater.*

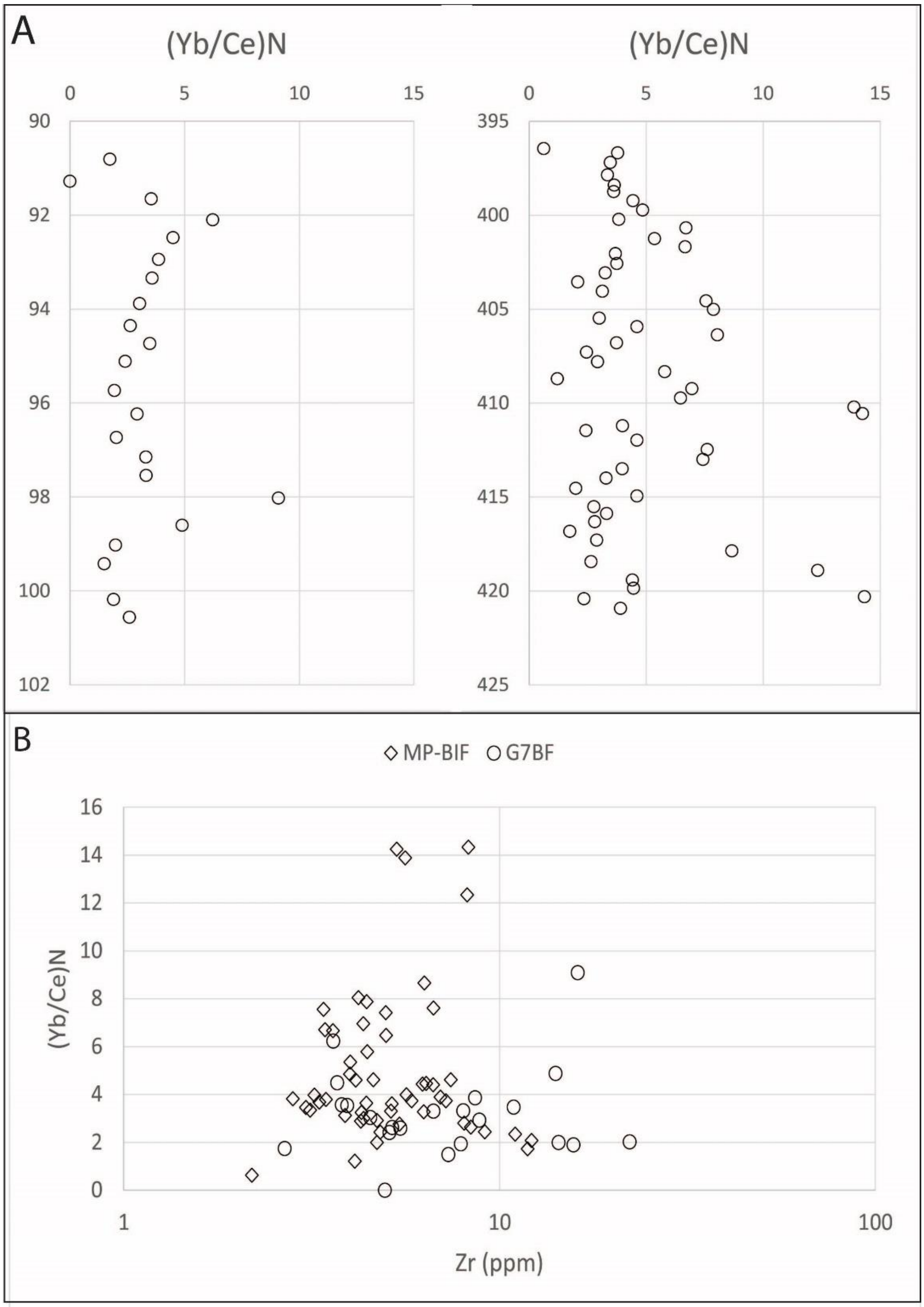

Figure 16: (A) (Yb/Ce) ratios plotted over depth (m) for the G7BF section (left) and the MP-BIF section (right). Error bars are added in the lower-right corner. (See text for further discussion). (B) Y/Ho ratio vs Zr(ppm). There is no clear correlation present between (Ce/Yb) and Zr abundances.

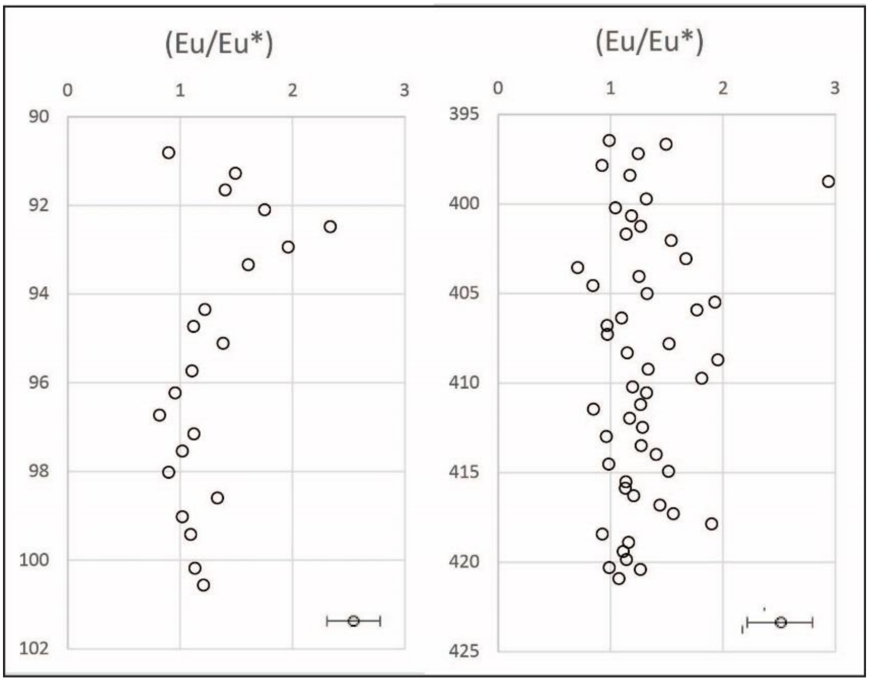

Figure 17: Europium anomaly plotted over depth (m) for the G7BF section (left) and the MP-BIF section (right). Error bars are added in the lower-right corner. (See text for discussion)

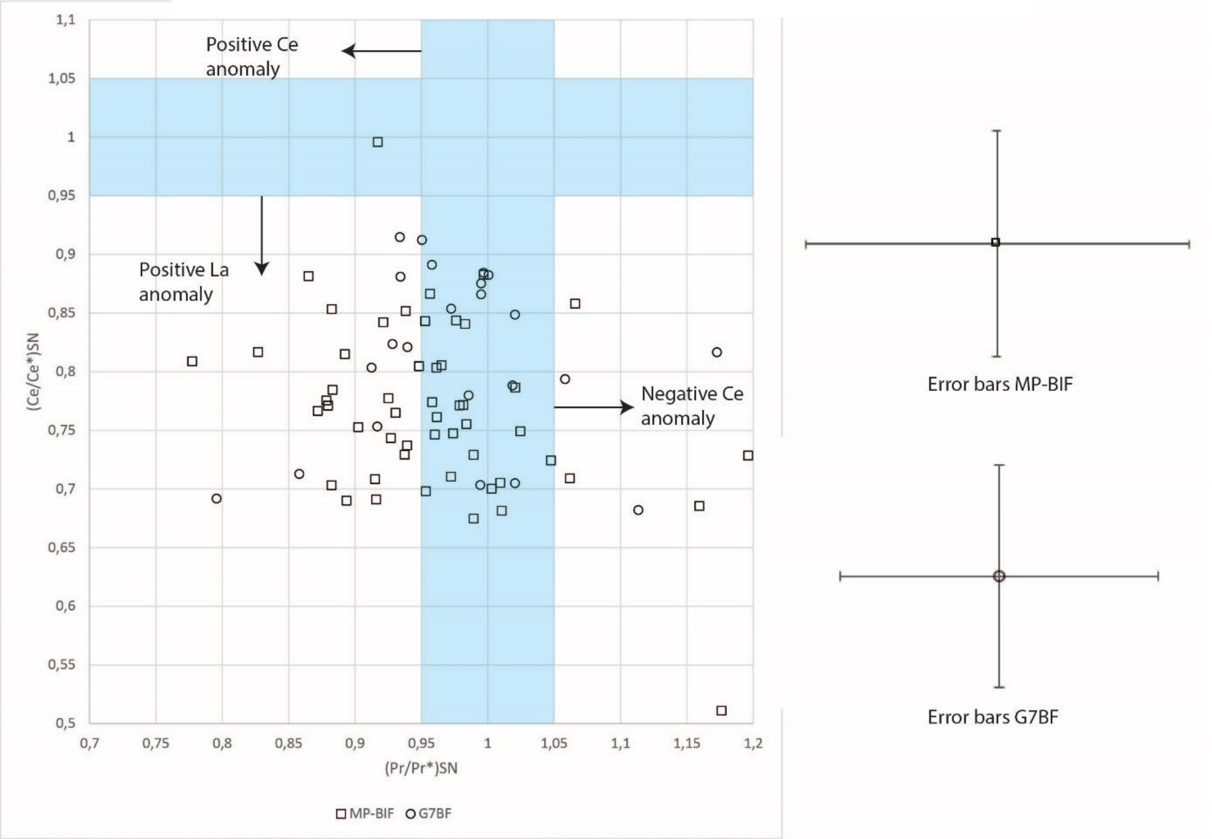

Figure 18: (Ce/Ce*) versus (Pr/Pr*) (after Bau and Dulski, 1996) for all measured samples in the G7BF and MP-BIF sections. The shaded area represent the field where there are neither La nor Ce anomalies present. Nearly all samples show a positive La anomaly. Only a few samples have a negative Ce anomaly. The S.D. error bars for the G7BF and MP-BIF sections have been added on the right-hand side. These are calculated using the general error propagation formula: $\frac{\delta w}{w} = \sqrt{\left(a\frac{\delta x}{x}\right)^2 + \left(b\frac{\delta y}{y}\right)^2}$ (see text for further discussion).

There is variation of (Eu/Eu*) within the 2 BIF cores as well (Figure 17). The Eu anomaly in the G7BF core remains fairly uniform at ~ 1 for the bottom 7 meters, after which there is an increase towards the peak value of 2.34 at 92.5 meters depth. After this peak the Eu anomaly gradually decreases back to ~ 1 at the top of the core. The Eu anomaly in the MP-BIF core does not show a distinct trend, but mostly remains between 1 and 2 throughout the core. There is an anomalous peak at 399 meters depth, with a value of 2.94 and a rapid increase from 0.93 to 1.90 at 418 meters depth. The average (Eu/Eu*) for the G7BF and MP-BIF cores is 1.28 and 1.29 respectively.

Figure 18 shows the (Ce/Ce*) vs (Pr/Pr*) to identify the presence of true La and Ce anomalies. There is a clear true positive La anomaly present in the majority of the samples and no distinct negative Ce anomaly. Note that the error bars on the (Ce/Ce*)N and (Pr/Pr*)N plot are large, however the La anomaly is outside analytical error while the Ce anomaly is not. The large errors then bring into question the few samples that do contain a negative Ce anomaly, since the error bars reach as far as the shaded area where neither anomaly is present.

There is a super-chondritic Y/Ho ratio present on both the cores, which is a characteristic primary seawater signature. Figure 19A shows that the Y/Ho ratios range between 30 and 80 in both cores. This corresponds well with values representing modern seawater (~40) (Bau et al., 1996). The Y/Ho ratio in the G7BF shows a substantial increase at ~ 95 meter depth changing from 40 towards 60 in only 2-3 meters. The MP-BIF core also shows an increase in Y/Ho ratio but this is much more gradual. The Y/Ho ratio has a clear relationship with Zr, where Y/Ho decreases with increasing Zr (Figure 19B).

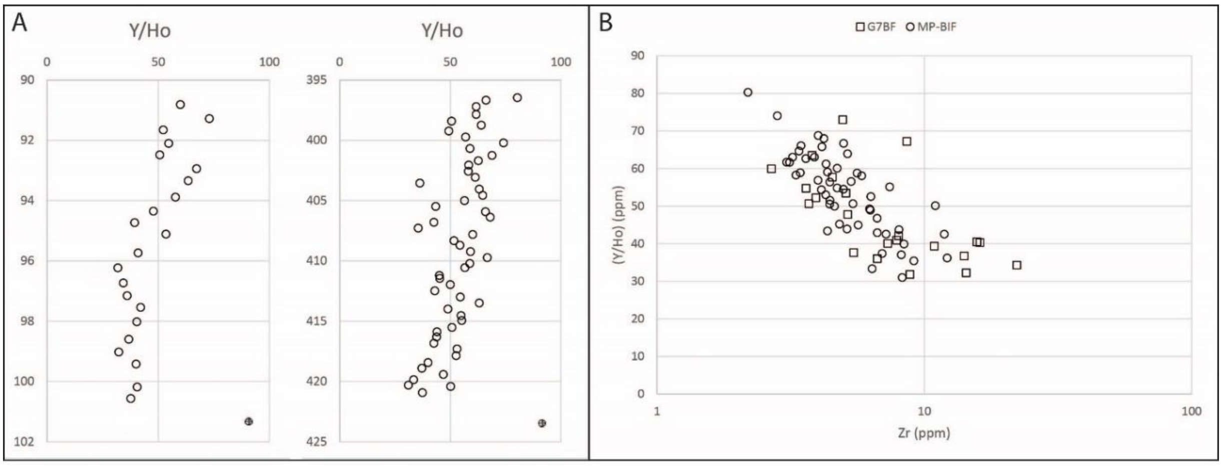

Figure 19: (A) Y/Ho ratio's plotted over depth (m) for the G7BF section (left) and the MP-BIF section (right). There is a stratigraphic increase towards the top of both sections. Error bars are added in the lower-right corner. (See text for further discussion). (B) Y/Ho ratio vs Zr(ppm). There is a clear correlation present, where Y/Ho decreases with increasing Zr abundances.

4.6 C isotope data

The results from $\delta^{13}C$ isotope measurements are shown in Figure 20. The $\delta^{13}C$ values of all bulk rock samples range from -20.7 to -13.7 ‰ for the MP-BIF core and from -18.4 to -11.4 ‰ for the G7BF core. This corresponds well with the carbonate-poor IF of the Hotazel formation reported by Tsikos et al. (2003). The first 4 meters of the MP-BIF are characterized by a rather sharp decrease from -17.8 to -20.7 ‰, followed by a sharp increase back again to -17.7 ‰. The $\delta^{13}C$ values remain constant at ~ -18 ‰ for the next 12 meters after which there is a gradual increase towards -13.7 ‰ at the top of the core. The G7BF core also shows an excursion towards a more negative value, from -14.8 to -17.8 ‰ at the base, where the $\delta^{13}C$ remains constant for 3 meters. Following this there is a sharp increase towards a 4 meter long trail with values of ~ -12.7 ‰. There is another increase at the top of the core with elevated values of -11.4 ‰. Schneiderhan et al. (2006) also observed an excursion to more negative $\delta^{13}C$ values above the lowermost Mn-oxide body. However, the few measurements that were made in this specific portion of the stratigraphy could not fully constrain the geometry of the curve. The higher amount of measurements presented in this thesis can. The extremely low $\delta^{13}C$ values of ~20 ‰ have not been observed before in any BIFs of the Transvaal Supergroup. When plotting $\delta^{13}C$ against CaO wt% it becomes apparent that these largely negative $\delta^{13}C$ values more than often correspond with low CaO wt%, which was also observed by Tsikos et al. 2003 and Schneiderhan et al. 2006 (Figure 21). Also note that the calcitic samples from Tsikos et al. (2003) have increased $\delta^{13}C$ values compared to the ankerite-kutnahorite samples. Since the BIF in this particular succession of the Hotazel formation is often carbonate-poor, the low $\delta^{13}C$ is in agreement with the previous observation.

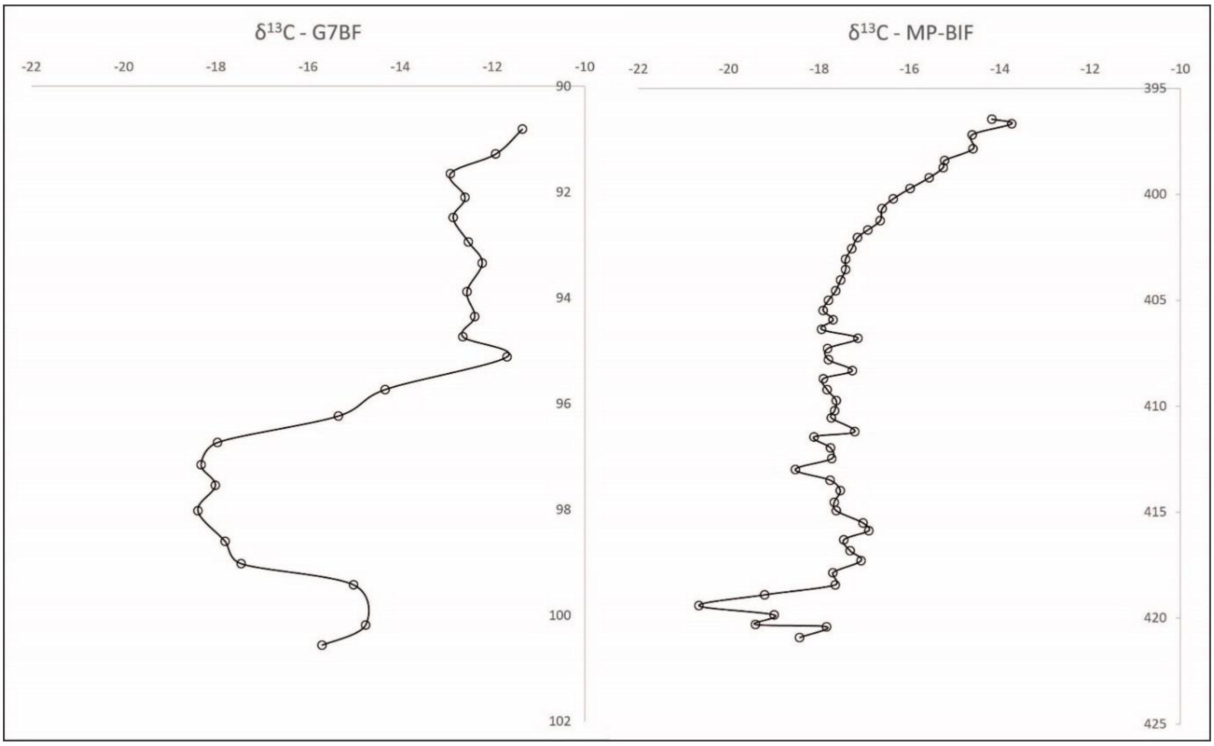

Figure 20: $\delta^{13}C$ (in ‰) plotted over depth (m) for the G7BF section (left) and the MP-BIF section (right). The $\delta^{13}C$ values range between -18.39 and -11.35 ‰ in the G7BF section and between -20.7 and -13.7 ‰ in the MP-BIF section (see text for discussion).

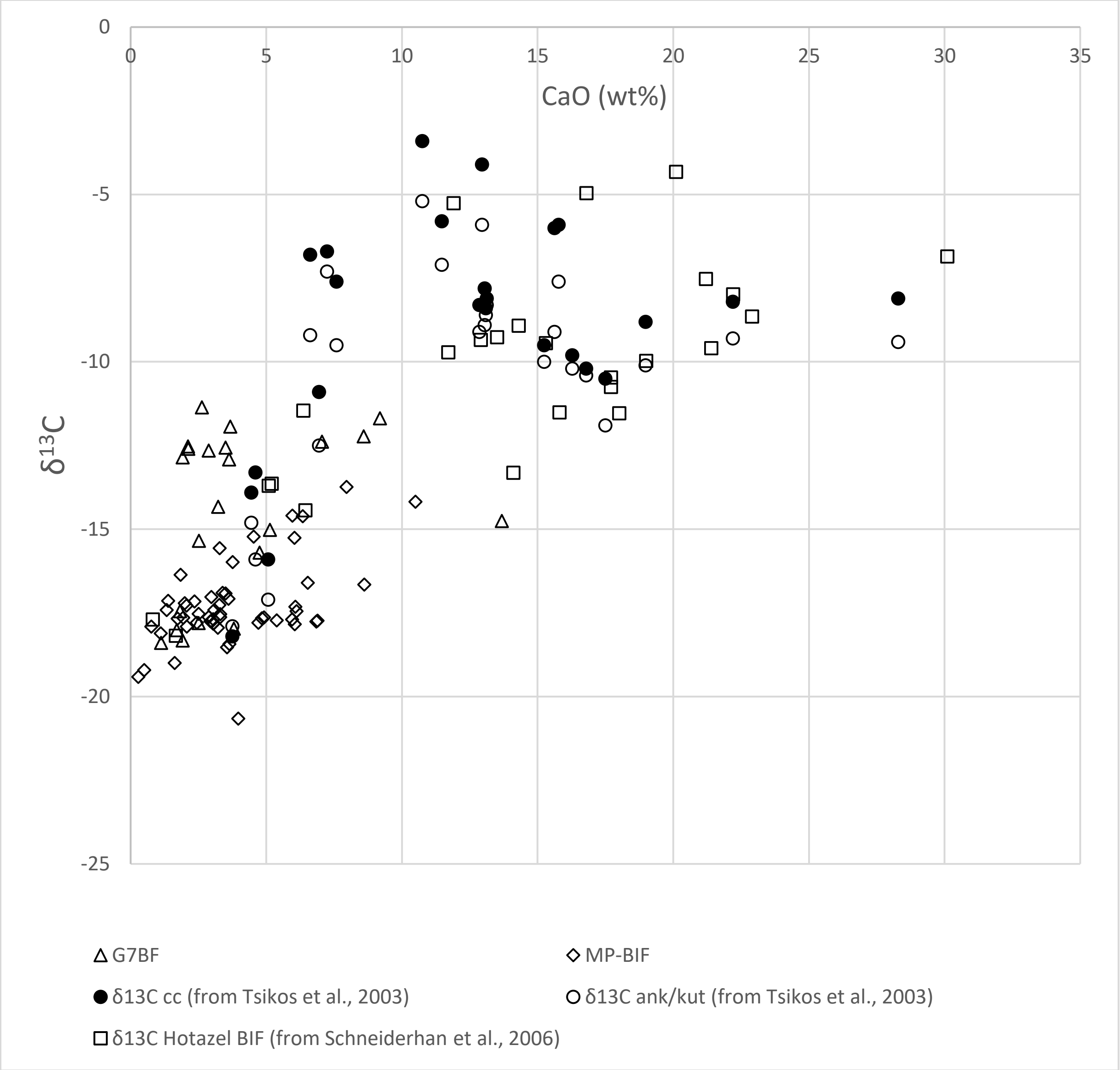

Figure 21: $\delta^{13}C$ (in ‰) plotted over CaO (wt%) for the G7BF and MP-BIF section. $\delta^{13}C$ values of cc and ank/kut from Tsikos et al., (2003) and Schneiderhan et al., (2006) are added for comparison. There is a notable hyperbolic progression of higher $\delta^{13}C$ with increasing CaO (wt%).
Abbreviations: cc = calcite; ank/kut = ankerite – kutnahorite.

5. Discussion

5.1 Accuracy of the data set

5.1.1 Mineral data

The presence of chert, magnetite, ankerite, greenalite and minnesotalite in the majority of the selected samples is in agreement with XRD data from Tsikos and Moore (1997). Siderite and calcite have been reported present in the first BIF of the Hotazel formation as well by the same authors. The presence of microcrystalline calcite bands throughout the stratigraphy of the Hotazel formation suggests that this mineral phase is most likely not solely present in secondary veins. In this thesis siderite was confirmed in the entire MP-BIF core, while it is largely lacking in the G7BF. Calcite on the other hand is present throughout the G7BF core, while nearly absent in the MP-BIF. The presence of hematite in both the drill-cores has not been reported by Tsikos and Moore (1997). The absence of stilpnomelane and riebeckite in the BIF however, is confirmed here. Their absence is also confirmed by the XRF data where Na (hosted by riebeckite) and K (hosted by stilpnomelane) are virtually absent throughout the stratigraphy. Minnesotalite can from as a reaction product from stilpnomelane during low-grade metamorphism (Klein, 2005). The Hotazel formation has been affected by metamorphism with temperatures up to 200 °C during burial of the sediments (Gutzmer and Beukes, 1996) and could account for the absence of stilpnomelane, usually a common mineral phase in BIFs, in both sections. The mineral phases hematite, stilpnomelane, riebeckite and pyrite however have been reported higher up the stratigraphy of the Hotazel formation.

5.1.2 Major element data

The average Fe_2O_3 and SiO_2 concentrations agree with previous data of Tsikos and Moore (1997) and Schneiderhan et al. (2006). The low CaO concentrations (<10 wt %) are also in line with data for the first BIF of the Hotazel formation. The BIFs higher up the stratigraphy of the Hotazel formation contain higher CaO concentrations. Tsikos and Moore (1997) also reported the increase of CaO towards the top of the first BIF in the Hotazel formation, as reflected by the MP-BIF core. The MnO concentration of the MP-BIF core is 1.04 wt% on average and is thus higher than the G7BF core (0.62), the first BIF of Tsikos and Moore (1997) (0.33) and Schneiderhan et al. (2006) (0.43). The MgO and Al_2O_3 concentrations are very similar to those reported in the literature. Concentrations of Na_2O, K_2O and P_2O_5 are very low and more than often below the detection limit, which is in agreement with previous research as well.

5.1.3 Trace element data

The trace element data overall corresponds well with previous research (Tsikos and Moore, 1997; Schneiderhan et al., 2006), however there are a few discrepancies. Strontium values measured in the G7BF and MP-BIF cores remain below 80 ppm, with a few peaks of 200 – 300 ppm. Tsikos and Moore (1997) reported Sr values ranging from 45 to 905 ppm, while Schneiderhan et al. (2006) measured Sr values up to 1236 ppm. The Cu concentration is about 10 ppm lower than that reported by Tsikos and Moore (1997) and the Zr concentration is elevated compared to Schneiderhan et al. (2006), who reported Zr levels to be beneath the detection limit in the BIFs of the

Hotazel formation. Both drill-cores showed a stratigraphic increase in crustal sourced elements and transition metals towards to base of the stratigraphy. No such stratigraphic trends are reported by Tsikos and Moore (1997) and Schneiderhan et al. (2006). However the density of measurements in this thesis is much higher than any of the previous literature and could account for additional information seen in the stratigraphic trends. The REE + Y distribution of the Hotazel BIF of Tsikos and Moore (1997) shows a positive La, Eu, Gd and Y anomaly, no negative Ce anomaly and the HREEs are enriched compared to the LREEs and thus is in agreement with the MP-BIF and G7BF cores. The Hotazel hematite-chert BIF reported by Lantink et al. (2018) is lacking a positive La and Gd anomaly and shows no negative Ce anomaly. There is a distinct positive Eu anomaly and the HREEs are enriched compared to the LREEs. The strong Eu anomaly and the absence of a positive La and Gd anomaly deviate compared to the REE + Y distributions of Tsikos and Moore (1997) and the BIF presented in this thesis. Lantink et al. (2018) investigated the contact between the Hotazel Fm. and the underlying volcanic andesite of the Ongeluk Fm. It is not inconceivable that the lowermost part of the Hotazel formation was sourced by the delivery of hydrothermal fluids, since they directly cover the hydrothermally altered Ongeluk lavas. This will then account for the positive Eu anomaly, reflecting the presence of hydrothermal activity. The Y/Ho ratio was in agreement with the data presented here, having a super chondritic value of 40-80. Bau and Alexander (2006) reported a distinct negative Ce anomaly in the Mn-oxide intercalation of the Hotazel formation. The Mn-oxide was interpreted to have been deposited in a highly oxygenated marine environment compared to the anoxic marine environment in which the BIFs were deposited. No other negative Ce anomaly has been observed however in the Hotazel formation (Tsikos and Moore, 1997; Lantink et al., 2018), in the Koegas subgroup (Schier et al., 2018) and the Kuruman and Griquatown formations (Oonk et al., 2018) stratigraphically below the Hotazel formation in the Transvaal Supergroup. The validity of the negative Ce anomaly from Bau and Alexander (2006) and the ocean's oxygenic state during deposition of the Hotazel Fm. will be further discussed in 5.3.2.

5.1.4 $\delta^{13}C$ data

The $\delta^{13}C$ values of all bulk rock samples range from -20.7 to -13.7 ‰ for the MP-BIF section and from -18.4 to -11.4 ‰ for the G7BF section. This corresponds well with the carbonate-poor IF of the Hotazel formation reported by Tsikos et al. (2003), where $\delta^{13}C$ values ranged from -18.2 to -13.3 ‰. The carbonate-rich and manganese ore samples showed less negative values between -10.9 and -3.4‰. Schneiderhan et al. (2006) reported $\delta^{13}C$ values ranging from -4.7 to -18.2 ‰ in the Hotazel formation, where the most negative values again reflect a depletion in CaO and LOI concentrations. They also reported an excursion towards more negative values in the BIF above the first Mn-oxide intercalation and an overall increase in $\delta^{13}C$ and TIC (Total Inorganic Carbon) from the base to the top of the Hotazel Fm. This trend can be observed in the $\delta^{13}C$ data presented in this thesis as well. The exact geometry of the curve however is much more precise due to the high measurement density in the G7BF and MP-BIF core, as opposed to the limited data presented in Schneiderhan et al. (2006). The extremely depleted $\delta^{13}C$ values of ~-20 ‰ present in the MP-BIF core have not been reported in any of the Transvaal BIFs literature before.

5.2 Stratigraphic Correlation

5.2.1 XRD and Optical Microscope

The XRD detected minerology does not show a lot of correlative features. All samples consist mostly of quartz in the form of chert, together with magnetite. There is some variability in the relative abundance of ankerite, hematite, minnesotalite and greenalite but none of them have a clear stratigraphic trend in both sections. The presence and absence of siderite in the MP-BIF and G7BF section respectively creates an even harder task to fully correlate the two sections. The calcite shows an opposite relationship to siderite and is mostly present in the G7BF section, just once in the MP-BIF. G7BF-19 is the only sample to contain siderite in this section. This can then be correlated to ~MP-BIF-33 sharing a very similar mineral assemblage of chert, magnetite, siderite and greenalite. In addition, both of these samples have a similar $\delta^{13}C$ value of -18 supporting this correlation (see Discussion 5.2.4.). The measurement density of the XRD and the optical microscope is much lower than the XRF and LA-ICP-MS data, so changes and trends within the section are harder to correlate in detail. Also, minerology in banded iron formations changes within the thickness of the banding, which is mm to cm scale in this case. The error and change of minerology is thus quite large in small scale structures, which makes it less usable for correlating the two drill-cores.

5.2.2 Major element data

The top 15 meters of the MP-BIF section shows similar features to those of the G7BF. From 410 to 405 meters depth there is a strong increase in Fe_2O_3 matched by the bottom 3 meters of the G7BF (Figure 22). Subsequently this match is also present in the SiO_2 data, which anti-correlates with iron. After this, the Fe_2O_3 concentration remains fairly constant at 40 wt% in each section. The top meter of both sections significantly agree as well. The abrupt decrease in Fe_2O_3, together with the sharp increase in SiO_2 are characteristic in both cores. However, the CaO and MnO show a different trend in each individual core (see Figures 9 and 10). Whereas CaO and MnO concentrations show a gradual increase towards the top 4 meters of the MP-BIF core, the concentrations remain rather constant in the G7BF core. The Al_2O_3 concentrations show a similar trend to those of the HFSE, following an increase from near zero values towards 0.4 wt% in the MP-BIF core and 1.0 wt% in the G7BF. This trend is also observed in the MnO/CaO ratio, with somewhat extreme values (>1.0) at the base of the MP-BIF section (see Figure 11). Further trends in the Major elements oxides are hard to find. There is some scatter in the data related to the compositional change on mm and cm scale. The scatter does become larger towards the base of each section, showing a wider range of chemical composition relative to the top. Still, on average the chemical composition remains fairly similar.

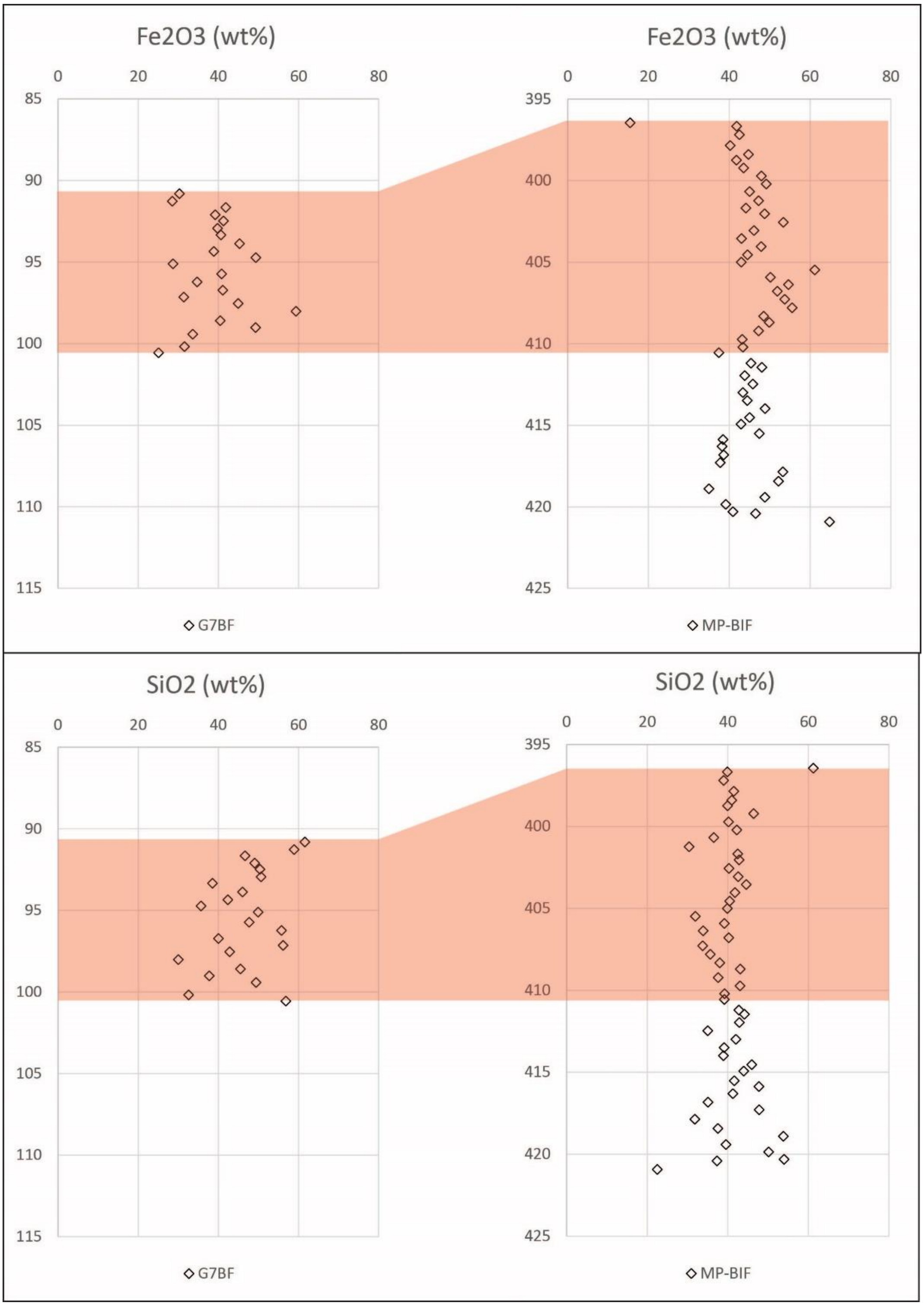

Figure 22: Fe_2O_3 and SiO_2 (in wt%) over depth (in m). The correlation is highlighted in red and links the entire G7BF section with the MP-BIF stratigraphic interval from 411 to 397 m depth. (See text for further discussion)

5.2.3 Trace element data

The trace element concentrations at the top of both sections are nearly all equal, sharing the same, often minimum values, present in the section. The top of each section can then be considered equivalent to one another. The black shale stratigraphically on top of both cores enhances the idea for this correlation. Measured values of the immobile high field strength elements (HFSE) elements Sc, Ti, Zr, Th and the transition metals V, Cr, Mo all increase substantially towards the base of the succession. The trend can be seen in both the MP-BIF core and the G7BF core, where the increase is even greater. The succession of the MP-BIF core shows a smaller but noticeable increase in these HFSE towards the middle part of the core as well, with a peak value at 407 meter depth. The bottom of the G7BF section could then be correlated to a) the middle part at 407 meter depth of the MP-BIF core, or b) the bottom of the MP-BIF core. In order for option b to be correct, precipitation rates must be vastly different squeezing 25 meters of the MP-BIF core in 10 meters of G7BF. For option a, the thickness would be equivalent between the two cores and precipitation rates are equal. This option is then more favourable over option b.

5.2.4 $\delta^{13}C$ data

The correlation for the $\delta^{13}C$ measurements is not as straight forward. The curves show large differences between one another, which requires an explanation. The part which does correspond and can possibly correlate the two sections reflects the $\delta^{13}C$ values of ~-17; -18 ‰. The MP-BIF core shares these values from 405.5 meters depth to 418.4 and the G7BF core from 96.7 to 99.0. So there is a large thickness variation present in the sections reflecting these values. After this correlation in values of both cores, there is an increase in $\delta^{13}C$ towards the top of the sections. This increase is gradual in the MP-BIF section yet sharp in the G7BF. This difference could be explained by a different precipitation rate of the two sections. In this scenario the change in $\delta^{13}C$ are assumed to be equal over time in both cores but the precipitation rate is higher in the MP-BIF core, recording in much more detail the $\delta^{13}C$ over time. The precipitation rate of the G7BF would then be much lower, recording this change in only 2 meters of sediment instead of 10 meters in the MP-BIF. However, such large difference in precipitation rate is not likely as Altermann and Nelson (1997) noted that for the deep shelf to tidal facies range, Archaean and Phanerozoic chemical and clastic sedimentation rates are comparable and thus do not deviate much from one another. Another possible theory to explain the difference in gradual and sharp increase could be a fast topographic change as a result of tectonic shift in the G7BF section. The G7BF section is suggested to have been deposited on a local dome of extruded lava from the Ongeluk formation (Van der Merwe, 1997). If this was exposed to a sudden tectonic movement the section could have become unstable and slipped vertically over the slope. So a growth fault may cause the rather sharp $\delta^{13}C$ increase seen in the G7BF core. Differential rate's in subsidence then explain the difference of gradual and steep increase of the $\delta^{13}C$ notable in both cores. Figure 23 visualized this conceptual model on the deposition of the MP-BIF and G7BF sections.

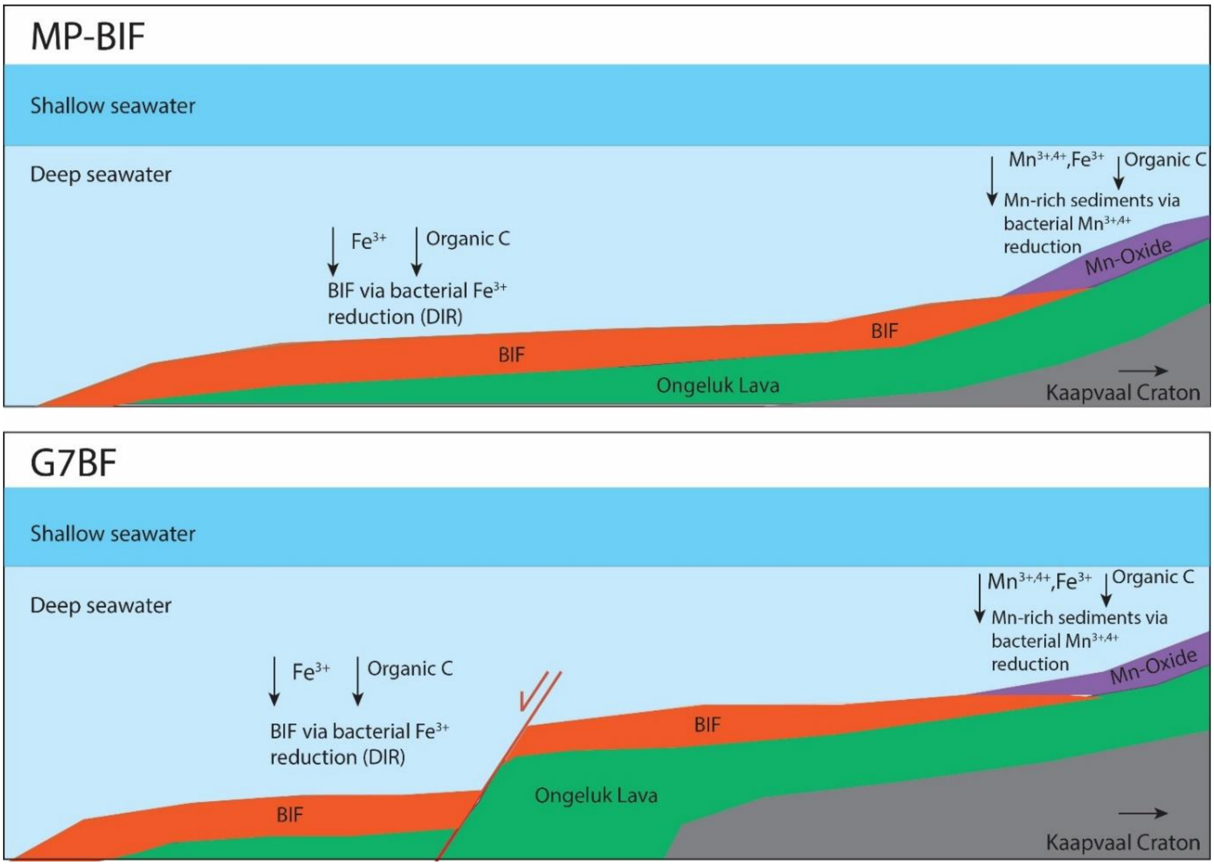

Figure 23: Conceptual model for the deposition of the MP-BIF and G7BF sections. The MP-BIF sections shows a gradual increase in water depth further away from the Kaapvaal craton. The G7BF section is located on top of a dome-like structure of the Ongeluk Fm. making it more prone to tectonic instability and subsequent movement over a fault. These different basin geometries are reflected in the δ^{13}C data and the Y/Ho ratio.

If the top part of the MP-BIF section would have continued with its deposition, the δ^{13}C would have possibly reached the -11 values present in the G7BF section. The gradual increase of the MP-BIF section is thus somewhat compressed in the sharp increase observed in the G7BF. The base of both sections shows the largest discrepancy in δ^{13}C. The G7BF core shows an increase in δ^{13}C towards ~-15 ‰, while the MP-BIF core shows an excursion towards more negative values. In this part of the section the most negative δ^{13}C values of – 20.7 ‰ are present. So a correlation between the bases of both sections seems very unlikely. The correlation of the δ^{13}C can then be divided in three separate sections (Figure 24): A) the agreement in δ^{13}C values of -18 by both sections, B) where the gradual increase in δ^{13}C from the MP-BIF section is condensed into 2 meters of the G7BF and C) the δ^{13}C values of -13 present in the G7BF section which would presumably have been matched by the MP-BIF if deposition had continued.

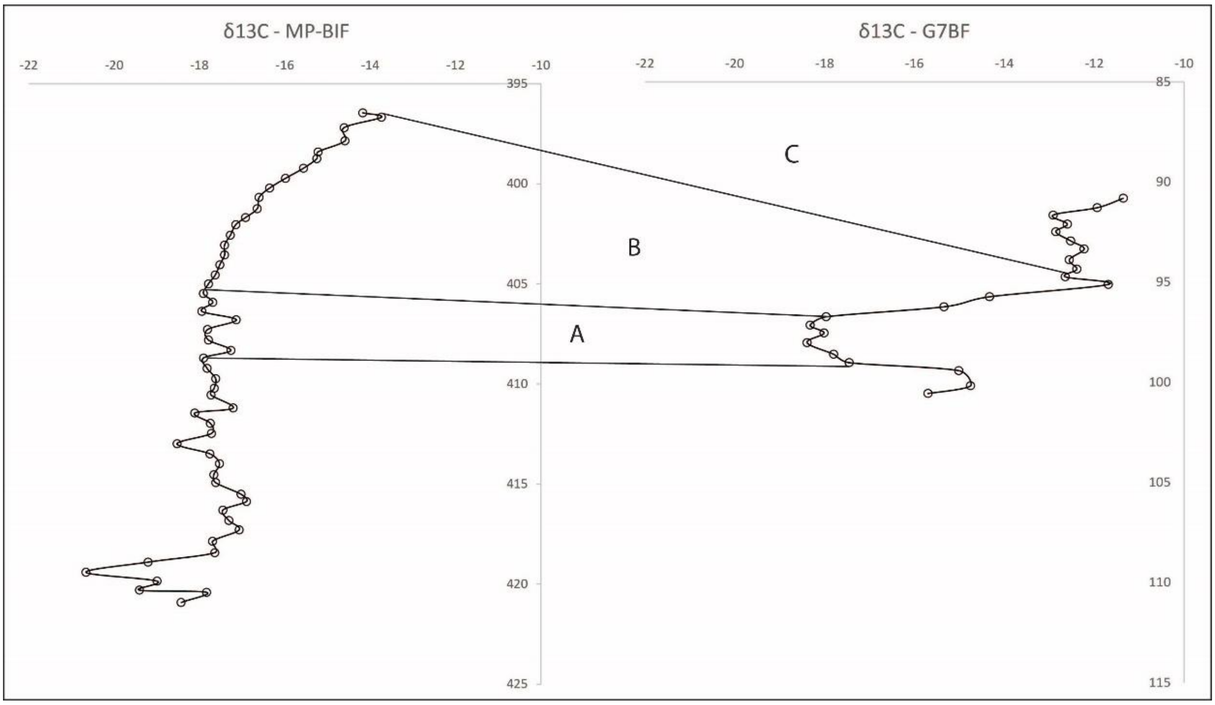

Figure 24: The δ^{13}C values of both the MP-BIF and G7BF sections, with the correlation distinguished in 3 separate units: A, B and C. (See text for discussion).

5.2.5 Overall Correlation

The bases of both sections are enriched in crustal sourced elements, which is presumably an imprint from the stratigraphically lower Mn-Oxide intercalation and follows the decrease in detritus or volcanic ash towards the deeper parts of the basin. The δ^{13}C data shows its largest discrepancies at the base of both sections and displays no relationship in this part of the stratigraphy. The agreement in δ^{13}C values of ~ -18 with a subsequent increase in both sections favours the correlation between the top 13 meters of the MP-BIF into the G7BF in its entirety. The agreement in trace element data, being depleted in crustal sourced elements and some transition metals, strengthens the correlation between the top of both sections. The major element data also favours this correlation containing similar features in the top 13 meters of the MP-BIF and the whole G7BF stratigraphy. The top meter enhances this even more, where both sections show a decrease in Fe_2O_3 and MgO, and an increase in SiO_2. The black shale deposited directly on top, is a clear chronostratigraphic marker bed, further supporting this correlation (Figure 25). The BIF of the G7BF section is thus not a condensed version of the MP-BIF section, but rather a specific stratigraphic interval of approximately equal thickness.

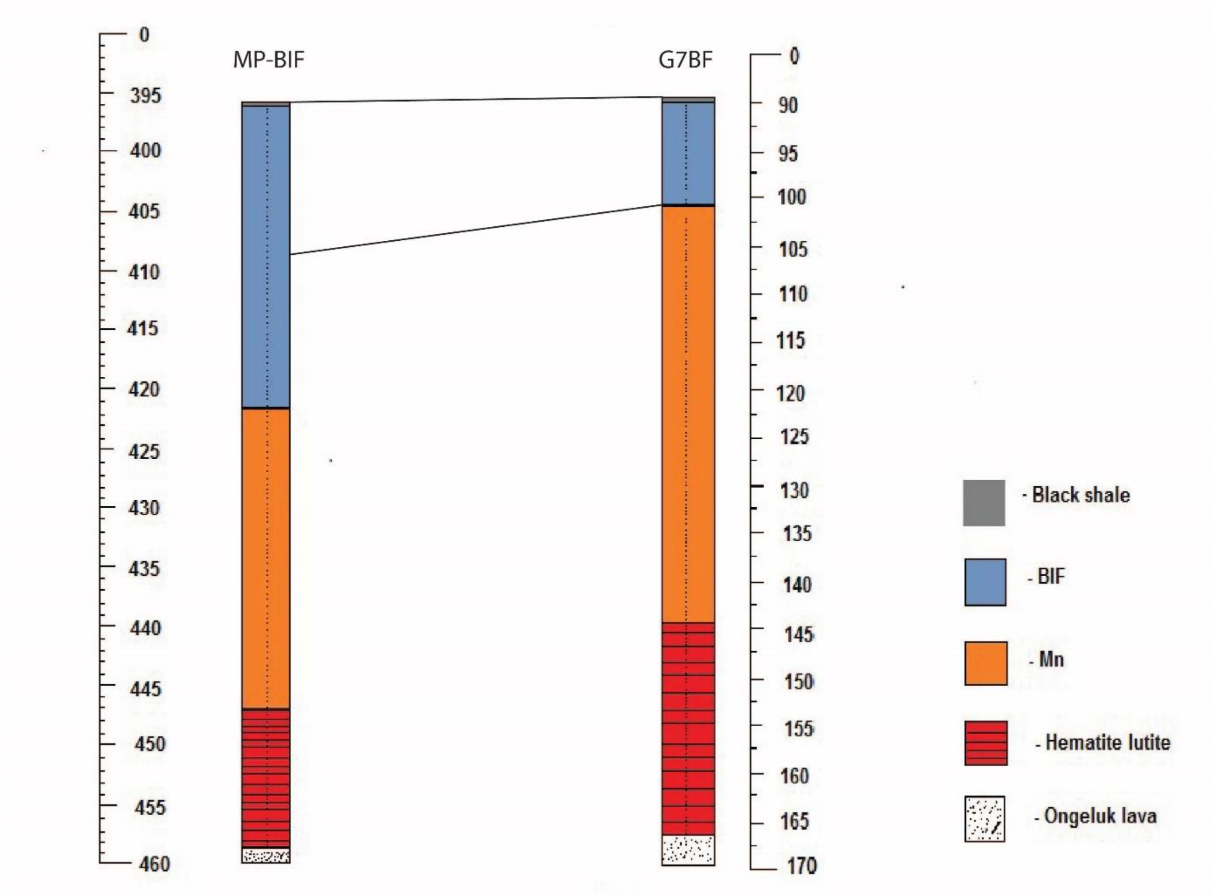

Figure 25: A visual representation of the two sections MP-BIF and G7BF, with their respective lithology. The correlation between the two sections is located at the top.

5.3 Paleo-depositional environment

5.3.1 Trace element controls

Although there is a clear trend of increasing crustal sourced elements (Al, Ti, Sc, Zr, and Th) towards the base of the core, the total abundance remains low. It is thus not likely that the detritus is fluvial in origin, which would contain a much higher abundance in crustal sourced elements. The lack of any sedimentological structures in the drill-core such as turbidite flows strengthens the idea that the detritus is not fluvial. This indicates that the BIFs were deposited in a distal position with respect to the continent, which is in agreement with Thibon et al. (2019). Aeolian transport would be a more logical explanation, as this mechanism would be able to transfer detrital particles over a larger distance, and it would account for the low abundance of the detritus. Figure 26 shows the Cr/Th vs Th/Sc of both drill cores, which can elaborate on the origin and composition of the detritus. The detrital input shares a similar composition as that of Archean shale deposits (values from Condie, 1993), which in turn corresponds to the average continental Archean crust. The Th/Sc values for the average continental Archean crust are ~0.1-0.3 higher than the ones measured in this thesis. The source rock is thus slightly more mafic in composition, as mafic rocks are richer in Sc. Lantink et al. (2018) argued that the mudstone intervals of the bottom 3 meters of the Hotazel formation could be linked to episodes of increased volcanism from the Ongeluk Formation's volcanic andesite. The influx of volcanic ash leaves a signature of allochthonous material within the sediments, which is reflected mostly by Al and Ti. Due to the large difference in Al/Ti, Al/Zr and Ti/Zr between the G7BF and MP-BIF section of the Hotazel formation and the underlying Ongeluk formation (Table 3), it is unlikely detritus would originate from weathered volcanic andesite or volcanic ash of the Ongeluk Fm.

	G7BF	MP-BIF	Ongeluk Fm.
Average Al/Ti	10,3	8,3	22,6
Average Al/Zr	152,9	83,6	689,5
Average Ti/Zr	13,7	10,9	30,5

Table 3: Average Al/Ti, Al/Zr and Ti/Zr ratio's for the G7BF and MP-BIF sections of the Hotazel BIF and the stratigraphically lower Ongeluk Fm (values from Cornell et al., 1996).

Chromium and Neodymium showed a strong correlation with Zr, which argues that these elements originate from detritus or volcanic-ash (Figure 28). Mn and U do not correlate with Zr and have their origin somewhere else in the basin. Chromium abundances are often dominated by detrital input and the strong correlation with Zr strengthens this idea. However, this does not necessarily have to be accurate. The Cr/Ti ratio evaluates whether the chromium is authigenic or brought in as detritus. Authigenic Cr enrichment can be calculated by dividing Cr by Ti and then normalizing to the upper continental crust (0.035) (Konhauser et al., 2011) (values from Condie, 1993), which then discards the change in detrital input. The largest Cr/Ti ratios are observed in BIFs coinciding with the GOE. This is due to oxidative weathering of sulphides, causing acidity which would have enhanced dissolution of Cr-bearing minerals (Konhauser et al., 2011). The Cr/Ti ratio values range from 0.12 – 1.7 (Figure

27) and is thus 3.5 - 50 times higher than those of the evolving Archean crust and coincide with the idea of oxidative weathering of sulphides that occurred during the GOE and in turn during the deposition of the Hotazel formation. The chromium increase towards the base of the two sections is thus not necessarily related to detritus. Neodymium was selected since it reflects the enrichment in LREEs that are typically most affected by allochthonous material (Viehmann et al., 2015). The correlation with Zr suggest that the LREEs were controlled by detritus or volcanic ash. The slope of the REEs, or the (Yb/Ce) ratio however does not track Zr abundances, which contradicts the previous argument. A correlation with Zr thus does not necessarily reflect allochthonous input, it may be related to different processes. The decrease in crustal sourced elements from the base towards the top of both sections is a gradual transition towards lower abundances from the Mn-oxide intercalation towards the BIF. The Mn-oxide contained enriched Zr and Pb values with respect to its upper IF (Schneiderhan et al., 2006) and hosted Ba and Sr in much higher abundances.

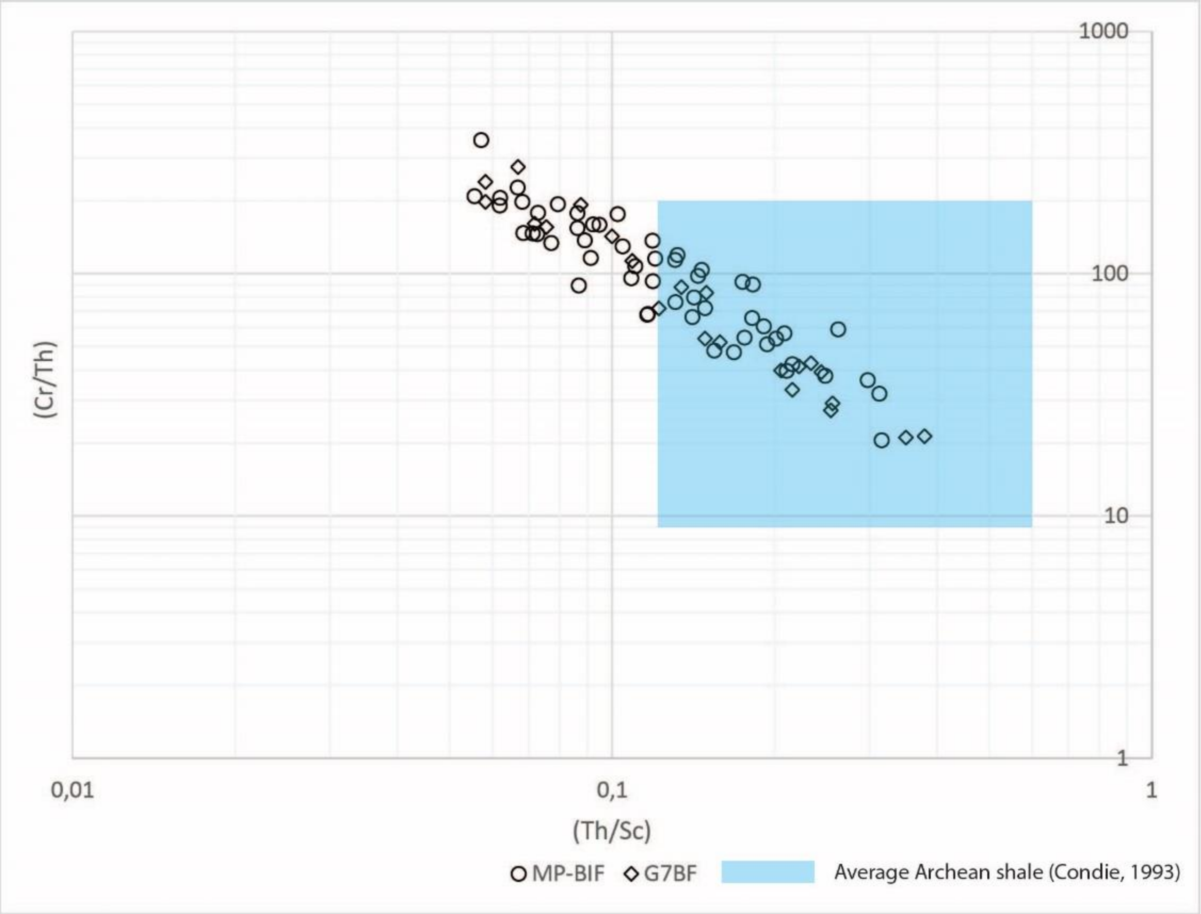

Figure 26: Cr/Th ratio plotted over Th/Sc for both G7BF and MP-BIF sections to evaluate the origin of the detritus of volcanic-ash. Values for the average Archean shale added (taken from Condie, 1993).

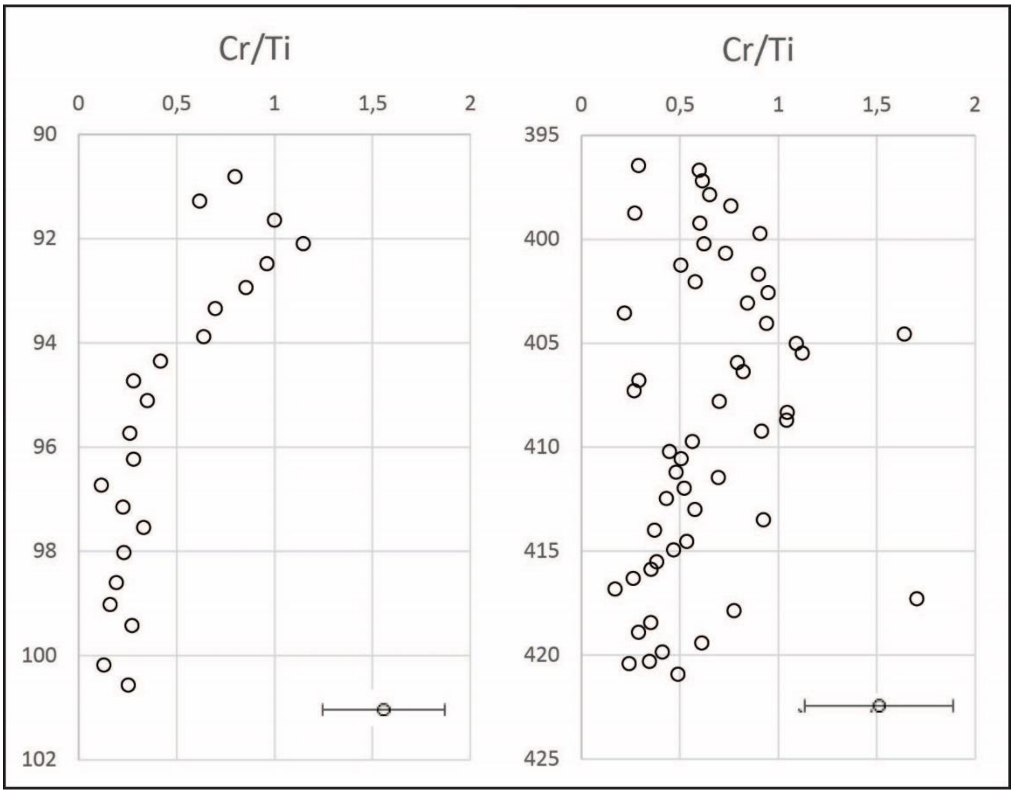

Figure 27: Cr/Ti ratio plotted over depth (m) for the G7BF section (left) and the MP-BIF section (right). The error bars are added and located in the lower-right corner of each plot.

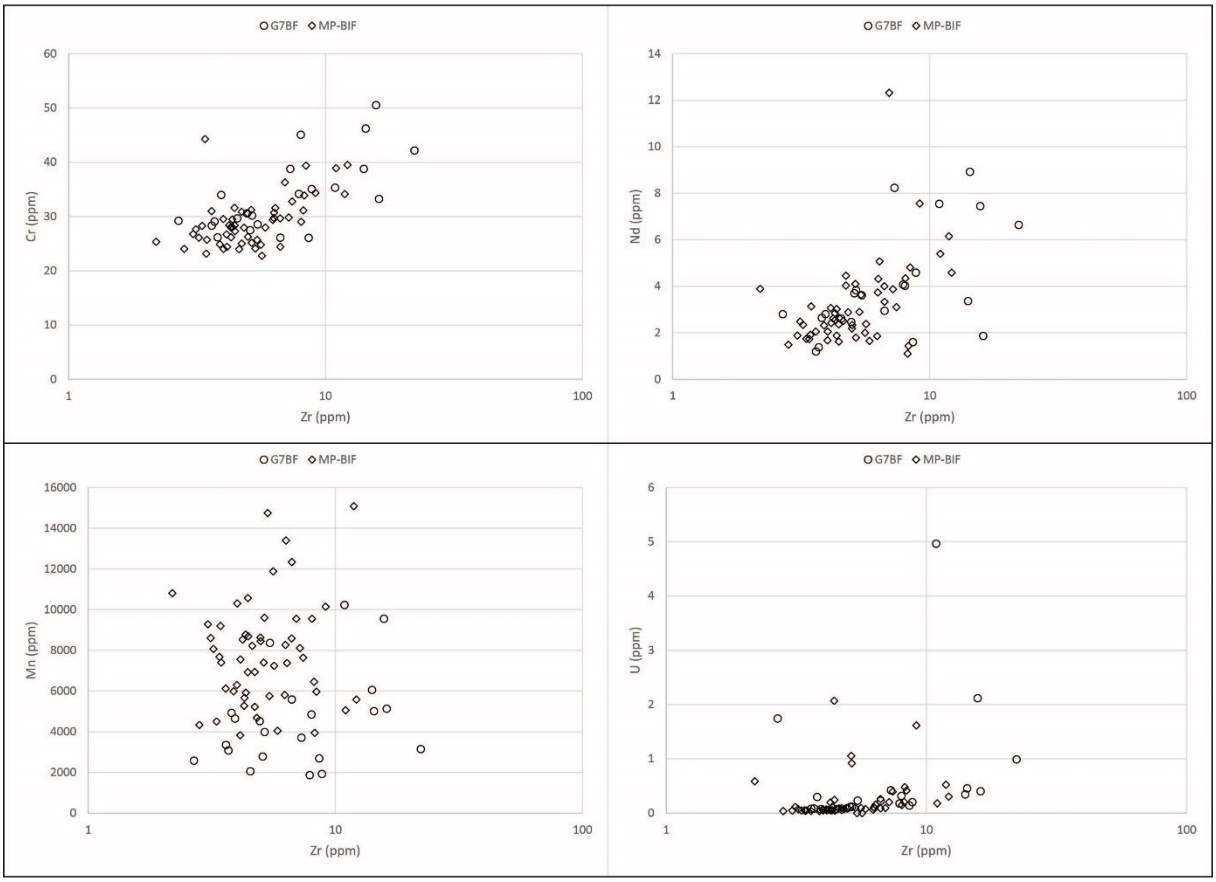

Figure 28: Diagram of Zr vs Cr, Nd, Mn and U showing all the samples of both the G7BF and MP-BIF sections. Cr and Nd show a clear correlation of increasing values with increasing Zr. Mn and U do not show this or any other trend.

5.3.2 Rare-Earth Element and Y characteristics of ancient seawater.

The positive La anomaly present in both sections can be explained by its enhanced stability in seawater which is related to its empty inner 4D electron shell and is a characteristic for ancient seawater (Byrne and Kim, 1990; De Baar et al., 1991). The presence or absence of a true negative Ce anomaly may indicate whether an ocean was oxygenated or anoxic during deposition of the sediment, respectively. Negative Ce anomalies are due to oxidation of Ce^{3+} to the less soluble Ce^{4+} and a subsequent removal from the seawater by scavenging of particles/Mn-nodules. The microbial oxidation pathways of Mn and Ce are closely related with one another. Although the electron potential for Ce oxidation is higher than for Mn, under most conditions Mn can still be divalent while Ce is already oxidized. So the absence of a negative Ce anomaly in modern seawater like patterns visible in most BIFs indicate that seawater was still reducing enough to prevent the formations of manganese oxides. Bau and Alexander (2006) observed the presence of a negative Ce anomalies in the Hotazel formation and stated that the Mn-oxides had been deposited in a highly oxygenated marine environment. However, the overlying Mooidraai formation did not contain a negative Ce anomaly, indicating that marine oxygenation was fluctuating during the GOE. Lantink et al. (2018) investigated the bottom 3 meters of the Hotazel formation and its contact with the underlying basaltic andesite of the Ongeluk formation. No Ce anomalies were present in the hematite-lutite of the Hotazel formation indicating an anoxic marine environment at time of deposition. The deposition of the early Hotazel formation was thus pre-GOE. Figure 18 shows that there is no negative Ce anomaly present in the G7BF and MP-BIF core. So whereas the Mn-oxide does contain a negative Ce anomaly, both the stratigraphically lower hematite-lutite and the upper BIF do not contain such anomaly. If the presence of the negative Ce anomaly in the Mn-oxides from Bau and Alexander (2006) is correct, then oxygen levels were fluctuating rapidly throughout the deposition of the Hotazel formation. However, the Hotazel data provided by Bau and Alexander, (2006) is based on only one sample presented in a REY diagram. Their Hotazel data is not included in the (Ce/Ce*) vs (Pr/Pr*) plot and therefore may have not taken into account the magnitude of the positive La anomaly, which in turn questions the magnitude of the Ce anomaly in their study in total. No other literature reported a negative Ce anomaly in the Mn-oxide intercalation of the Hotazel formation. Mhlanga et al. (2018) reported bulk-rock REE data and revealed neither negative nor positive Ce anomalies throughout the Hotazel stratigraphy and indicated that primary oxidation of Mn(II) to Mn(IV) most likely did not occur*.* This all implies that marine conditions were anoxic from deposition of the bottom of the Hotazel formation to at least the top of the first BIF.

Positive Eu anomalies in chemical sediments indicate the presence of hydrothermal activity in the ocean or basin (Bolhar et al., 2004). In high temperature fluids, hydrothermal extraction of divalent Eu is more efficient than other trivalent rare earth elements (Bau and Moller, 1993). These fluids will subsequently contain a positive Eu anomaly. Positive Eu anomalies are present in numerous iron formations. However, BIFs that are associated with Snowball Earth conditions often lack a true positive Eu anomaly (Tsikos and Moore, 1997). The (Eu/Eu*) of the G7BF and MP-BIF cores are 1.28 and 1.29 respectively and do not show a characteristic positive Eu anomaly, indicating little to no hydrothermal activity during time of deposition. This then coincides with the above mentioned statement, as the Hotazel formation has been deposited in the aftermath of the Snowball Earth. The positive Gd anomalies present in both sections are attributed to increased solution stability and decreased surface complexation related to a half-filled inner 4f shell of Gd (e.g. Byrne and Kim, 1990; Kim et al., 1991) and is also a primary signature for modern and ancient seawater.

In modern day seawater, Y behaves anomalously with respect to Ho, which is its geochemical twin based on charge and radius (Bau and Dulski, 1996). This behaviour has been attributed to surface complexation effects, where differences in chemical bonding signify that Y binds less strongly to surface-complexes compared to other REEs, and is therefore less prone to removal from the seawater, creating superchondritic Y/ Ho ratios in the oceans (Bau and Dulski, 1996). Superchondritic Y/Ho ratios (values of 40-80) in BIFs have therefore been interpreted as a primary seawater signature (Bolhar, et al., 2004). There is a super-chondritic Y/Ho ratio present in both sections, with values ranging from 30 at the base to 80 at the top of each section. Y/Ho ratios are indicative for change in water depth (Høgdahl et al.,1968; Bau et al., 1995; Nozaki et al., 1997). Multiple mechanisms have been proposed to be responsible for this Y and Ho fractionation in seawater: Differences in solution and surface complexation behaviour, variable solubility of Y and Ho phosphate minerals and fractionation during chemical weathering of continental material (Nozaki et al., 1997; Bolhar et al., 2004). Figure 19A shows that the Y/Ho ratio decreases with core depth, indicating an overall decrease in water depth. So the base of both drill-cores would have been deposited in a shallower marine setting, with an increase in water depth over time. Since the bases of both cores are stratigraphically on top of the Mn-oxide intercalation, this enhances the idea of Mn precipitation in a shallower marine environment. There is a clear correlation between Zr concentration and Y/Ho ratio, with increasing Zr concentration over decreasing Y/Ho ratio. This in turn indicates an increase in allochthonous material over decreasing water depth and favours contamination of detrital particles. Deposition of chemical sediments in a shallower basin, closer to the continental shelf, would naturally be more prone to detrital contamination. However, the stratigraphic correlation in Y/Ho remains, even when only the low Zr samples are considered. By filtering out the Zr samples of > 7 ppm, it can be verified whether or not the stratigraphic trend is truly controlled by the input of Zr or not. Since the stratigraphic trend of increasing Y/Ho towards the top remains, the Y/Ho ratio responds to different processes that are not controlled by detritus. The MP-BIF and G7BF core are both enriched in HREEs relative to the LREEs, so the REE + Y patterns have a positive slope, which is also a key primary seawater signature. This can be constrained by the (Yb/Ce)N ratio, which reflects the slope of the REE + Y plots. The average (Yb/Ce)N values presented in this thesis are 4.9 and 3.4 for the MP-BIF and G7BF cores respectively and there does not seem to be a strong stratigraphically controlled trend in the plots. Also the (Yb/Ce)N ratio is not controlled by allochthonous input, as there is no correlation with Zr noticeable. This in contrary to the Kuruman and Griquatown formations, which showed a stratigraphic increase towards the top of the Kuruman Fm. and a subsequent decrease towards the top of the Griquatown Fm. (Oonk et al., 2018). Furthermore, Zr showed a correlation against Nd for their bulk-rock samples and a correlation against (Yb/Pr)N in the oxide and silicate fraction of the BIF, reflecting input from volcanic ash.

5.3.3 $\delta^{13}C$ controls

The $\delta^{13}C$ excursion towards more negative values just above the base of the MP-BIF section is reflected by a substantial increase in HFSE and crustal sourced elements. Even minor amounts of detrital materials can alter the geochemical bulk-rock signal significantly for minor and trace elements (Viehmann et al., 2015). This in turn may then also alter the carbon isotope ratios. The magnitude of $\delta^{13}C$ depletion in this instance can be attributed to the relative supply of organic carbon versus marine bicarbonate to the chemical sediment. If the organic carbon supply is related to terrestrial processes, the link between the crustal sourced elements can be made. The increase in MnO wt% and MnO/CaO is also substantial towards the base and does have a larger contribution to the bulk rock percentage. So their respective influence on the carbon isotopes may be stronger. There is a notable antithetic relationship present between the MnO/CaO and the $\delta^{13}C$ (Figure 29). The increased MnO/CaO values of the G7BF-15-19 correspond to the depleted $\delta^{13}C$ values of -18 ‰, only present in that part of the section. The extreme MnO/CaO peaks at the base of the MP-BIF section also reflect the lowest $\delta^{13}C$ values of -20.7 in this study. The increase in $\delta^{13}C$ towards the base of the G7BF section can be related to the transition towards the Mn-oxide intercalation stratigraphically below. This transition was also reflected in the decreasing Fe/Mn in the same part of the stratigraphy (Figure 12). One would expect this transition to be more expressive in the G7BF section, where the Mn-oxide intercalation was thicker and had been deposited over a longer period of time. This will presumably leave a subsequent mark on the first few meter of the G7BF BIF instead of the MP-BIF, where the Mn-oxide intercalation is much thinner. The gradual increase of $\delta^{13}C$ towards the top of the MP-BIF core is reflected by the CaO concentration, which shares a similar gradual trend, and the Y/Ho ratio increase which is more linear. The Y/Ho ratio also reflects the sharp increase at the middle of the G7BF core, where the $\delta^{13}C$ values increase from -18 to -12 ‰ within 2 meters. The CaO wt% also mimics this change and increases from 3 to 9 wt% in just 2 meters. This is a massive change in $\delta^{13}C$ values over just a small portion of the section. As suggested before this could be due to a fast topographic change as a result of a tectonic shift. The sharp increase in Y/Ho ratio favours the idea of a tectonic movement, which explains the rapid change in water depth as well. If the sharp increase is indeed caused by a growth fault this would possibly also mobilize detrital particles. The higher amount of detrital components observed in the G7BF core would perfectly fit with this hypothesis. Schneiderhan et al. (2006) attributed the observed increase in $\delta^{13}C$ from the base to the top of the Hotazel Fm. to a slowly increasing contribution of carbonate mud from the Mooidraai platform into the BIF and Mn-oxide lithology's, which is in agreement with the gradual CaO increase found in the MP-BIF section. The top meter of the G7BF core contains the highest value of $\delta^{13}C$. This section shows a sudden decrease in iron and increase in silica, indicating a more chert-rich sediment. This compositional change may then influence the carbon isotope ratio. The large difference in overall $\delta^{13}C$ values between both cores is possibly due to the different minerology of the sediments. The G7BF core is richer in calcite and ankerite and lacks the presence of siderite. The MP-BIF core is lacking calcite while siderite is present in almost all measured samples. The $\delta^{13}C$ values are then reflected by minerology, where the calcite and ankerite ($CaCO_3$) rich section (G7BF) shows more elevated $\delta^{13}C$ values compared to the more siderite ($FeCO_3$) rich section (MP-BIF). However the minerology does not control the $\delta^{13}C$, it merely reflects its variation. The $\delta^{13}C$ controls are related to long-term fluctuations in relative rates of primary organic carbon supply versus ferric iron species. Thus the variations in the source of organic matter versus the changing contribution of other electron acceptors like Mn-oxides or seawater SO_4^{2-} to the oxidation of organic carbon (Tsikos et al., in prep.). The redox reaction between ferric oxyhydroxide and organic carbon would have then taken place before burial, within the ambient water column, following the principles of DIR (Dissimilatory Iron Reduction). Therefore carbon isotopes can also be used as a powerful chemostratigraphic tool for the correlation of BIFs as used in this thesis.

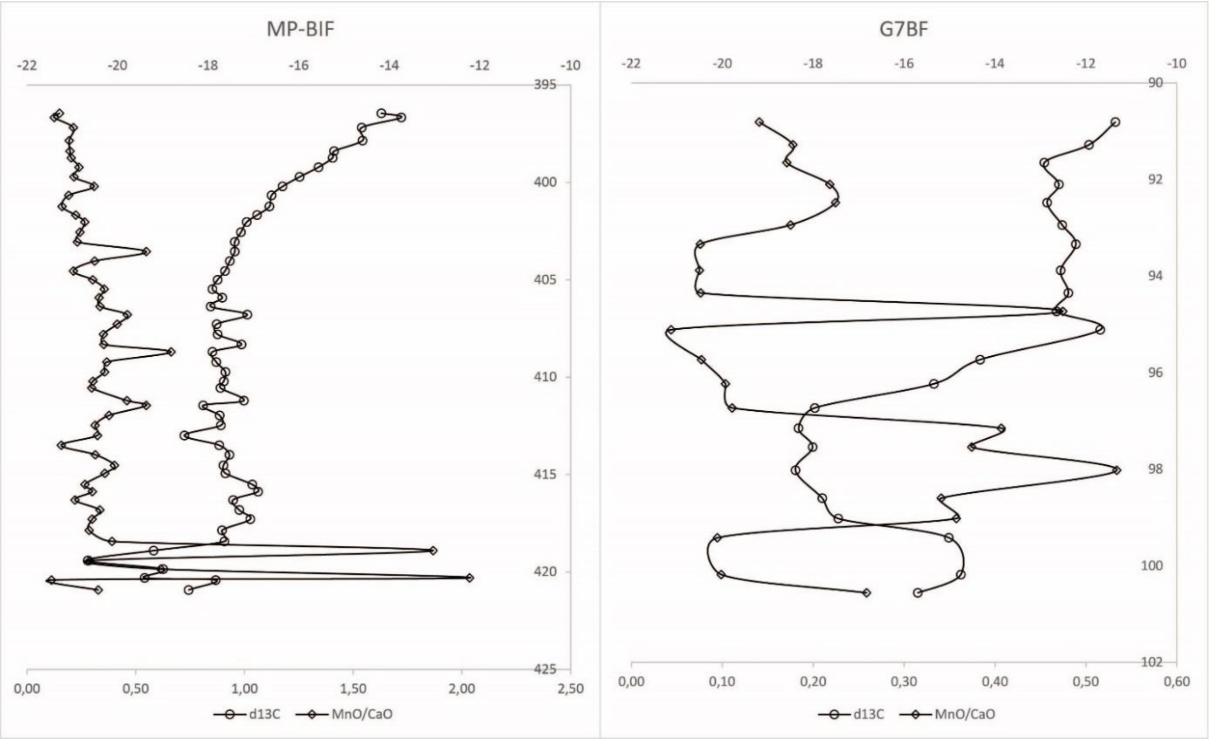

Figure 29: $\delta^{13}C$ and MnO/CaO plotted over depth (in m) for the MP-BIF section (left), and the G7BF section (right). The $\delta^{13}C$ shows an antithetic relationship with the MnO/CaO where $\delta^{13}C$ decreases with increasing MnO/CaO.

5.4 Context of Hotazel in broader Transvaal supergroup

5.4.1 Rare-earth element and Y characteristics of the Transvaal supergroup.

In Figure 30 the REE + Y distribution of the average MP-BIF and G7BF cores are compared to the hematite-chert BIF from the base of the Hotazel formation from Lantink et al. (2018), the Hotazel BIF from Tsikos and Moore (1997) and modern seawater (Bau et al., 1996). The Hotazel BIF from Tsikos and Moore (1997) shows a positive La, Eu, Gd and Y anomaly, no negative Ce anomaly and the HREEs are enriched compared to the LREEs and thus do not deviate much from the MP-BIF and G7BF cores. The Hotazel hematite-chert BIF lacks a positive La and Gd anomaly and shows no negative Ce anomaly. There is a distinct positive Eu anomaly and the HREEs are enriched compared to the LREEs. The strong Eu anomaly and the absence of a positive La anomaly stands out compared to the REE + Y distribution of Tsikos and Moore (1997) and the BIF presented in this thesis.

Figure 31 shows the REE + Y distribution of the average MP-BIF and G7BF cores and different formations of the Transvaal supergroup, lower in the stratigraphy. These consist of the average BIF of the Griquatown and Kuruman formation of the Asbestos hill group taken from Oonk et al. (2018), the Rooinekke limestone and the Klipput dolostone both taken from Schier et al. (2018). The REE + Y signal of the Griquatown and Kuruman formation show large similarities to those presented in this thesis containing a positive La, Gd and Y anomaly and enriched HREEs relative to LREEs. However, the positive Eu anomaly is larger in both the Kuruman (1.49) and the Griquatown formation (1.35) compared to that of the Hotazel formation (1.28). The Rooinekke limestone REE + Y signal shares a similar distribution, where the only difference compared to the BIFs is the larger Y anomaly. The Eu anomaly of 1.32 is lower than those of the Kuruman and Griquatown formations lower in the stratigraphy but larger than those of the Hotazel formation higher up the stratigraphy. The Klipput dolostone has a much more anomalous REE + Y distribution than any other presented in Figure 31 with a clear positive Eu anomaly, no positive La, Gd and Y anomaly and an enrichment in MREEs relative to the LREEs and HREEs. There is an overall decrease in Eu anomaly towards to top of the Transvaal supergroup stratigraphy, with the lowest values present in the Hotazel formation.

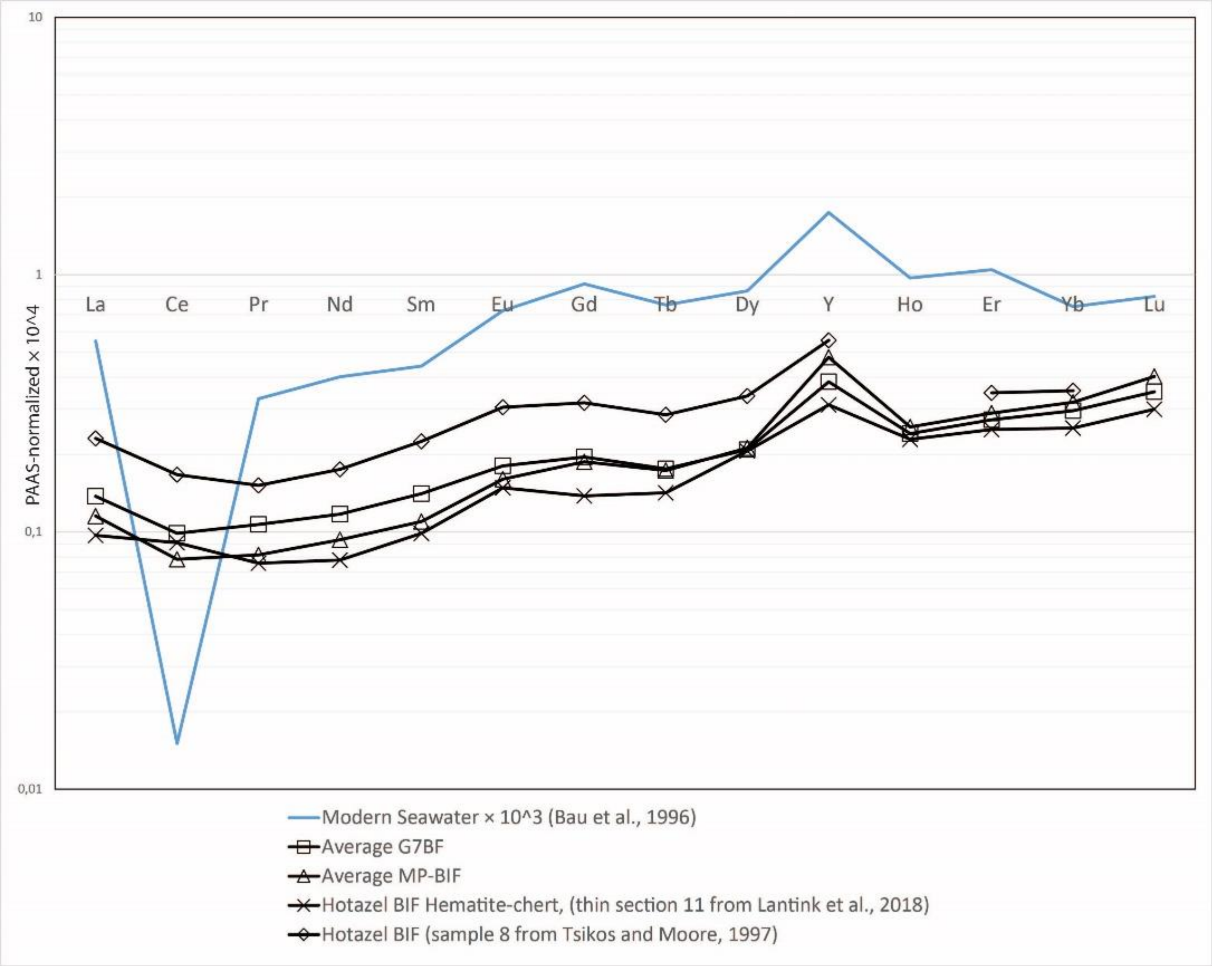

Figure 30: Plots of rare earth element data normalized to post Archean Australian shale (PAAS). REE + Y concentrations (ppm) of the average G7BF and average MP-BIF are compared with modern seawater (Bau et al., 1996), the Hotazel BIF Hematite-chert stratigraphically at the base of the Hotazel Fm. (Lantink et., 2018) and the BIF stratigraphically on top of the first Mn-Oxide (Tsikos and Moore, 1997). (See text for further discussion.)

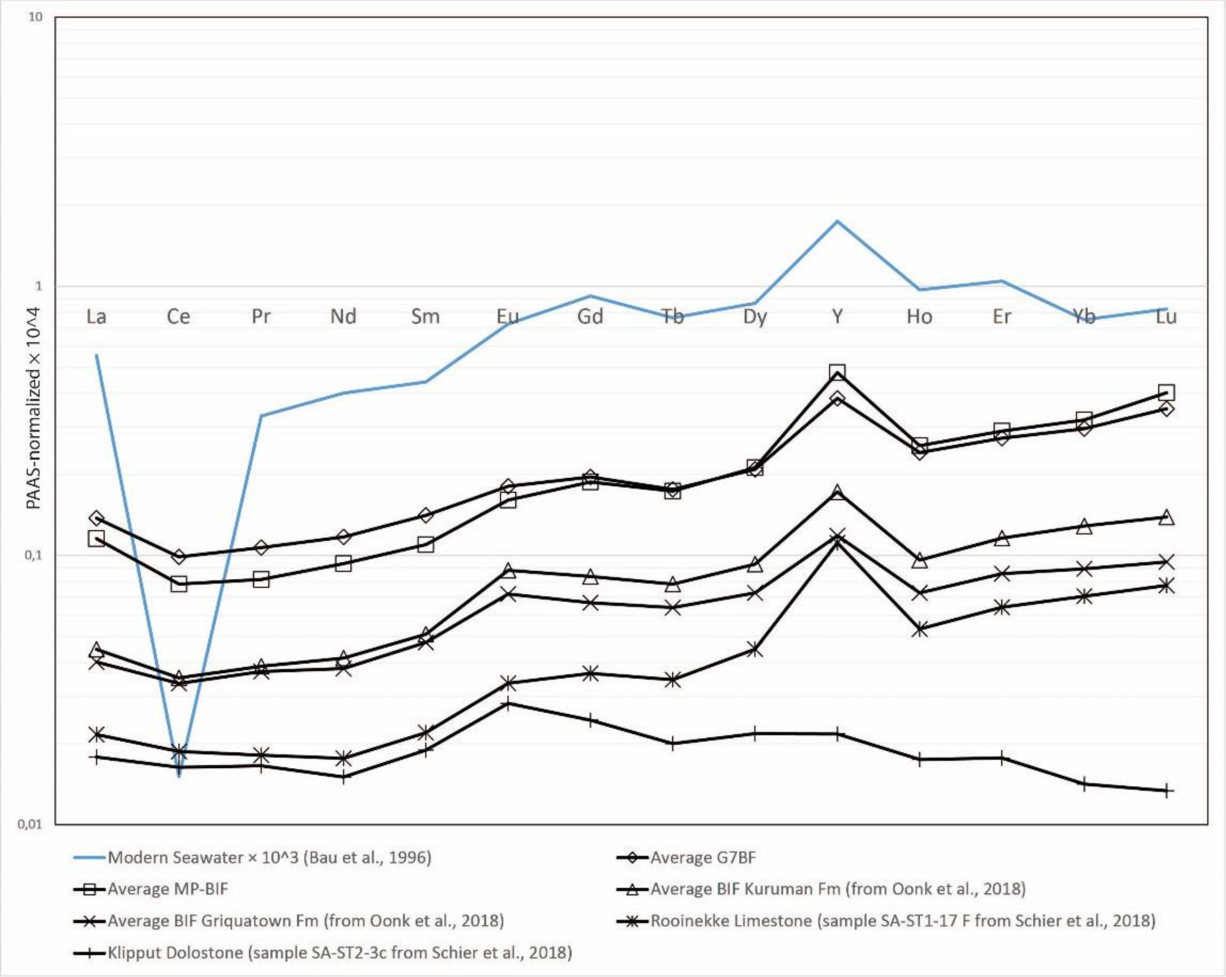

Figure 31: Plots of rare earth element data normalized to post Archean Australian shale (PAAS). REE + Y concentrations (ppm) of the average G7BF and average MP-BIF are compared with modern seawater (Bau et al., 1996), the average Griquatown and Kuruman formations (Oonk et al., 2018), the Rooinekke limestone and the Klipput dolostone, both from the Koegas formation (Schier et al., 2018) (See text for further discussion.)

The (Eu/Eu*) of the G7BF and MP-BIF cores are 1.28 and 1.29 respectively and thus do not show a characteristic positive Eu anomaly, indicating little hydrothermal activity during time of deposition. Figure 32 shows that the Eu anomaly decreases from 1.48 in the Kuruman formation, 1.35 in the Rooinekke limestone of the Koegas subgroup gradually to 1.28 in the Hotazel formation. So there is an overall decrease in hydrothermal input over time during deposition of the Transvaal supergroup, with the lowest values present during the GOE. There is however one discrepancy in this trend. The contact between the Ongeluk formation and the Hotazel formation does show a positive Eu anomaly (Lantink et al., 2018). The volcanic andesite of the Ongeluk formation did have hydrothermal activity which left its mark onto the base of the Hotazel formation. This indicates one generic episode of increased hydrothermal activity in an overall decreasing trend in the Transvaal Supergroup (Figure 32). Oonk et al. (2018) reported a decrease in (Yb/Ce)N ratio from the Kuruman formation to the stratigraphically higher Griquatown formation, where the average bulk rock values decrease from 3.7 to 2.4 and the largest decrease was observed in the acetate fraction, from 9.2 to 4.4. They proposed contamination by detrital input as an explanation for this flattening, since there was a strong correlation between (Yb/Ce)N and Zr. The average (Yb/Ce)N values presented in this thesis are 4.9 and 3.4 for the MP-BIF and G7BF cores respectively and thus are similar to those of the Asbestos Hills subgroup. However, there does not seem to be a stratigraphically controlled trend in the plots. Also the (Yb/Ce)N ratio is not controlled by detrital input, as there is no correlation with Zr noticeable (Figure 16B). This then indicates that the slope of the REE + Y pattern is not anymore controlled by a crustal contaminant and is thus a primary seawater signature.

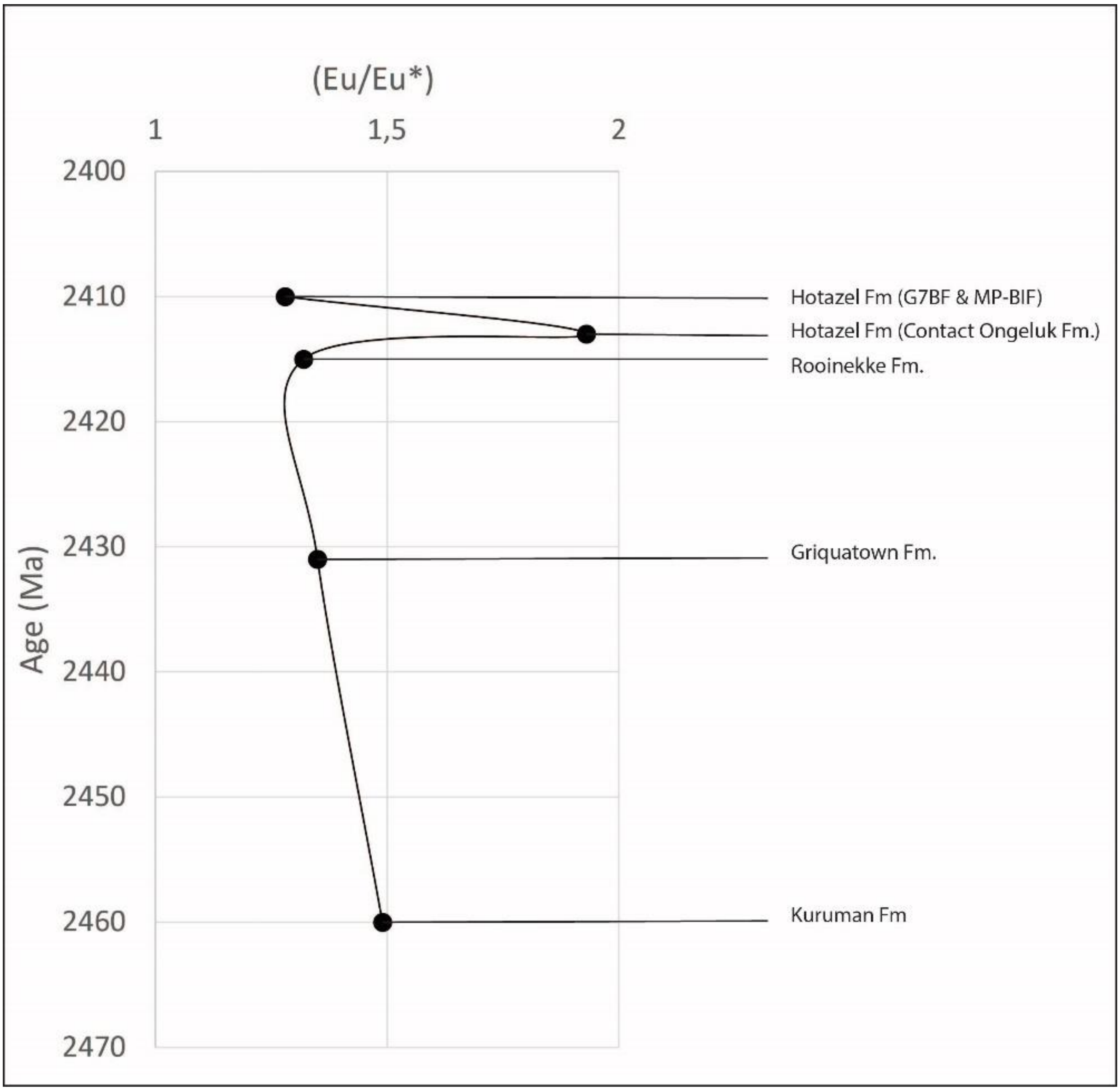

Figure 32: (Eu/Eu) vs sediment age indicating the overall decreasing trend of hydrothermal activity during deposition of the Transvaal Supergroup.*
Hotazel Fm age from Gutzmer and Beukes, (1996).
Rooinekke Fm age from (Schroder et al., (2011)
Griquatown Fm age from (Trendall et al., (1990)
Kuruman Fm age from Pickard, (2003) (see text for discussion).

5.4.2 Source of Iron and Manganese and subsequent precipitation

The sources of Fe, Mn and other metals are not crustal and must have been brought in through hydrothermal activity. During deposition of the Hotazel formation hydrothermal activity was limited. It is thus unlikely that the source of Fe and Mn was active during time of the Hotazel deposition. Dissolved iron and manganese were then brought in when hydrothermal activity was present, prior to or during time of the Asbestos Hills deposition. The stratified basin was then enriched in dissolved Fe(II) with a Fe/Mn ratio of ~(50/1) and contained a near-zero δ^{57}Fe composition. The preferential precipitation of Fe with respect to Mn, together with long-term Mn recycling in the water column resulted in an enrichment of dissolved Mn in the bottom, anoxic waters. In these anoxic to sub-oxic aqueous environment manganese concentrations can build up significantly, e.g. in the Orca Basin, where Mn^{2+} concentrations reach > 400µM (Van Cappellen et al,. 1998). Rayleigh fractionation of oxide-dominated BIF would then result in a terminal depositional basin for the Hotazel formation, where Mn-oxide could precipitate in a basin with a Fe/Mn ratio of ~(15/1). These Fe/Mn ratios are reflected within the G7BF and MP-BIF sections as well. The averages of 45 and 66 of the MP-BIF and G7BF sections agree with the notion of a stratified basin enriched in dissolved Fe(II). The notable decrease towards the base of the G7BF core, with values of 18 – 21 in the bottom first meter of this section then starts the transition towards the Mn-oxide. The increased values of Mn in the Hotazel formation were initially thought to be caused by an increase in Mn input due to enhanced hydrothermal activity. However no other elements show a strong increase in concentration contradicting the argument of enhanced hydrothermal activity (Oonk et al., 2018). Furthermore, contemporaneous hydrothermal vent fluids have Fe/Mn ratios which are an order of magnitude lower than those of the Asbestos Hills subgroup (German and Von Damm, 2006). The generic episode of hydrothermal activity during extrusion of the Ongeluk formation's volcanic andesite may have brought in extra dissolved Fe or Mn. Assuming no further input of Mn during deposition of the Hotazel formation, due to the lack of hydrothermal activity within the basin, the total amount of dissolved Mn would now decrease over time. Transgression-regression cycles (Tsikos and Moore, 1997) may then control the cyclicity of the Hotazel Fm. and in turn whether or not Mn is able to precipitate in these large quantities. A possible way to verify this hypothesis would be to measure the Y/Ho ratio extensively throughout the entire stratigraphy of the Hotazel formation. If this trend, which represents the change in water depth during deposition of the chemical sediment, would follow the transgression-regression cycles proposed by Tsikos and Moore (1997), the cyclicity of the Hotazel formation might be verified.

Other theories proposed to explain the deposition of Hotazel BIFs are 1) a volcanic-exhalative origin of the Hotazel formation, where Fe-Mn sediments are rapidly deposited in the proximity of the Ongeluk hydrothermal vent site (Cornell and Schütte, 1995; Cornell et al., 1996; Kopp et al., 2005; Kirschvink and Kopp, 2008) and 2) precipitation of Mn(IV) brought in from the Ongeluk volcanic system in the aftermath of a Snowball Earth (Kirschvink et al., 2000; Kirschvink et al., 2011). Such large amounts Mn precipitation could have occurred as a consequence of the accumulation of dissolved Mn in the ice-covered oceans during the Snowball Earth glaciation event. Upwelling of seawater after the global glaciation transported dissolved Fe and Mn to a shallow-marine environment. Due to the higher oxidation potential of Mn compared to Fe (Kopp et al., 2005), precipitation of Fe would occur first and the dissolved Mn would then accumulate in a shallower marine environment. High levels of cyanobacteria in the aftermath of the Snowball Earth glaciation then subsequently caused oxidation and precipitation of Mn-oxides. Both theories however fail to explain the cyclic nature of the Mn-oxide deposition in the Hotazel formation and do not account for the uniquely high concentration of Mn.

5.4.3 Environmental change of the Transvaal basin.

The two drill-cores MP-BIF and G7BF each have their own characteristic stratigraphic history. Both BIFs are stratigraphically on top of the first Mn-oxide intercalation of the Hotazel formation. The thickness of this intercalation however varies from 25 meters in the MP-BIF core to 43 meters in the G7BF core. This thickness variation is antithetic with respect to the upper BIF, investigated in this thesis. The variation in thickness could be due to a differential precipitation rate of each chemical sediment. However, the total thickness of each core from the bottom contact with the Ongeluk formation to the black shale is equal, so large variation in precipitation rate is unlikely. BIFs are thinly bedded and change in chemical composition can vary from mm to cm scale. Each individual band may have been deposited with a different precipitation rate, resulting in an average stable precipitation rate while on a smaller scale these rates may differ substantially. Furthermore, the antithetic relationship would not make sense if the difference in BIF and Mn-oxide composition would influence the precipitation rate. Another possibility to explain the thickness variation is a local change in depositional environment. The two drill-cores are located in laterally different parts of the basin. The depositional environment could have been more favourable for Mn-oxide deposition in the G7BF section over a longer period of time. This while BIF deposition quickly became more favourable in the MP-BIF section. Oxidation state and depth of the water column would arguably influence the precipitation of Mn-oxide with respect to BIFs the most. The difference in paleo-depositional environment of both sections will influence trace element distribution and subsequently leave a chemical and compositional mark on the BIF deposited after the Mn-oxide intercalation. Correlating the top 13 meters of the MP-BIF section with the 10 meter thick G7BF core indicates these chemical sediments were deposited during roughly the same time interval and that precipitation rates were equal. The bottom 15 meters of the MP-BIF section then subsequently have been deposited at the same interval as the Mn-oxide of the G7BF section. The decrease in Y/Ho towards the base of both sections (and the Mn-oxide) indicates a transition towards a shallower part of the basin. The increase in detrital or volcanic ash particles towards the base support this notion. The Mn-oxide intercalation is then deposited in a shallower part of the basin near the manganese chemocline. During the same time the BIF in the bottom MP-BIF section is deposited at a laterally different, deeper part of the basin by either aerobic or anaerobic iron-oxidation mechanisms. The black shale stratigraphically above the first BIF in both sections has then been deposited in a more carbonate rich environment, deeper in the basin and further away from the continental shelf. This would all imply that a given environment in a stratified basin, under the right conditions can produce compositionally contrasting styles of chemical sedimentation at the same time.

Conclusion

X-Ray Diffraction, Optical microscopy, XRF, LA-ICP-MS and Carbon isotope analyses were carried out to construct a stratigraphic correlation between the G7BF and MP-BIF sections and to obtain in detail the mineralogical and chemical composition, redox conditions and the paleo-depositional environment of the first BIF in the Hotazel formation. The results and subsequent interpretations have led to the following conclusions.

The REE + Y distribution of both sections showed depleted LREEs relative to the HREEs, positive La, Gd and Y anomalies and no negative Ce anomaly. Apart from the absence of a negative Ce anomaly, which suggests a marine anoxic environment, the water column resembled that of modern (and ancient) seawater. The lack of a distinct positive Eu anomaly indicated little to no hydrothermal activity during deposition of the Hotazel Fm. There is a strong increase in detrital or volcanic ash particles towards the Mn-oxide intercalation. Also, there is a decrease in Y/Ho ratio towards the base of both sections related to a decrease in water depth. Both these factors strengthen the idea of Mn deposition in a shallower marine environment closer to the continental shelf. Carbon isotopes are largely depleted with $\delta^{13}C$ values ranging from -20.7 to -11.4‰. There is a gradual increase towards the top of the MP-BIF section, which follows the increase in CaO (wt%). There is a rather sharp increase towards the top of the G7BF which is interpreted to be caused by a sudden tectonic shift. Differential rate's in subsidence then explain the difference in gradual and steep increase of the $\delta^{13}C$ notable in both sections. The difference in overall $\delta^{13}C$ values between both sections is reflected by the different minerology of the chemical sediments, where the calcite ($CaCO_3$) rich section (G7BF) shows more elevated $\delta^{13}C$ values compared to the more siderite ($FeCO_3$) rich section (MP-BIF). Based on $\delta^{13}C$ data in conjunction with chemical composition and mineralogical assemblages the top 13 meters of the MP-BIF section are correlated with the entire G7BF section. The 10 meters thick G7BF drill-core is thus not a condensed version of the MP-BIF but a specific stratigraphic interval. Precipitation rates would have then been nearly equal for both sections during deposition. This would subsequently imply that the bottom of the MP-BIF section had been deposited during the same time interval as the Mn-oxide intercalation of the G7BF, indicating that indeed different types of chemical sediments, under the right conditions, can precipitate simultaneously at laterally different parts of the basin.

Acknowledgements

I would like to thank my supervisors Prof Dr Paul Mason from University Utrecht and Dr Harilaos Tsikos from Rhodes University for their guidance, constructive discussions and scientific contribution throughout the entire project. Also a special thanks to the following technical staff members of the UU Earth Sciences department: Jan van Tongeren, Helen de Waard, Arnold van Dijk and Anita van Leeuwen-Tolboom, which were all very helpful during my time in the lab. Furthermore, I would like to thank Yorick Veenma and Luuk Muthert for their peer reviews and the feedback on my English writing. Lastly I would like to thank my family and friends for the moral support throughout the project.

References

Alibert, C. (2016). Rare earth elements in Hamersley BIF minerals. *Geochimica et Cosmochimica Acta*, *184*, 311-328.

Altermann, W. and Nelson, D. R. (1998). Sedimentation rates, basin analysis and regional correlations of three Neoarchaean and Palaeoproterozoic sub-basins of the Kaapvaal craton as inferred from precise U–Pb zircon ages from volcaniclastic sediments. *Sedimentary Geology*, *120*(1-4): 225-256.

Bau, M. and Alexander, B. (2006). Preservation of Primary REE Patterns without Ce Anomaly during Dolomitization of Mid-Paleoproterozoic Limestone and the Potential Re-Establishment of Marine Anoxia Immediately after the 'Great Oxidation Event.' *South African Journal of Geology* 109(1–2): 81–86.

Bau, M. and Dulski, P. (1995). Comparative Study of Yttrium and Rare-Earth Element Behaviours in Fluorine-Rich Hydrothermal Fluids. *Contributions to Mineralogy and Petrology* 119(2–3): 213–23.

Bau, M. and Dulski, P. (1996). Distribution of Yttrium and Rare-Earth Elements in the Penge and Kuruman Iron-Formations, Transvaal Supergroup, South Africa. *Precambrian Research* 79(1–2): 37–55.

Bau, M. and Möller, P. (1993). Rare earth element systematics of the chemically precipitated component in Early Precambrian iron formations and the evolution of the terrestrial atmosphere-hydrosphere-lithosphere system. *Geochimica et Cosmochimica Acta*, *57*(10), 2239-2249.

Bekker, A., Holland, H.D., Wang, P.L., Rumble, D., Stein, H.J., Hannah, J.L., Coetzee, L.L. and Beukes, N.J. (2004). Dating the Rise of Atmospheric Oxygen. *Nature* 427(6970): 117–20.

Beukes, N. J. and Gutzmer, J. (2008). Origin and Paleoenvironmental Significance of Major Iron Formations at the Archean-Paleoproterozoic Boundary. *Reviews in Economic Geology* 15: 5–47.

Bolhar, R., Kamber, B.S., Moorbath, S., Fedo, M. and Whitehouse, M.J. (2004).

Characterisation of Early Archaean Chemical Sediments by Trace Element Signatures. 222: 43–60.

Byrne, R. H. and Kim, K. H. (1990). Rare earth element scavenging in seawater. *Geochimica et Cosmochimica Acta*, *54*(10), 2645-2656.

Cairns-Smith, A. G. (1978). Precambrian solution photochemistry, inverse segregation, and banded iron formations. *Nature*, *276*(5690), 807.

Chung, D., Zhou, M. F., Gao, J. F. and Chen, W. T. (2015). In-situ LA–ICP-MS trace elemental analyses of magnetite: The late Palaeoproterozoic Sokoman Iron Formation in the Labrador Trough, Canada. *Ore Geology Reviews*, *65*, 917-928.

Cloud, P. E. (1965). Significance of the Gunflint (Precambrian) Microflora: Photosynthetic oxygen may have had important local effects before becoming a major atmospheric gas. *Science*, *148*(3666), 27-35.

Condie, K. C. (1993). Chemical Composition and Evolution of the Upper Continental Crust: Contrasting Results from Surface Samples and Shales. *Chemical Geology* 104(1–4): 1–37.

Cornell, D. H. and Schütte, S. S. (1995). A volcanic-exhalative origin for the world's largest (Kalahari) manganese field. *Mineralium Deposita*, *30*(2), 146-151.

Cornell, D. H., Schütte, S. S. and Eglington, B. L. (1996). Prerumbrinn Reseurth The Ongeluk Basaltic Andesite Formation in Griqualand West , South Africa : Submarine Alteration in a 2222 Ma Proterozoic Sea.” *Precambrian Research* 79 (1996): 101–23.

Craig, H. (1957). Isotopic Standards for Carbon and Oxygen and Correction Factors for Mass-Spectrometric Analysis of Carbon Dioxide. *Geochimica et Cosmochimica Acta* 12(1–2): 133–49.

De Baar, H. J. (1991). On cerium anomalies in the Sargasso Sea. *Geochimica et Cosmochimica Acta*, *55*(10), 2981-2983.

Garrels, R. M., Perry, E. A. and Mackenzie, F. T. (1973). Genesis of Precambrian iron-formations and the development of atmospheric oxygen. *Economic Geology*, *68*(7), 1173-1179.

Gumsley, A. P., Chamberlain, K.R., Bleeker, W., Soderlund, U., De Kock, M.O., Larsson, E.R. and Bekker, A. (2017). Timing and Tempo of the Great Oxidation Event. *Proceedings of the National Academy of Sciences* 114(8): 1811–16.

Gutzmer, J. and Beukes, N. J. (1996). Mineral Paragenesis of the Kalahari Manganese Field, South Africa. *Ore Geology Reviews* 11(6): 405–28.

Høgdahl, O. T., Melsom, S. and Bowen, V. T. (1968). Neutron Activation Analyses of Lanthanide Elements in Seawater. *Central Inst. for Industrial Research, Oslo*.

Holland, H. D. (1984). The chemical evolution of the atmosphere and oceans. *Princeton University Press.*

Isley, A. E. (1995). Hydrothermal Plumes and the Delivery of Iron to Banded Iron

Formation. *The Journal of Geology* 103(2): 169–85..

James, H. L. (1954). Sedimentary facies of iron-formation. *Economic Geology*, *49*(3), 235-293

Johnson, J. E., Webb, S.M., Thomas, K., Ono, S., Kirschvink, J.L. and Fischer, W.W. (2013). Manganese-Oxidizing Photosynthesis before the Rise of Cyanobacteria. *Proceedings of the National Academy of Sciences* 110(28)

Kappler, A., Pasquero, C., Konhauser, K. O. and Newman, D. K. (2005). Deposition of banded iron formations by anoxygenic phototrophic Fe (II)-oxidizing bacteria. *Geology*, *33*(11), 865-868.

Kim, K. H., Byrne, R. H. and Lee, J. H. (1991). Gadolinium behavior in seawater: a molecular basis for gadolinium anomalies. *Marine chemistry*, *36*(1-4), 107-120.

Kirschvink, J. L., Gaidos, E.J., Bertani, L.E., Beukes, N.J., Gutzmer, J., Maepa, L.N. and Steinberger, R.E. (2000). Paleoproterozoic Snowball Earth: Extreme Climatic and Geochemical Global Change and Its Biological Consequences. *Proceedings of the National Academy of Sciences* 97(4): 1400–1405.

Kirschvink, J. L., Sekine, Y., Tajika, E., Tada, R., Hirai, T., Goto, K.T., Kuwatani, T., Goto, K., Yamamoto, S., Tachibana, S. and Isozaki, Y. (2011). Manganese Enrichment in the Gowganda Formation of the Huronian Supergroup: A Highly Oxidizing Shallow-Marine Environment after the Last Huronian Glaciation. *Earth and Planetary Science Letters* 307(1–2): 201–10.

Kirschvink, J. L. and Kopp, R. E. (2008). Palaeoproterozoic ice houses and the evolution of oxygen-mediating enzymes: the case for a late origin of photosystem II. *Philosophical Transactions of the Royal Society of London B: Biological Sciences*, *363*(1504), 2755-2765.

Klein, C. (2005). Some Precambrian Banded Iron-Formations (BIFs) from around the World: Their Age, Geologic Setting, Mineralogy, Metamorphism, Geochemistry, and Origin. *American Mineralogist* 90(10): 1473–99.

Klemm, D. D. (2000). The Formation of Palaeoproterozoic Banded Iron Formations and Their Associated Fe and Mn Deposits, with Reference to the Griqualand West Deposits, South Africa. *Journal of African Earth Sciences* 30(1): 1–24.

Kopp, R. E., Kirschvink J. L., Hilburn, I. A. and Nash, N.C. (2005). The Paleoproterozoic Snowball Earth: A Climate Disaster Triggered by the Evolution of Oxygenic Photosynthesis. *Proceedings of the National Academy of Sciences* 102(32)

Lantink, M. L., Oonk, P.B.H., Floor, G.H., Tsikos, H. and Mason, P.R.D. (2018). Fe Isotopes of a 2.4 Ga Hematite-Rich IF Constrain Marine Redox Conditions around the GOE. *Precambrian Research* 305: 218–35.

Lyons, T. W., Reinhard, C. T. and Planavsky, N. J. (2014). The Rise of Oxygen in Earth's Early Ocean and Atmosphere. *Nature* 506(7488): 307–15.

Mhlanga, X. R., Tsikos, H., Lee, B. K., Lyons, T. W., Boyce, A. (2018). Trace Element Evidence from the 2.4 Ga Hotazel Fe-Mn Formation, South Africa, Constrain

Marine Redox Conditios at the Onset of the Great Oxidation Event [abstract]. In AGU Fall Metting; 2018 Dec 10-14; Washington, DC. Philadelphia (PA): AGU.

Moore, J. M. and Tsikos, H. (1997). Petrography and Geochemistry of the Paleoproterozoic Hotazel Iron-Formation, Kalahari Manganese Field, South Africa: Implications Form Precambrian Manganese Metallogenisis. *EconomiGc eology* 92(September): 87–97.

Moore, J. M., Tsikos, H. and Polteau, S. (2002). Deconstructing the Transvaal Supergroup , South Africa : Implications for Palaeoproterozoic Palaeoclimate Models. *African Earth Scinces* 33(2001): 437–44.

Nadoll, P., Angerer, T., Mauk, J. L., French, D. and Walshe, J. (2014). The chemistry of hydrothermal magnetite: A review. *Ore Geology Reviews*, *61*, 1-32.

Nozaki, Y., Zhang, J. and Amakawa, H. (1997). The fractionation between Y and Ho in the marine environment. *Earth and Planetary Science Letters*, *148*(1-2), 329-340.

Ohmoto, H., Watanabe, Y., Ikemi, H., Poulson, S.R. and Taylor, B.E. (2006). Sulphur Isotope Evidence for an Oxic Archaean Atmosphere. *Nature* 442(7105): 908–11.

Oonk, P.B.H., Mason, P.R.D., Tsikos, H. and Bau, M. (2018). Fraction-Specific Rare Earth Elements Enable the Reconstruction of Primary Seawater Signatures from Iron Formations." *Geochimica et Cosmochimica Acta* 238: 102–22.

Oonk, P.B.H., Tsikos, H., Mason, P.R.D., Henkel, S., Staubwasser, M., Fryer, L., Poulton, S.W. and Williams, H.M. (2017). Fraction-Specific Controls on the Trace Element Distribution in Iron Formations: Implications for Trace Metal Stable Isotope Proxies. *Chemical Geology* 474(June): 17–32.

Pickard, A. L. (2003). SHRIMP U–Pb zircon ages for the Palaeoproterozoic Kuruman Iron Formation, northern Cape Province, South Africa: evidence for simultaneous BIF deposition on Kaapvaal and Pilbara cratons. *Precambrian Research*, *125*(3-4), 275-315.

Schier, K., Bau, M., Munker, C., Beukes, N. and Viehmann, S. (2018). Trace Element and Nd Isotope Composition of Shallow Seawater Prior to the Great Oxidation Event: Evidence from Stromatolitic Bioherms in the Paleoproterozoic Rooinekke and Nelani Formations, South Africa. *Precambrian Research* 315(January): 92–102.

Schneiderhan, E. A., Gutzmer, J., Strauss, H., Mezger, K. and Beukes, N.J. (2006). The Chemostratigraphy of a Paleoproterozoic MnF-BIF Succession - The Voëlwater Subgroup of the Transvaal Supergroup in Griqualand West, South Africa. *South African Journal of Geology* 109(1–2): 63–80.

Schröder, S., Bedorf, D., Beukes, N. J. and Gutzmer, J. (2011). From BIF to red beds: Sedimentology and sequence stratigraphy of the Paleoproterozoic Koegas Subgroup (South Africa). *Sedimentary Geology*, *236*(1-2), 25-44.

Swart, Q. D. (2012). Carbonate rocks of the Paleoproterozoic Pretoria and Postmasburg Groups, Transvaal Supergroup (Doctoral dissertation).

Taylor, S. R. and McLennan, S. M. (1985). The continental crust: Its evolution and composition. *Lon on: Blackwell*.

Thibon, F., Blichert-Toft, J., Tsikos, H., Foden, J., Albalat, E. and Albarede, F. (2019). Dynamics of Oceanic Iron Prior to the Great Oxygenation Event. *Earth and Planetary Science Letters* 506: 360–70.

Trendall A. F., Nelson D., Thorne A., Compston W., Williams I. and Armstrong R. (1990). Precise zircon U-Pb chronological comparison of the volcano-sedimentary sequences of the Kaapvaal and Pilbara cratons between about 3.1 and 2.4 Ga. In: Glover, J.E., Ho, S.E. (Eds.), *Proceedings of the Third International Archaean Symposium, Perth, 1990, Extended Abstracts*, pp. 81–83. Geoconferences (W.A.) Inc., Perth

Trendall, A. F. (2002). The significance of iron-formation in the Precambrian stratigraphic record. *Precambrian sedimentary environments: A modern approach to ancient depositional systems*, 33-66.

Tsikos, H. (1994). The mineralogy and geochemistry of the Voelwater banded iron-formation, Northern Cape Province: *Unpublished MSc thesis, Rhodes Univ., South Africa*, 190 p.

Tsikos, H., Beukes, N. J., Moore, J. M. and Harris, C. (2003). Deposition, Diagenesis, and Secondary Enrichment of Metals in the Paleoproterozoic Hotazel Iron Formation, Kalahari Manganese Field, South Africa. *Economic Geology* 98(7): 1449–62.

Tsikos, H., Matthews, A., Erel, Y. and Moore, J. M. (2010). Iron Isotopes Constrain Biogeochemical Redox Cycling of Iron and Manganese in a Palaeoproterozoic Stratified Basin. *Earth and Planetary Science Letters* 298(1–2): 125–34.

Tsikos, H., Rafuza, S., Oonk, P.B.H., Mhlanga, X.R., Papadopoulos, V., Boyce, A.C., Mason, P.R.D., Harris, C., Grocke, D.R. and Lyons, T.W. (in prep.). Carbon Isotope Evidence for Water-column Formation of Iron Formation Carbonates.

Van Cappellen, P., Voillier, E. and Roychoudhury, A. (1998). Biogeochemical Cycles of Manganese and Iron at the Oxic-Anoxic Transition of a Stratified Marine Basin (Orca Basin, Gulf of Mexico). *Environmental Science and Technology* 32(19): 2931–39.

Van der Merwe, S. J. (1997). Basin Analysis of the Kalahari Manganese Basin. *Unpublished MSc thesis, Rhodes Univ., South Africa*.

Viehmann, S., Bau, M., Hoffmann, J. M. and Münker, C. (2015). Geochemistry of the Krivoy Rog Banded Iron Formation, Ukraine, and the Impact of Peak Episodes of Increased Global Magmatic Activity on the Trace Element Composition of Precambrian Seawater. *Precambrian Research* 270: 165–80.

Appendix

1. Photographs of the drill-cores

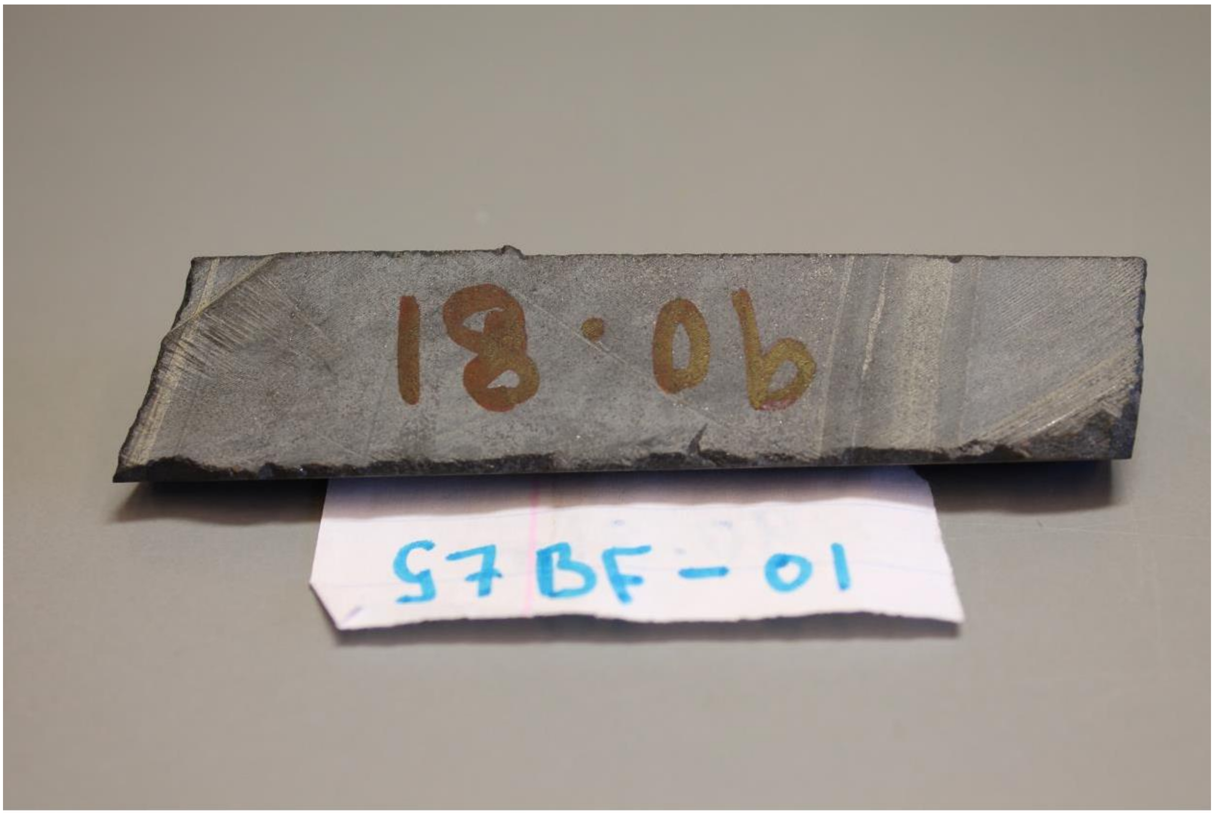

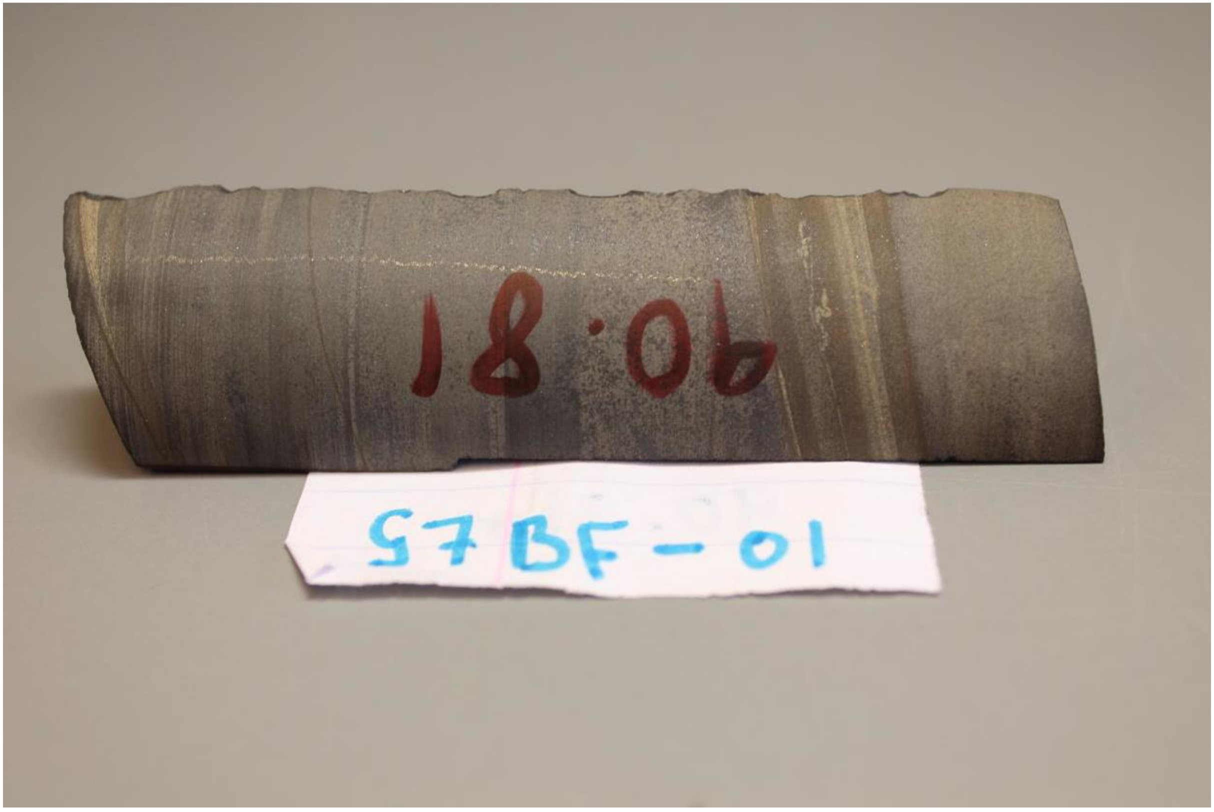


57 BF-02


91.28
57 BF-02

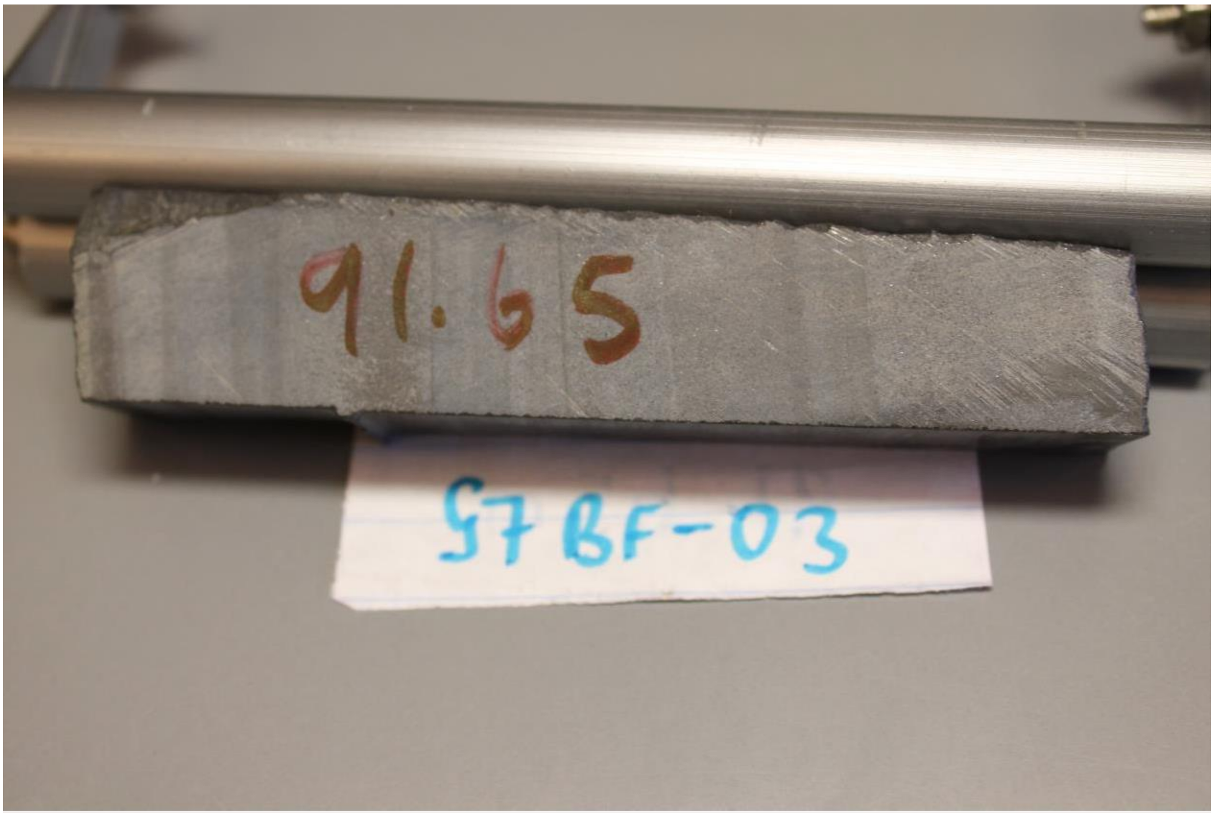
91.65
§7 BF-03

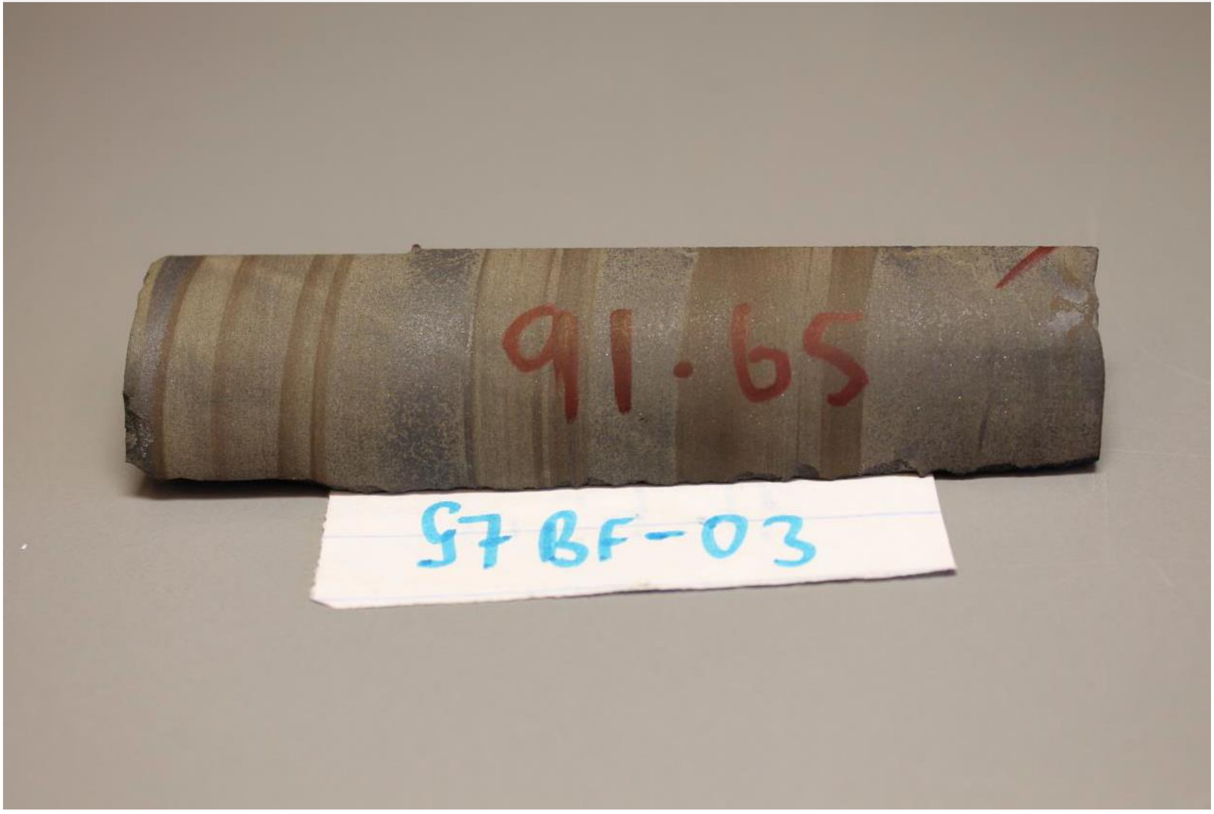
91.65
§7 BF-03

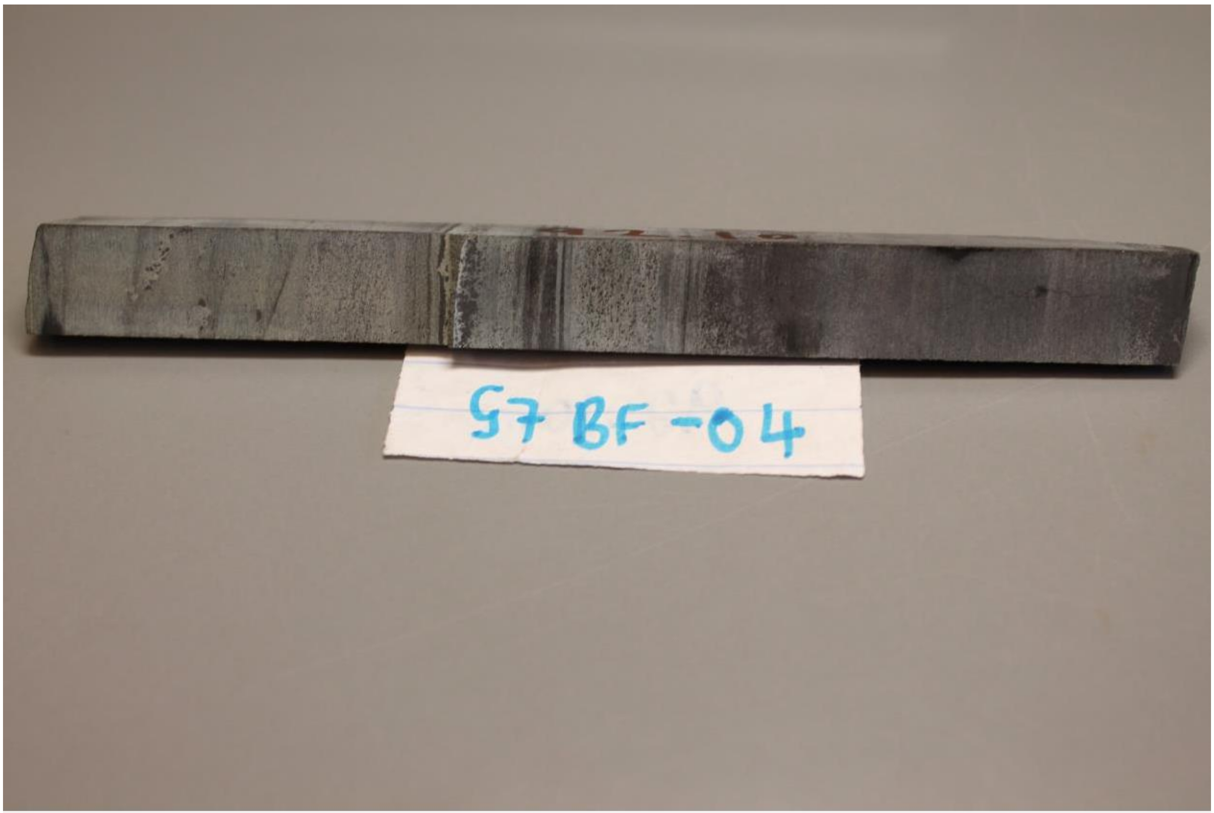
S7 BF-04

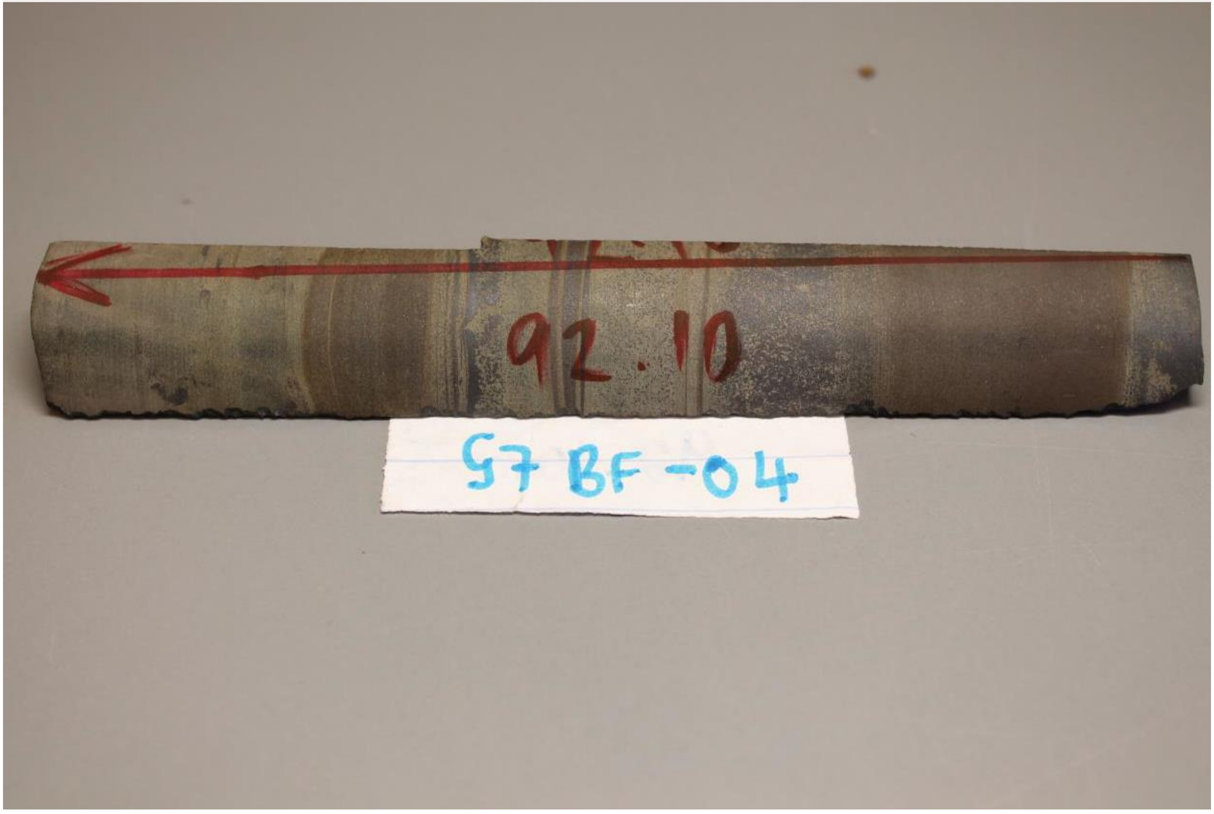
92.10
S7 BF-04


92.48
92.48
G7 BF-05

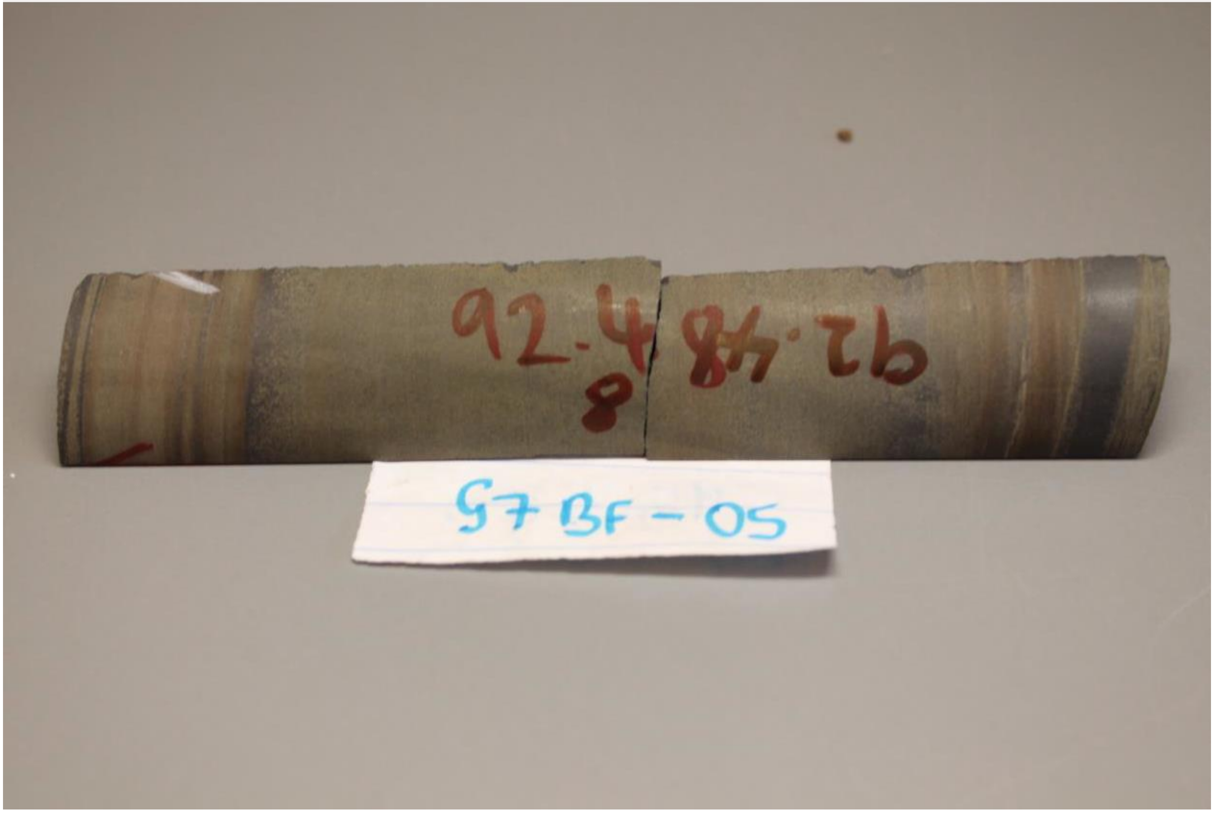
92.48
92.48
G7 BF-05


G7BF-06


92.94
92.94
92.94
G7BF-06


G7 BF-07

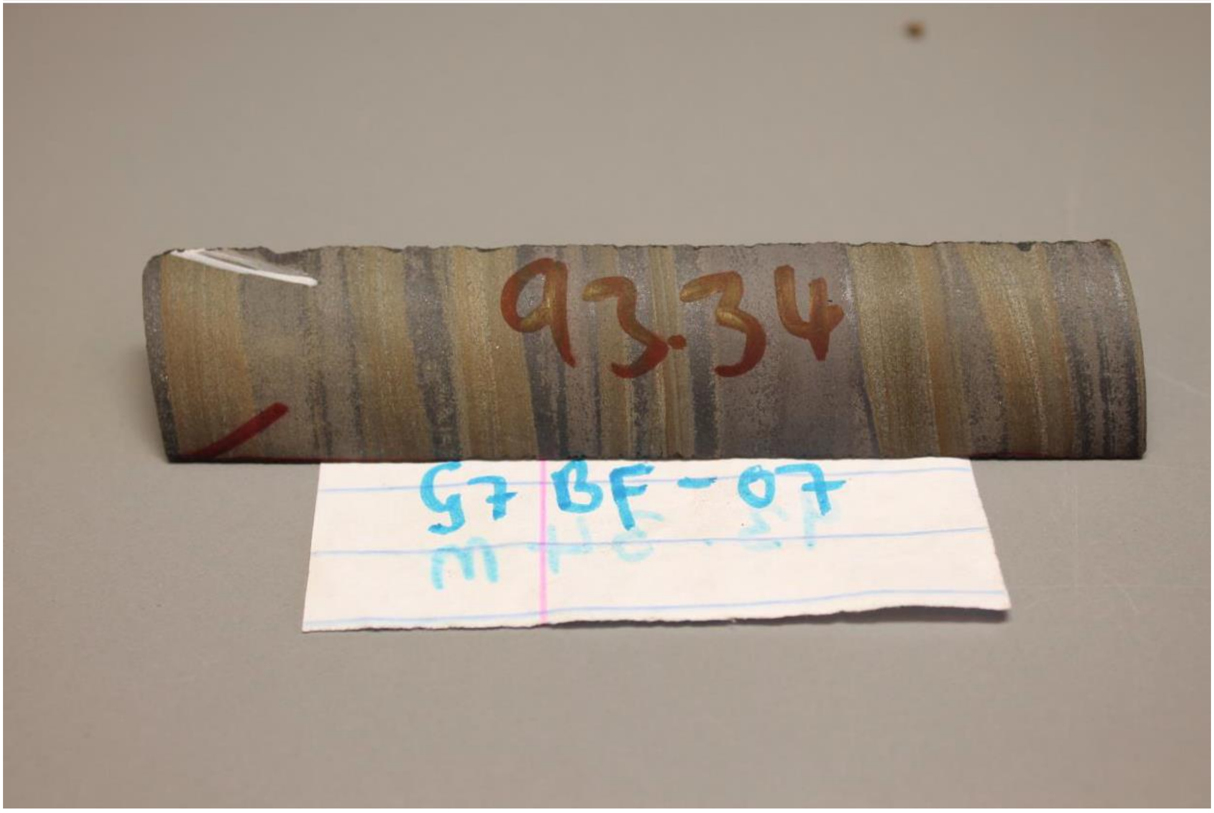
93.34
G7 BF-07

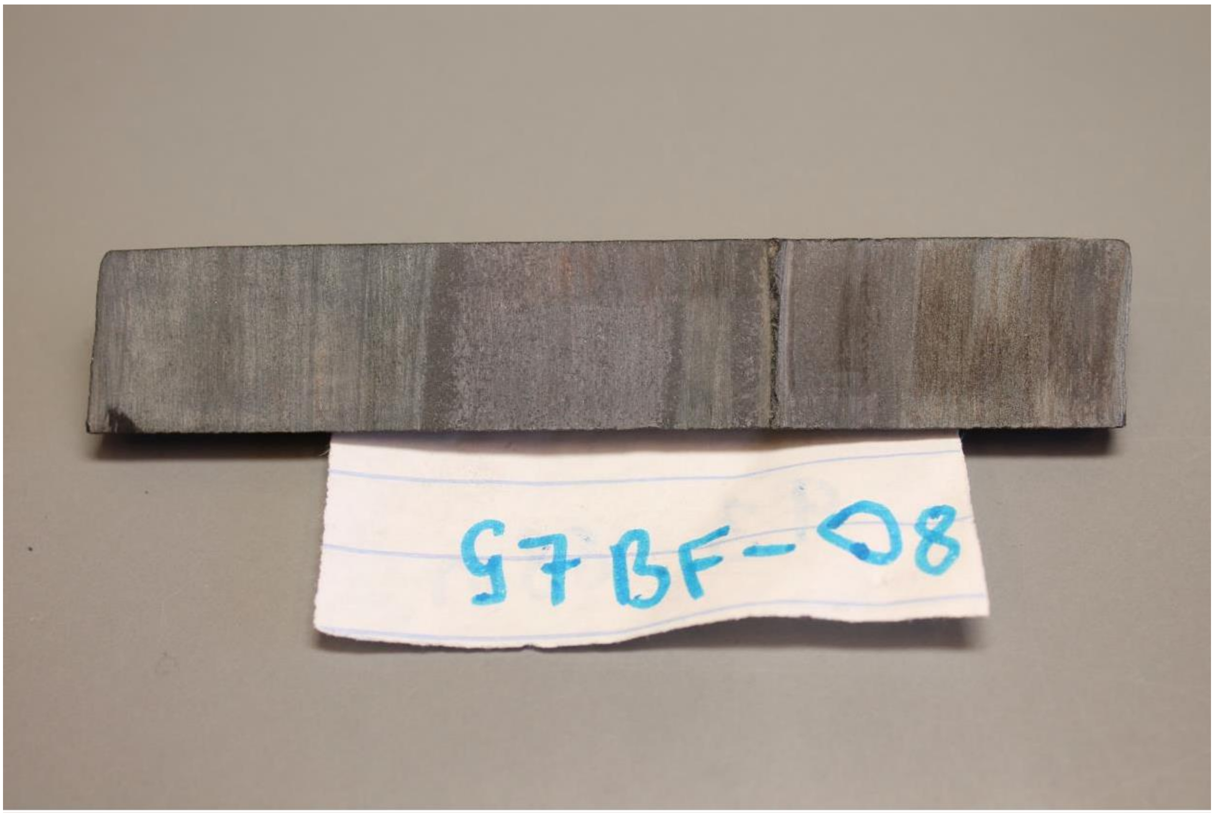
97BF-08

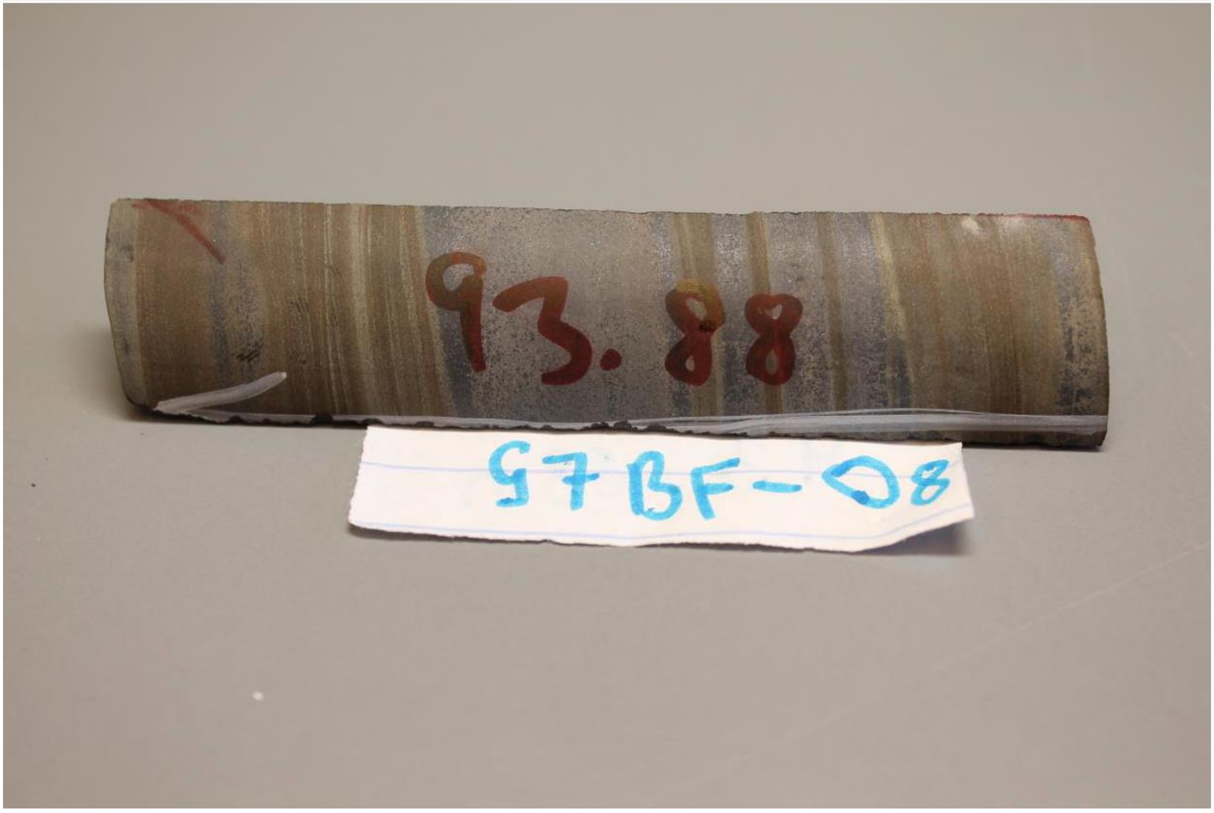
93.88
97BF-08

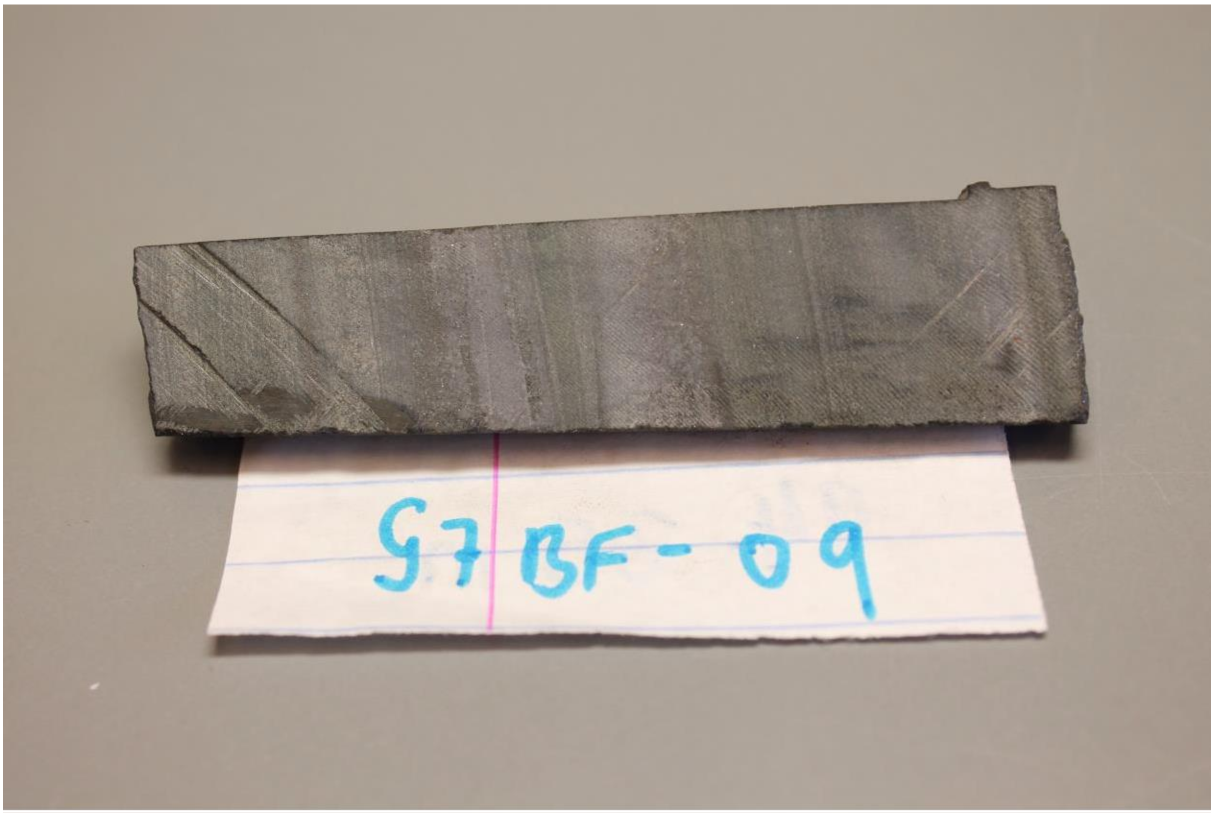
97 BF-09

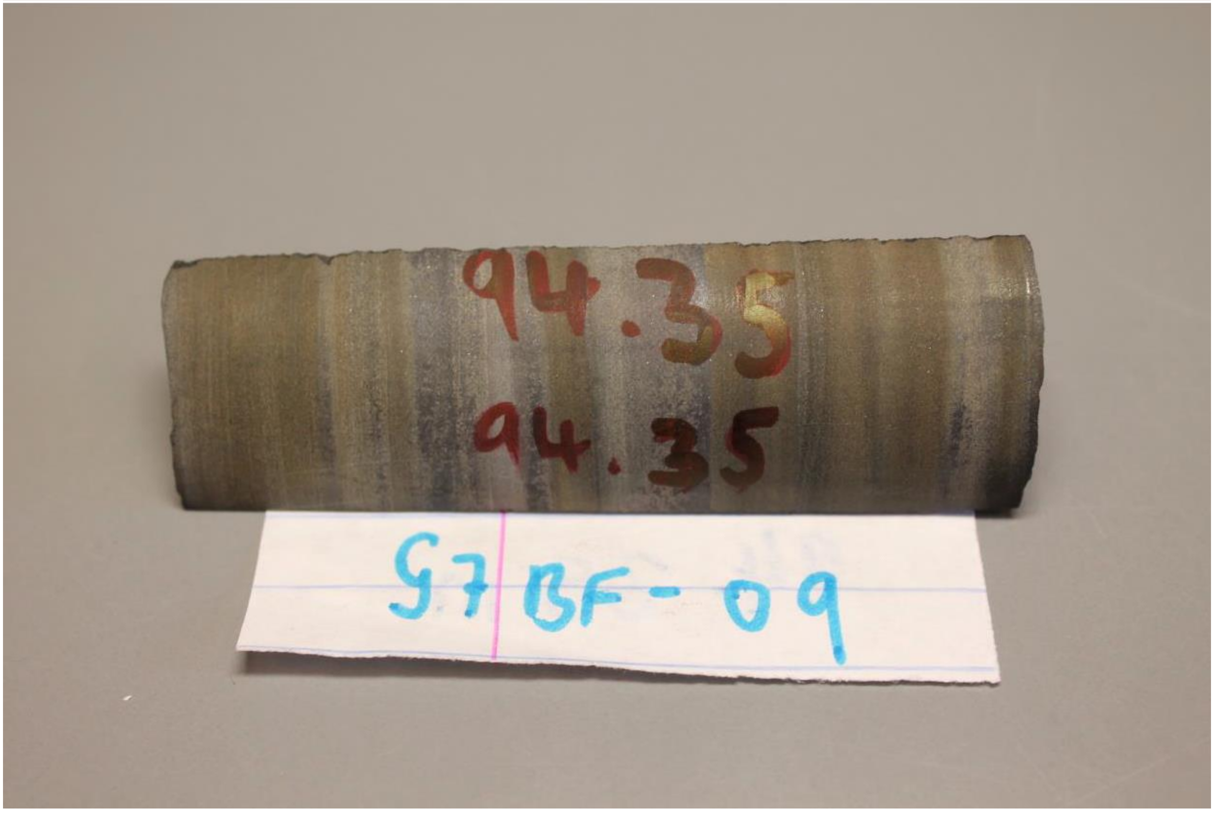
94.35
94.35
97 BF-09

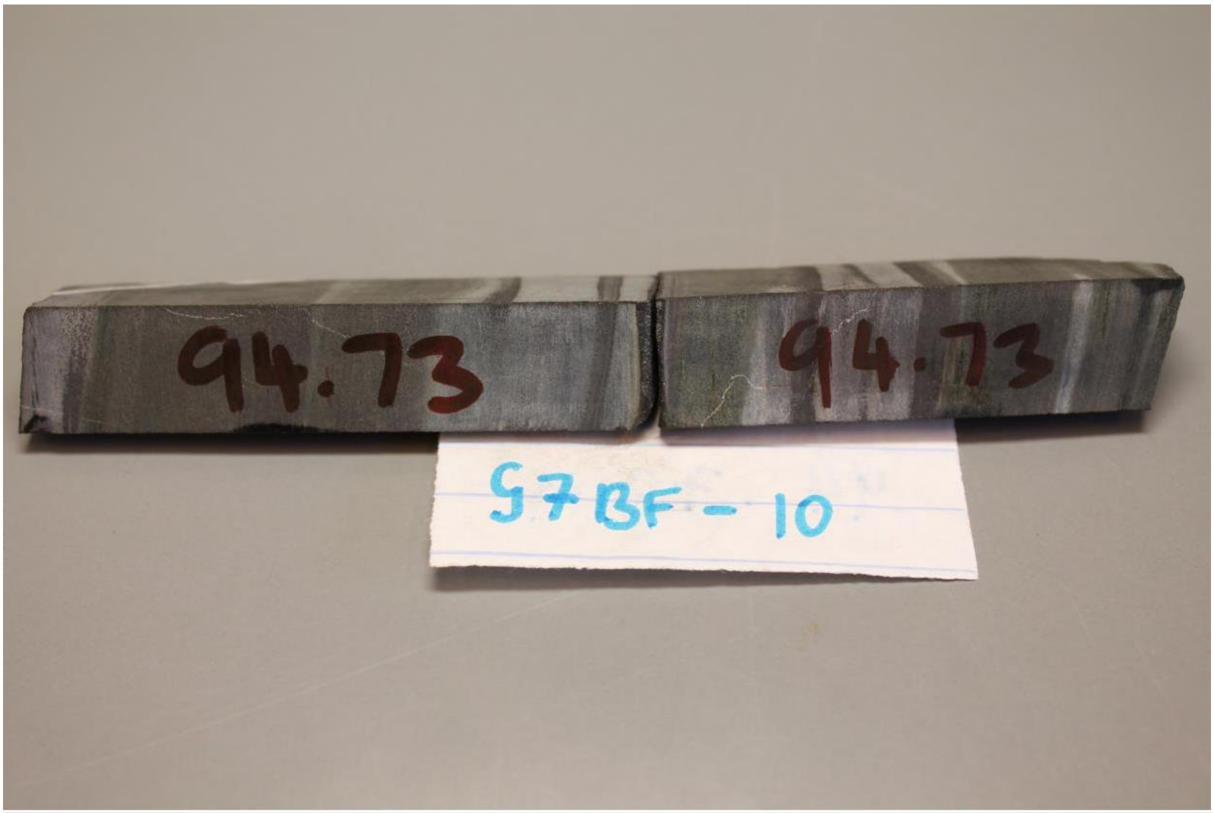
94.73
94.73
S7BF - 10

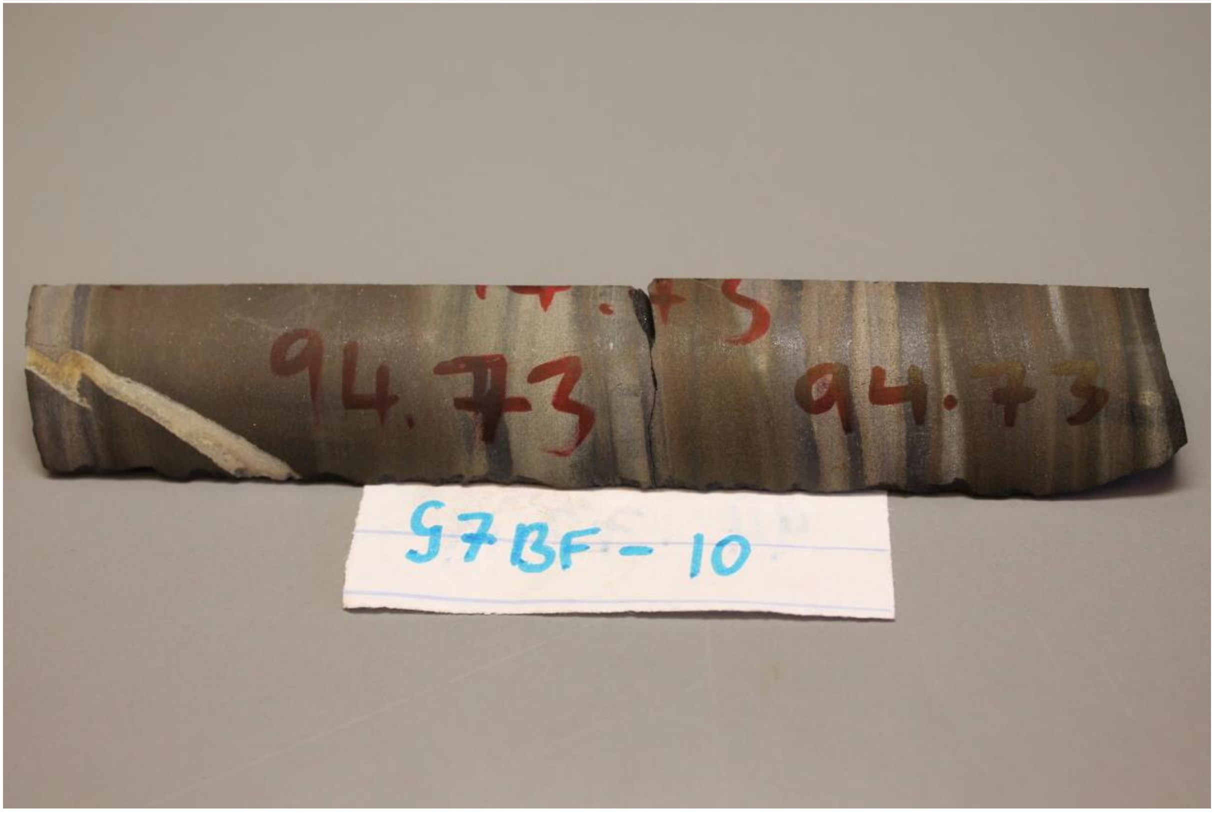
94.73
94.73
S7BF - 10

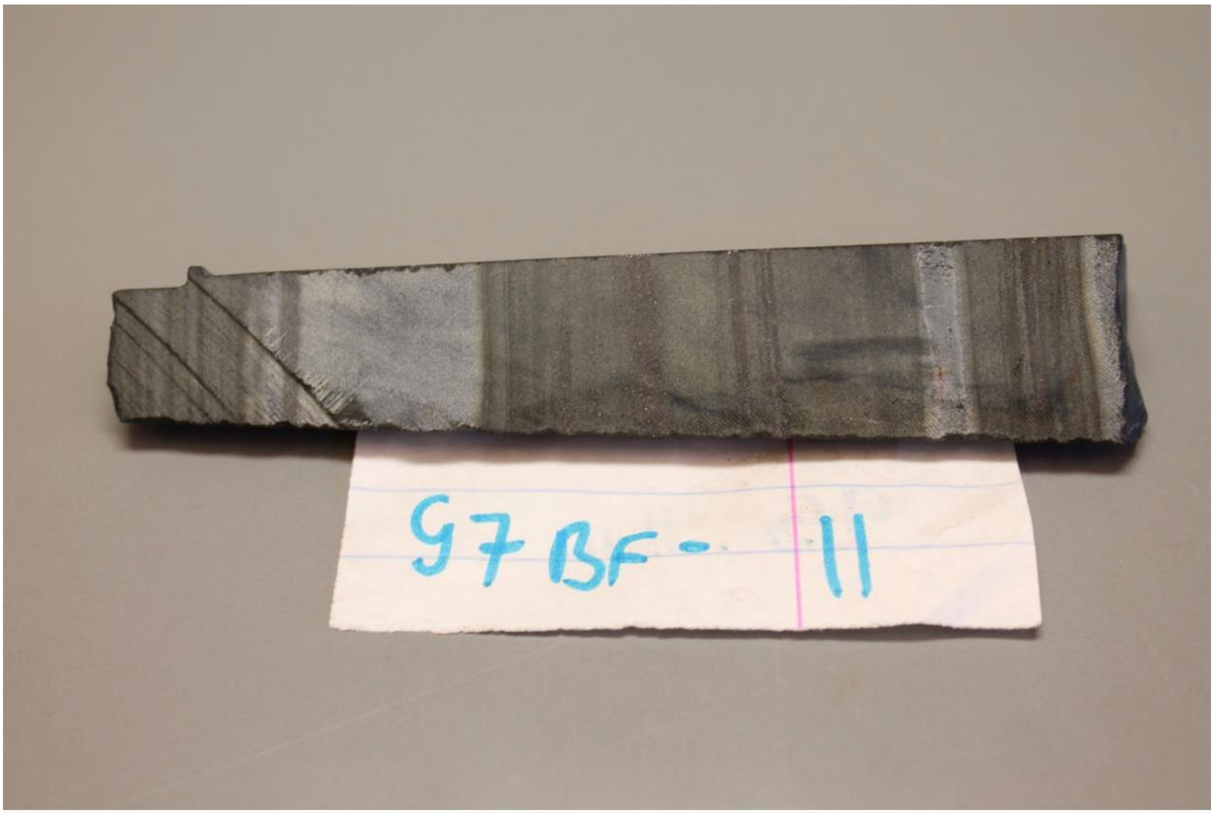
97BF- 11

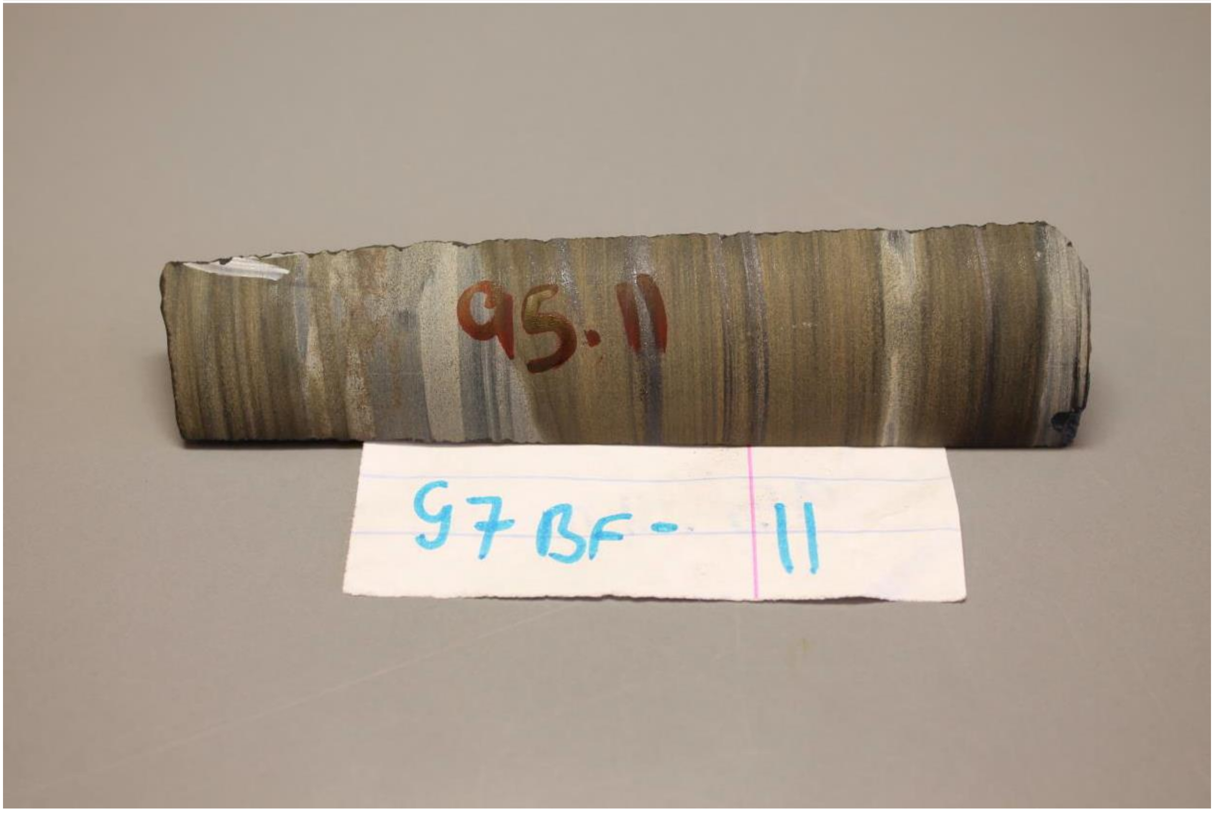
95.11
97BF- 11

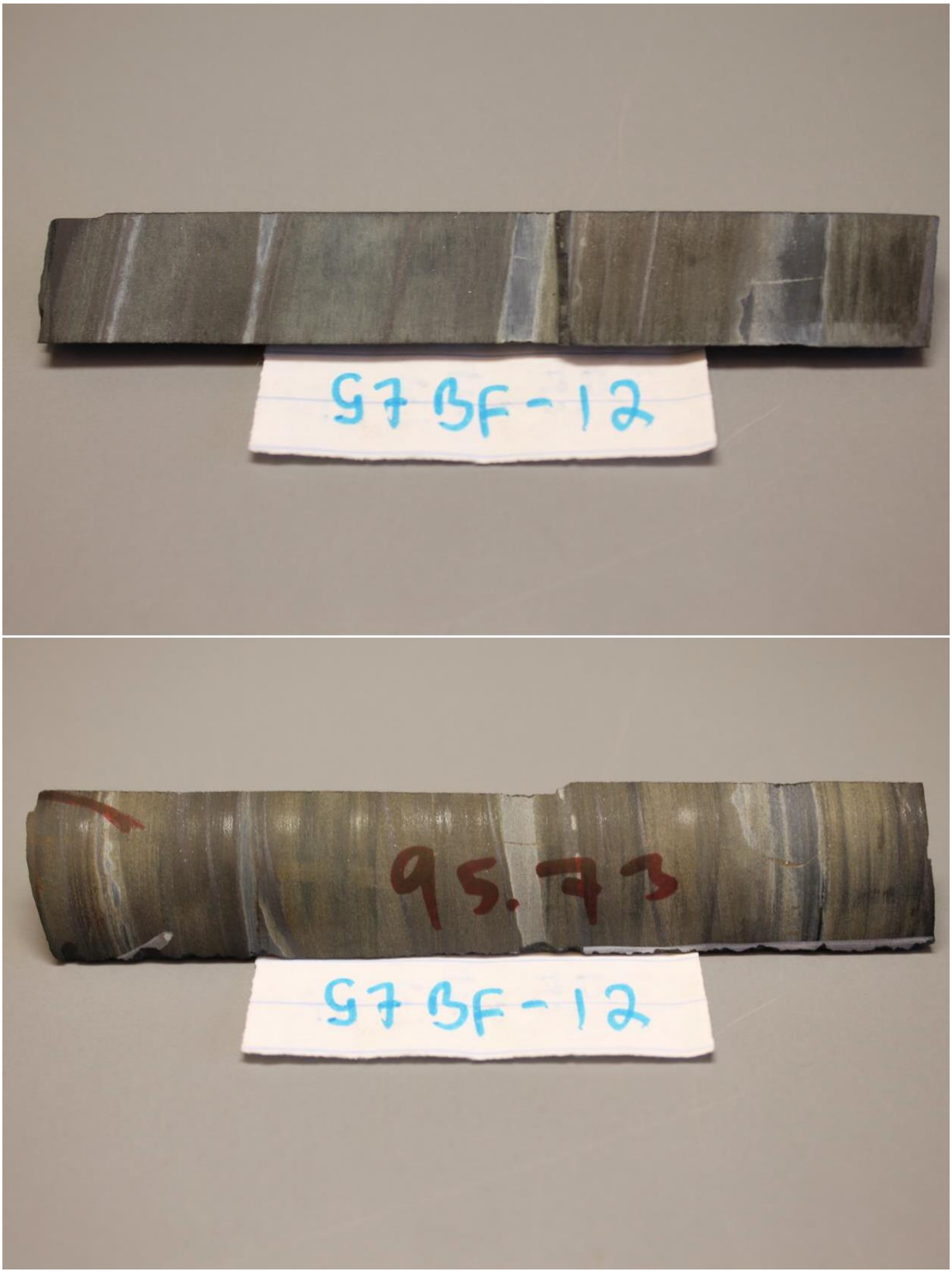
S7 BF-12
95.73
S7 BF-12


97 BF - 13

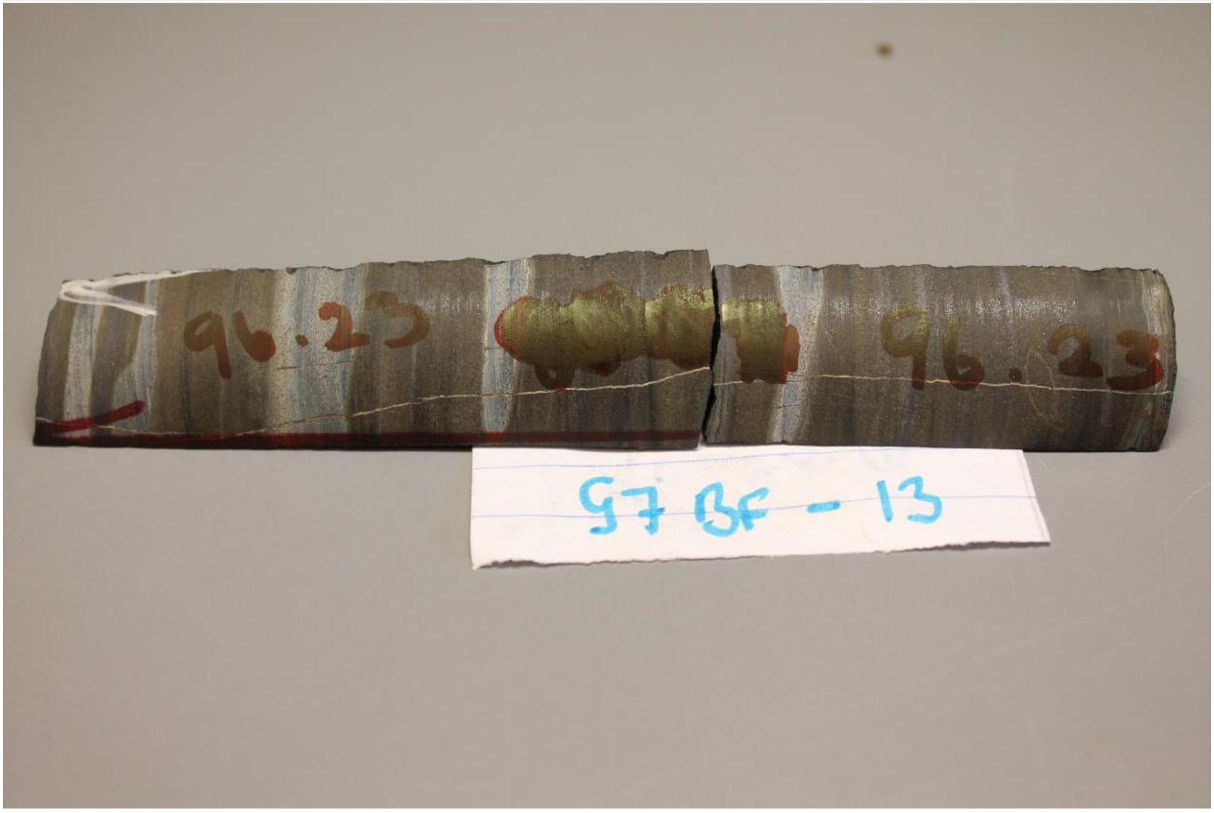
96.23
96.23
97 BF - 13

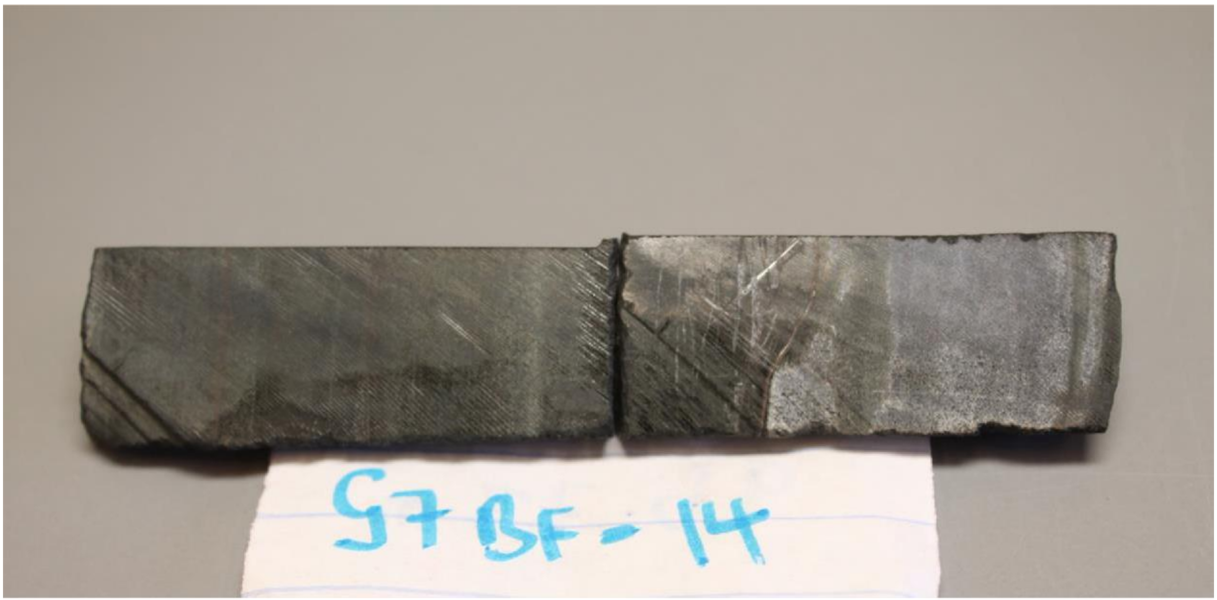
57 BF-14

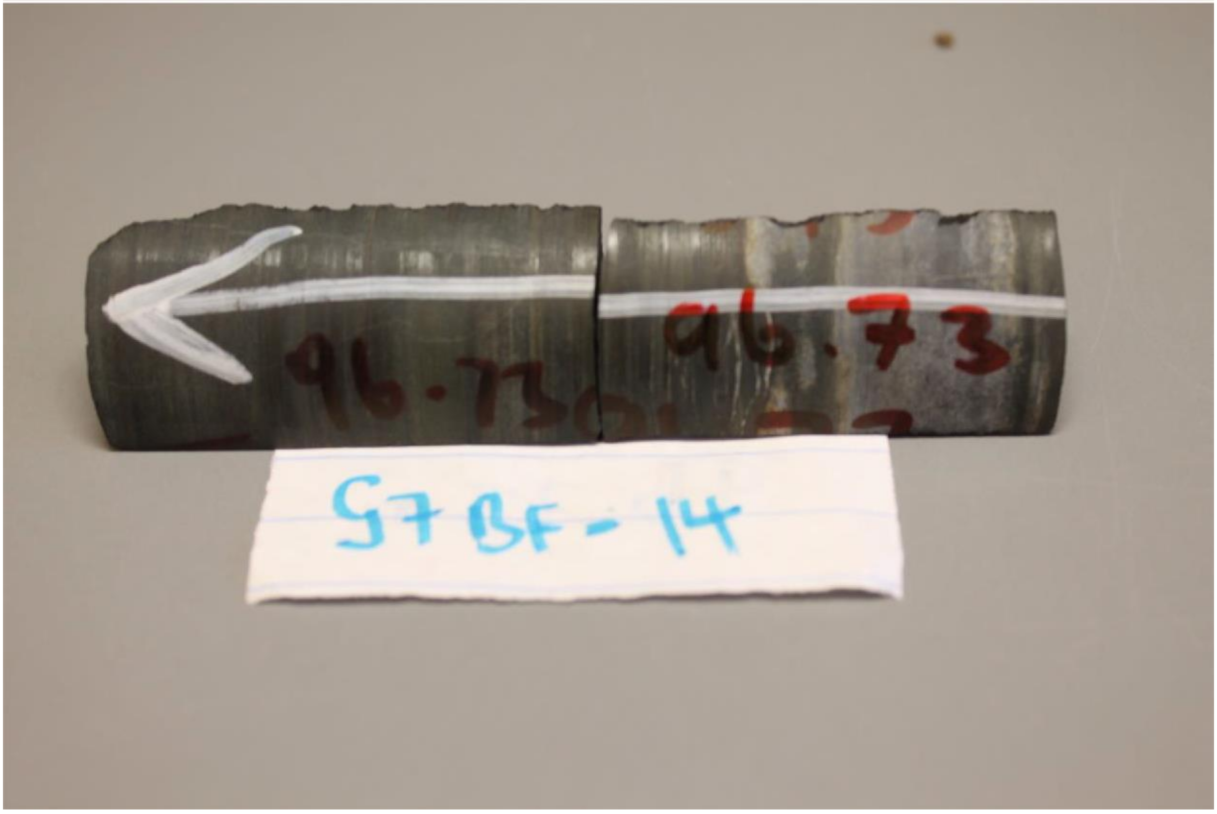
96.73
96.73
57 BF-14


97 BF - 15

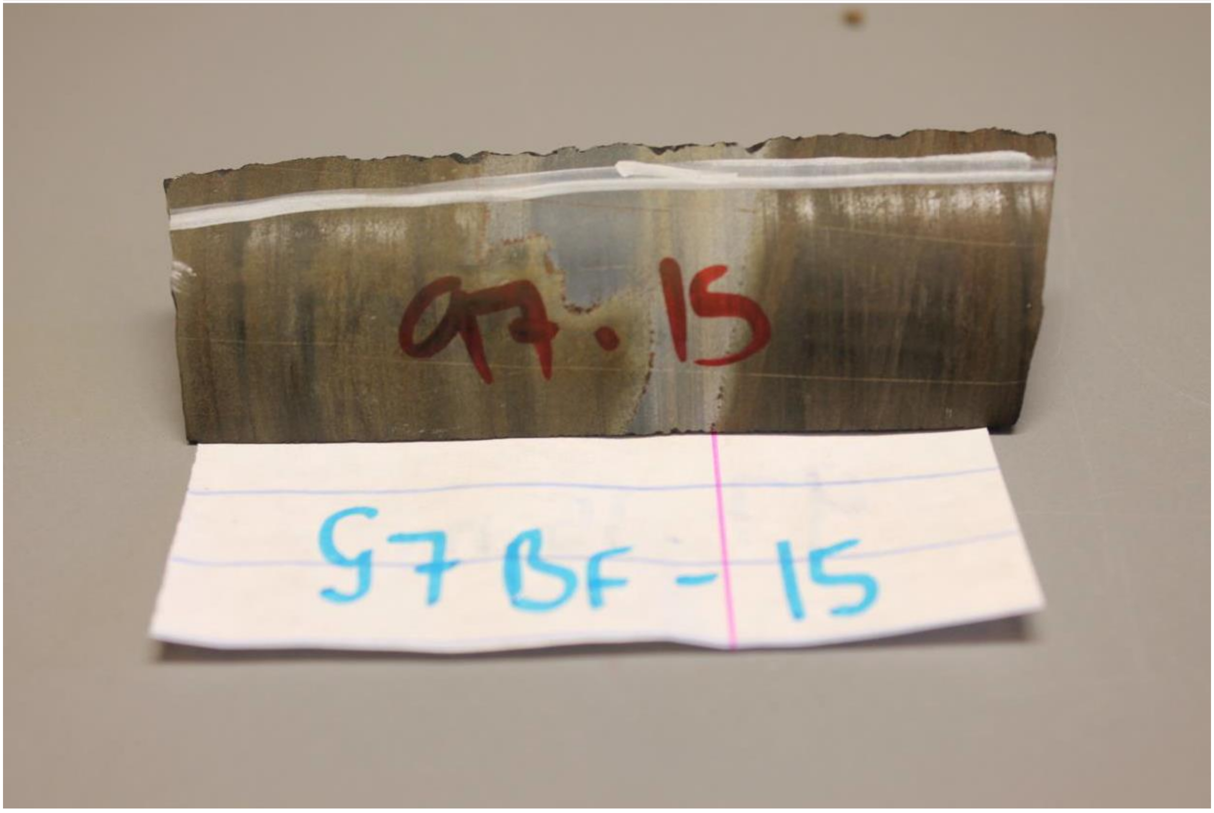
97.15
97 BF - 15

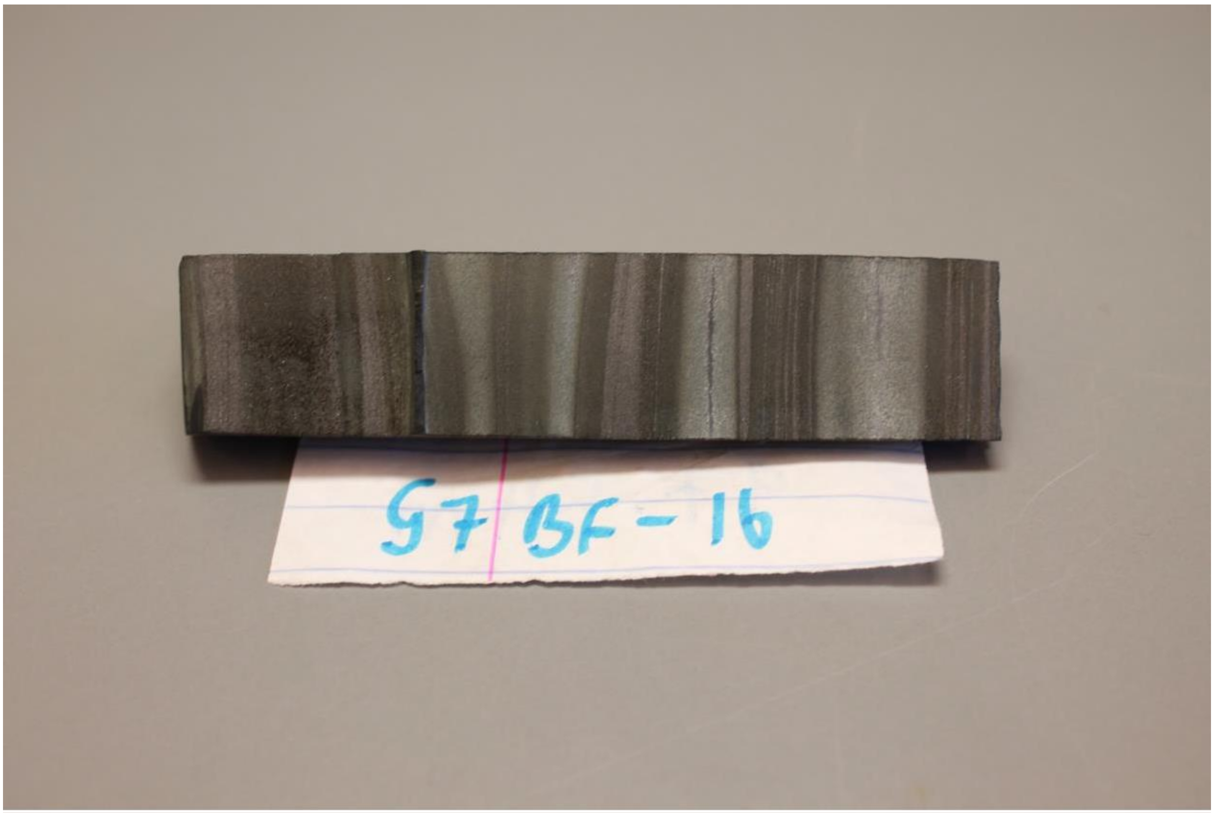
97 BF-16


97.54
97.54
97 BF-16


57 BF-17


98.02
57 BF-17


G7BF - 18


98.60m
G7BF - 18


G7 BF - 19


99.02
G7 BF - 19

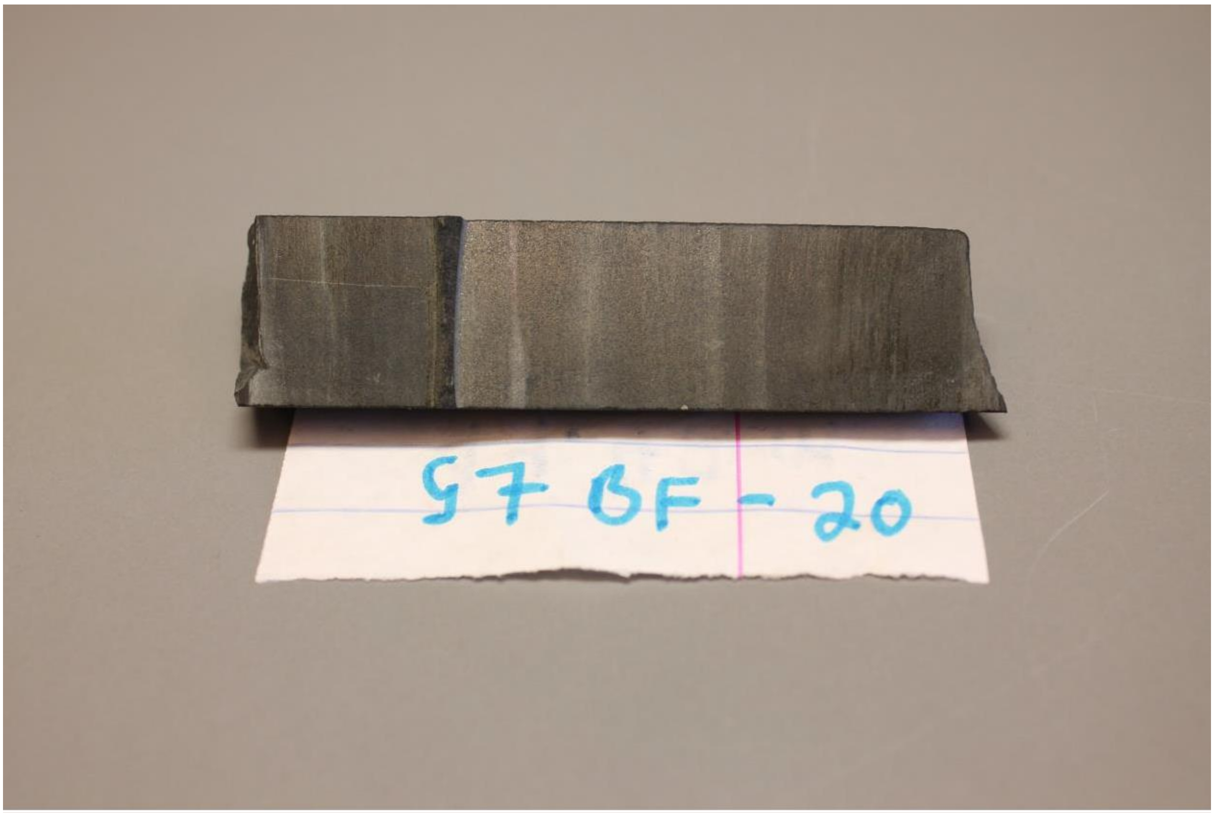
57 BF-20

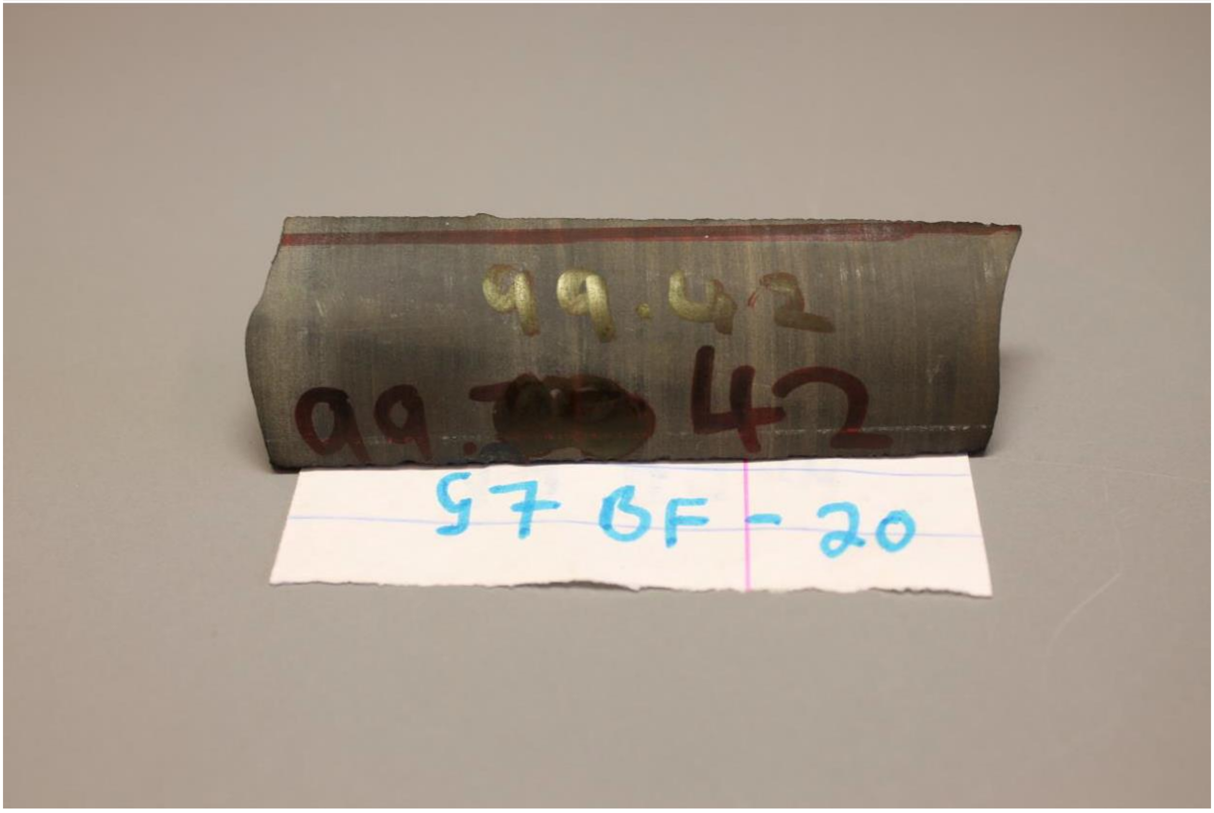
99.42
99. 42
57 BF-20

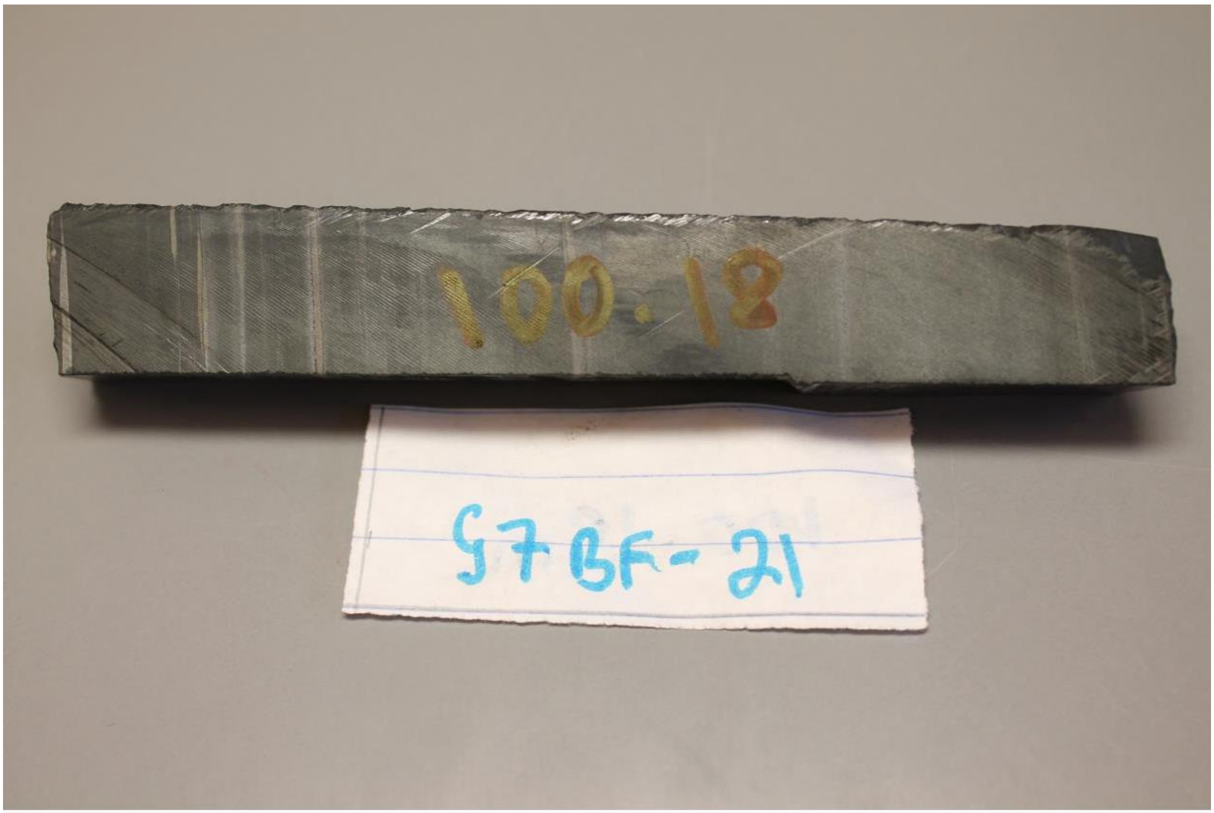
100.18
G7 BF-21


100.18
G7 BF-21


97 BF-22


95.00
97 BF-22

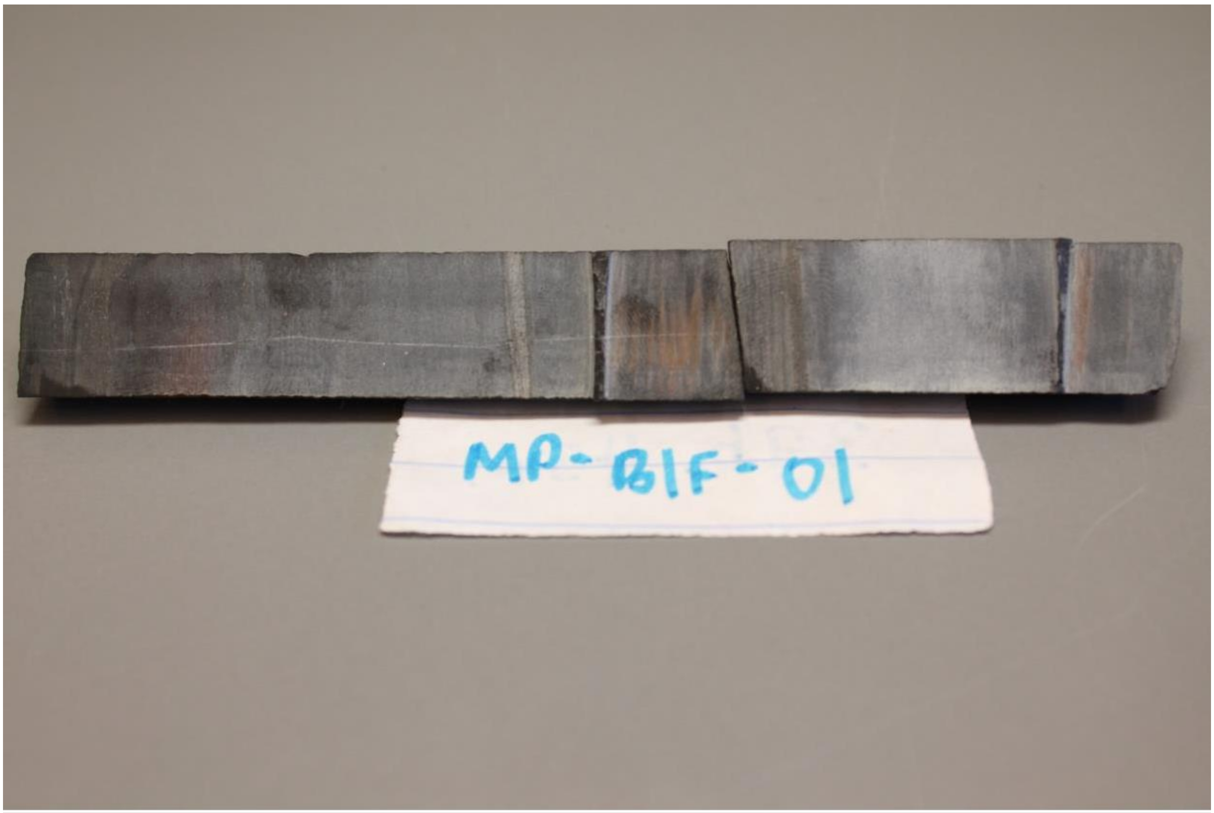
MP-BIF-01

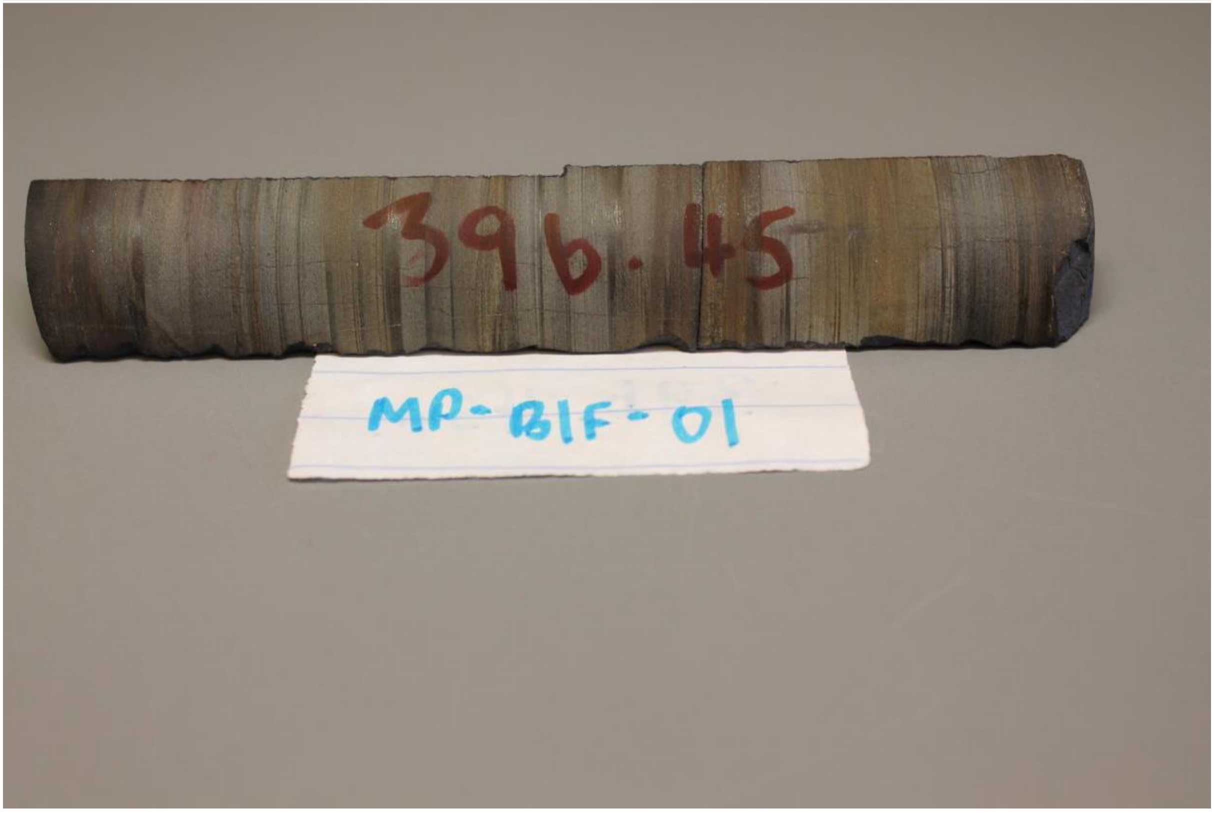
396.45
MP-BIF-01

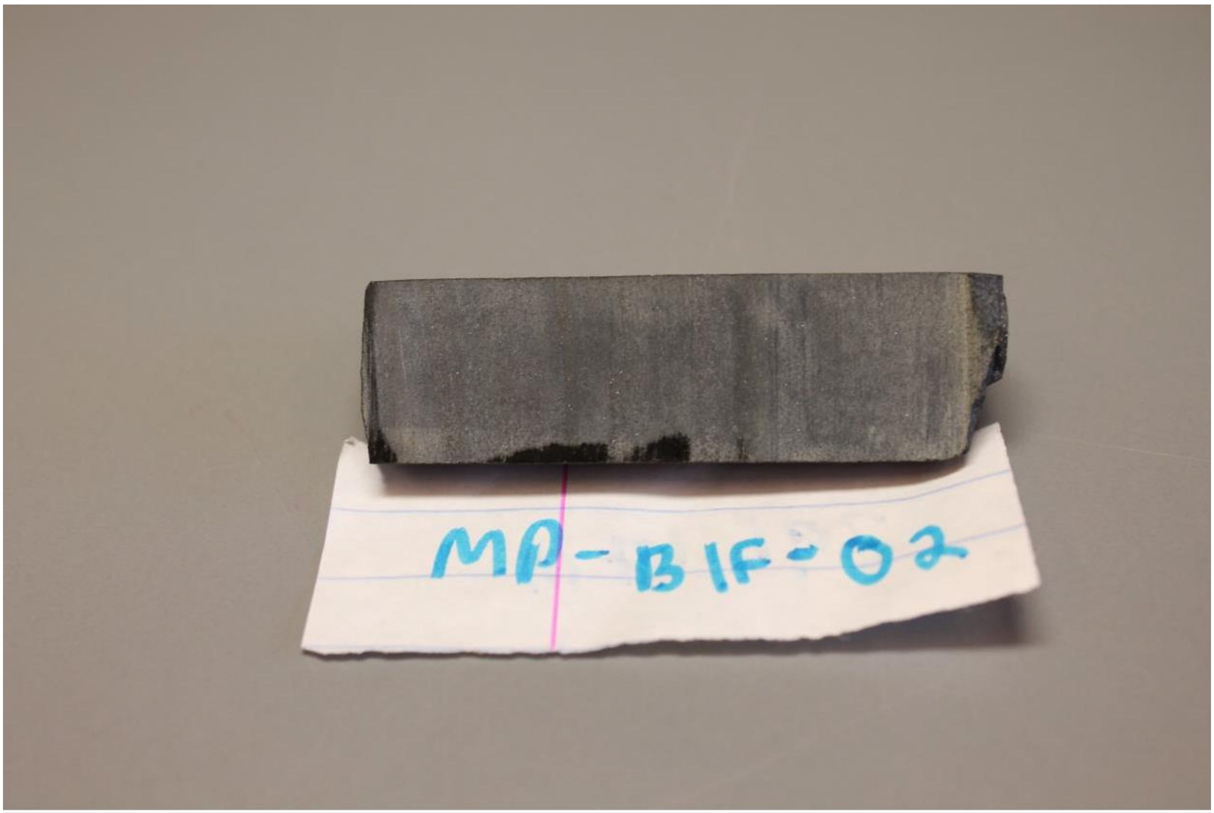
MP-BIF-02

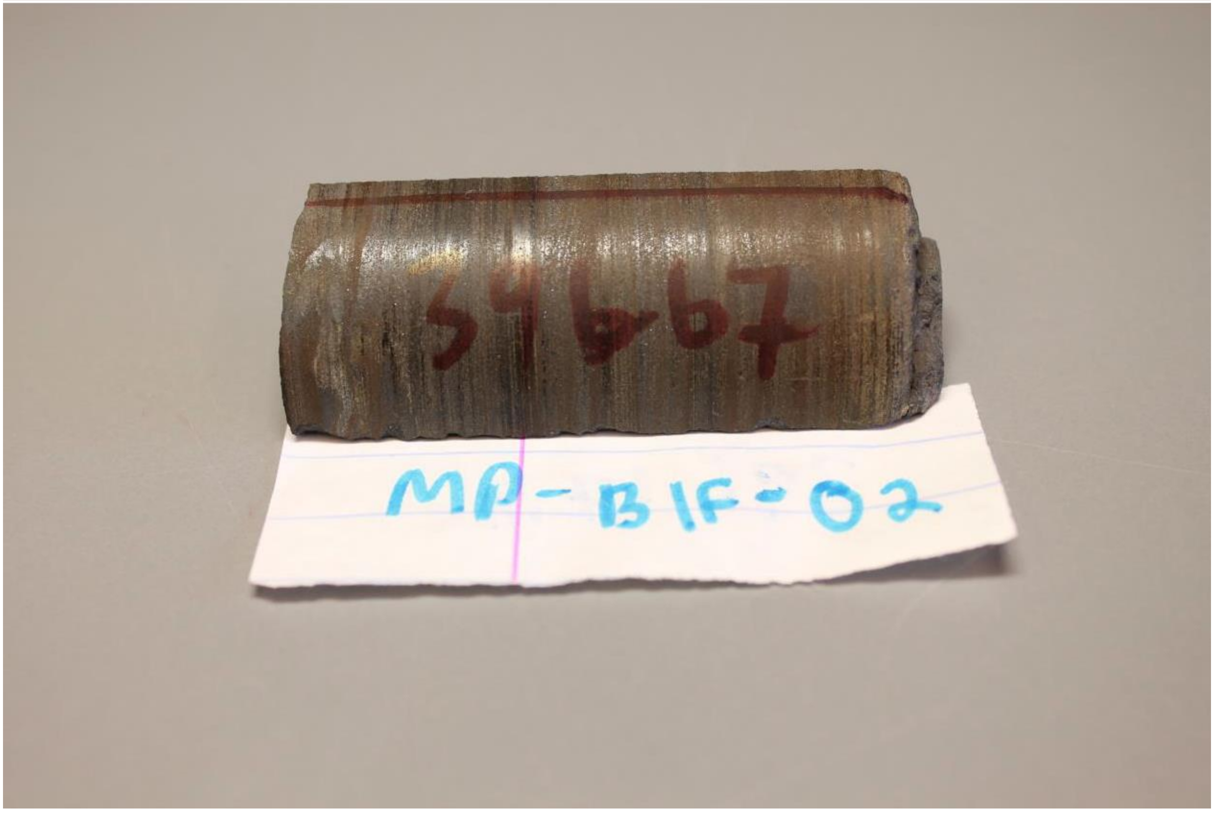
54667
MP-BIF-02

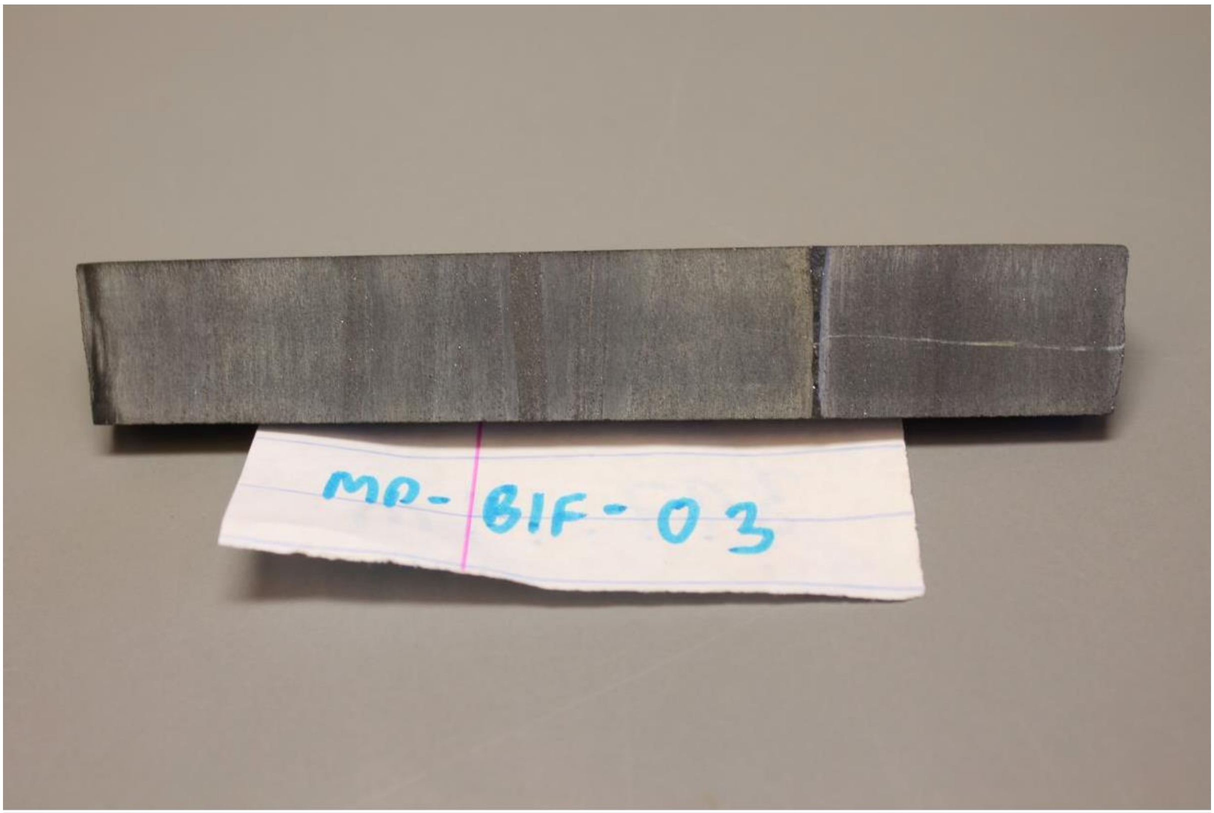
MP-BIF-03

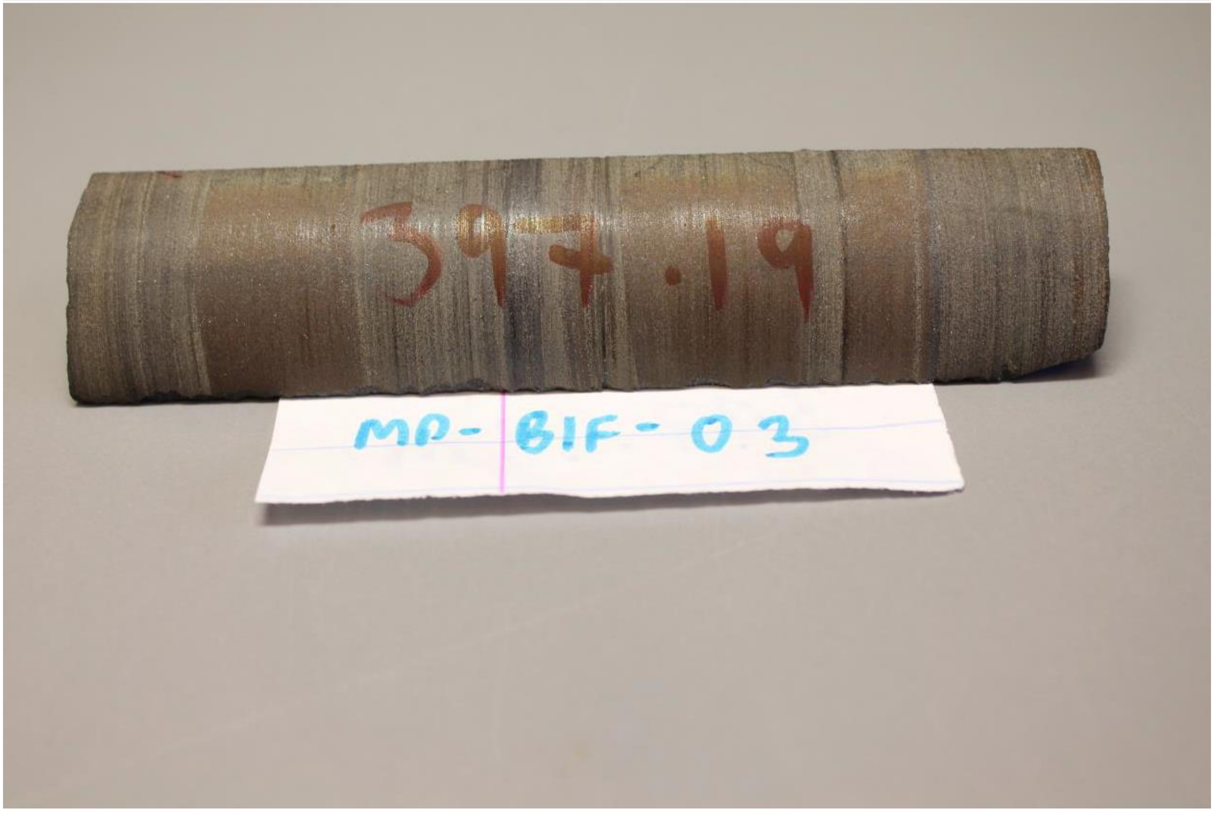
397.19
MP-BIF-03

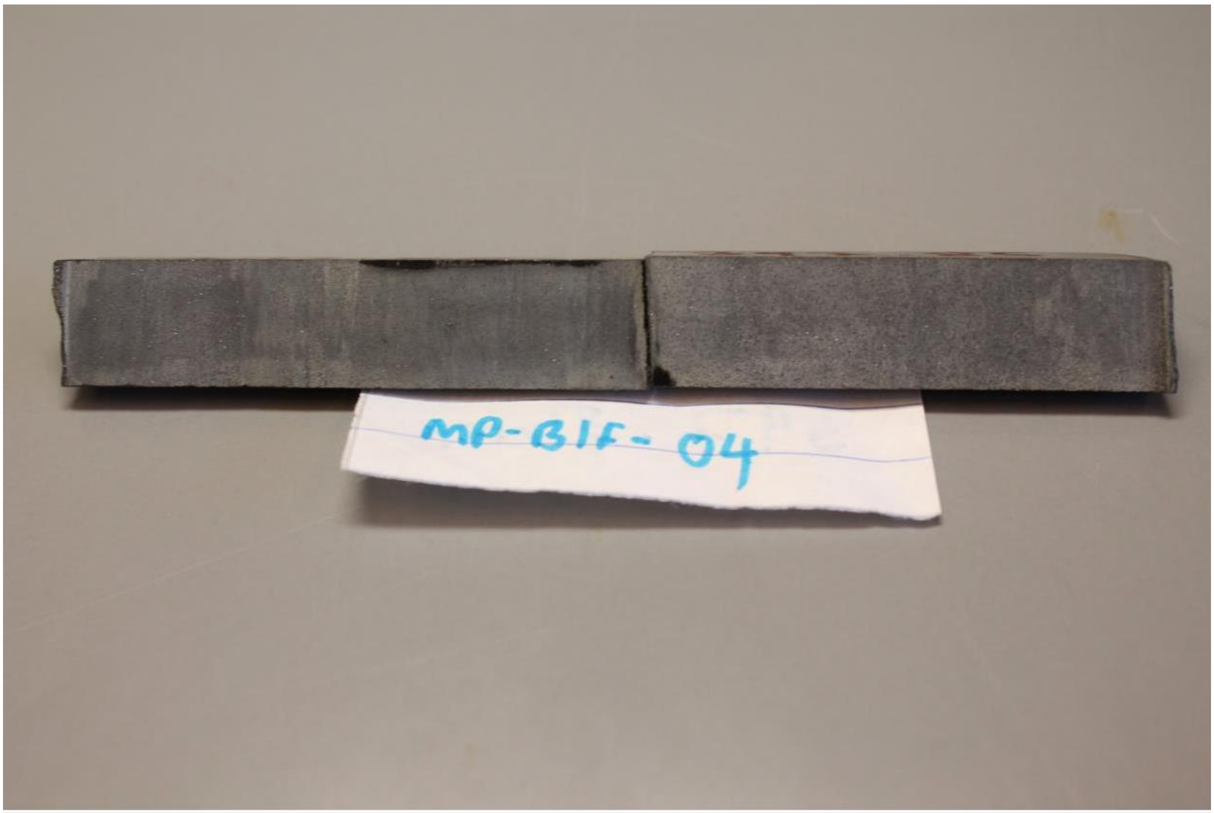
MP-BIF- 04

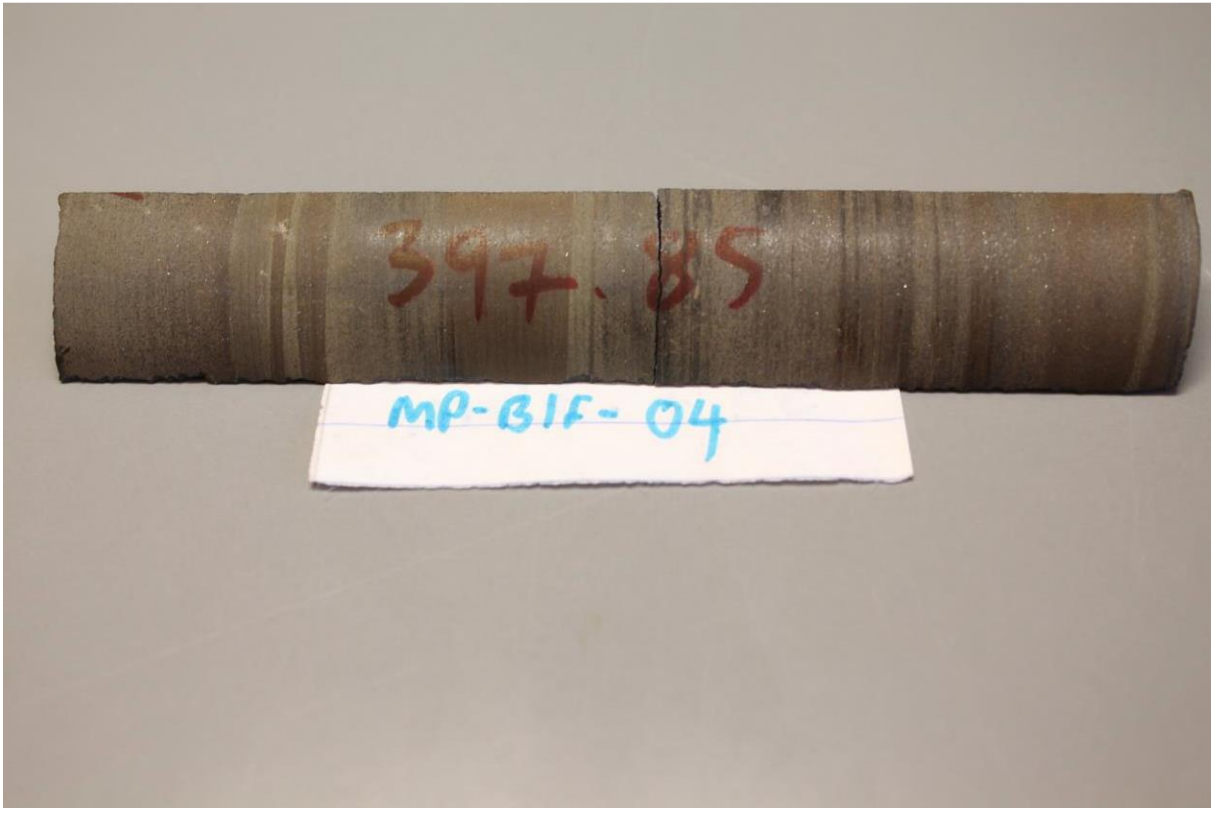
397.85
MP-BIF- 04

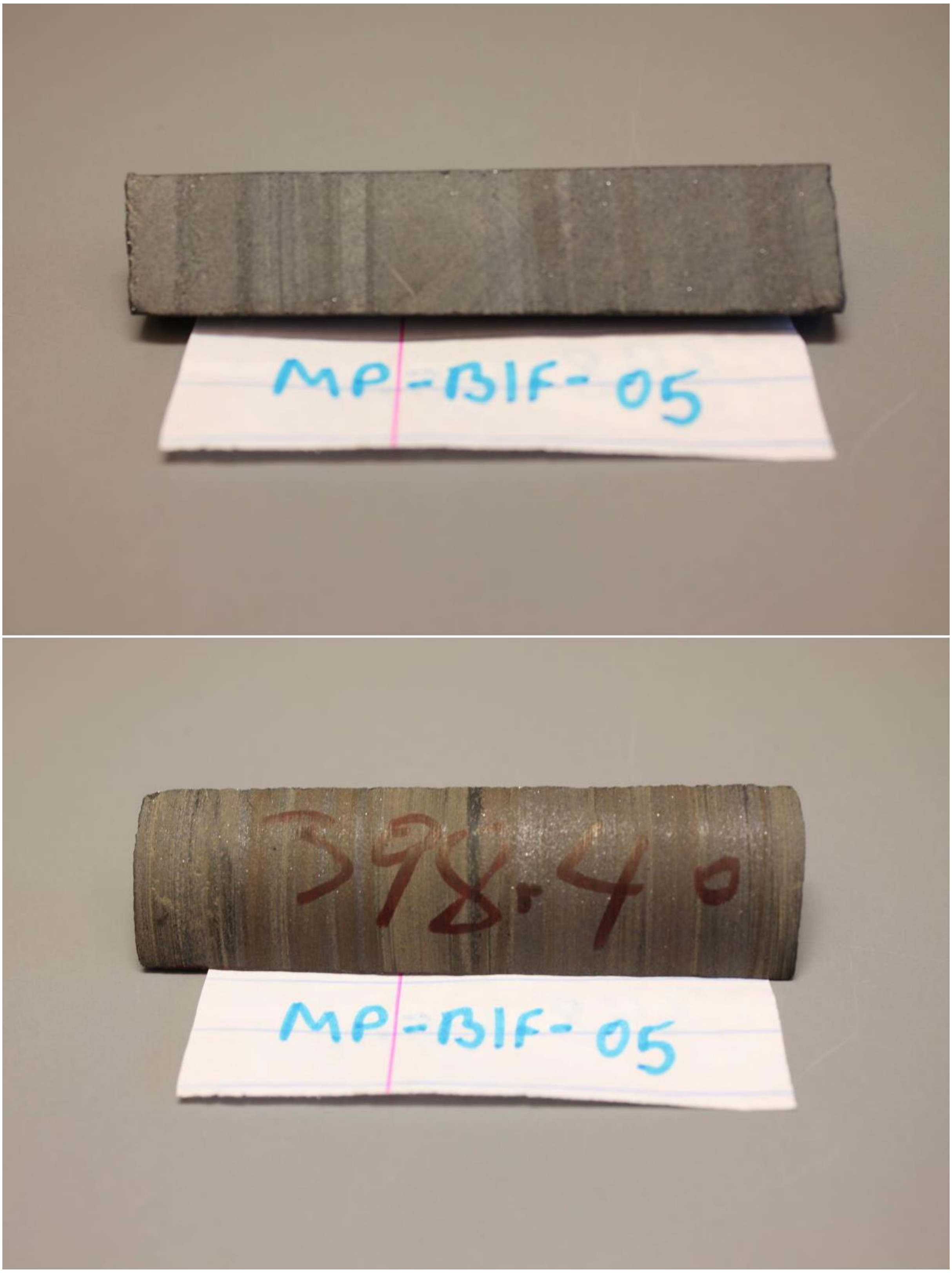
MP-BIF-05
398.40
MP-BIF-05


MD-BIF-06

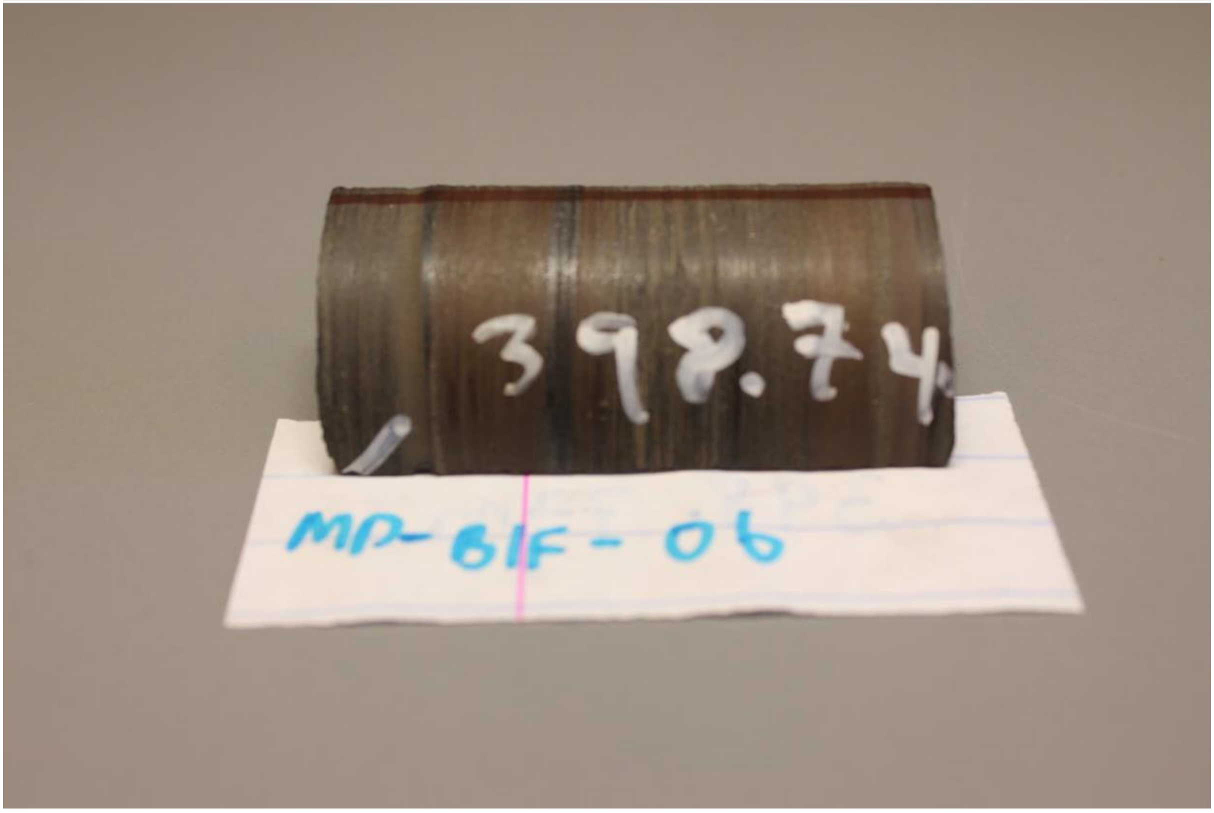
398.74
MD-BIF-06


MP- BIF- 07


399.22
399.22
MP- BIF- 07

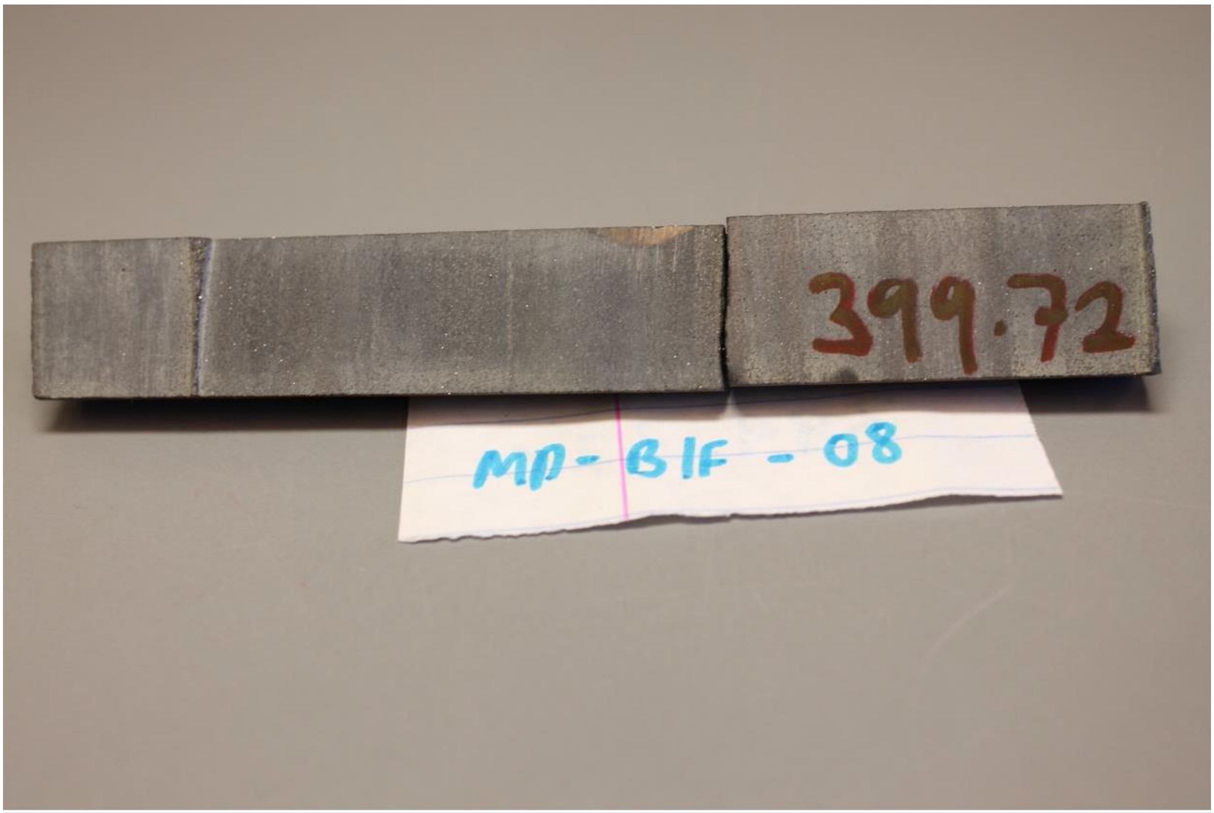
399.72
MP-BIF-08

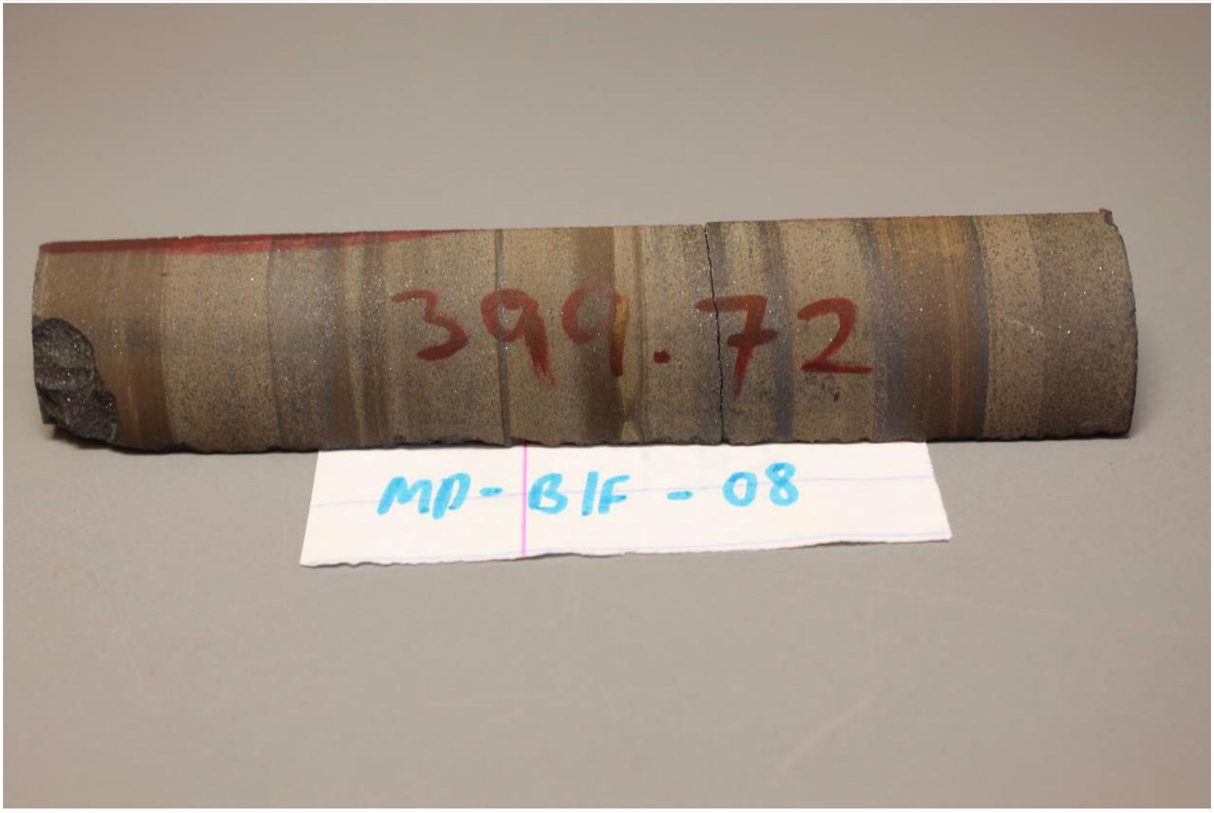
399.72
MP-BIF-08


MP - BIF - 09

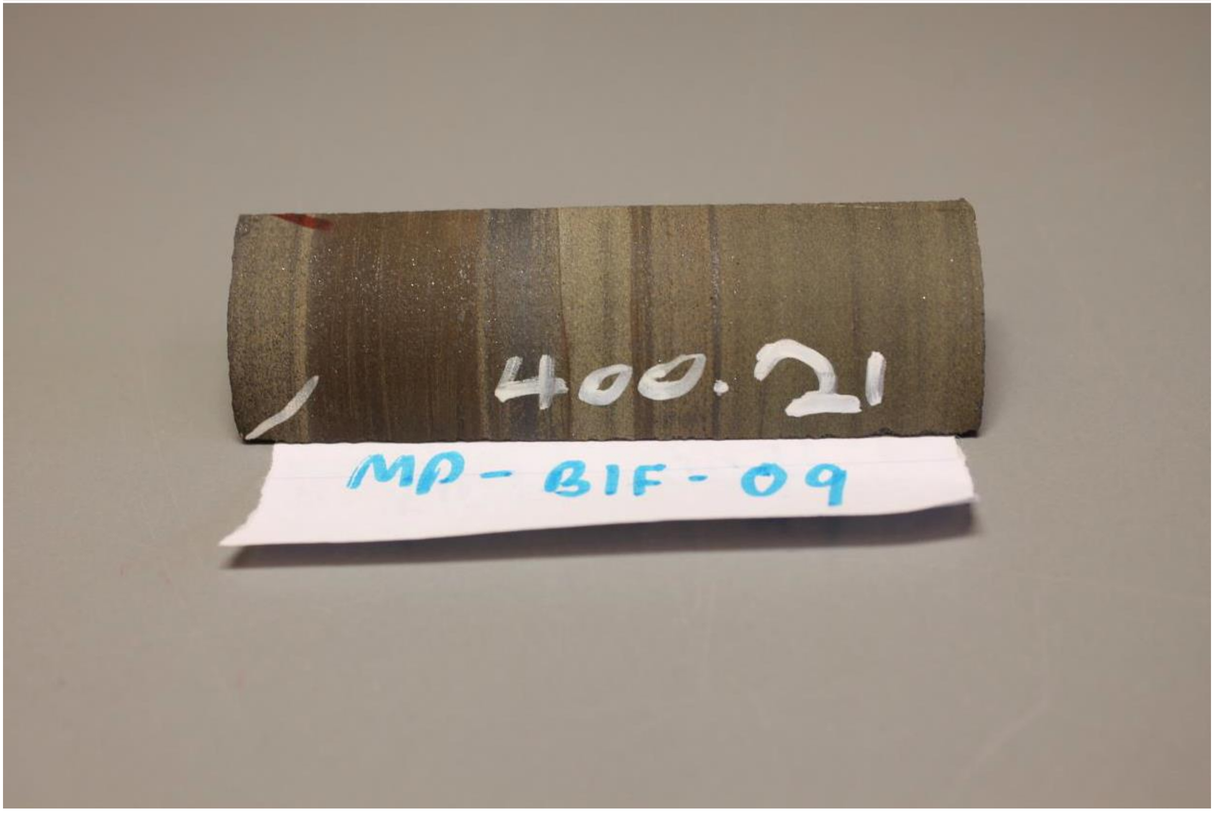
400.21
MP - BIF - 09

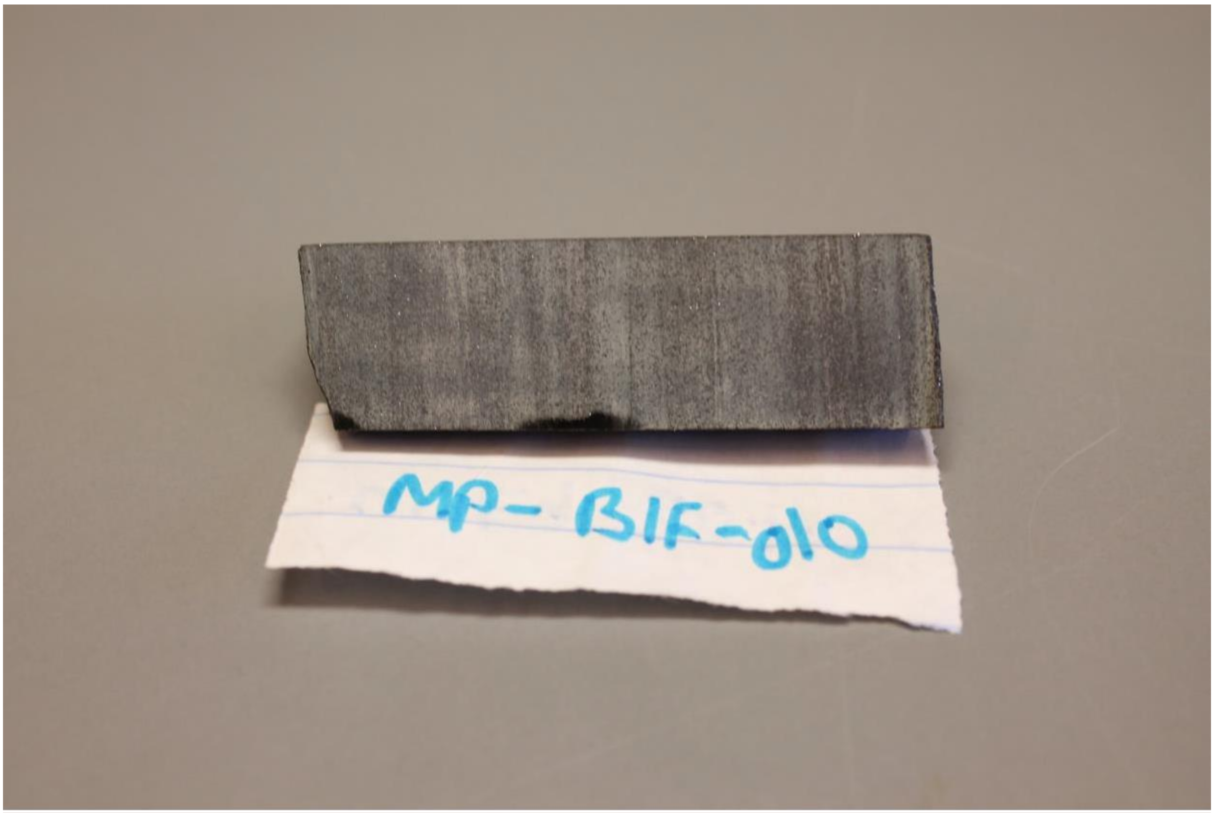
MP- BIF-010

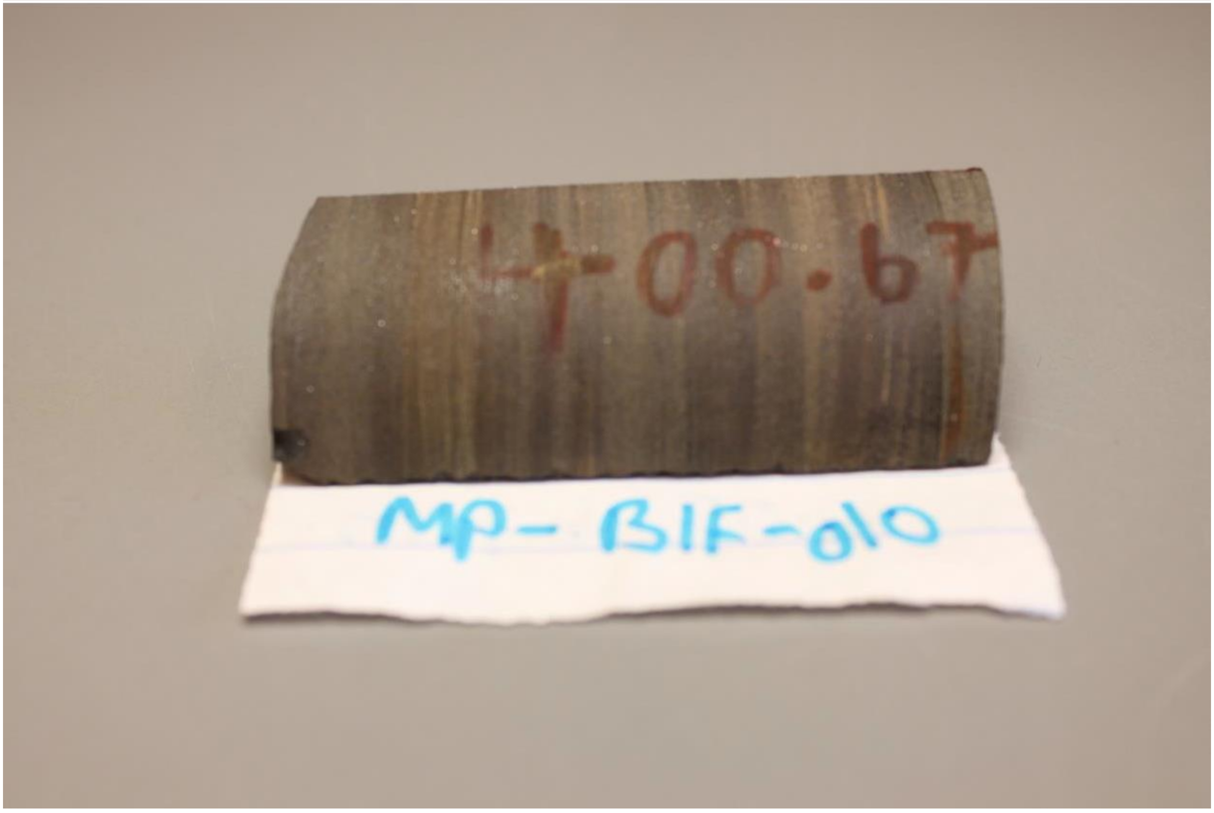
400.67
MP- BIF-010

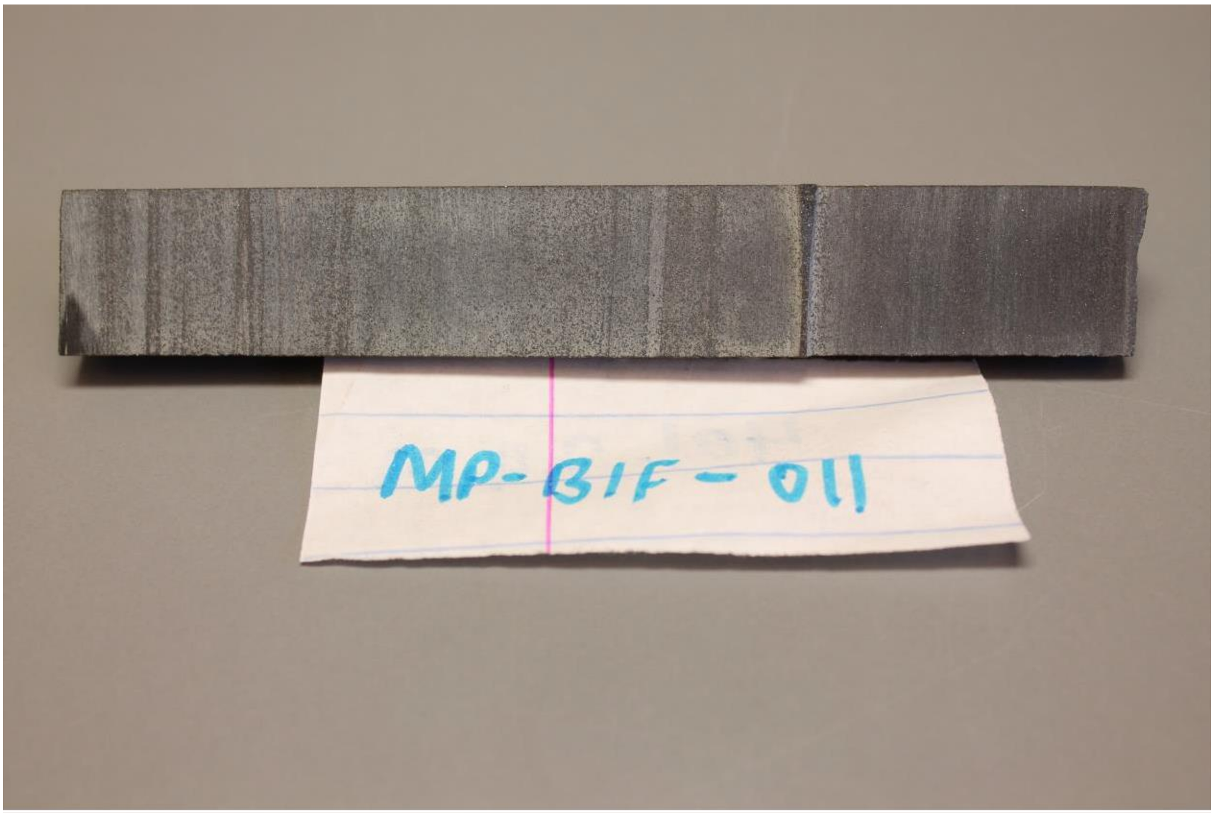
MP-BIF-011

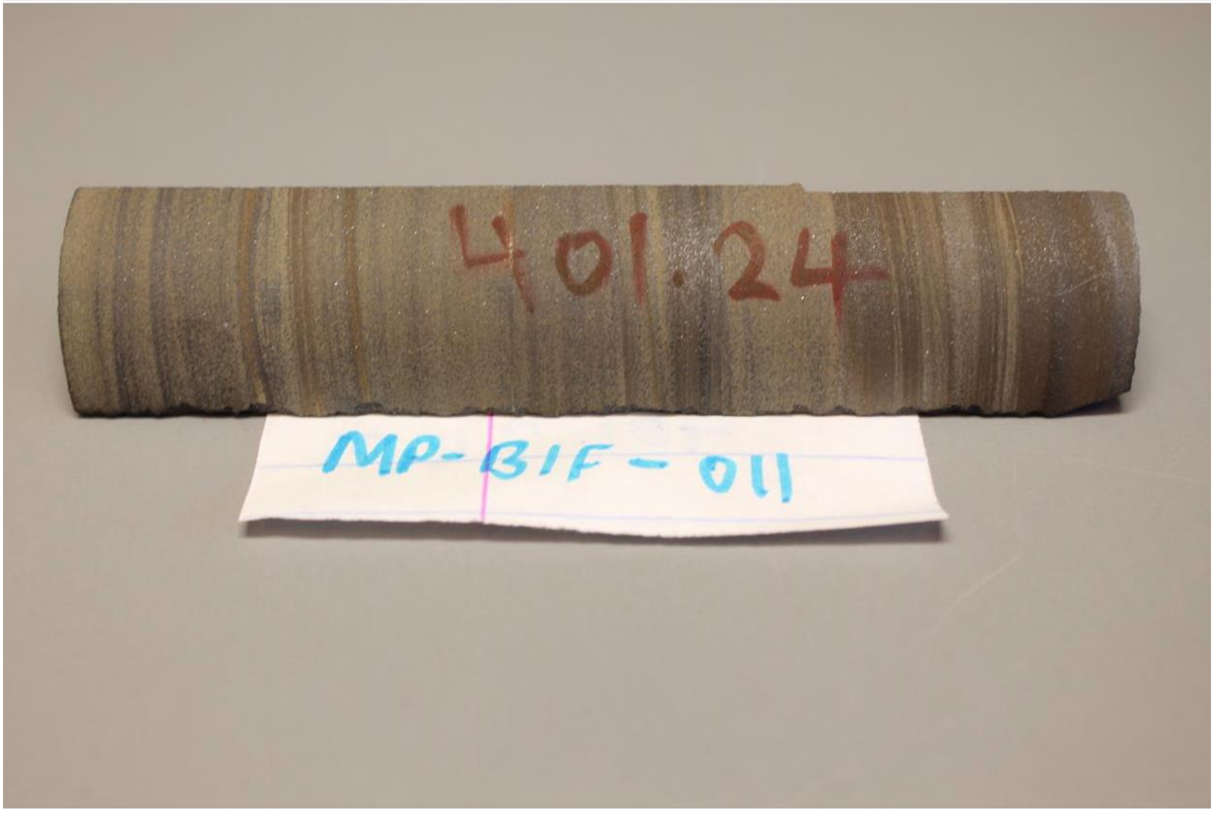
401.24
MP-BIF-011

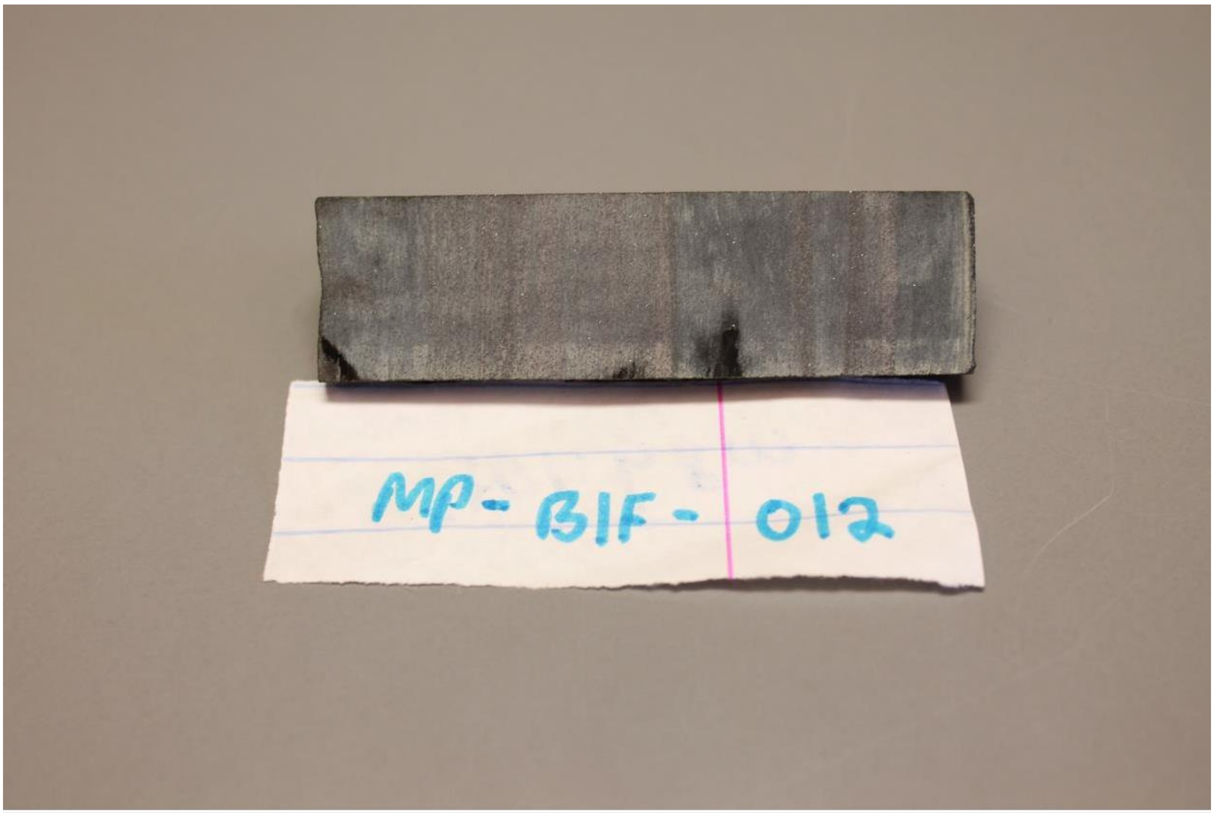
MP-BIF-012

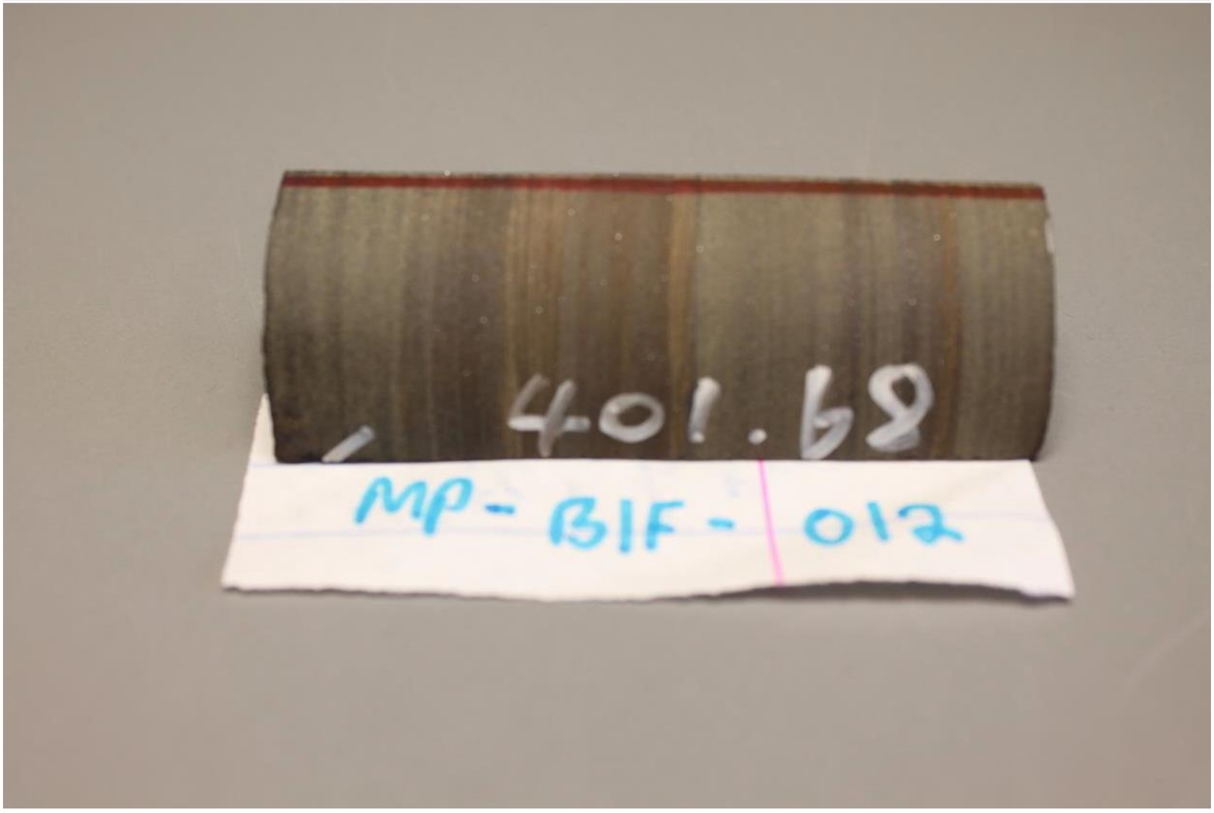
401.68
MP-BIF-012

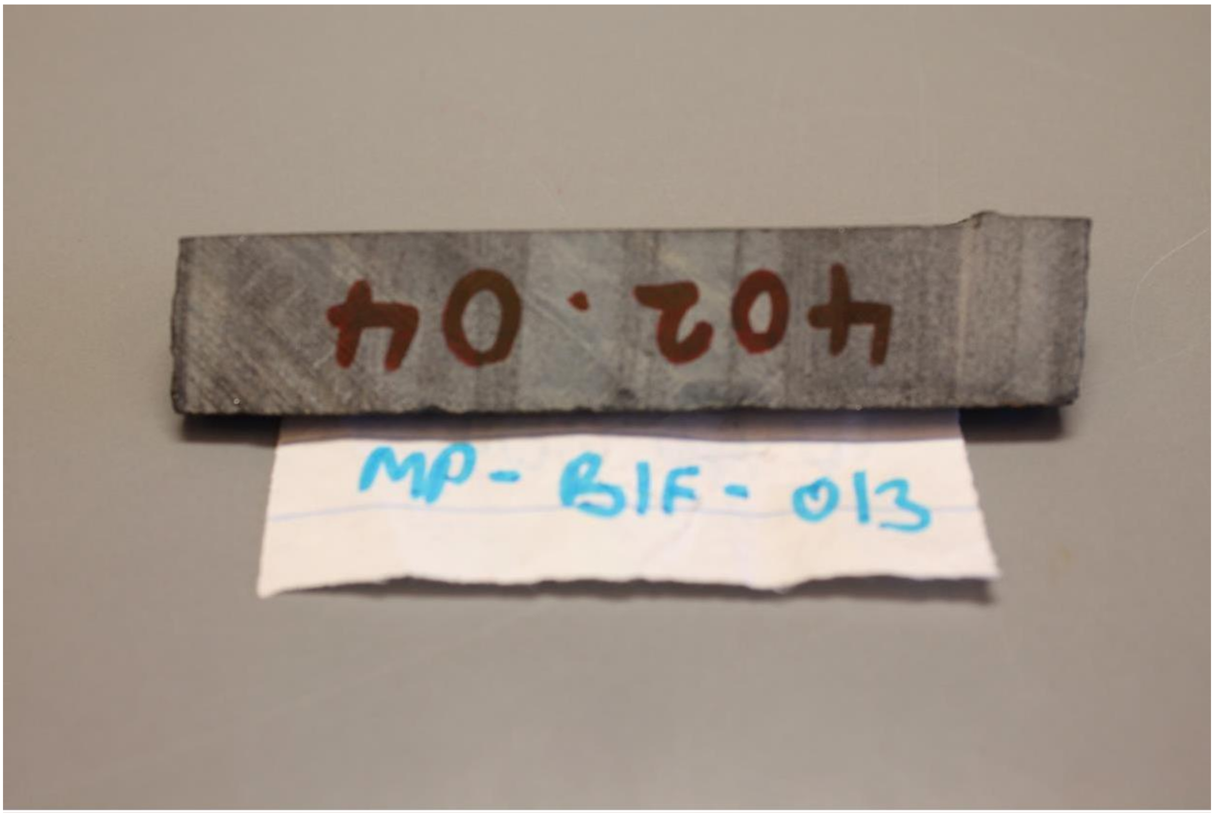
402.04
MP-BIF-013

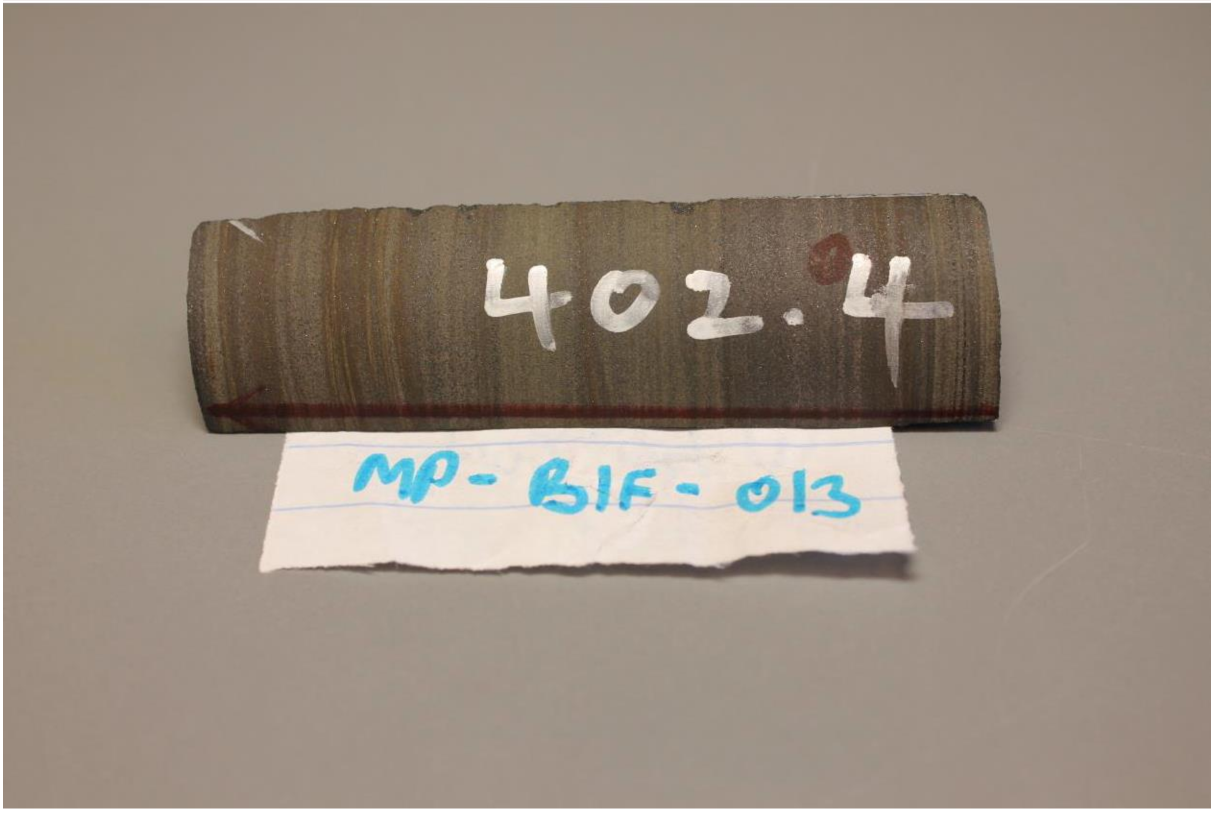
402.4
MP-BIF-013

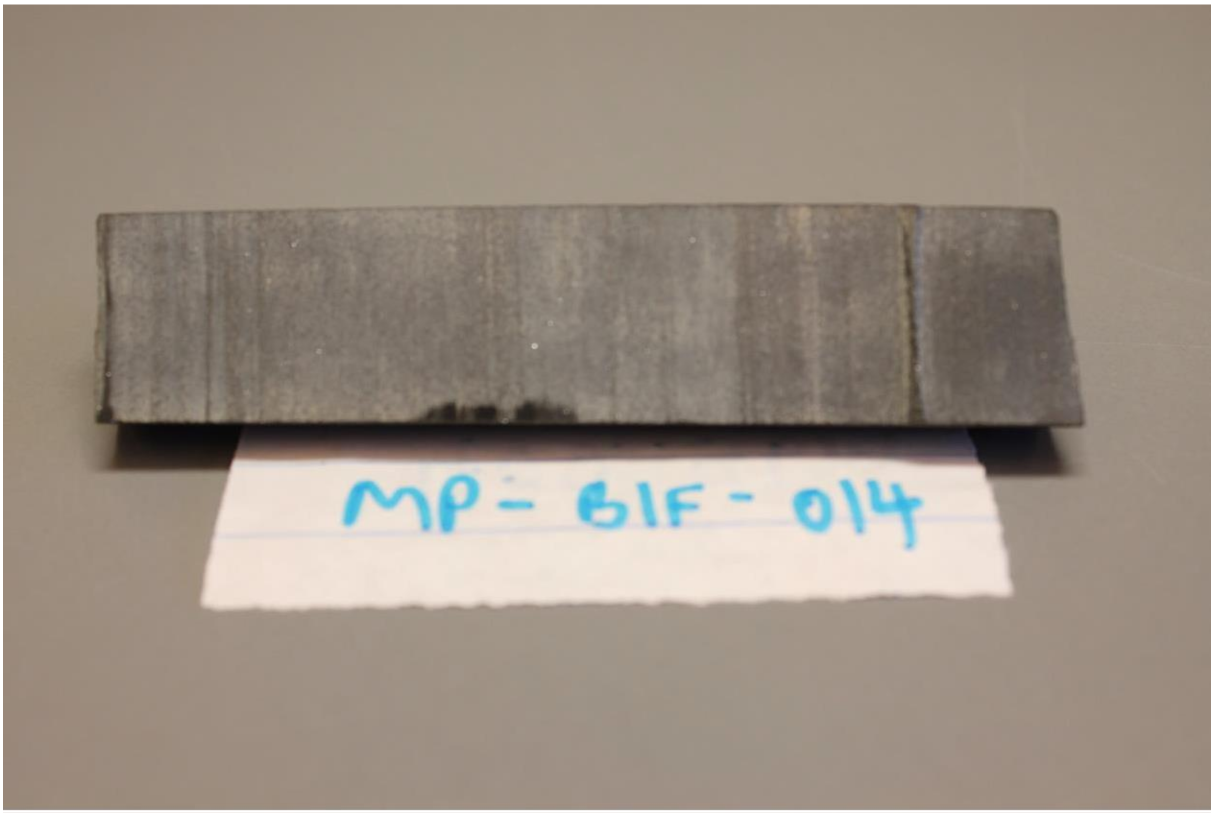
MP- BIF- 014

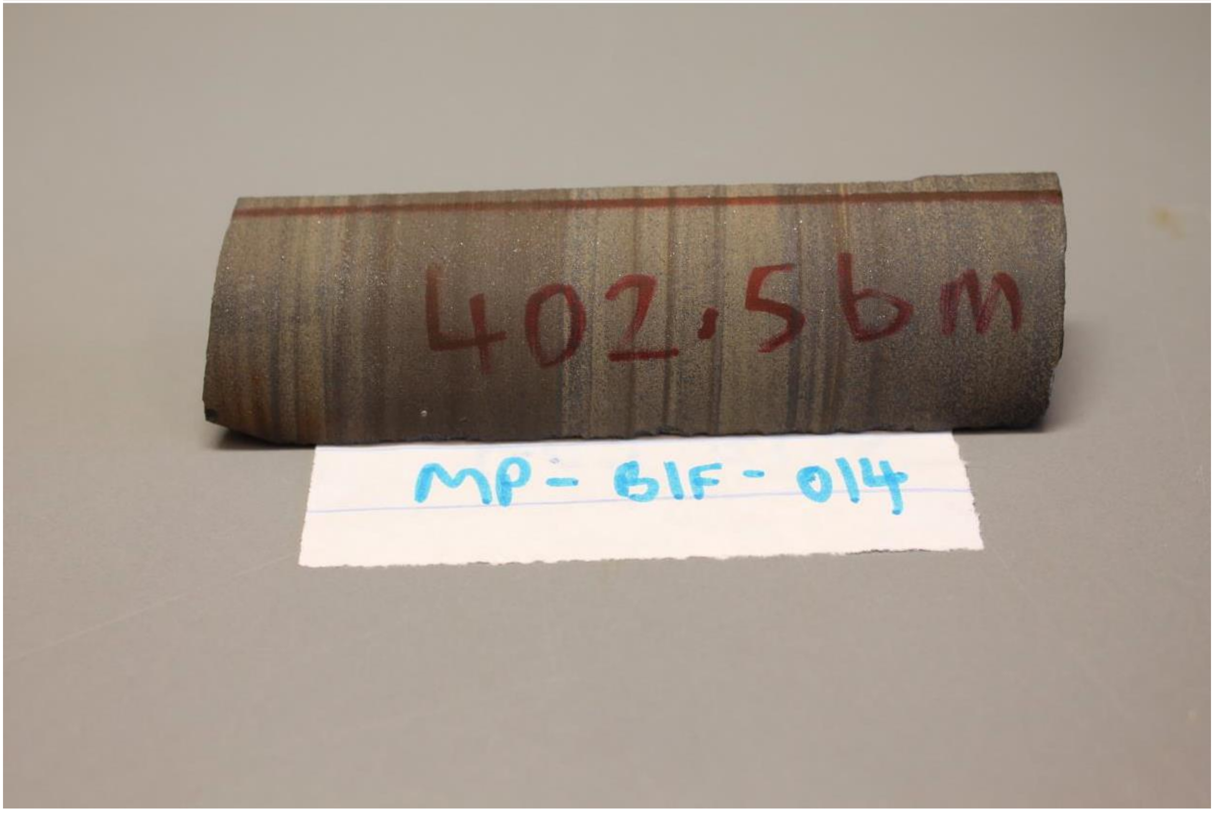
402.56m
MP- BIF- 014

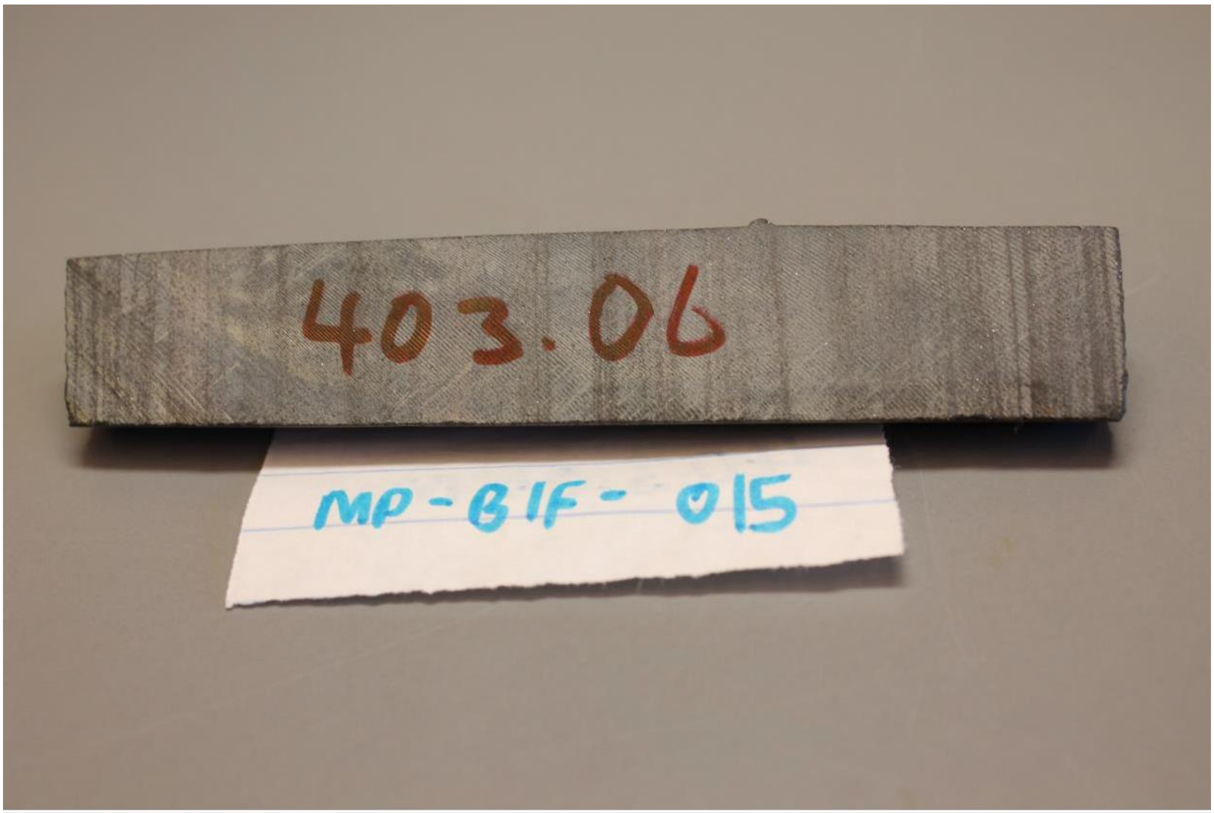
403.06
MP-BIF-015

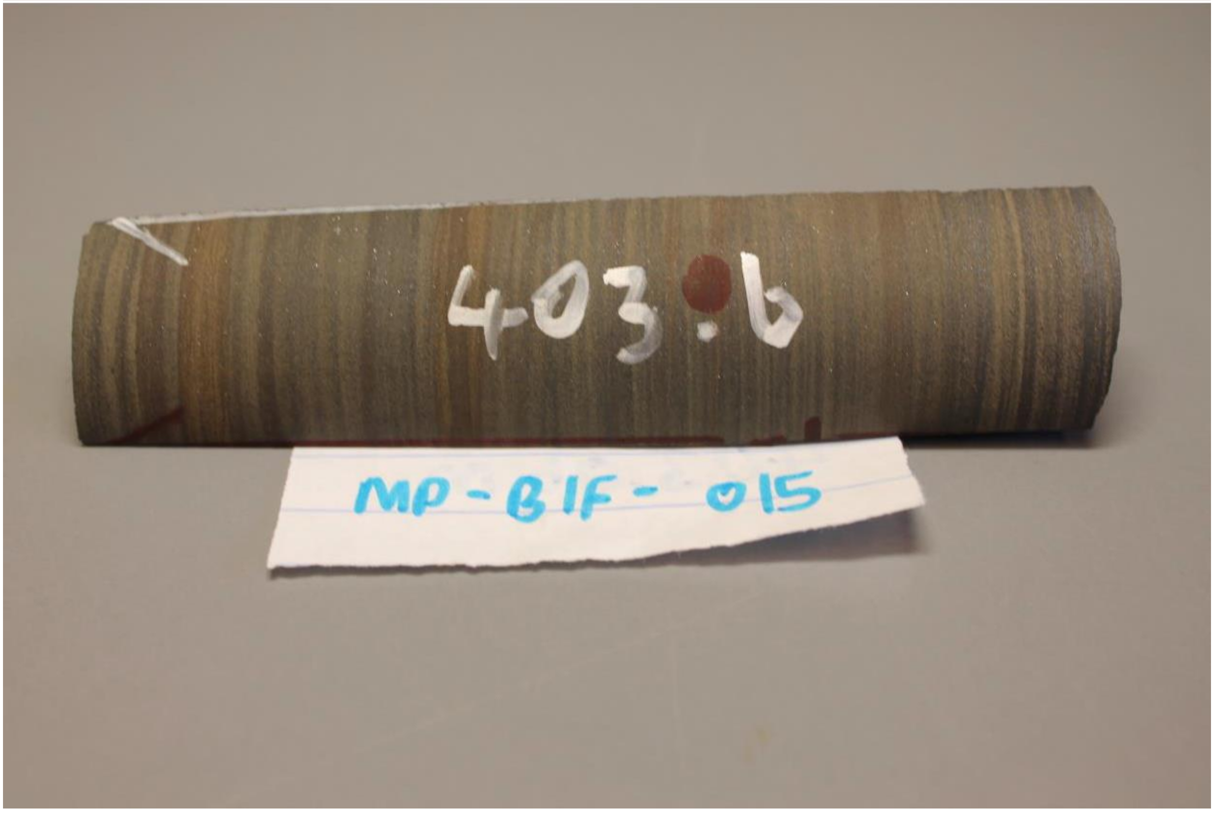
403.6
MP-BIF-015

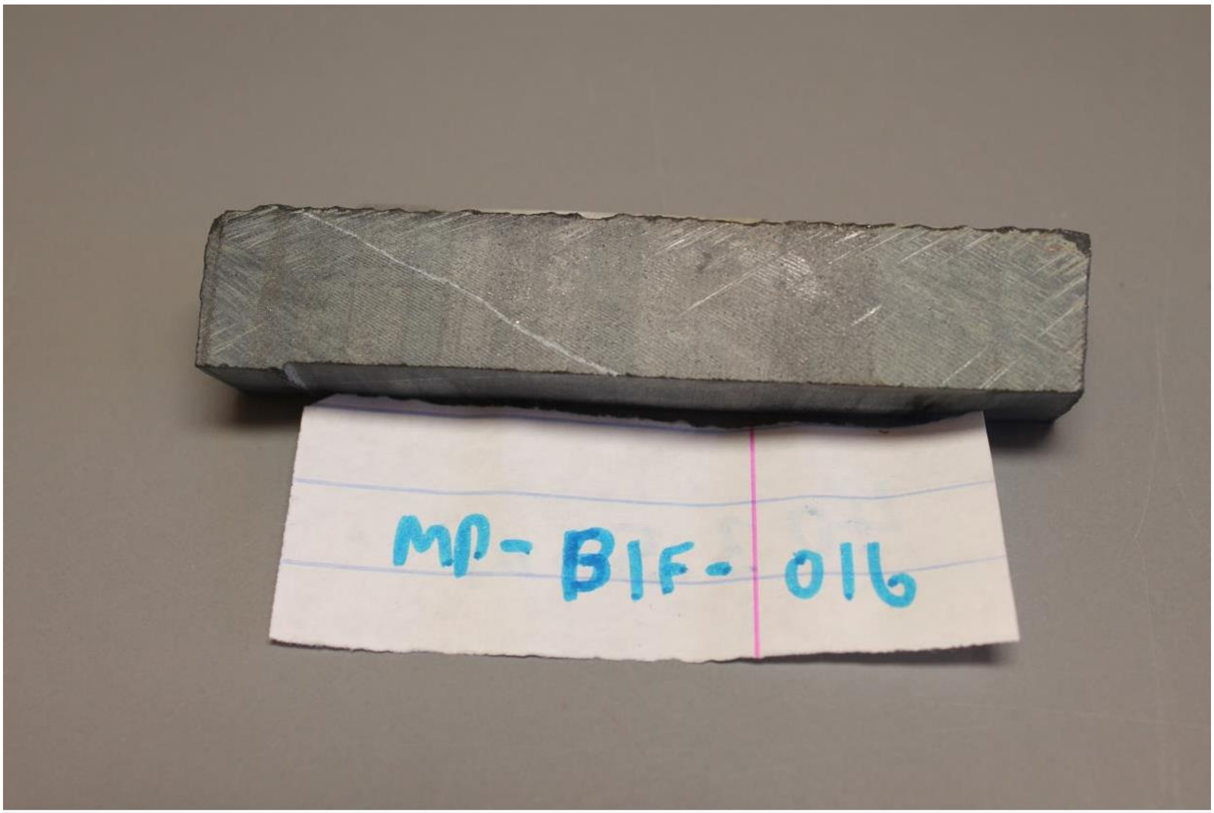
MP- BIF- 016

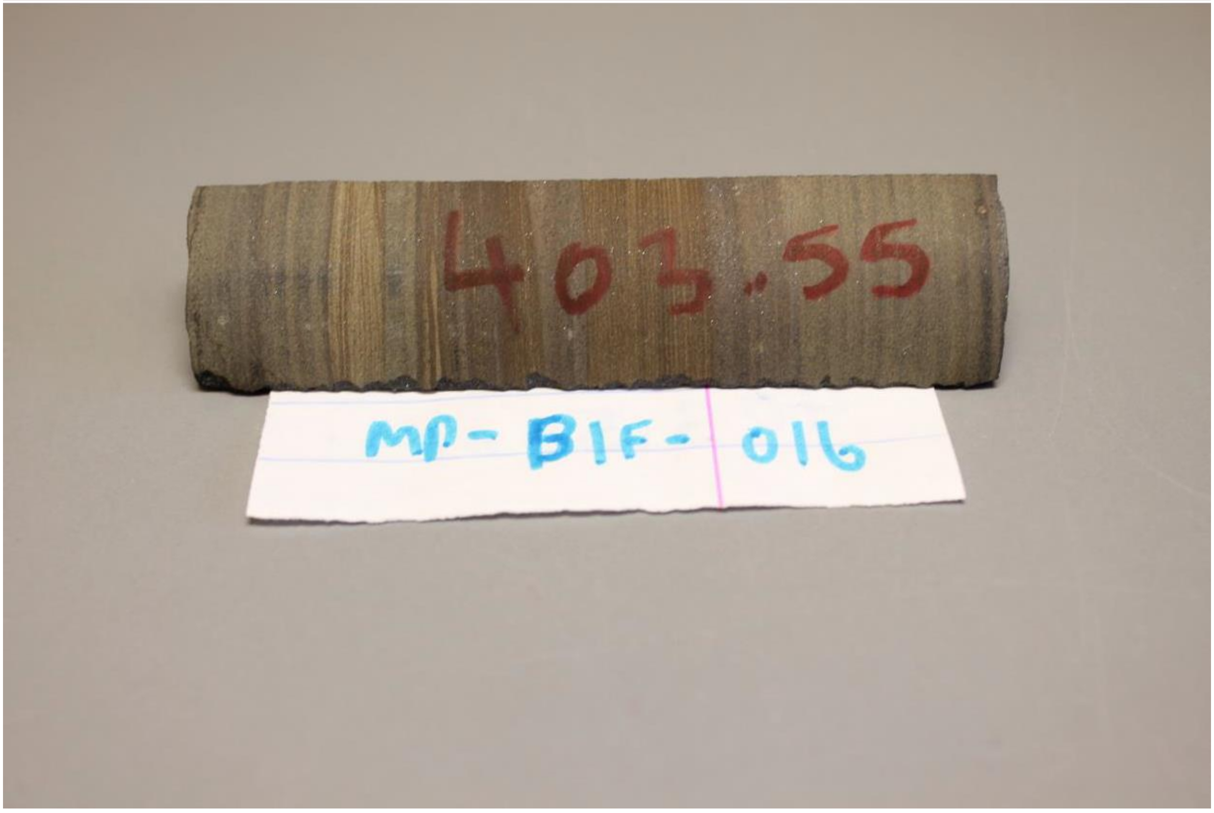
403.55
MP- BIF- 016


404.04
MP-BIF-017

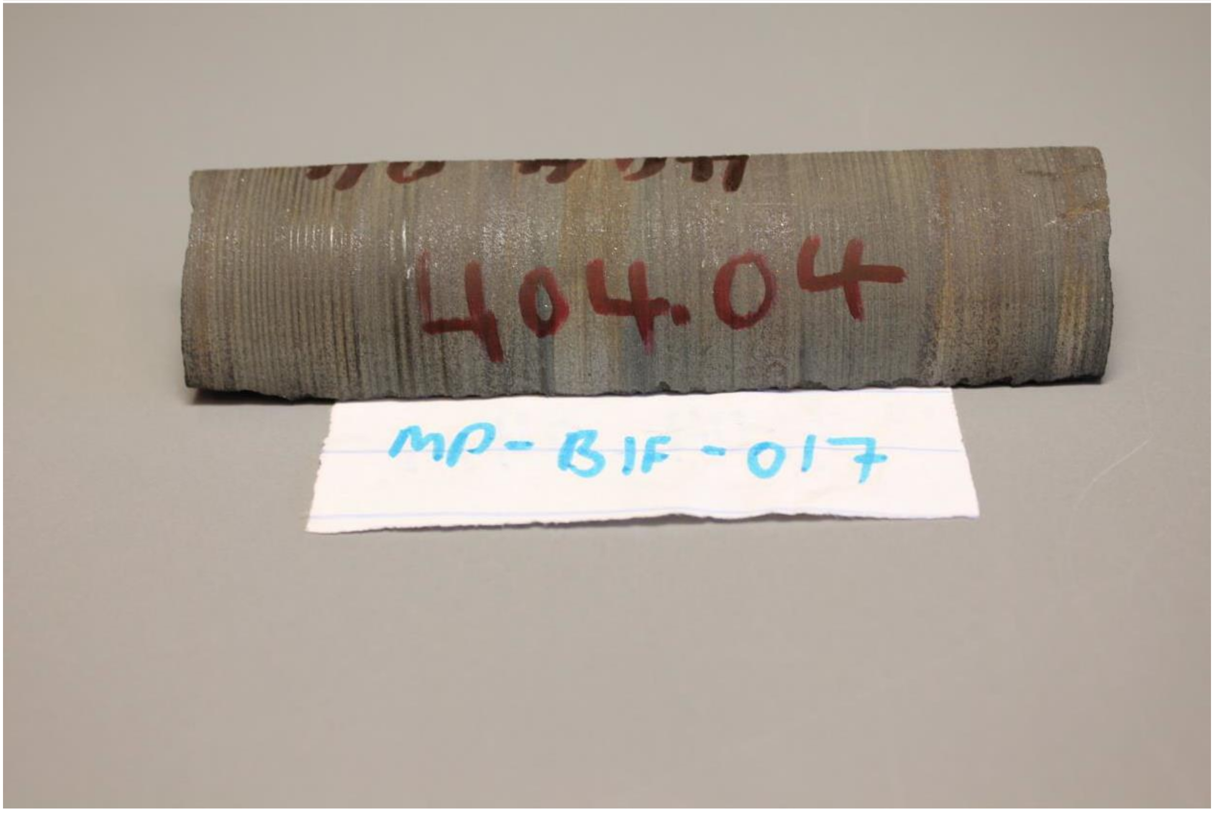
404.04
MP-BIF-017

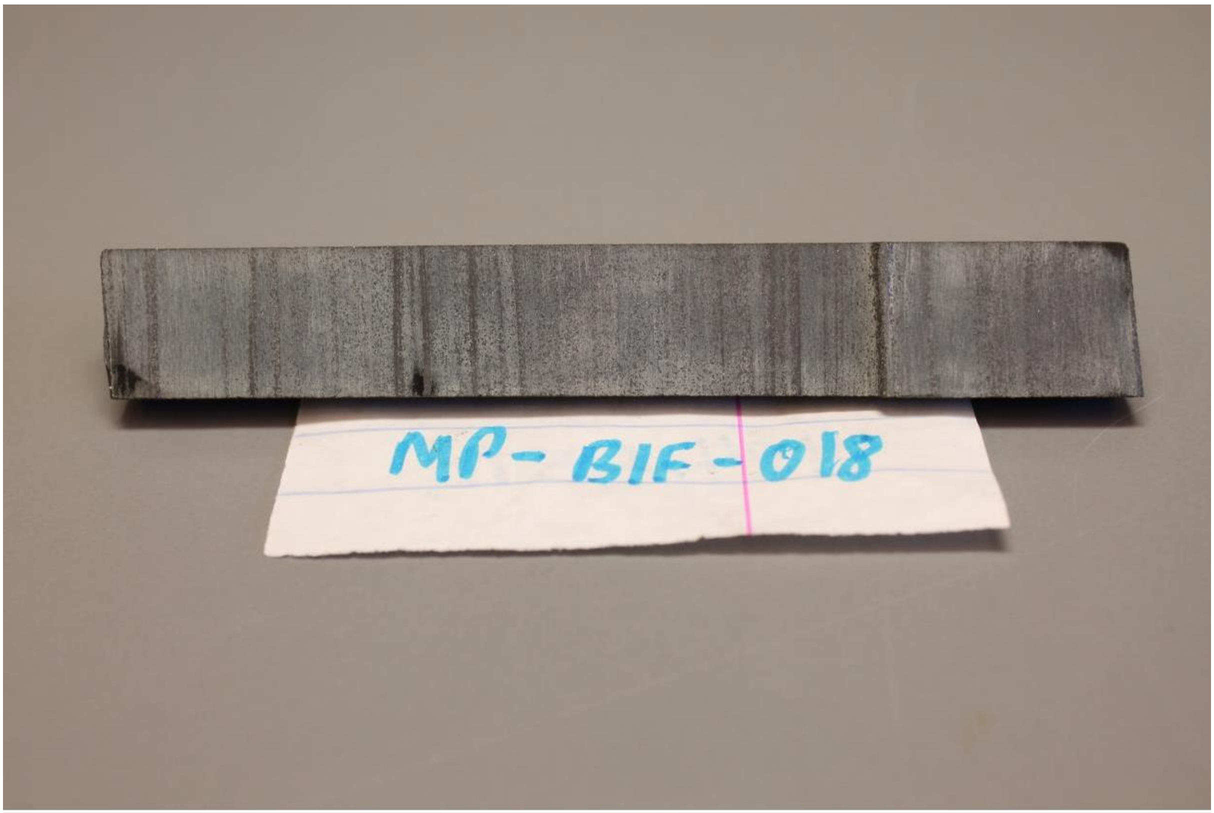
MP- BIF - 018

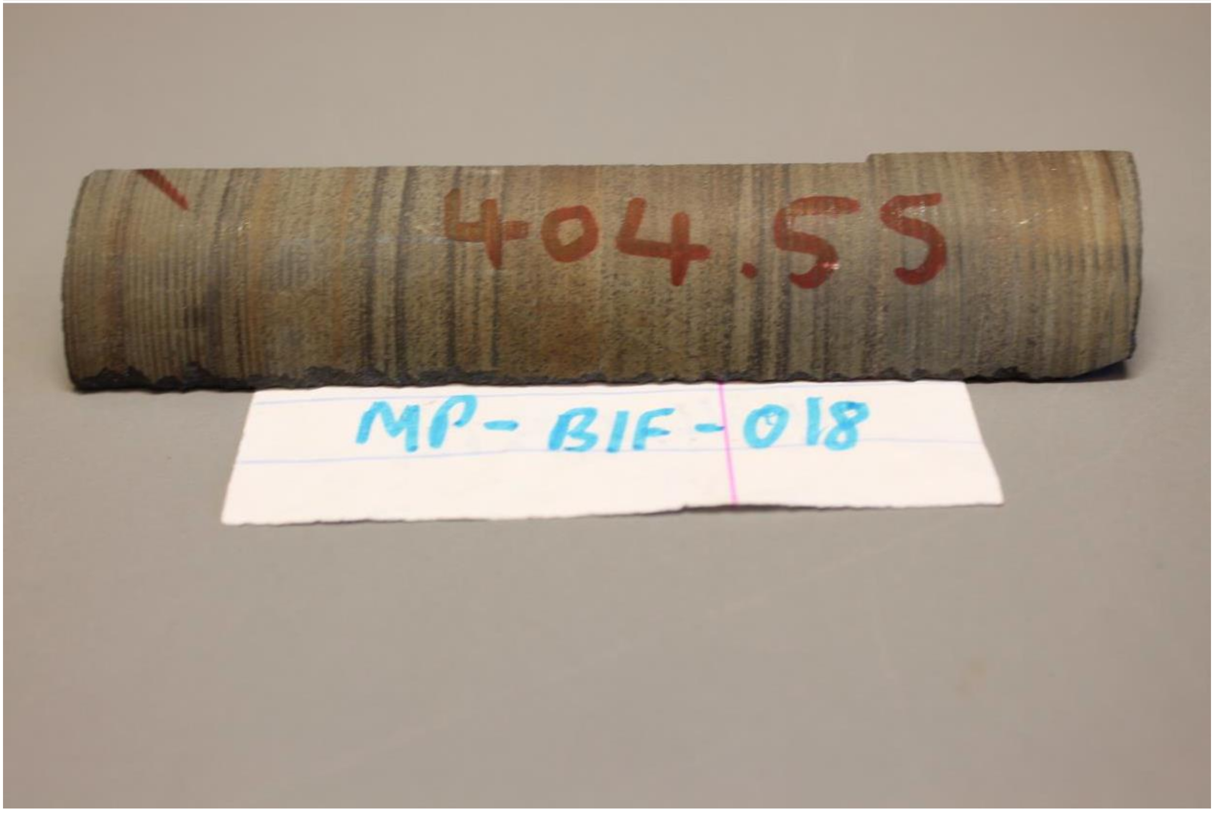
404.55
MP- BIF - 018

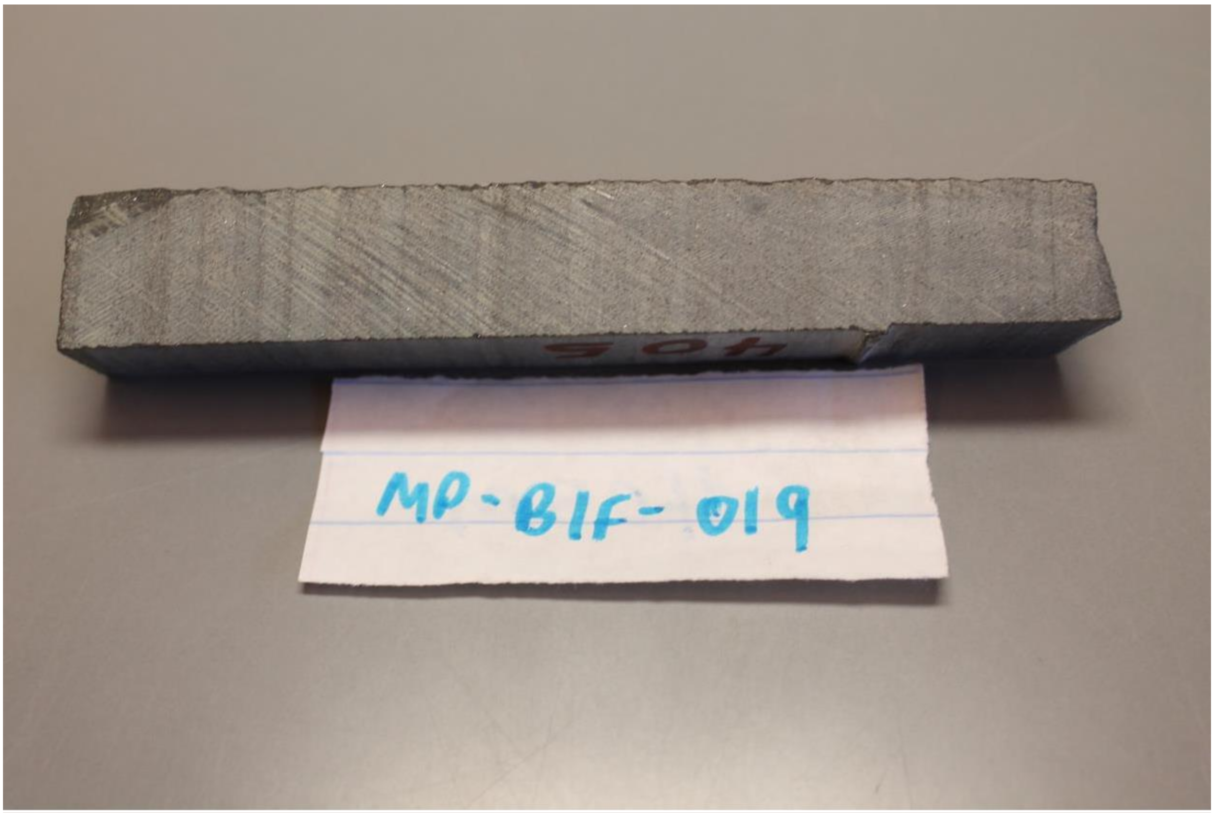
405
MP-BIF-019


405
MP-BIF-019


MP- BIF- 020

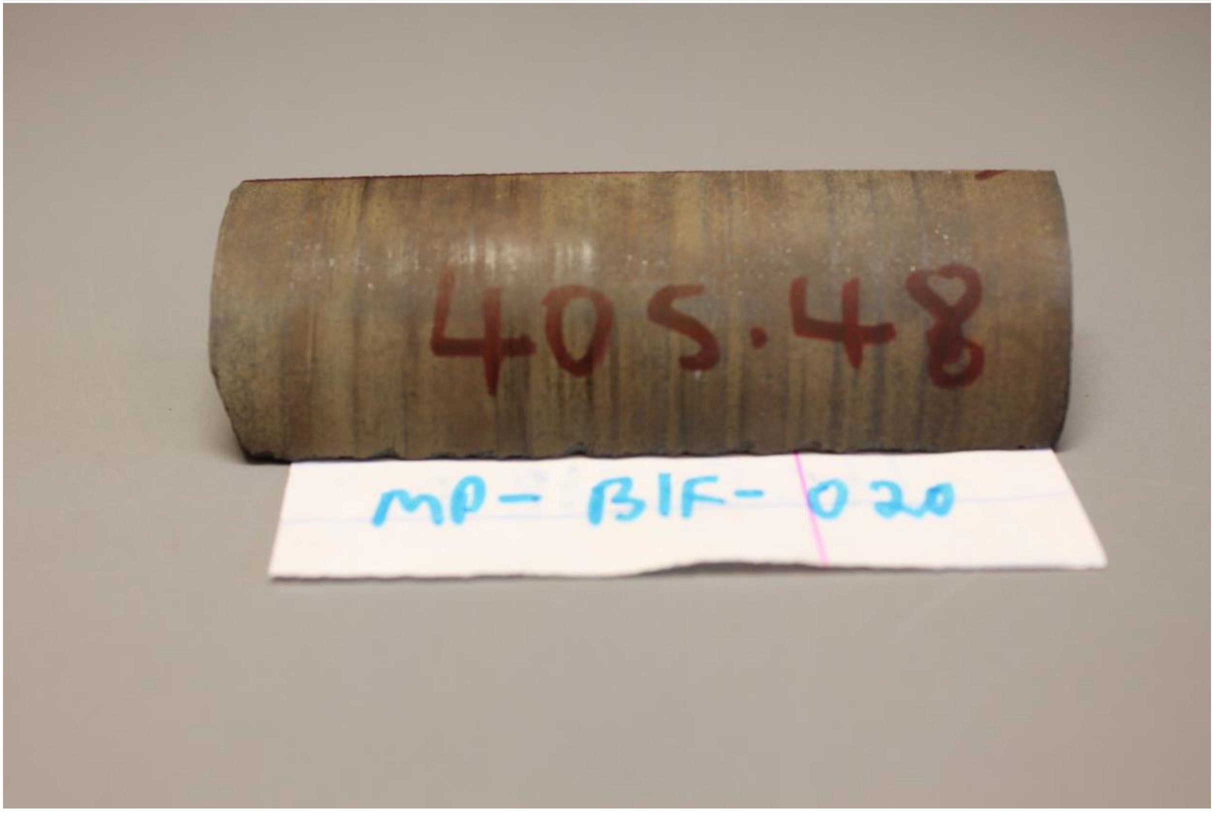
405.48
MP- BIF- 020


MP-BIF-021

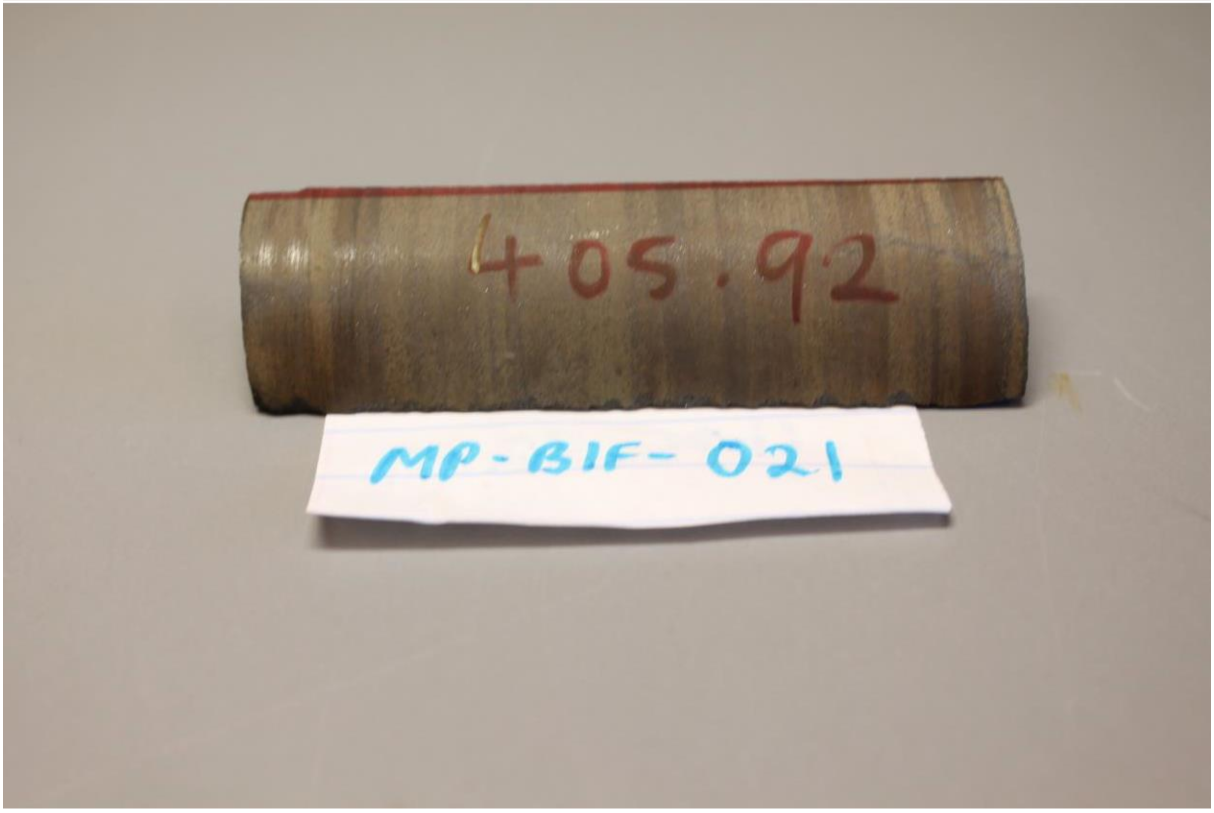
405.92
MP-BIF-021

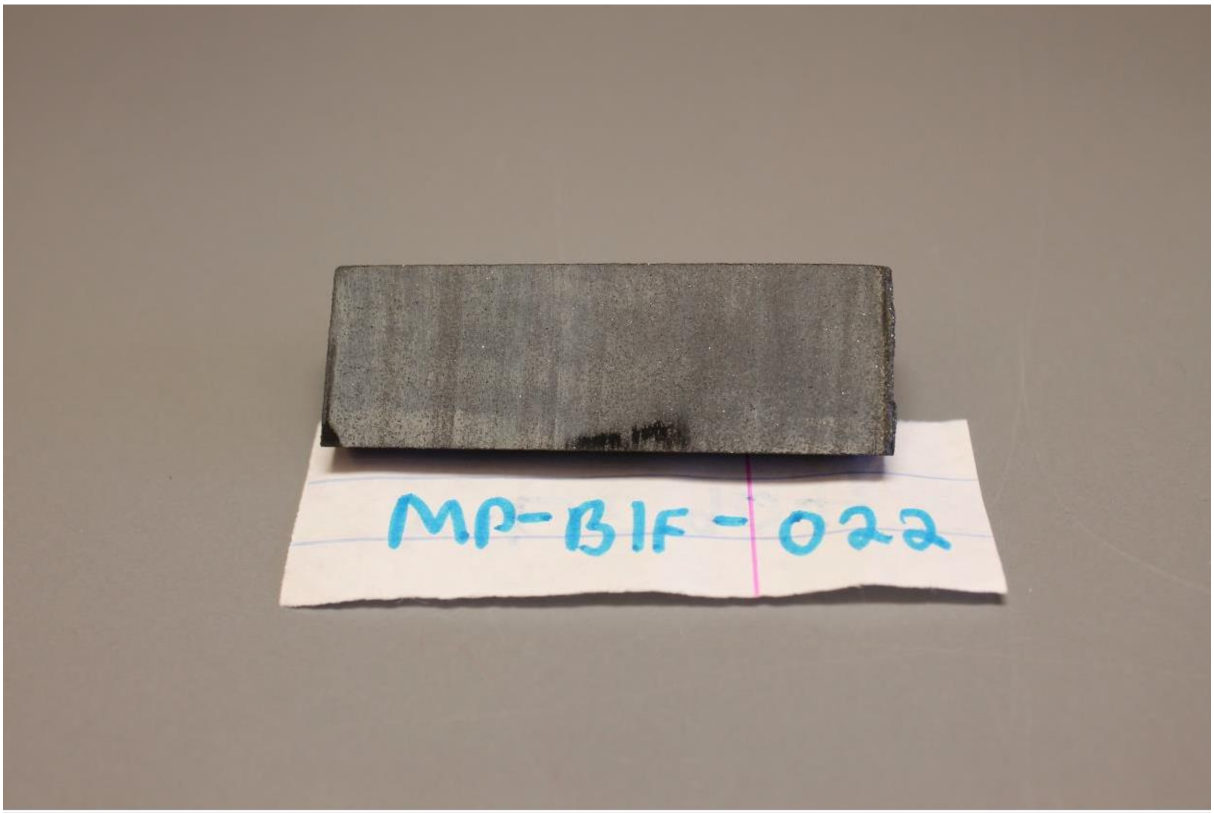
MP-BIF-022


4-06.37
MP-BIF-022


MP-BIF-023


406.79
MP-BIF-023


MP-BIF- 024

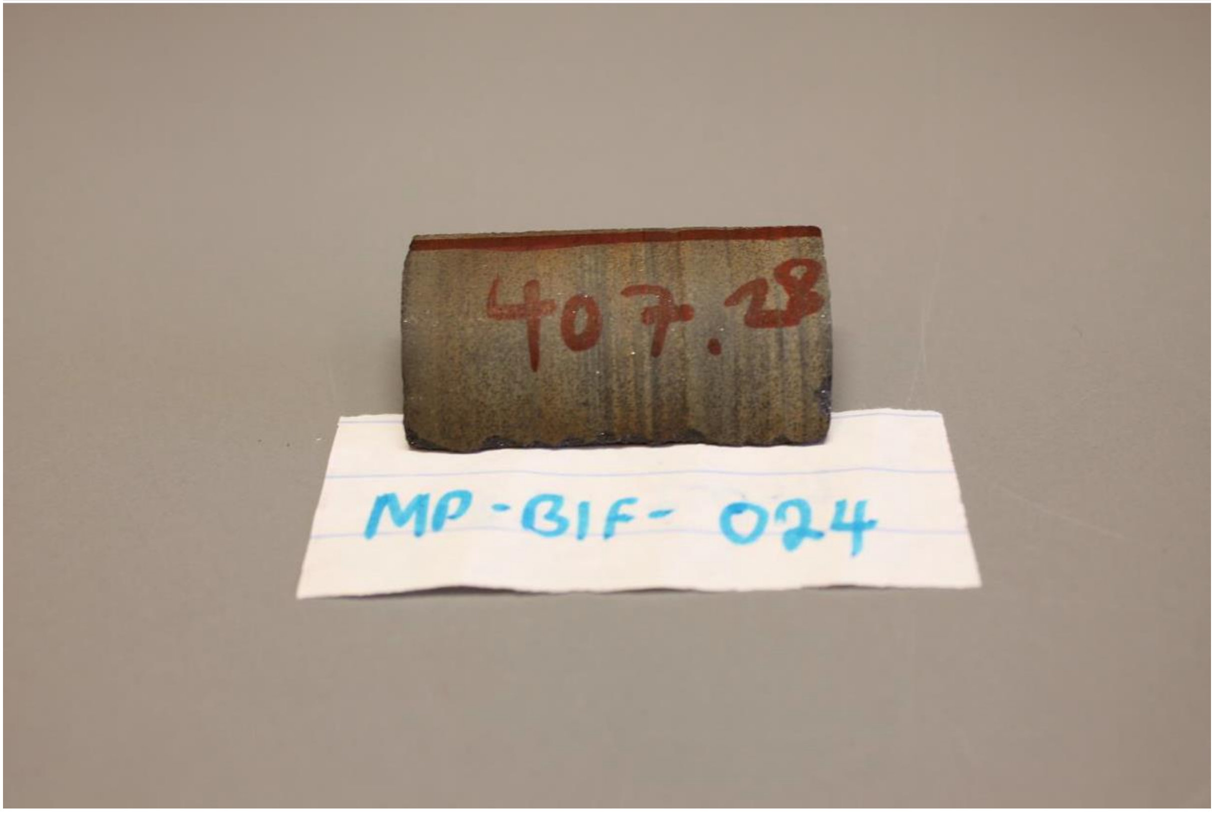
407.28
MP-BIF- 024


MP-BIF-025

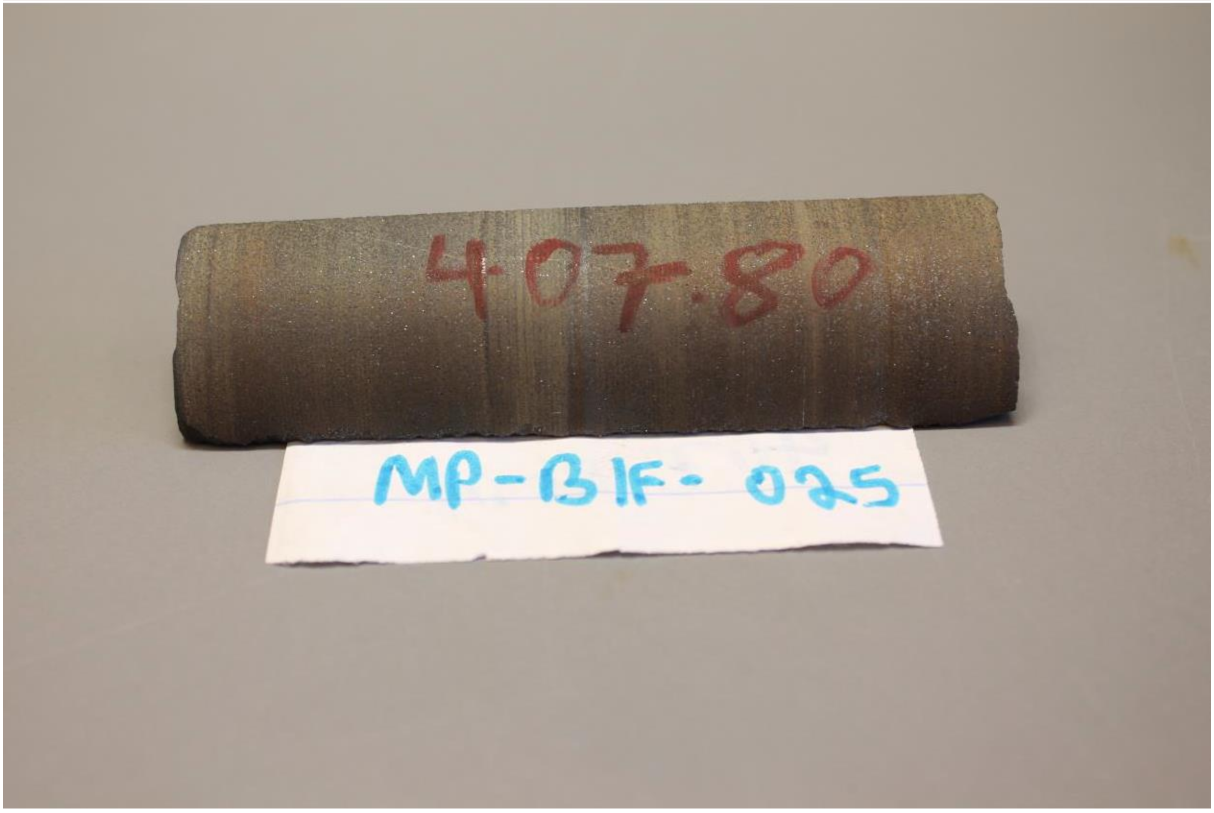
407.80
MP-BIF-025


MP-BIF-026

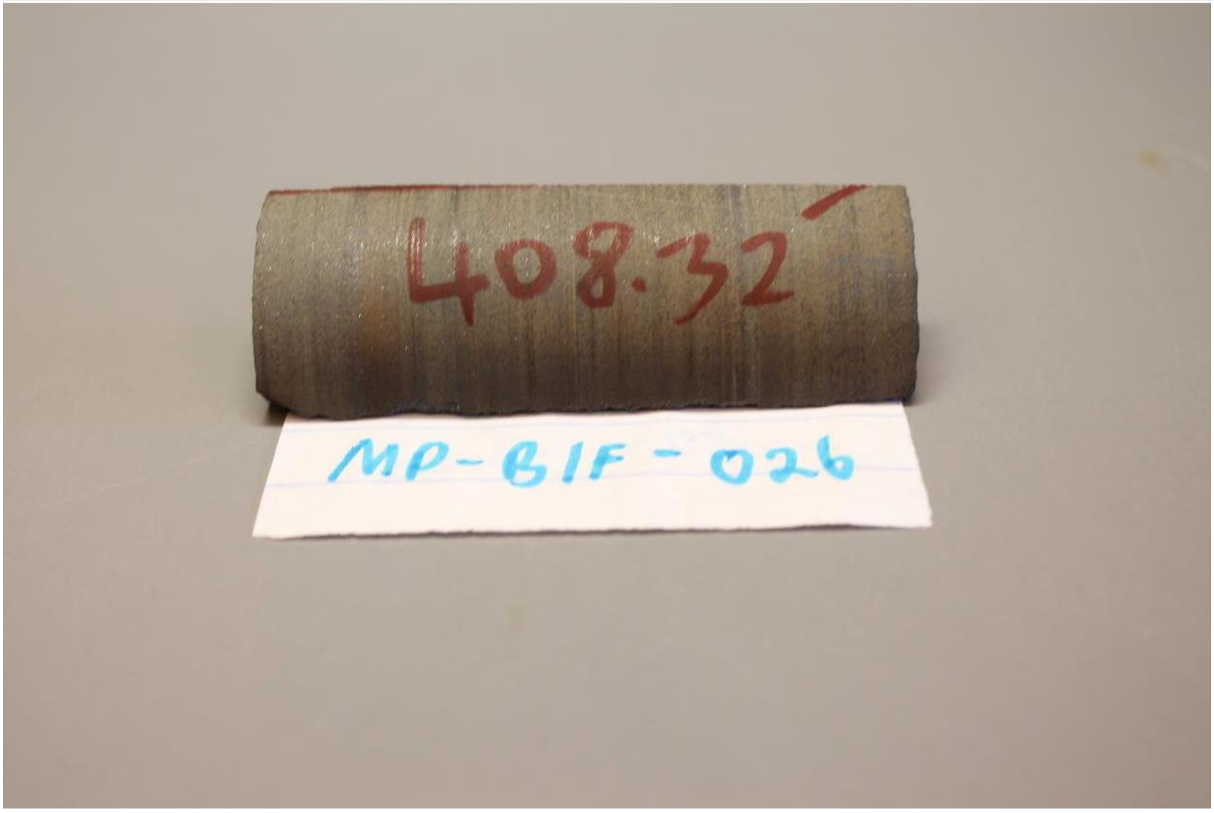
408.32'
MP-BIF-026

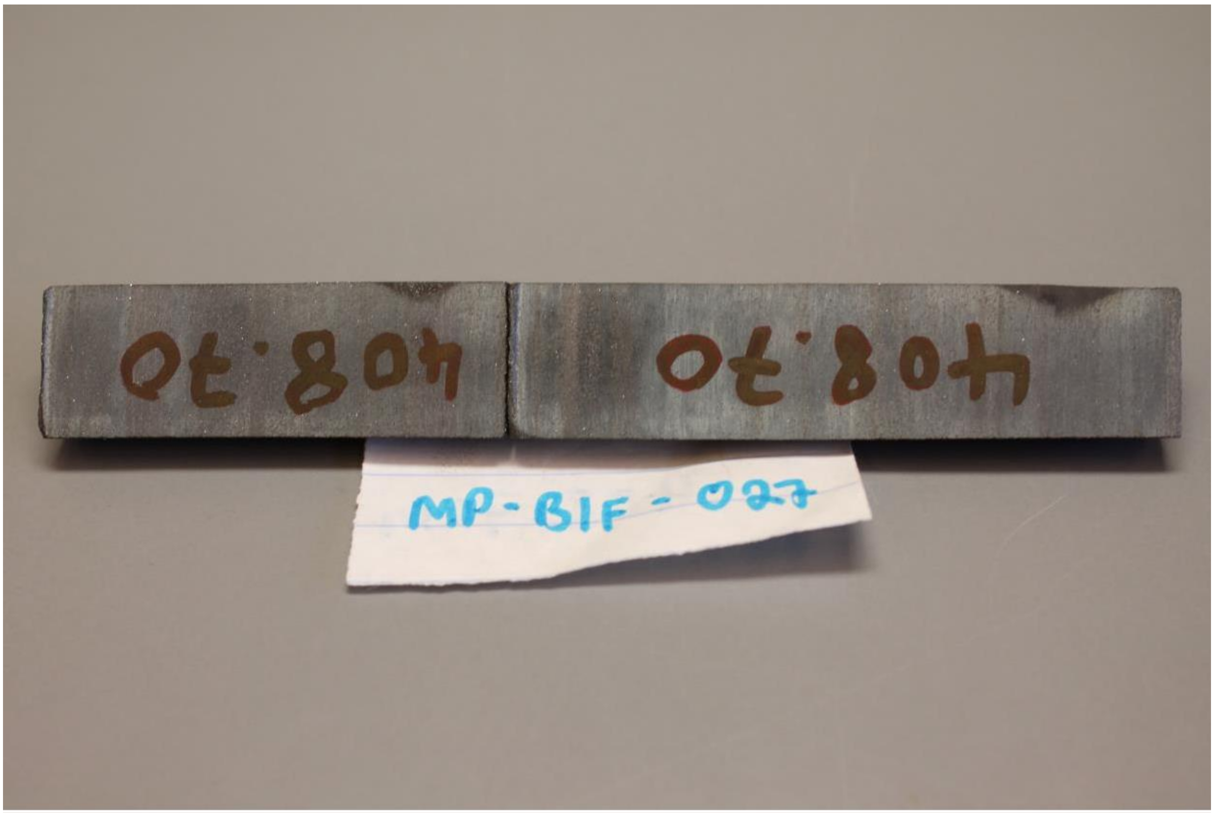
408.70
408.70
MP-BIF-027

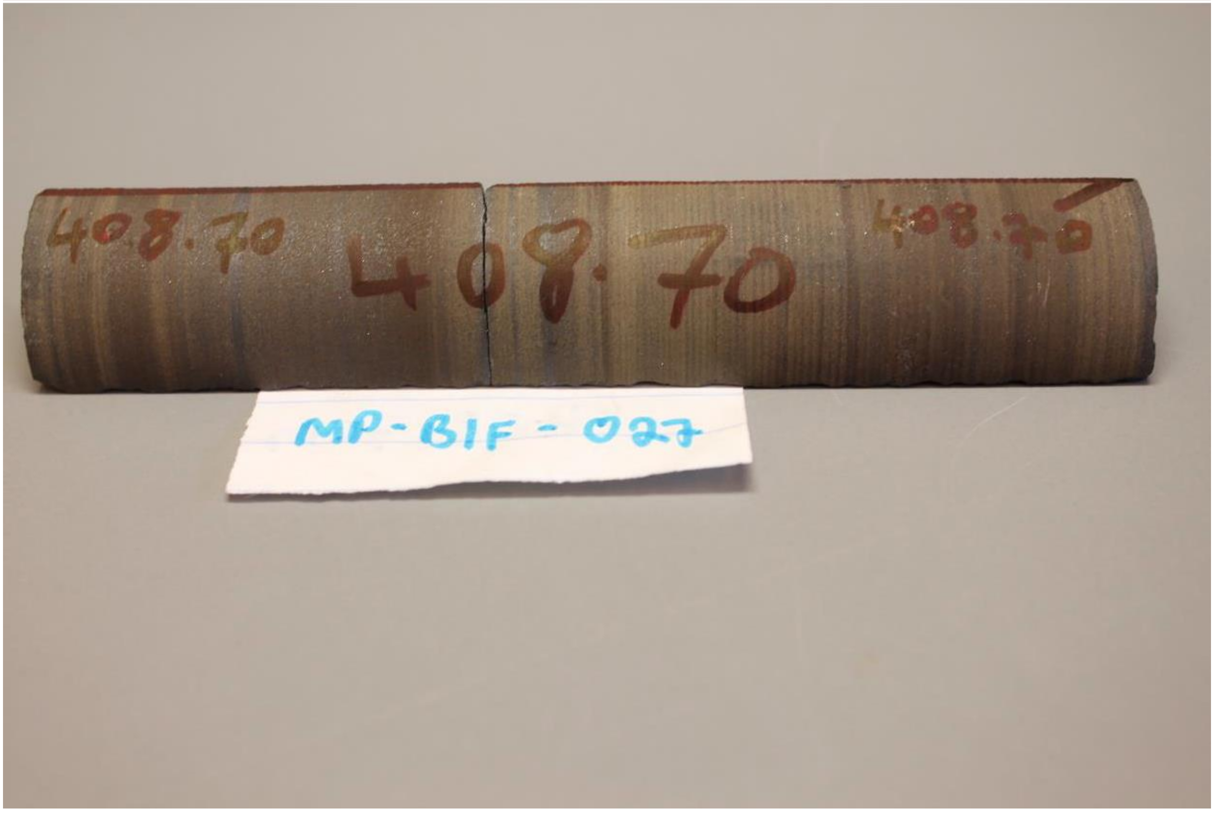
408.70
408.70
408.70
MP-BIF-027


MP-BIF-028

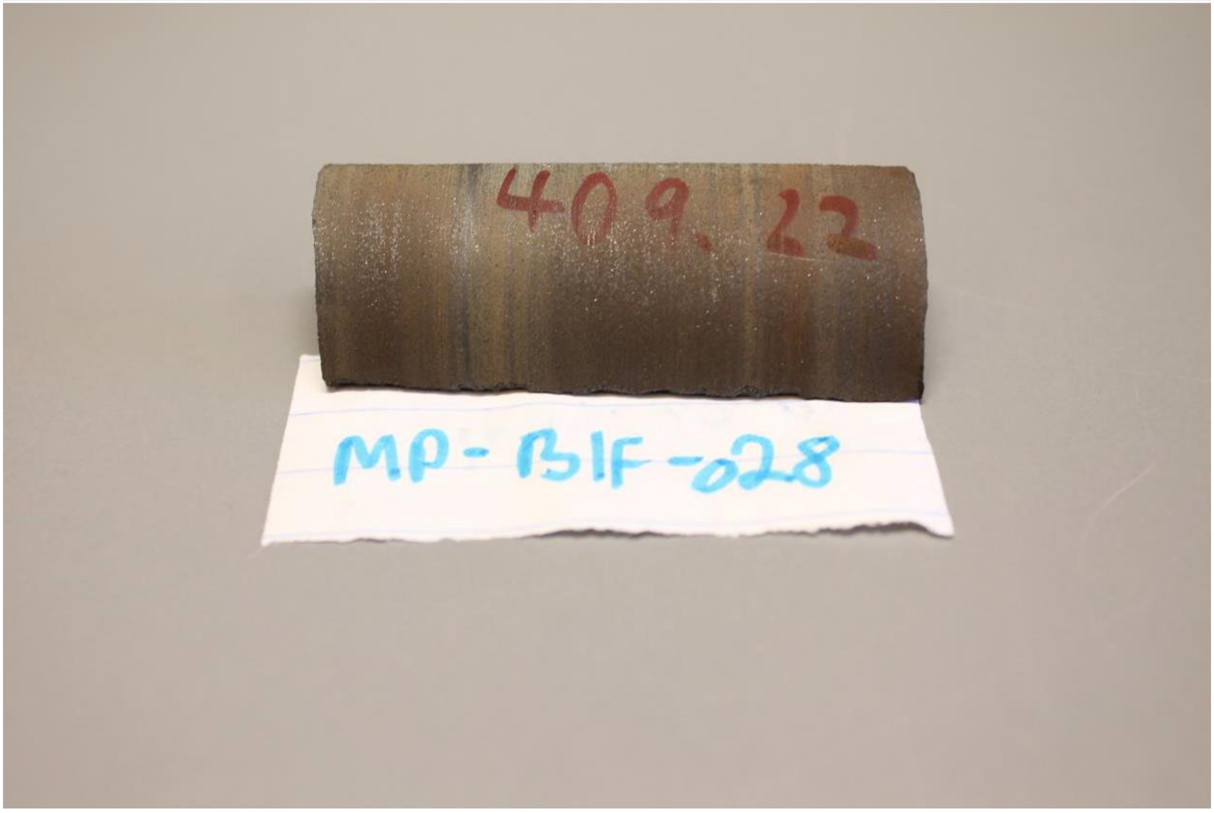
409.22
MP-BIF-028


MP-BIF-029

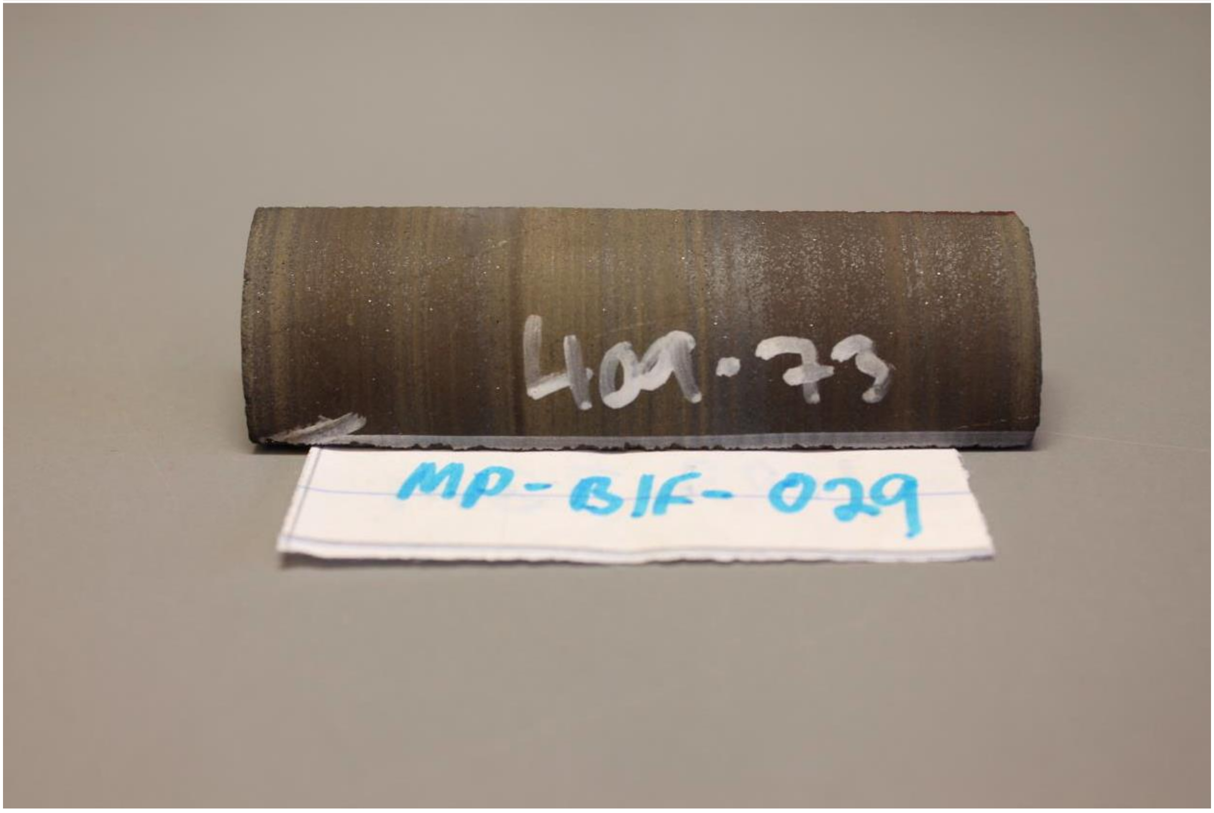
409.73
MP-BIF-029


MP- BIF- 030

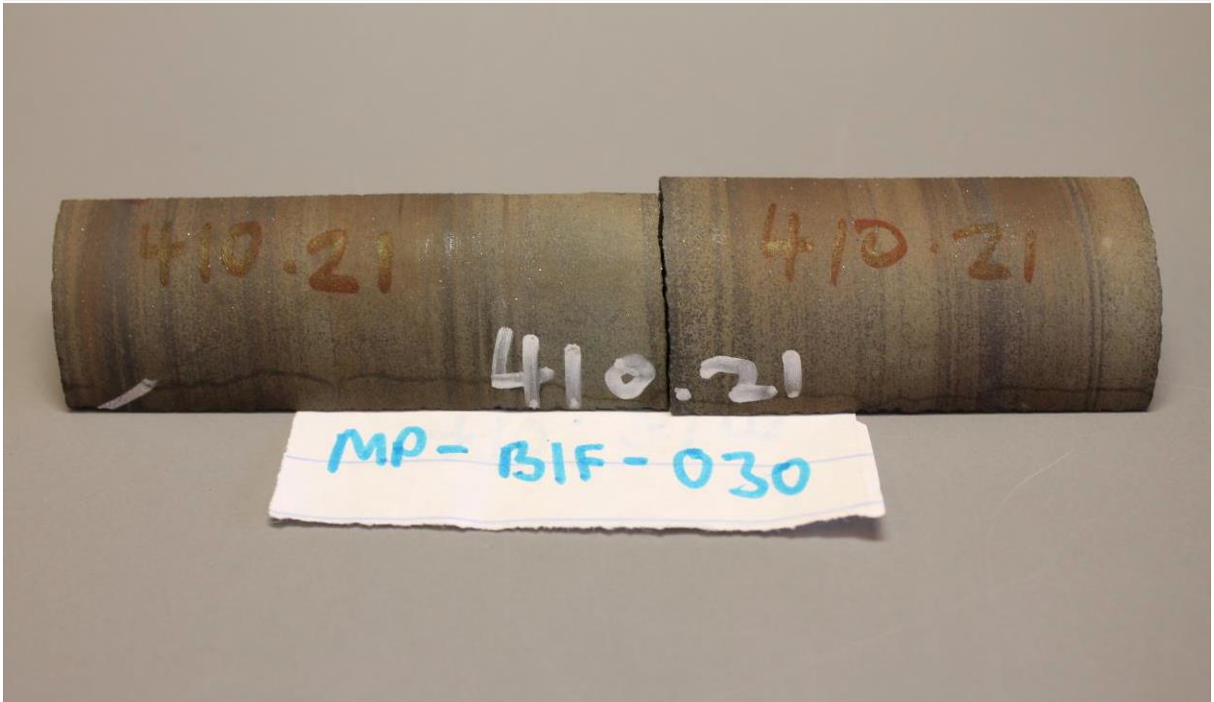
410.21
410.21
410.21
MP- BIF- 030


MP-BIF-031

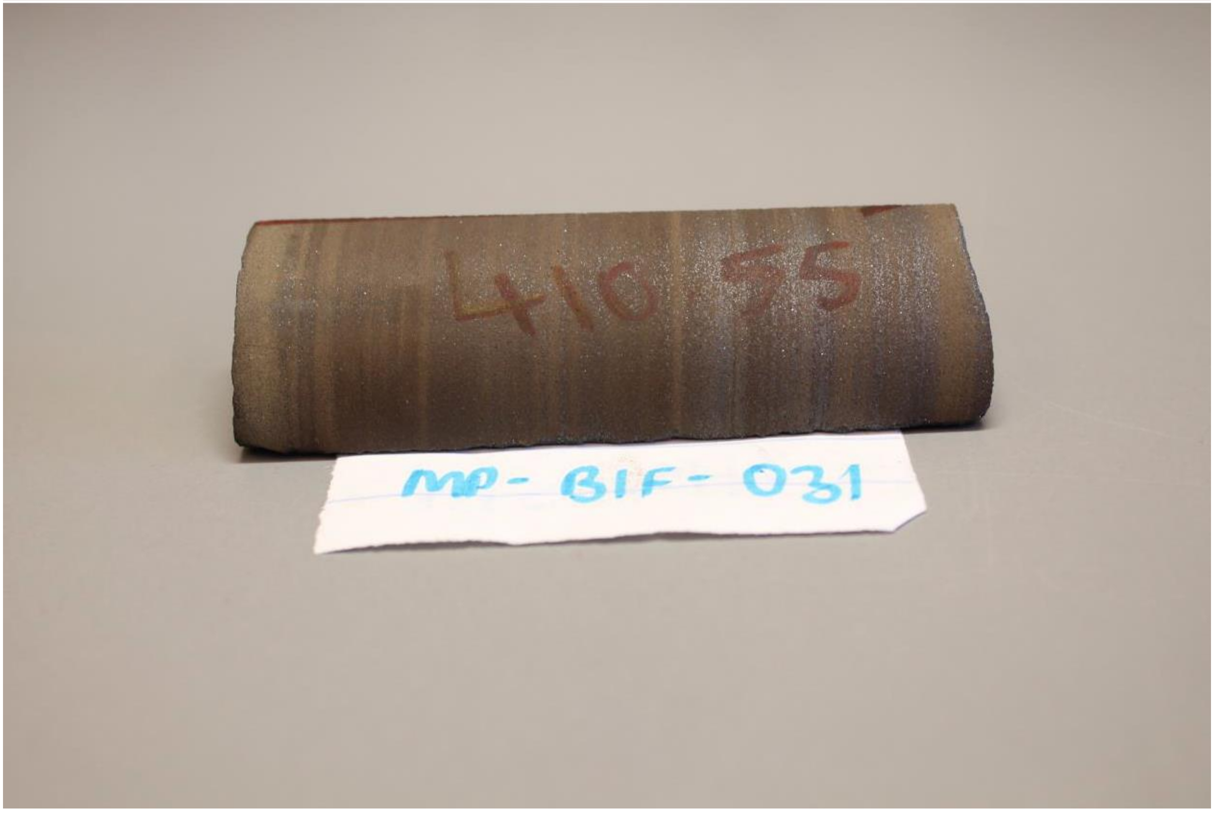
410.55
MP-BIF-031

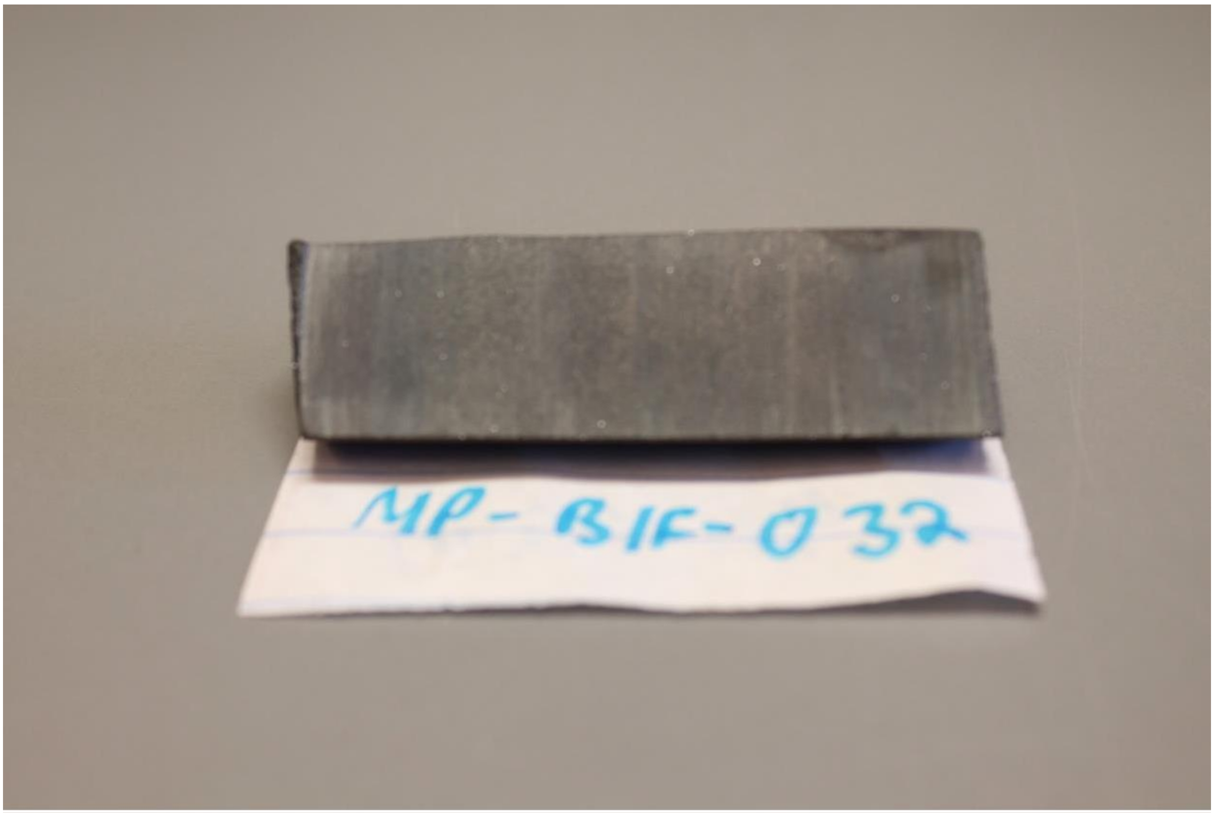

MP- BIF- 032

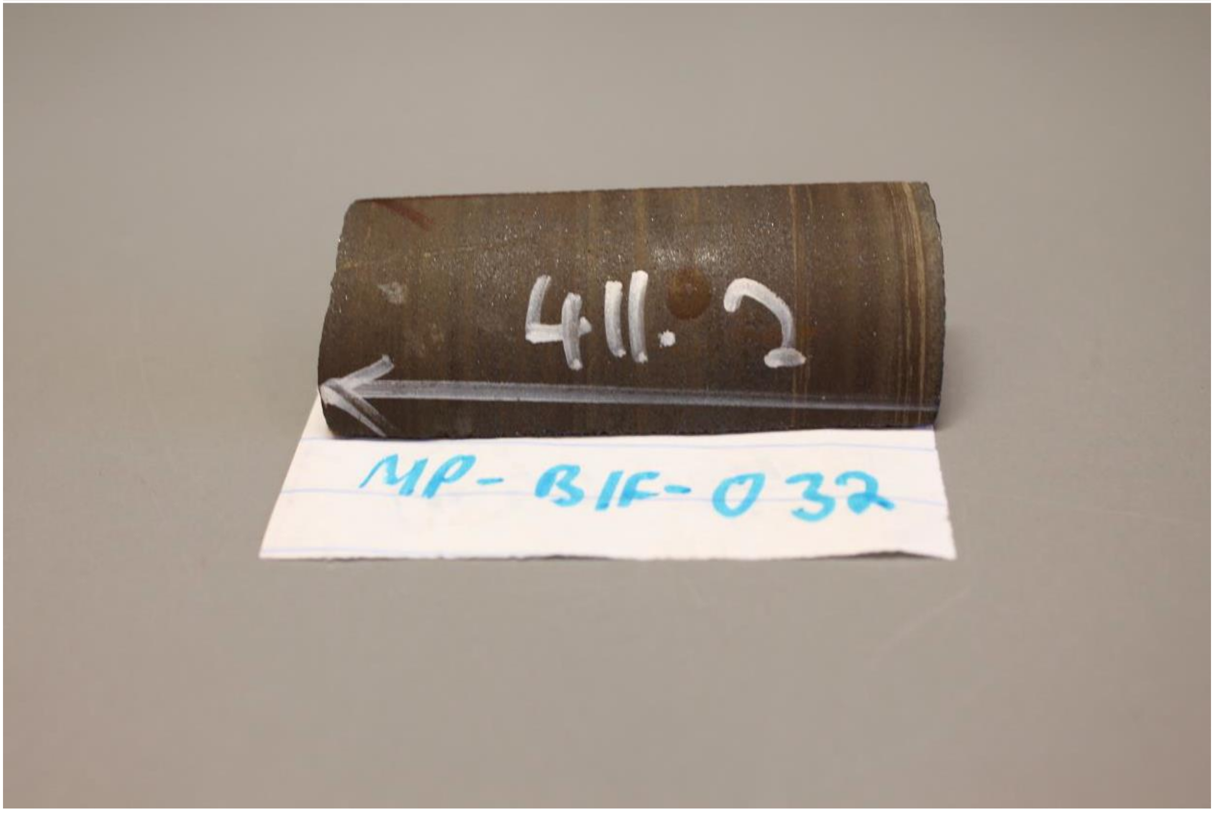

411.2
MP- BIF- 032

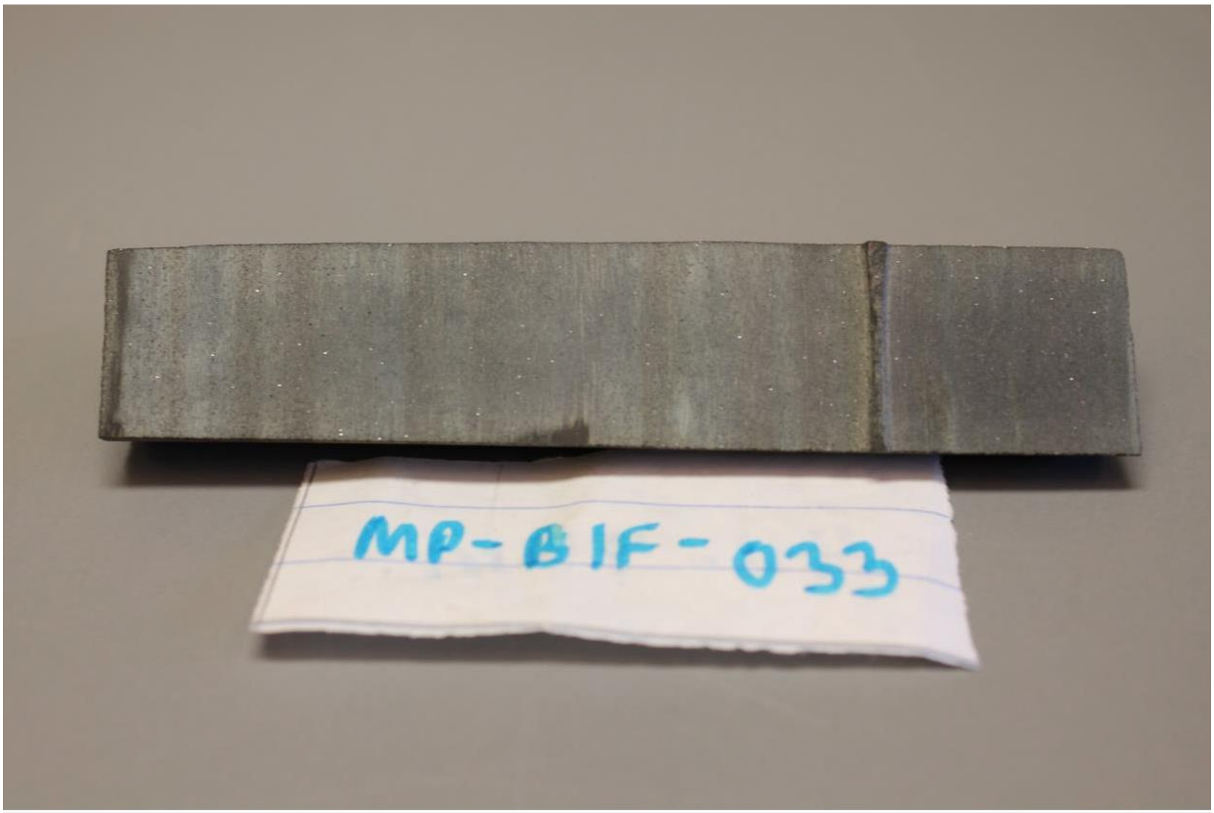

MP-BIF-033

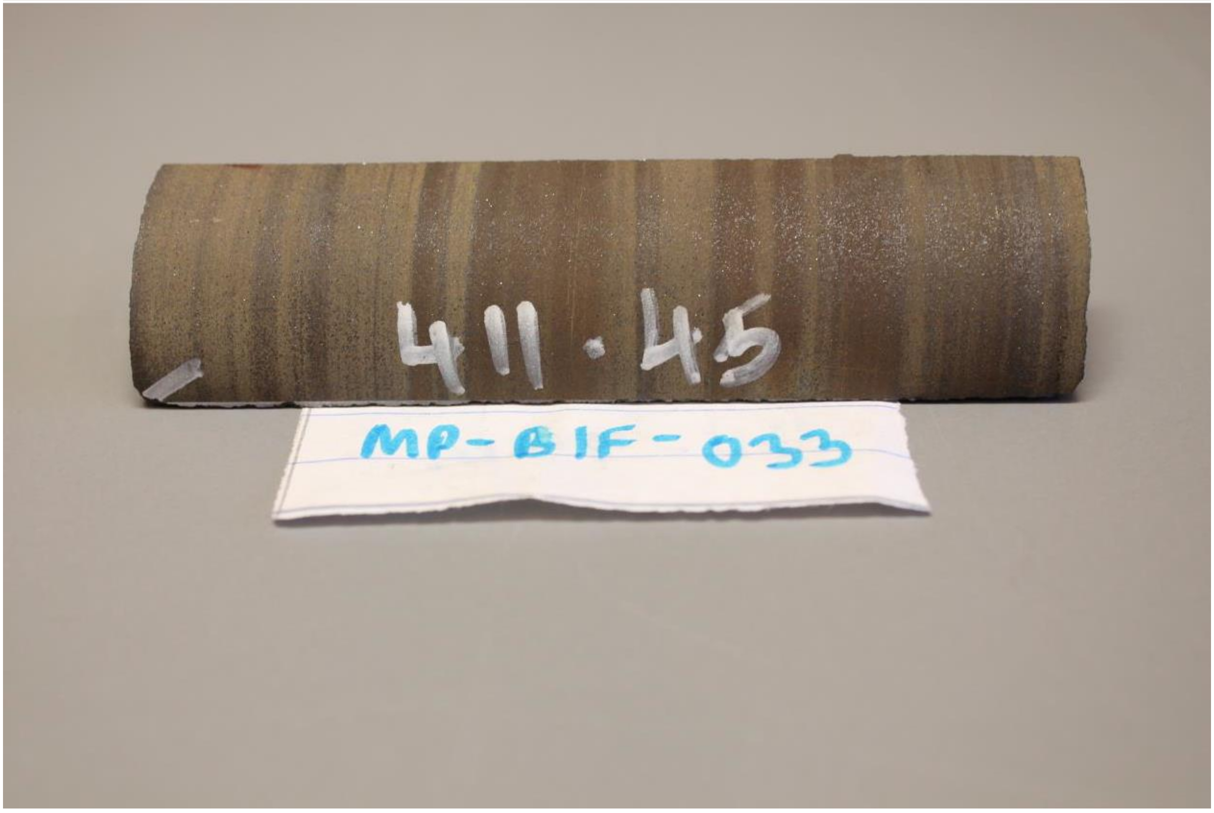

411.45
MP-BIF-033


MP - BIF - 034

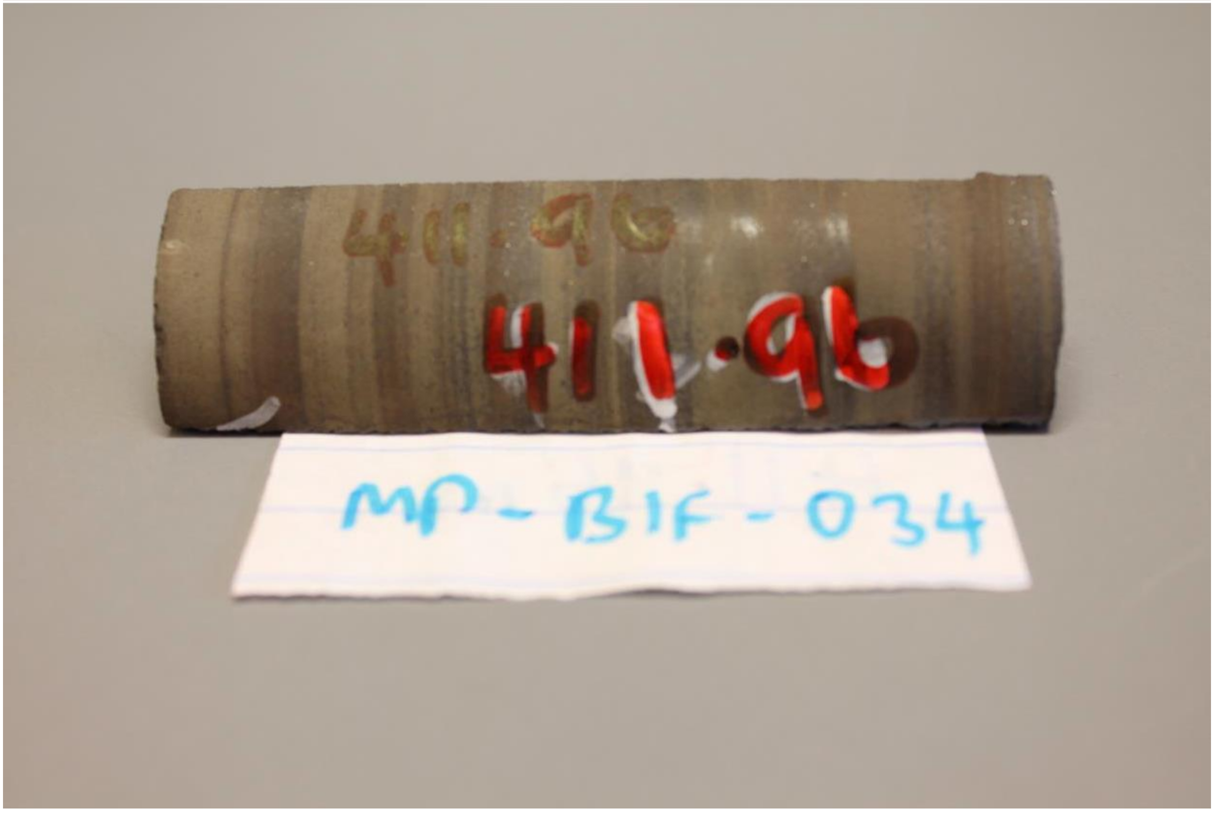
411.96
411.96
MP - BIF - 034


412.47
MP-BIF-035


412.47
MP-BIF-035


412.99
MP-BIF-036

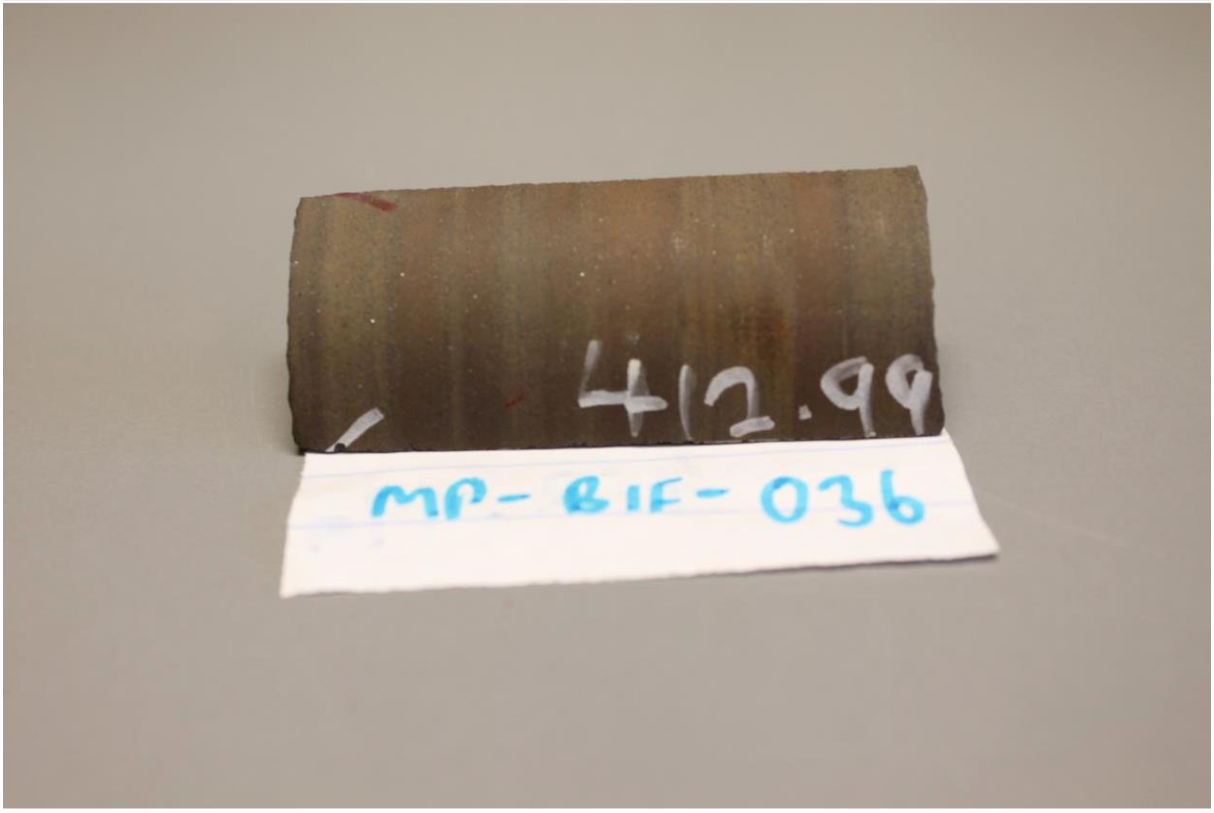
412.99
MP-BIF-036

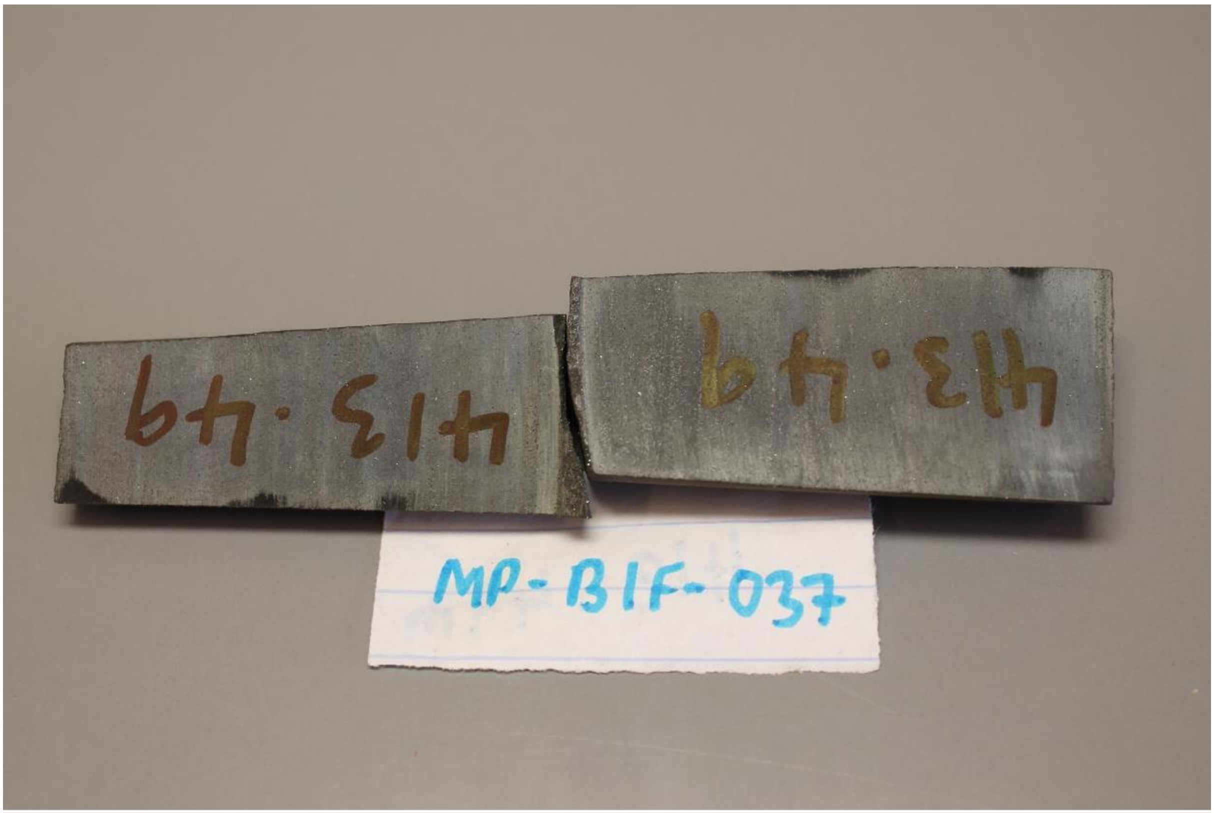
413.49
413.49
MP-BIF-037

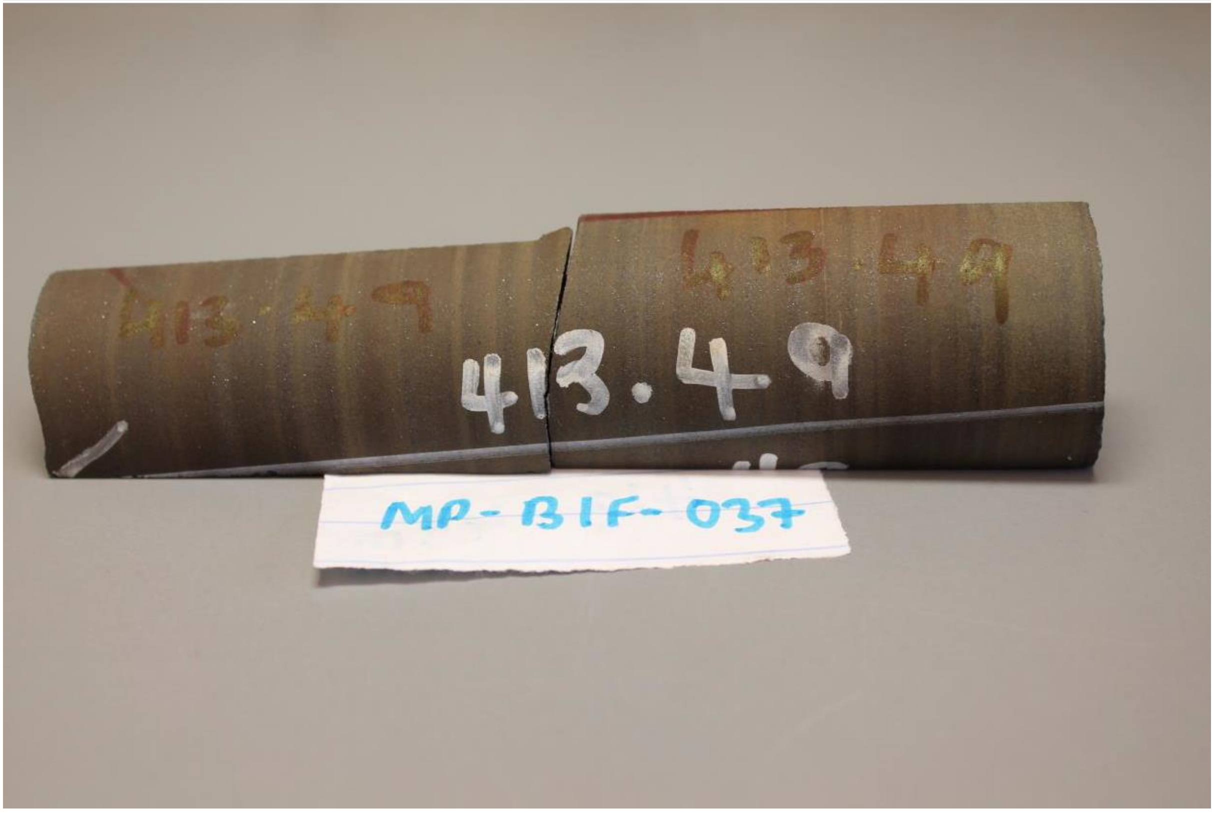
413.49
413.49
413.49
MP-BIF-037


413.98
MP-BIF-038

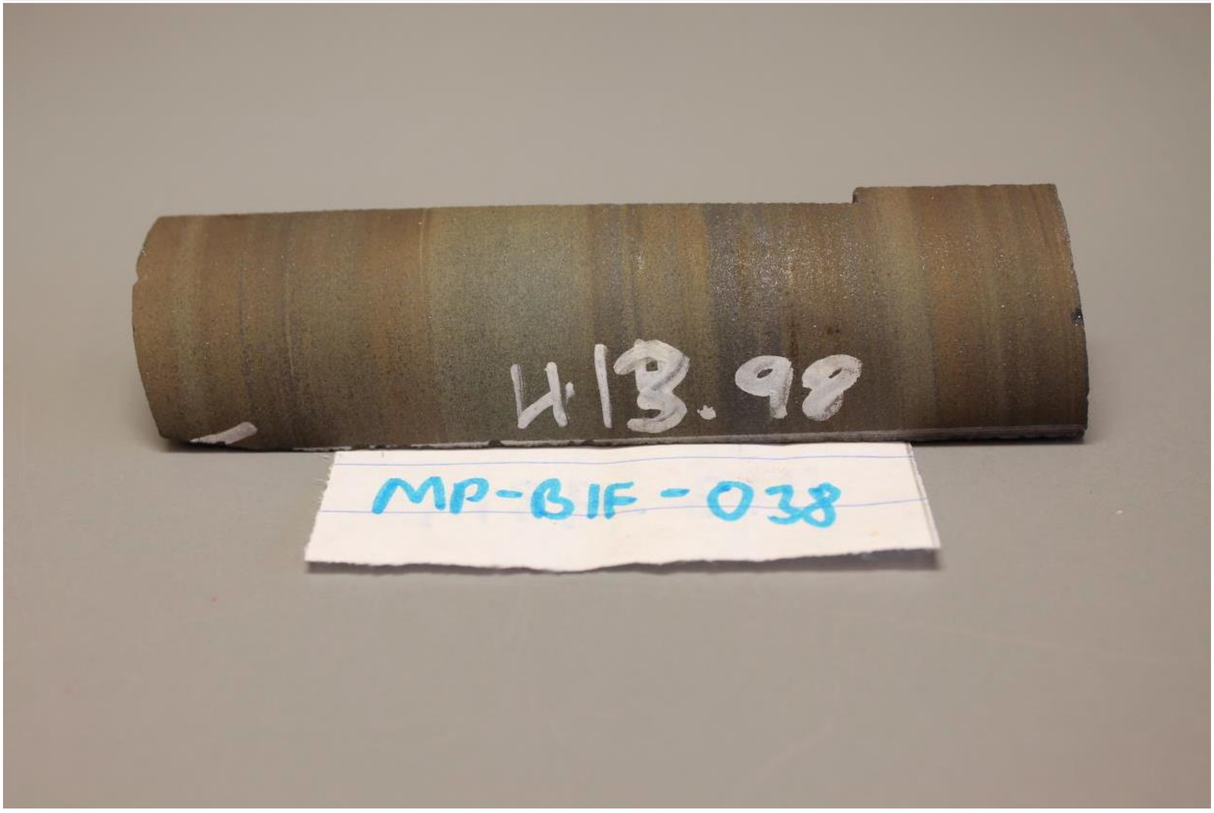
413.98
MP-BIF-038

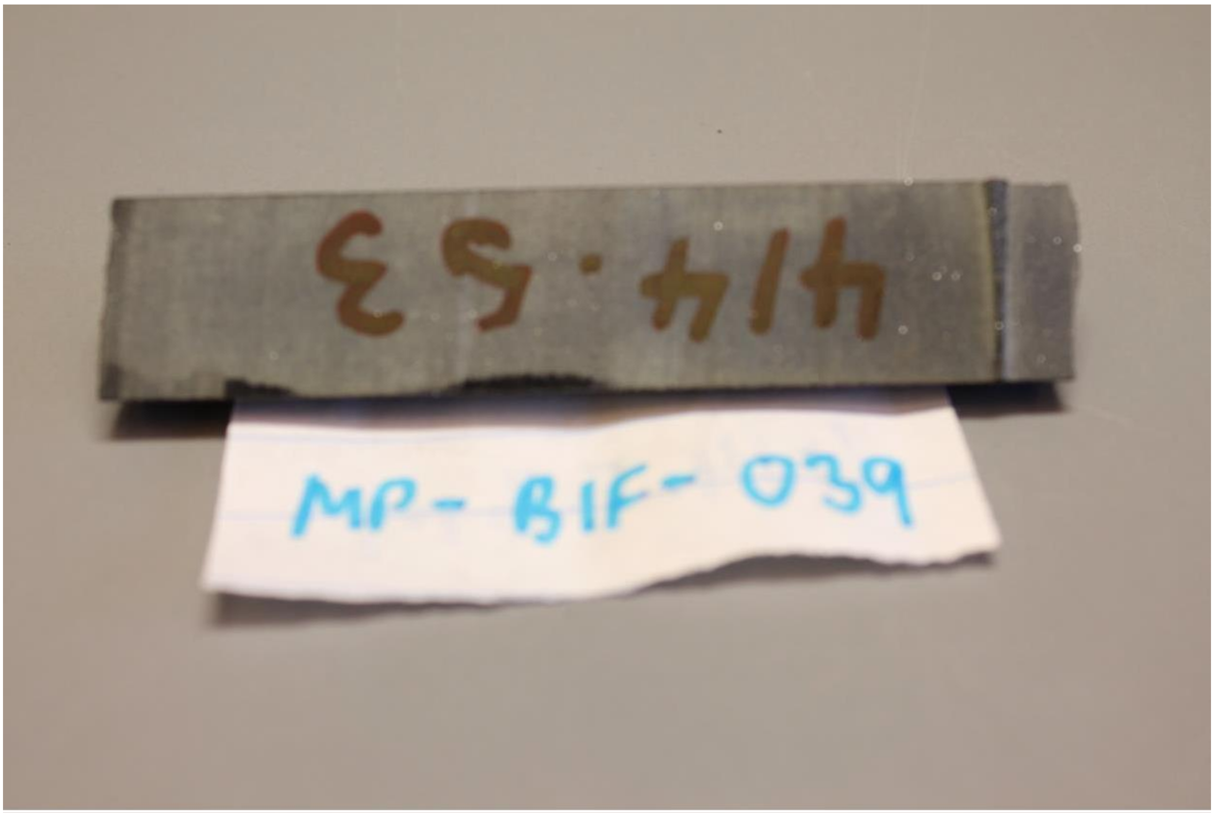
414.53
MP- BIF- 039

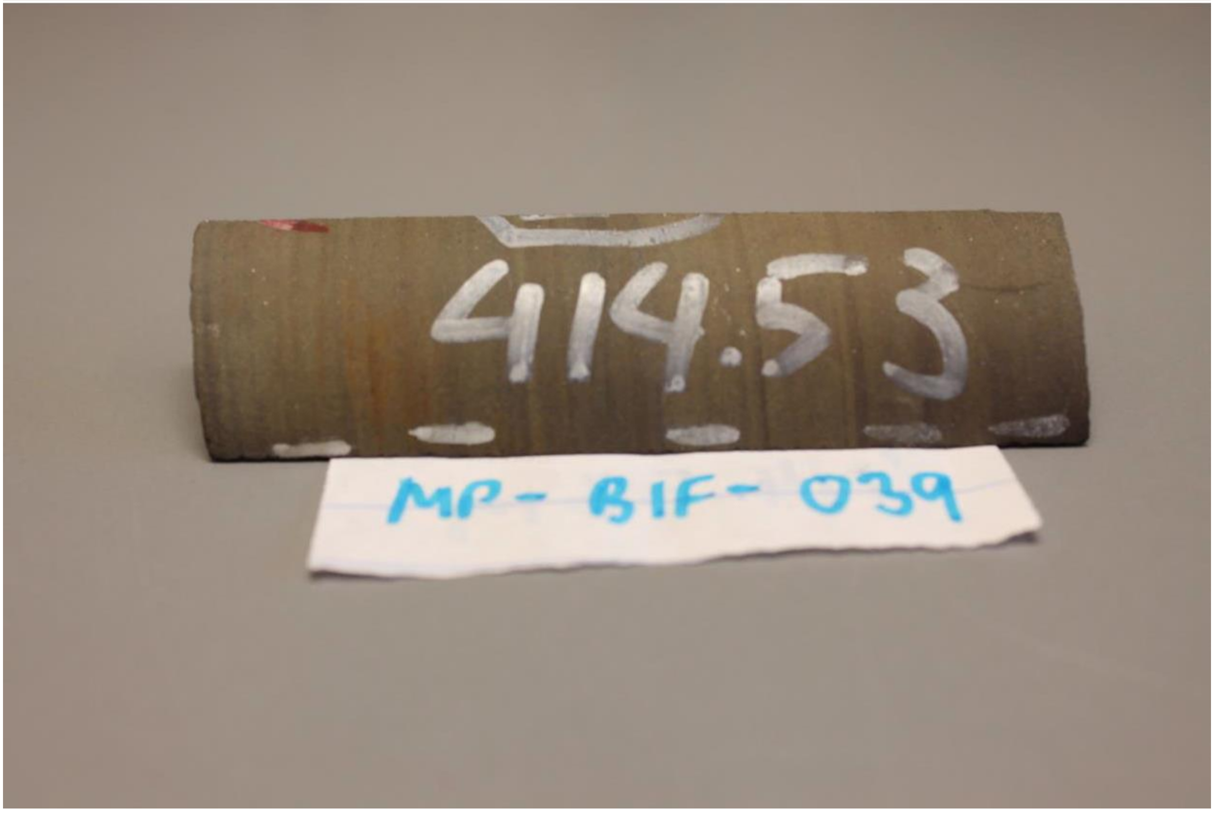
414.53
MP- BIF- 039

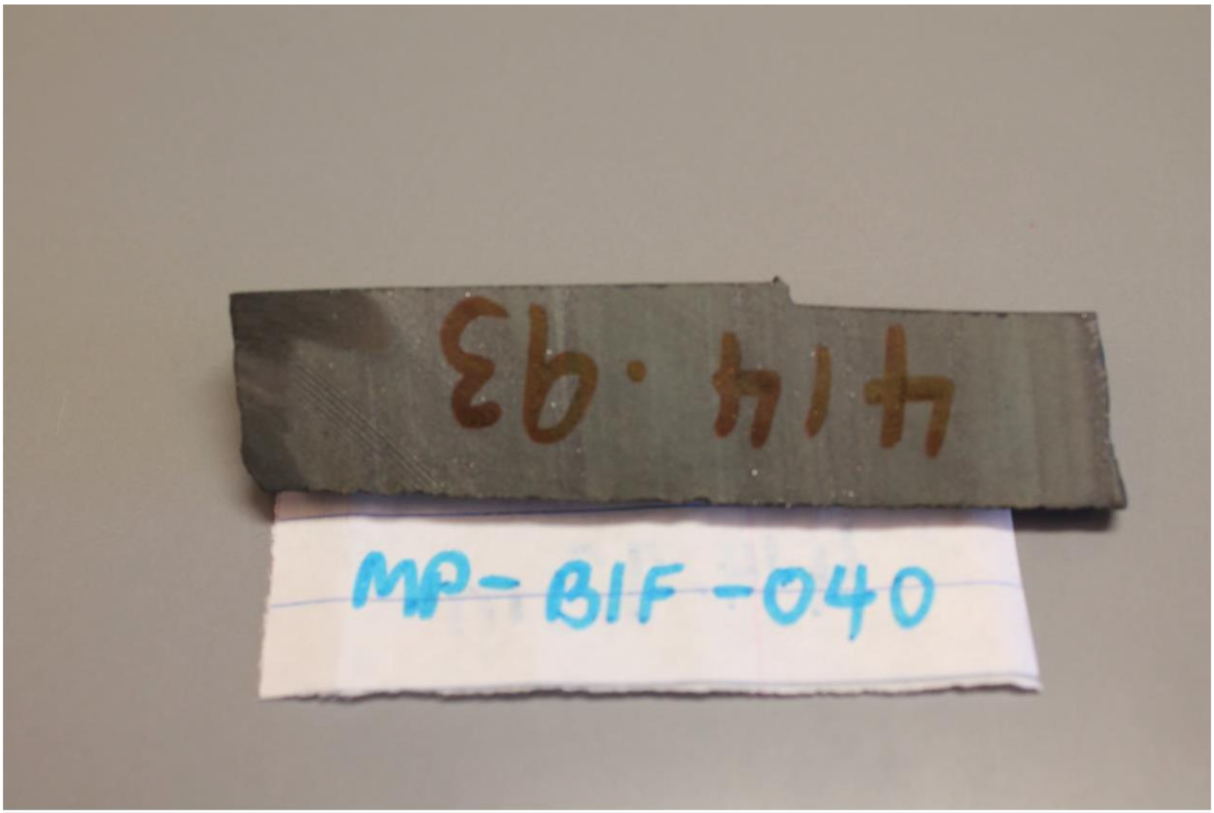
414.93
MP-BIF-040

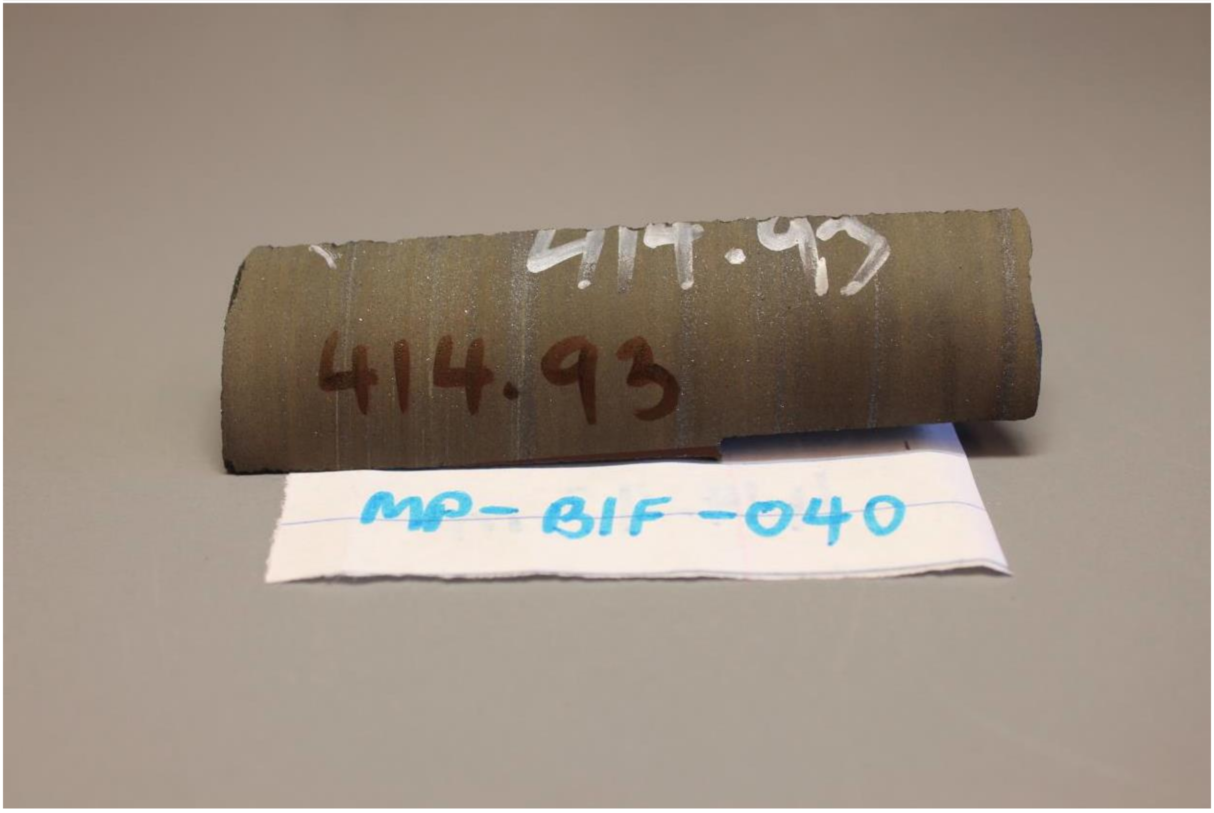
414.93
414.93
MP-BIF-040


415.51
MP-BIF-041

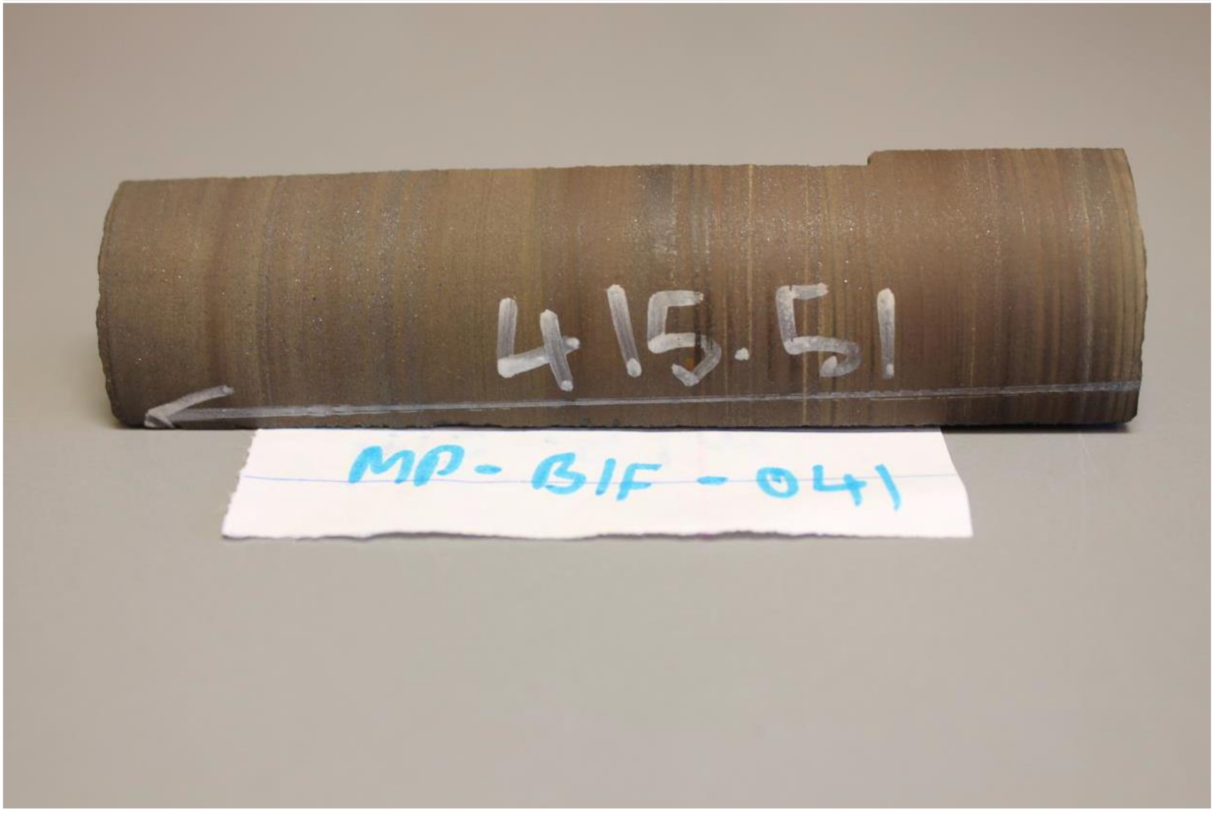
415.51
MP-BIF-041


415.87
MP- BIF- 042

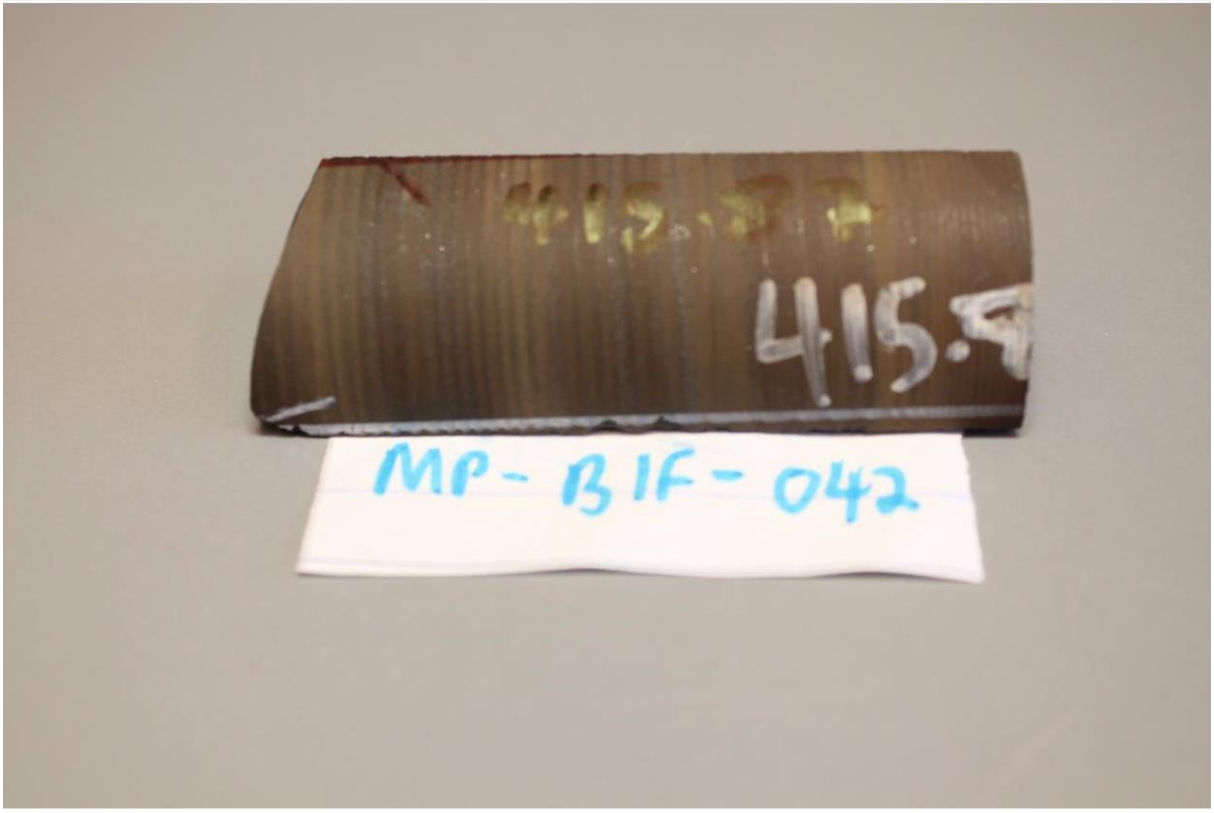
415.87
415.
MP- BIF- 042

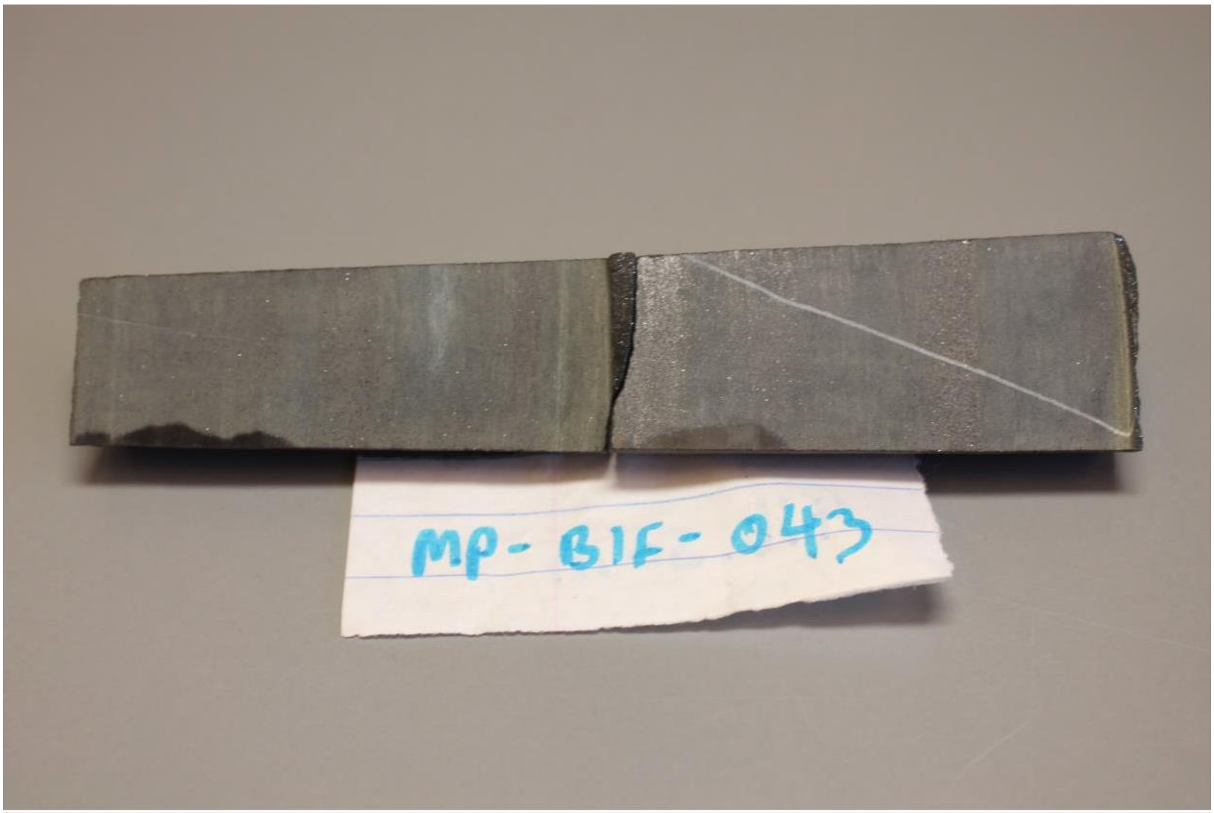
MP-BIF-043

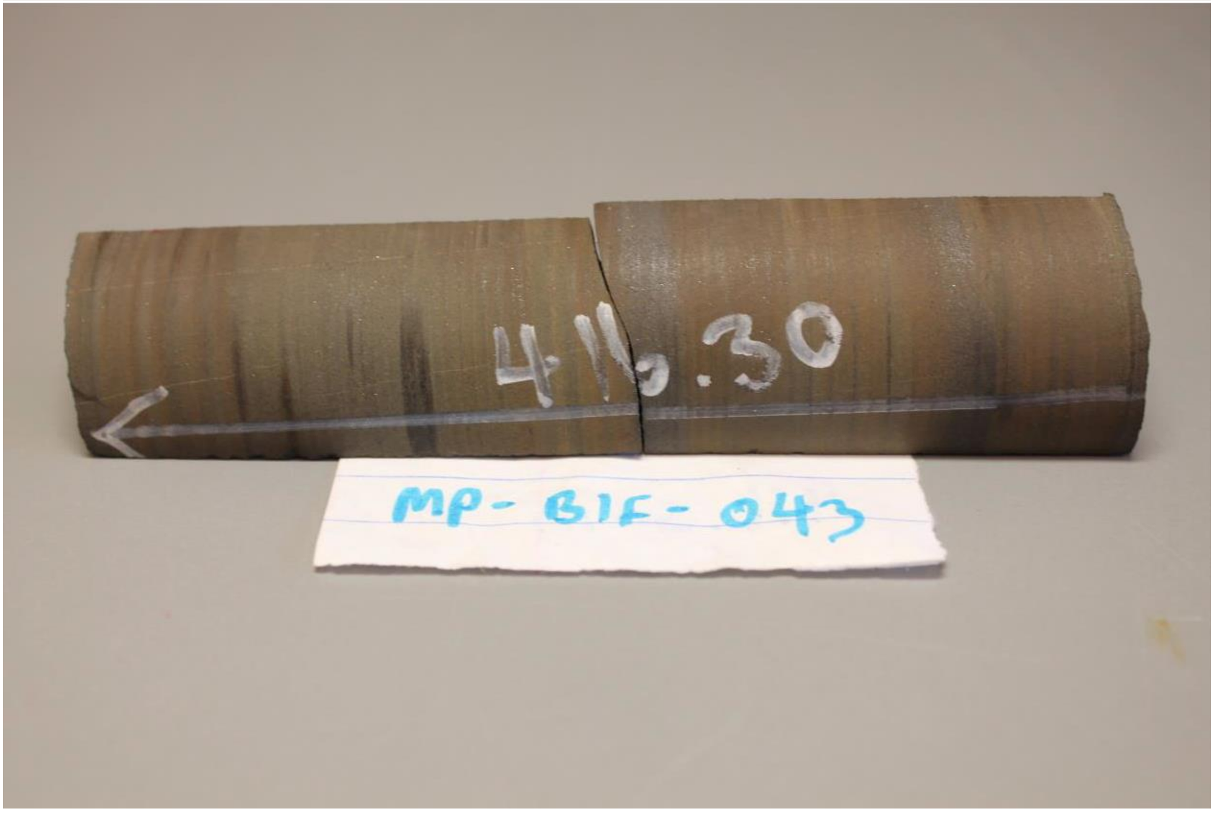
416.30
MP-BIF-043


MP- BIF- 044


416.82
MP- BIF- 044


MP - BIF - 045

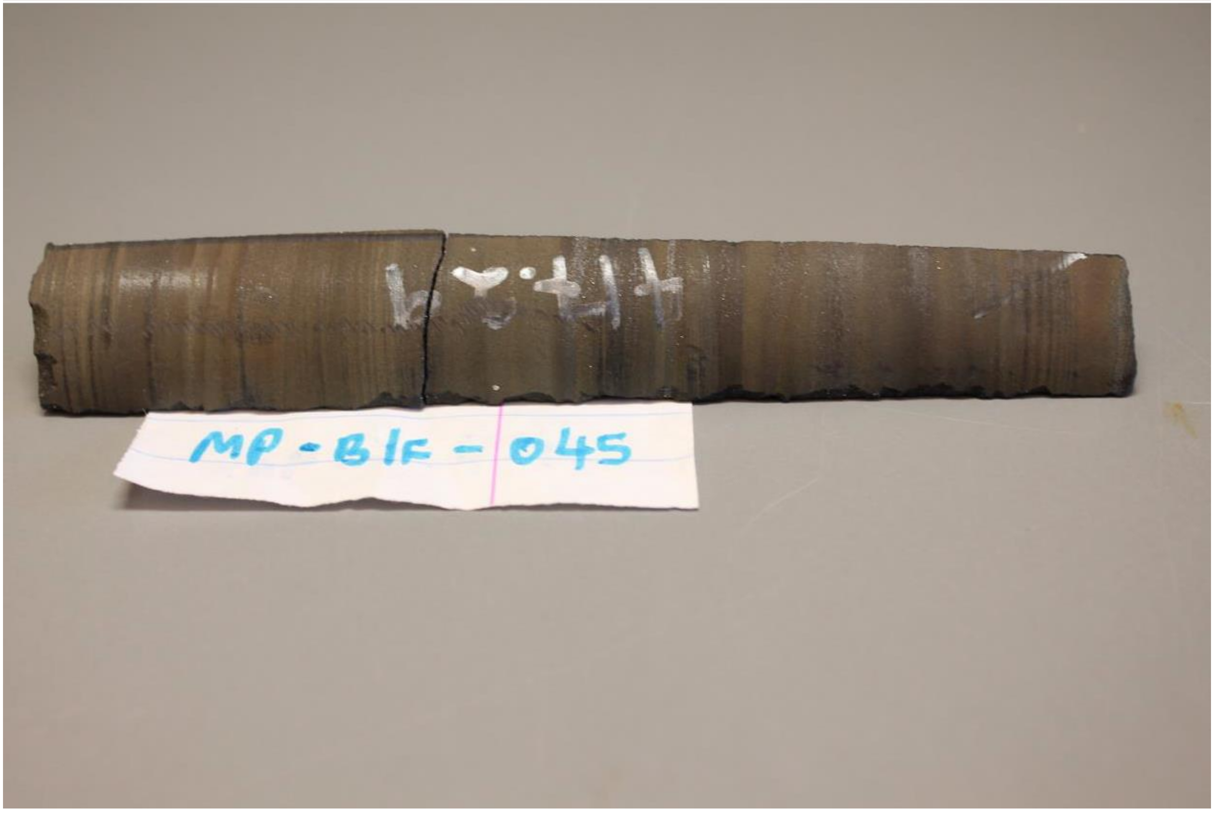
MP - BIF - 045


MP-BIF-046

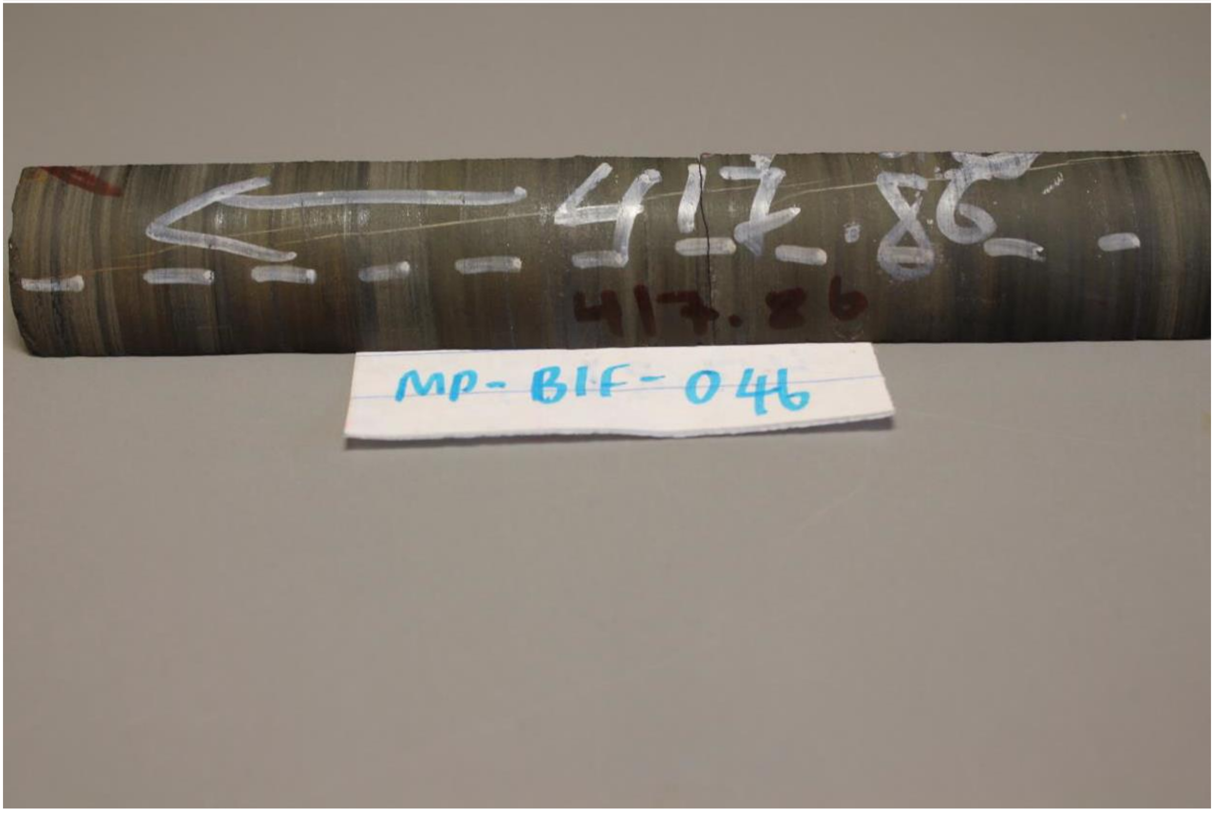
417.86
417.86
MP-BIF-046


MP-BIF - 047


49.43
MP-BIF - 047

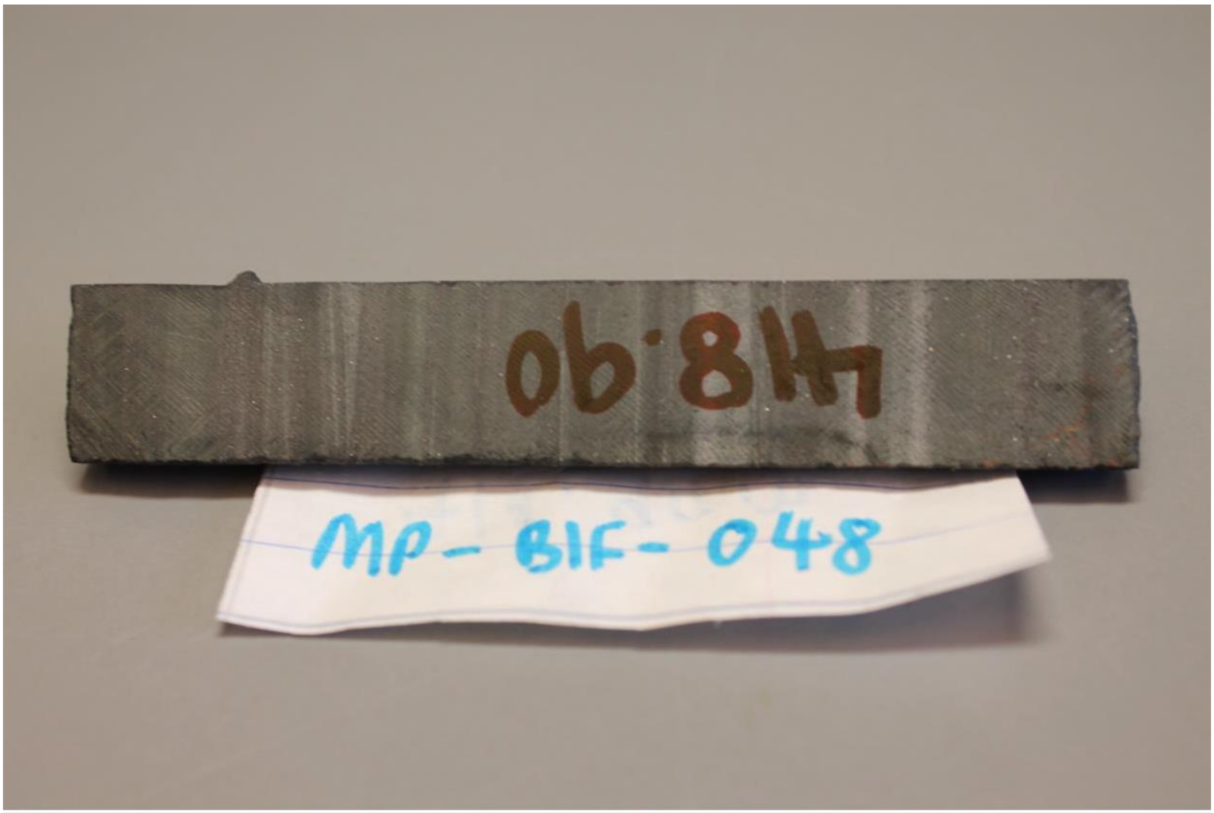
418.90
MP- BIF- 048


418.90
MP- BIF- 048

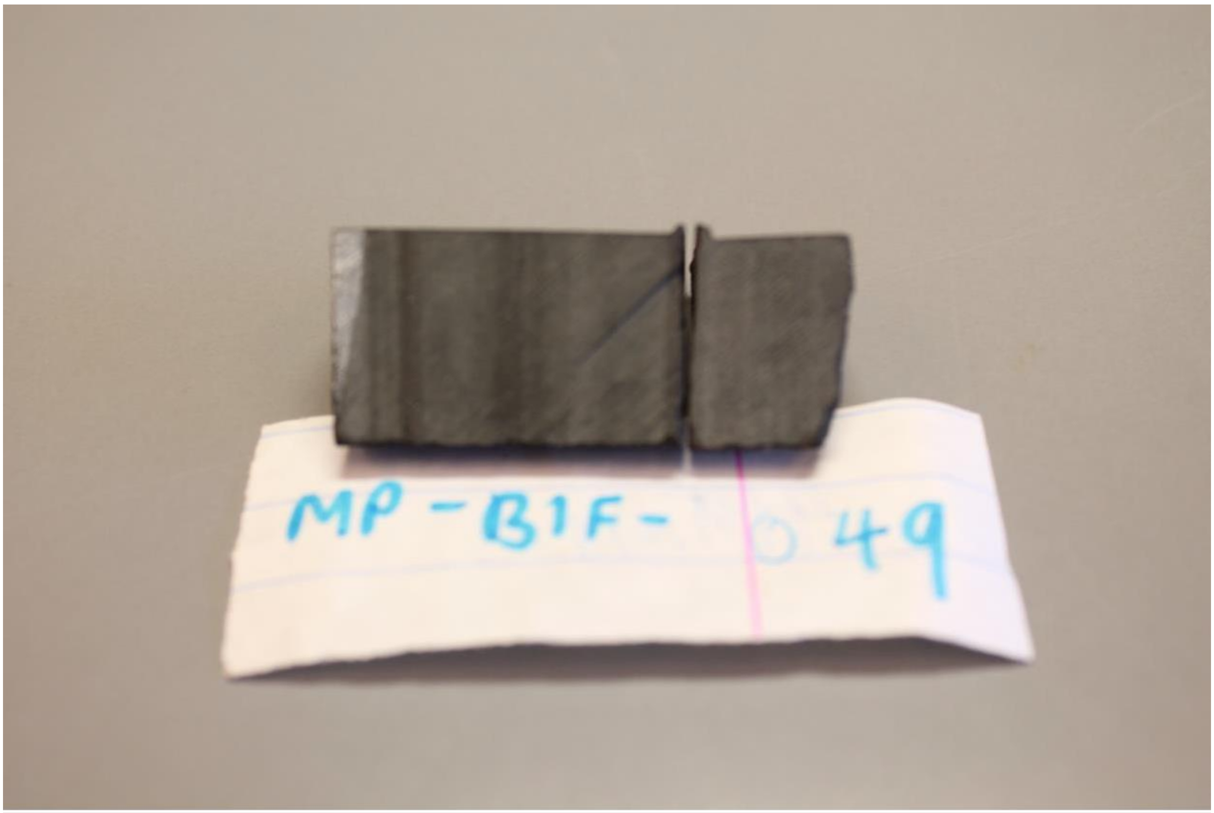
MP-BIF-049

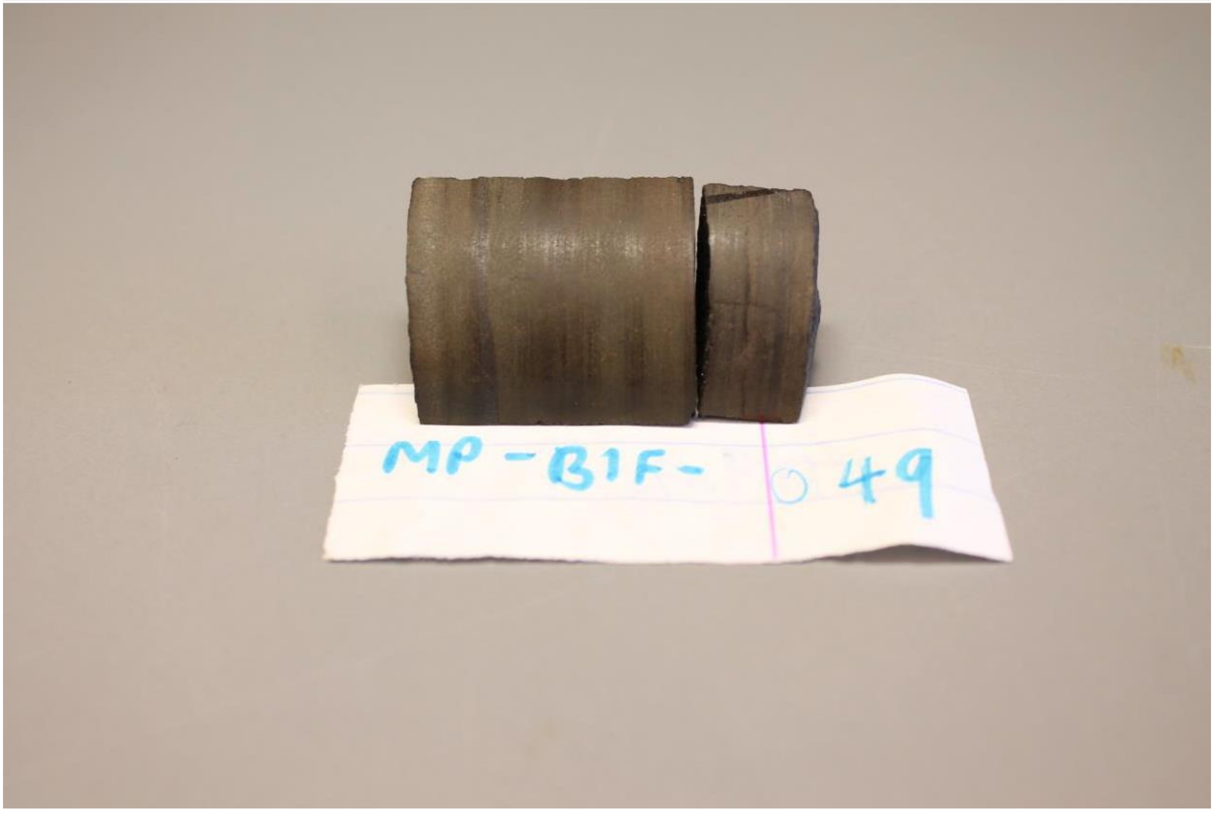
MP-BIF-049


MP-BIF-050


419.85
MP-BIF-050


420.30
MP-BIF-051


420.30
420.30
MP-BIF-051

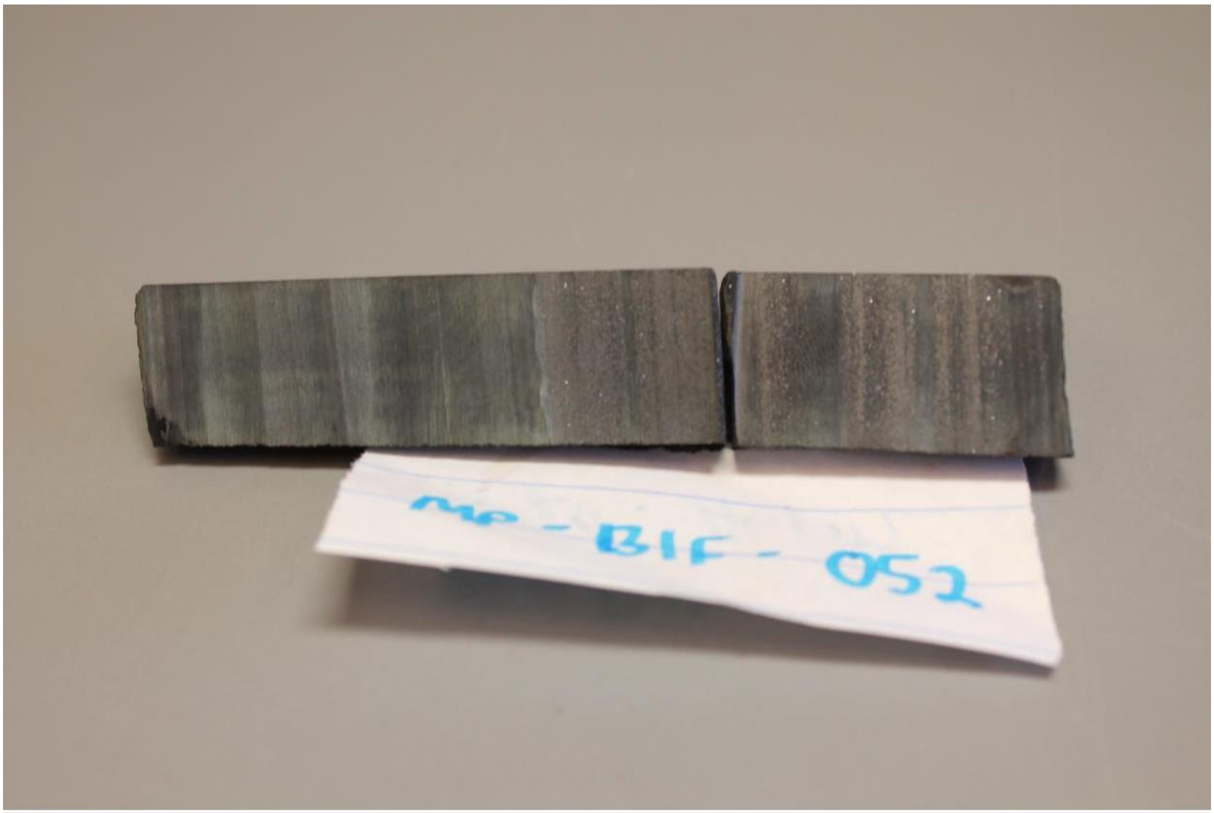
MP - BIF - 052


MP - BIF - 052

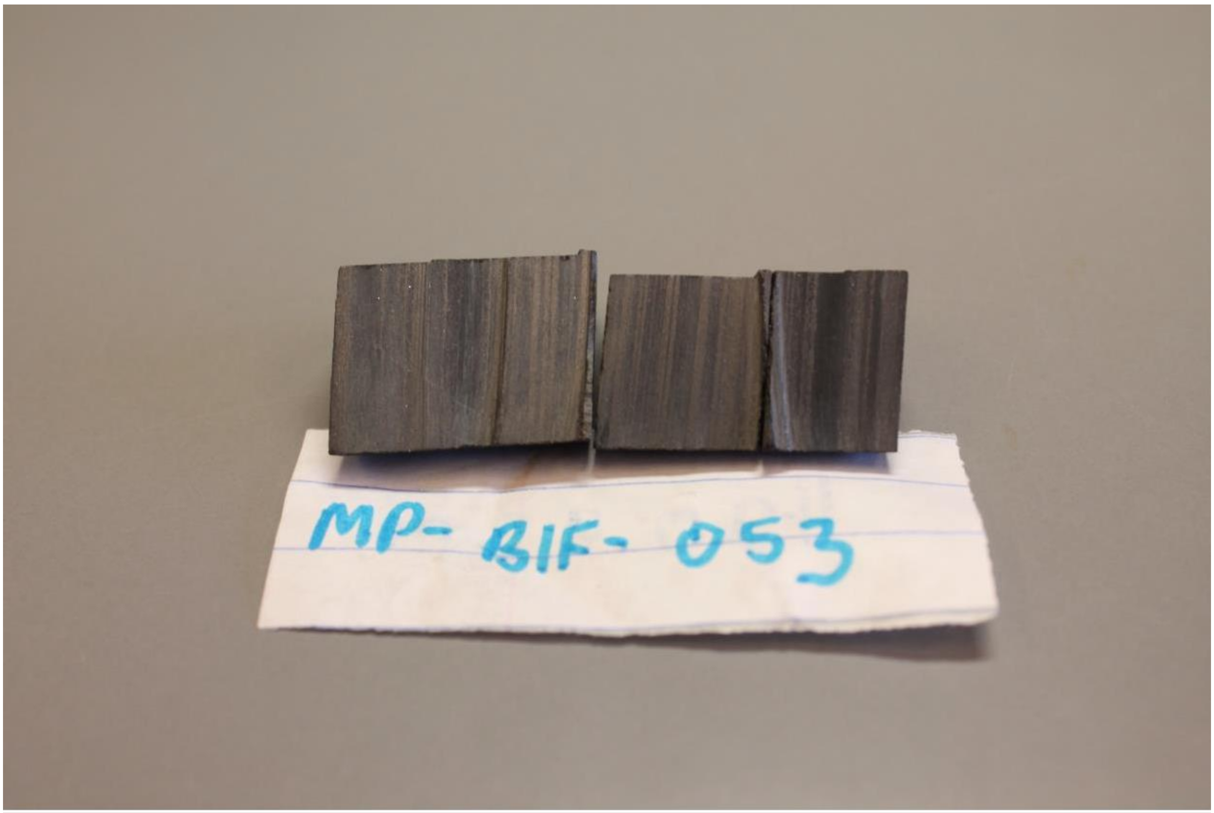
MP- BIF- 053

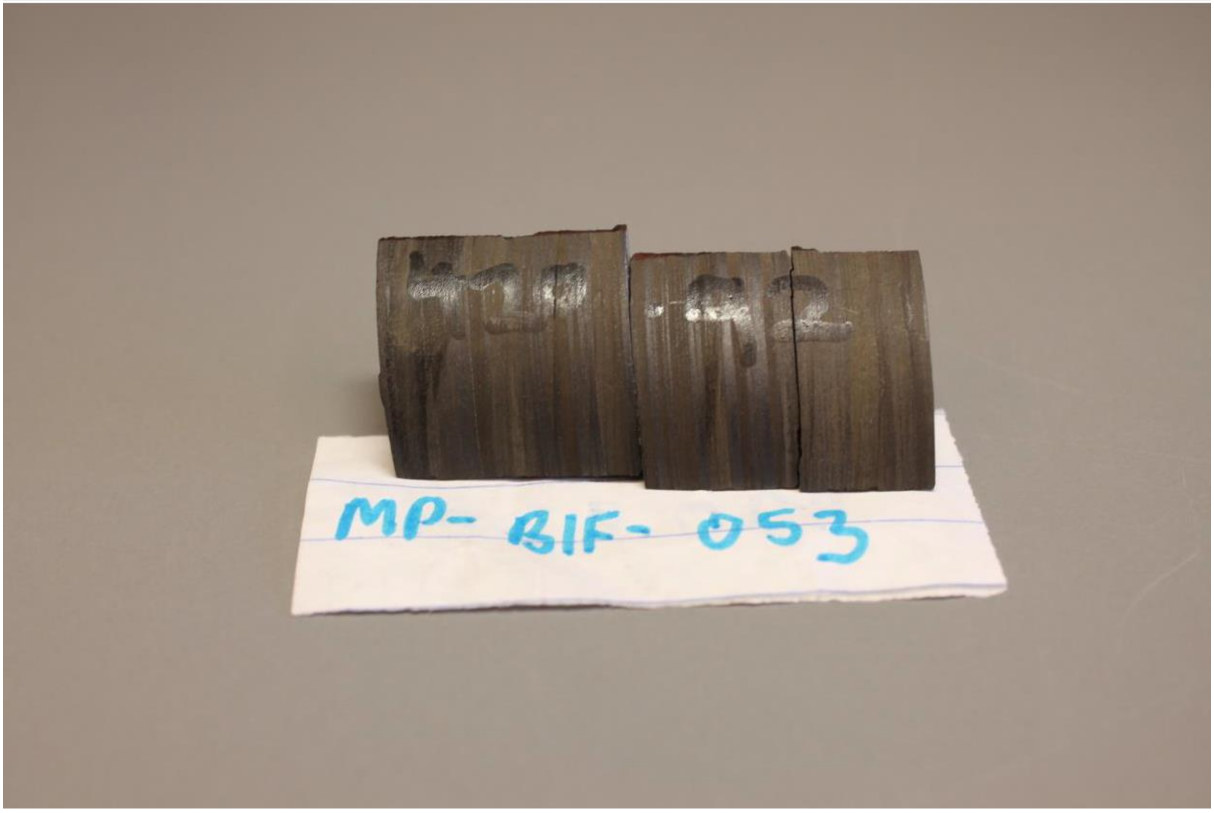
MP- BIF- 053

2. XRF: Major Element Oxides

Table 1: Overview of the XRF measurements containing the major element oxides, LOI and the total weight in wt% for all selected samples

Oxide/Element	**Al2O3**	**CaO**	**Fe2O3**	**K2O**	**MgO**	**MnO**	**Na2O**	**P2O5**	**SiO2**	**TiO2**	**LOI**	**TOTAL**
Sample code	%	%	%	%	%	%	%	%	%	%	%	%
G7BF-01	0,04	2,62	30,32	0,00	0,80	0,37	0,00	0,07	61,59	0,00	3,012	98,81
G7BF-02	0,08	3,67	28,56	0,04	2,36	0,65	0,00	0,11	58,93	0,00	5,364	99,76
G7BF-03	0,03	3,63	41,89	0,04	2,31	0,62	0,00	0,24	46,67	0,00	4,471	99,89
G7BF-04	0,01	2,12	39,26	0,05	4,56	0,46	0,00	0,04	49,06	0,00	3,521	99,09
G7BF-05	0,04	1,91	41,32	0,05	3,11	0,43	0,00	0,05	50,41	0,00	2,472	99,79
G7BF-06	0,04	2,11	39,80	0,05	3,12	0,37	0,00	0,09	50,66	0,00	2,697	98,93
G7BF-07	0,05	8,58	40,64	0,03	2,04	0,65	0,00	0,12	38,58	0,00	8,497	99,18
G7BF-08	0,04	3,50	45,33	0,01	0,92	0,26	0,00	0,14	46,06	0,00	2,902	99,16
G7BF-09	0,13	7,05	38,88	0,01	1,94	0,54	0,00	0,16	42,39	0,00	7,464	98,56
G7BF-10	0,27	2,88	49,38	0,01	2,66	1,36	0,00	0,09	35,67	0,00	8,397	100,72
G7BF-11	0,16	9,19	28,70	0,04	1,87	0,40	0,00	0,06	49,92	0,00	8,668	99,02
G7BF-12	0,26	3,22	40,82	0,07	3,25	0,25	0,00	0,03	47,70	0,00	4,424	100,02
G7BF-13	0,27	2,51	34,71	0,04	2,37	0,26	0,00	0,06	55,76	0,00	3,893	99,87
G7BF-14	0,88	3,80	41,14	0,03	4,07	0,42	0,00	0,05	40,03	0,03	8,375	98,83
G7BF-15	0,23	1,91	31,42	0,05	3,04	0,78	0,00	0,05	56,16	0,00	6,325	99,96
G7BF-16	0,34	1,69	44,95	0,03	3,37	0,63	0,00	0,09	42,86	0,00	5,394	99,36
G7BF-17	0,59	1,12	59,38	0,02	3,58	0,60	0,00	0,01	30,04	0,00	5,178	100,51
G7BF-18	0,46	2,50	40,48	0,03	3,12	0,85	0,00	0,05	45,55	0,01	7,35	100,40
G7BF-19	0,75	1,82	49,30	0,01	2,98	0,65	0,00	0,24	37,74	0,02	5,823	99,32
G7BF-20	0,37	5,12	33,61	0,05	3,66	0,48	0,00	0,15	49,41	0,00	6,833	99,69
G7BF-21	0,96	13,68	31,58	0,03	3,36	1,35	0,00	0,08	32,60	0,03	15,026	98,70
G7BF-22	0,35	4,75	25,13	0,01	3,18	1,23	0,00	0,06	56,87	0,00	8,286	99,86
G7BF-23	0,39	8,49	57,85	0,00	3,18	4,07	0,00	0,04	18,28	0,01	10,308	102,62
G7BF-24	0,31	31,92	18,58	0,00	4,40	6,27	0,00	0,05	10,73	0,01	28,638	100,89
MP-BIF-01	0,04	10,50	15,48	0,01	0,46	1,57	0,02	0,10	61,24	0,00	10,198	99,61
MP-BIF-02	0,03	7,95	41,81	0,01	1,36	1,00	0,00	0,13	39,89	0,00	8,488	100,66
MP-BIF-03	0,05	6,34	42,51	0,02	2,80	1,35	0,00	0,07	38,97	0,00	8,782	100,89
MP-BIF-04	0,08	5,96	40,21	0,03	2,83	1,16	0,00	0,08	41,49	0,00	8,183	100,02
MP-BIF-05	0,05	4,53	44,75	0,02	1,93	0,90	0,07	0,13	40,96	0,00	5,773	99,11
MP-BIF-06	0,13	6,04	41,77	0,02	2,29	1,23	0,00	0,05	39,97	0,00	8,504	100,00
MP-BIF-07	0,04	3,28	43,54	0,03	1,89	0,78	0,00	0,11	46,38	0,00	4,506	100,56
MP-BIF-08	0,02	3,76	47,95	0,01	1,56	0,81	0,00	0,10	40,17	0,00	4,58	98,96
MP-BIF-09	0,01	1,83	49,16	0,03	3,38	0,57	0,00	0,18	42,20	0,00	2,56	99,91
MP-BIF-10	0,01	6,53	45,06	0,02	2,22	1,25	0,00	0,11	36,48	0,00	8,038	99,72
MP-BIF-11	0,02	8,61	47,30	0,02	1,90	1,39	0,00	0,10	30,39	0,00	9,93	99,65
MP-BIF-12	0,00	3,49	44,10	0,03	3,50	0,78	0,00	0,19	42,46	0,00	4,55	99,10
MP-BIF-13	0,03	2,35	48,76	0,03	2,37	0,62	0,00	0,18	42,83	0,00	2,669	99,83
MP-BIF-14	0,02	2,05	53,38	0,02	1,40	0,50	0,00	0,16	40,29	0,00	1,688	99,51
MP-BIF-15	0,01	3,08	46,12	0,03	2,76	0,71	0,00	0,28	42,54	0,00	3,666	99,21
MP-BIF-16	0,38	1,33	43,02	0,01	2,26	0,73	0,00	0,06	44,55	0,01	7,765	100,11
MP-BIF-17	0,01	2,50	47,91	0,03	3,23	0,78	0,00	0,18	41,75	0,00	3,676	100,06
MP-BIF-18	0,02	4,91	44,50	0,03	2,96	1,05	0,00	0,11	40,44	0,00	6,417	100,43

MP-BIF-19	0,03	4,71	43,00	0,03	2,91	1,42	0,00	0,10	39,87	0,00	7,503	99,57
MP-BIF-20	0,00	2,06	61,16	0,02	1,59	0,73	0,00	0,31	31,92	0,00	2,168	99,97
MP-BIF-21	0,03	3,03	50,20	0,02	2,10	1,00	0,00	0,21	39,14	0,00	4,371	100,11
MP-BIF-22	0,00	3,21	54,65	0,01	1,64	1,08	0,00	0,23	33,90	0,00	4,494	99,20
MP-BIF-23	0,02	1,38	51,91	0,03	3,53	0,64	0,00	0,30	40,20	0,00	2,244	100,24
MP-BIF-24	0,25	3,06	53,75	0,01	2,82	1,27	0,00	0,18	33,74	0,00	5,313	100,38
MP-BIF-25	0,01	2,44	55,56	0,01	1,52	0,86	0,00	0,42	35,64	0,00	3,513	99,98
MP-BIF-26	0,03	3,27	48,54	0,06	2,39	1,15	0,44	0,17	37,98	0,00	5,346	99,39
MP-BIF-27	0,04	0,76	49,87	0,04	3,87	0,50	0,00	0,22	43,10	0,00	1,88	100,27
MP-BIF-28	0,02	3,03	47,28	0,03	2,41	1,11	0,00	0,09	37,58	0,00	8,691	100,25
MP-BIF-29	0,08	3,29	43,23	0,03	2,66	1,18	0,00	0,09	43,02	0,00	5,918	99,51
MP-BIF-30	0,07	4,84	43,38	0,02	2,94	1,47	0,00	0,02	39,21	0,00	8,401	100,35
MP-BIF-31	0,09	6,88	37,41	0,02	3,36	2,05	0,00	0,03	39,11	0,00	11,653	100,59
MP-BIF-32	0,09	1,98	45,36	0,03	3,12	0,91	0,00	0,04	42,74	0,00	5,953	100,23
MP-BIF-33	0,08	1,10	48,05	0,03	2,41	0,60	0,00	0,18	44,12	0,00	2,515	99,08
MP-BIF-34	0,10	2,93	43,85	0,04	3,19	1,11	0,00	0,10	42,88	0,00	6,292	100,49
MP-BIF-35	0,07	5,38	45,85	0,01	2,59	1,69	0,00	0,05	35,03	0,00	9,805	100,48
MP-BIF-36	0,08	3,55	43,36	0,03	2,66	1,15	0,00	0,05	41,99	0,00	6,533	99,40
MP-BIF-37	0,03	6,84	44,45	0,03	3,52	1,07	0,00	0,15	39,07	0,00	4,899	100,06
MP-BIF-38	0,06	3,29	48,84	0,01	1,89	1,03	0,00	0,10	38,92	0,00	5,922	100,07
MP-BIF-39	0,11	1,72	45,05	0,03	2,54	0,69	0,00	0,29	45,92	0,00	3,668	100,03
MP-BIF-40	0,21	2,87	42,91	0,02	2,11	1,03	0,00	0,10	43,92	0,00	6,381	99,55
MP-BIF-41	0,11	2,97	47,42	0,01	2,02	0,79	0,00	0,15	41,58	0,00	4,919	99,96
MP-BIF-42	0,21	3,38	38,46	0,01	2,33	1,02	0,00	0,13	47,69	0,00	6,793	100,03
MP-BIF-43	0,25	6,11	38,23	0,01	2,57	1,35	0,00	0,05	41,23	0,00	9,68	99,48
MP-BIF-44	0,64	6,07	38,61	0,02	4,30	2,03	0,00	0,16	35,08	0,01	13,896	100,81
MP-BIF-45	0,25	3,60	37,79	0,02	2,53	1,08	0,00	0,07	47,76	0,00	7,001	100,11
MP-BIF-46	0,04	5,94	53,30	0,01	2,49	1,69	0,00	0,21	31,80	0,00	4,782	100,27
MP-BIF-47	0,23	1,93	52,19	0,01	1,97	0,76	0,00	0,06	37,53	0,00	4,38	99,05
MP-BIF-48	0,29	0,49	34,96	0,01	2,70	0,92	0,00	0,01	53,77	0,00	7,233	100,37
MP-BIF-49	0,05	3,96	48,80	0,01	1,92	1,15	0,00	0,21	39,56	0,00	4,575	100,23
MP-BIF-50	0,24	1,62	39,14	0,01	2,76	0,99	0,00	0,12	50,14	0,00	4,426	99,45
MP-BIF-51	0,27	0,27	40,90	0,01	2,38	0,56	0,00	0,01	53,96	0,00	2,111	100,47
MP-BIF-52	0,35	6,04	46,50	0,01	3,02	0,68	0,00	0,11	37,30	0,01	5,479	99,50
MP-BIF-53	0,10	3,64	64,84	0,00	2,92	1,19	0,00	0,46	22,51	0,00	3,785	99,44

3. LA-ICP-MS

Table 2: LA-ICP-MS determined trace element abundance (in ppm) for all samples measured in triplex. Values starting with < are below the detection limit. The average standard deviation for the elemental concentration was calculated by applying the STDev in Excel to the three measurements of one sample.

Element/ Sample Nr.	*G7BF-01a-50*	*G7BF-01b-51*	*G7BF-01c-34*	*G7BF-02a-22*	*G7BF-02b-23*	*G7BF-02c-12*	*G7BF-03a-20*	*G7BF-03b-21*	*G7BF-03c-11*
Sc	1,81	2,39	2,08	2,41	2,12	2,92	2,11	1,83	2,11
Ti	21,22	60,13	28,4	46,26	54,68	47,86	17,23	31,96	36,05
V	7,3	7,73	6,54	7,84	6,71	7,61	6,27	6,96	8,32
Cr	24,96	28,09	34,53	31,39	29,43	30,95	34,49	32,04	35,4
Mn	2579,17	2559,77	2613,46	4480,56	4456,28	4623,49	4720,97	4622,46	4589,23
Co			43,9			28,27			22,86
Ni			18,83			15,03			39,71
Cu	4,38	3,43	5,31	9,59	6,42	9,09	12,95	7,25	12,4
Zn	18,33	17,19	28,92	49,28	31,34	33,22	24,02	17,75	24,81
Ga	0,88	1,24	<0,93	2,25	<1,51	<0,78	<2,49	<1,31	<0,42
As	6,24	7,27	5,95	7,16	6,55	5,13	<5,37	6,74	5,27
Rb	0,579	0,77	0,55	3,72	3,39	2,52	4,09	3,67	3,14
Sr	47,56	46,06	46,22	46,7	45,57	42,35	64,68	63,76	58,01
Y	6,78	7,05	6,19	10,5	10,03	8,97	12,2	13	11,15
Zr	2,86	2,78	2,4	4,76	5,36	4,73	3,97	3,72	4,09
Mo			0,174			0,198			0,235
Nb	0,115	0,102	0,42	<0,181	0,339	0,76	0,262	0,215	0,48
Cs	0,171	0,081	0,213	0,693	0,788	0,578	0,69	0,541	3,24
Ba	17,11	19,42	18,19	3,6	13,14	9,9	8,03	10,67	8,72
La	5,38	5,95	5,71	5,47	5,24	4,56	5,53	5,65	4,94
Ce	7,74	8,36	7,72	6,69	<0,73	5,63	5,86	6,19	4,82
Pr	0,75	0,77	0,76	0,513	0,81	0,595	0,628	0,827	0,547
Nd	2,89	2,94	2,56	3,1	2,1	2,19	3,2	3,07	2,12
Sm	0,82	0,57	0,66	0,49	0,71	0,29	0,61	0,55	0,4
Eu	0,09	0,1395	0,0895	0,1705	0,2175	0,1175	0,2005	0,1745	0,1255
Gd	0,43	0,33	0,6	<1,29	<1,06	0,67	<1,51	0,86	0,52
Tb	0,063	0,037	0,09	0,16	0,097	0,056	0,138	0,094	0,1
Dy	0,54	0,27	0,34	0,7	0,89	0,55	0,77	1,13	0,57
Ho	0,126	0,128	0,08	0,18	0,114	0,11	0,3	0,242	0,154
Er	0,31	0,44	0,53	0,56	0,48	0,4	<0,58	0,6	0,44
Yb	0,45	0,5	0,5	1,13	0,87	0,37	0,74	0,62	0,72
Lu	0,06	0,044	0,05	<0,079	0,11	0,106	0,15	0,182	0,133
Hf	0,037	<0,046	0,078	<0,158	<0,149	0,08	<0,232	0,124	0,072
Ta	0,91	0,7	0,76	3	2,89	2,45	2,9	2,65	2,15
Pb	0,81	1,28	0,75	1,08	0,68	0,72	1,28	1,23	0,95
Th	0,1	0,139	0,127	0,305	0,306	0,201	0,155	0,236	0,138
U	1,82	1,51	1,9	0,078	0,096	0,089	<3,71	0,068	0,078

Element/ Sample Nr.	*G7BF-04a-52*	*G7BF-04b-53*	*G7BF-04c-35*	*G7BF-05a-35*	*G7BF-05b-36*	*G7BF-05c-20*	*G7BF-06a-54*	*G7BF-06b-55*	*G7BF-06c-36*
Sc	1,57	1,88	1,15	3,43	1,7	2,42	2,28	2,1	2,27
Ti	25,6	21,79	26,78	28,36	31,86	30,49	32,49	30,82	28,21
V	8,39	9,06	7,8	8,73	7,71	8,49	7,33	9,19	7,93
Cr	29,38	28,17	27,44	28,16	25,82	33,22	26,56	25,75	25,86
Mn	3332,47	3351,1	3364,65	3220,01	3144,45	2889,49	2613,41	2669,88	2778,9
Co			42,01			26,36			30,93
Ni			21,65			23,07			19,32
Cu	3,22	3,37	4,61	7,58	6,09	7,97	4,48	5,32	3,01
Zn	30,68	27,76	29,06	37,69	25,91	34,4	16,24	25,13	30,26
Ga	1,37	0,41	1,07	<2,65	1,48	<0,75	0,94	0,81	<1,15
As	6,65	6,12	4,77	6,35	4,66	2,96	5,26	5,34	5,35
Rb	6,21	6,27	7,1	5,55	5,28	4,86	4,34	4,36	3,83
Sr	48,82	48,2	47,41	36,22	35,54	31,72	39,06	39,8	39,38
Y	6,26	6,61	6,45	6,59	6,45	5,6	8,48	8,95	7,91
Zr	3,4	4,39	3,04	3,8	4,13	3,16	8,23	8,76	8,82
Mo			0,091			0,198			0,159
Nb	0,207	0,182	0,39	0,196	0,197	0,373	0,208	0,183	0,53
Cs	0,96	1	0,787	0,912	0,768	0,688	0,868	0,69	0,778
Ba	9,76	7,73	8,98	14,53	10,63	6,96	11,34	10,78	10,88
La	2,57	2,48	2,51	3,28	3,28	2,81	3,63	3,73	3,59
Ce	1,93	2,08	2,15	2,96	2,88	2,53	3,77	3,55	3,33
Pr	0,273	0,209	0,151	0,281	0,275	0,291	0,393	0,478	0,466
Nd	1,25	1,14	1,21	1,58	1,25	1,3	1,8	1,51	1,49
Sm	0,252	0,239	0,179	<0,54	0,176	0,23	0,164	0,306	0,25
Eu	0,093	0,1155	0,083	0,182	0,1125	0,0725	0,071	0,1235	0,179
Gd	<0,28	0,22	<0,38	<1,78	<0,58	0,26	0,33	0,45	1,05
Tb	<0,031	0,052	0,062	<0,119	0,069	0,043	<0,023	0,075	0,064
Dy	0,41	0,146	0,24	<0,80	<0,33	0,43	0,7	0,62	0,54
Ho	0,125	0,126	0,102	0,119	0,115	0,134	0,155	0,115	0,107
Er	0,37	0,23	0,45	0,47	0,288	0,25	0,47	0,47	0,4
Yb	0,46	0,47	0,37	0,51	<0,30	0,35	0,54	0,52	0,36
Lu	0,059	0,071	0,058	<0,117	0,082	0,079	0,103	0,116	0,16
Hf	0,108	<0,028	<0,090	<0,33	0,22	0,065	0,203	0,236	0,28
Ta	0,7	0,97	0,74	3,44	3,16	2,48	0,87	0,93	0,85
Pb	0,79	2,19	0,74	1,48	1,03	0,8	0,8	0,69	0,49
Th	0,111	0,066	0,131	0,134	0,172	0,134	0,183	0,166	0,153
U	0,072	0,074	0,104	0,116	0,074	0,064	0,141	0,094	0,185

Element/ Sample Nr.	*G7BF-07a-26*	*G7BF-07b-27*	*G7BF-07c-14*	*G7BF-08a-24*	*G7BF-08b-25*	*G7BF-08c-13*	*G7BF-09a-37*	*G7BF-09b-38*	*G7BF-09c-29*
Sc	1,75	2,26	2,78	1,76	2,02	2,47	2,68	2,73	2,24
Ti	33,66	37,86	41,19	44,05	46,03	49,23	68,72	63,71	83,93
V	6,78	6,01	7,56	6,68	6,52	8,65	11,62	11,29	9,29
Cr	27,92	20,99	29,58	28	29,39	31,6	30,47	29,57	30,42
Mn	4961,53	4719,42	5101,2	2060,56	2017,94	2083,23	4148,2	3852,81	3955,01
Co			27,94			34,4			53,33
Ni			12,37			11,43			28,64
Cu	2,33	4,56	4,08	3,66	3,36	6,08	6,16	5,72	8,02
Zn	29,31	37,2	28,98	<16,28	29,44	29,32	19,45	16,05	28,62
Ga	<1,52	2,02	1,04	<2,17	<1,32	1,12	1,21	0,8	1,36
As	35,37	28,74	5,71	8,49	5,7	6,59	6,74	5,74	7,03
Rb	2,82	2,95	2,62	1,13	2,23	0,945	1	1	1,31
Sr	188,2	181,19	166	89,25	86,54	77,91	105,85	101,34	103,04
Y	12,01	11,57	10,27	9,13	8,9	8,11	12,4	12,53	12,98
Zr	3,65	4,05	3,71	5,25	4,21	4,13	5,36	4,96	5,2
Mo			0,178			0,23			0,422
Nb	0,284	0,133	0,92	0,213	0,19	0,73	0,285	0,247	0,59
Cs	0,493	0,521	0,486	0,205	0,382	0,443	0,427	0,38	0,364
Ba	24,83	20,89	20,74	22,54	22,25	18,88	18,68	15,97	17,77
La	5,83	6,02	4,76	5,02	4,9	4,31	6,45	6,56	6,6
Ce	6,18	6	5,15	5,5	5,4	4,69	8,09	7,78	8,38
Pr	0,706	0,74	0,575	0,473	0,668	0,574	0,82	0,8	0,96
Nd	3,36	2,59	1,99	2,29	3,37	2,18	3,41	4,17	3,92
Sm	0,39	<0,28	0,31	0,57	0,54	0,41	0,55	0,79	0,76
Eu	0,1685	0,228	0,0995	0,165	0,1405	0,1185	0,1875	0,1555	0,19
Gd	1,22	<0,77	0,71	1,18	<0,92	0,39	1,07	1,11	1,01
Tb	0,11	0,182	0,08	<0,151	<0,104	0,106	0,104	0,11	0,138
Dy	0,57	<0,49	0,46	0,9	1,19	0,57	1,02	0,81	1,12
Ho	0,181	0,201	0,151	<0,161	0,158	0,144	0,224	0,259	0,31
Er	0,77	0,519	0,6	<0,37	0,91	0,63	0,79	0,73	0,6
Yb	0,73	0,71	0,72	0,74	0,39	0,52	0,48	0,95	0,8
Lu	0,12	0,149	0,126	<0,092	0,116	0,122	0,135	0,155	0,191
Hf	<0,185	0,149	0,049	0,182	<0,134	0,053	0,051	0,043	0,102
Ta	2,94	2,79	2,22	3,37	3,9	2,64	0,98	0,92	0,92
Pb	1,4	1,32	0,92	1,67	1,11	0,99	1,05	0,58	1,09
Th	0,173	0,209	0,106	0,246	0,242	0,137	0,361	0,338	0,329
U	0,28	0,421	0,195	0,112	0,073	0,046	0,121	0,105	0,124

Element/ Sample Nr.	*G7BF-10a-52*	*G7BF-10b-53*	*G7BF-10c-47*	*G7BF-11a-39*	*G7BF-11b-40*	*G7BF-11c-30*	*G7BF-12a-33*	*G7BF-12b-34*	*G7BF-12c-19*
Sc	3,68	3,9	3,49	3,16	3,1	3,13	4,34	4,13	4,3
Ti	122,04	128,85	126,46	67,48	80,83	86,42	130,13	129,75	134,26
V	10,57	12,51	11,76	10,73	10,86	8,04	12,32	13,94	13,2
Cr	34,5	33,98	37,42	24,61	31,41	26,35	35,13	32,87	34,53
Mn	9865,64	9991,68	10829,48	2798,63	2776,41	2788,45	1859,02	1885,27	1853,44
Co			22,6			29,28			30
Ni			14,15			16,03			22,46
Cu	4,55	5,36	5,57	5,84	5,05	6,87	3,89	5,02	4,96
Zn	24,69	20,17	27,62	21,36	18,75	18,87	33,01	33,58	35,24
Ga	1,03	1,48	<0,46	1,05	0,8	1,14	<0,98	1,59	1,36
As	10,72	11,22	9,8	5,84	4,69	3,04	5,26	6,18	5,13
Rb	1	1,34	1,03	1,78	2,19	2,46	1,41	4,88	4,55
Sr	13,64	14,89	13,73	121,85	122,69	119,56	33,77	33,54	29,84
Y	18,56	19,58	16,69	8,85	8,77	9	8,37	8,33	6,74
Zr	9,62	10,04	13,02	5,27	4,94	5,05	7,88	8,09	7,67
Mo			0,506			0,19			0,52
Nb	0,672	0,59	0,94	0,252	0,317	0,52	0,646	0,61	0,79
Cs	0,503	0,59	0,516	0,583	0,582	0,447	1,23	1,35	1,2
Ba	8,78	10,48	10,09	17	17,01	18,02	10,43	9,95	9,21
La	11,13	11,93	10,45	6,27	5,96	6,15	6,95	7,97	6,34
Ce	16,27	17,6	16,44	7,75	7,93	8,04	9,65	9,39	8,89
Pr	2	2	1,72	0,91	0,85	0,82	1	1,37	0,89
Nd	7,25	7,5	7,89	3,64	3,46	4	4,29	4,22	3,72
Sm	1,27	1,21	1,1	0,51	0,58	0,61	1,05	1,13	0,76
Eu	0,3625	0,3285	0,2245	0,1175	0,1745	0,209	0,2495	0,1675	0,165
Gd	1,44	1,66	1,11	0,63	0,8	0,75	<0,59	1,05	0,65
Tb	0,244	0,253	0,26	0,117	0,092	0,095	0,13	0,104	0,076
Dy	1,76	1,76	1,54	0,75	0,96	0,91	0,74	0,75	0,75
Ho	0,464	0,48	0,45	0,193	0,183	0,122	0,164	0,261	0,148
Er	1,29	1,49	1,57	0,57	0,51	0,59	0,61	0,84	0,61
Yb	1,98	2,34	1,84	0,67	0,69	0,64	0,7	0,59	0,61
Lu	0,319	0,324	0,287	0,091	0,131	0,077	0,151	0,12	0,112
Hf	0,145	0,185	0,138	0,141	0,048	0,084	0,145	0,186	0,045
Ta	2,14	2,23	1,85	0,81	0,76	0,79	3,02	3,17	2,17
Pb	2,15	2,29	2,39	0,89	0,72	0,67	2,06	2,25	13,51
Th	0,825	0,918	0,96	0,369	0,378	0,399	0,623	0,665	0,61
U	0,094	14,63	0,171	0,088	0,092	0,157	0,214	0,17	0,15

Element/ Sample Nr.	*G7BF-13a-37*	*G7BF-13b-38*	*G7BF-13c-21*	*G7BF-14a-45*	*G7BF-14b-46*	*G7BF-14c-33*	*G7BF-15a-5*	*G7BF-15b-6*	*G7BF-15c-24*
Sc	3,69	4,69	4,34	5,59	6,7	5,37	3,13	3,71	2,71
Ti	116,17	131,44	128,08	352,38	363,98	374,62	118,15	117,47	111,45
V	12,13	13,02	12,6	19,61	20,82	18,79	10,76	11,48	11,11
Cr	31,76	34,99	38,42	37,76	48,06	40,67	26,39	24,94	26,98
Mn	1893,68	1973,49	1912,45	3163,1	3176,03	3115,82	5614,98	5441,11	5720,18
Co			31,16			24,17			17,58
Ni			42,28			29,06			18,77
Cu	4,23	3,06	4,84	5,19	7,15	9,04	9,2	8,13	5,74
Zn	22,47	31,19	25,97	20,13	36,97	27,56	29,36	21,37	24,24
Ga	1,73	2,17	1,24	1,91	1,49	1,77	1,32	0,95	0,82
As	5,11	<2,78	2,84	7,87	10,81	8,74	3,02	3,27	2,54
Rb	3,02	3,22	1,82	2,26	2,36	2,11	2,96	3,04	2,83
Sr	30,12	18,68	26,1	40,88	42,31	40,5	17,42	17,86	17,09
Y	8,84	8,85	8,03	12,88	13,61	11,92	7,49	7,6	6,7
Zr	9,32	9,28	7,88	21,76	23,4	21,41	6,76	7,19	6,05
Mo			0,583			1,53			0,495
Nb	0,572	<0,26	0,46	1,48	1,44	0,71	0,565	0,556	0,62
Cs	0,933	1,04	0,688	1,25	0,77	1,37	0,935	1	0,848
Ba	11,8	9,78	9,66	13,11	14,46	13,74	9	10,95	8,26
La	6,07	6,3	5,41	7,69	7,88	8,04	4,04	4,24	3,69
Ce	8,46	8,48	7,57	12,73	12,94	13,34	5,57	5,89	5,3
Pr	0,881	1,08	0,95	1,46	1,5	1,47	0,683	0,697	0,63
Nd	4,95	4,92	3,89	6,13	6,71	7,09	3,06	3,26	2,53
Sm	0,71	0,86	0,7	1,61	1,41	1,28	0,668	0,773	0,53
Eu	0,124	0,2025	0,1485	0,288	0,1685	0,2075	0,1615	0,1665	0,1535
Gd	0,65	<1,14	1,06	1,58	1,3	1,42	0,516	0,55	0,71
Tb	0,158	0,183	0,094	0,201	0,165	0,179	0,147	0,095	0,131
Dy	1,21	1,03	1,07	1,45	1,71	1,43	0,98	0,9	0,79
Ho	0,275	0,308	0,225	0,42	0,37	0,33	0,235	0,205	0,165
Er	0,53	0,74	0,54	1,13	1,42	1,04	0,67	0,76	0,68
Yb	1,13	0,61	0,77	1,15	0,68	0,95	0,58	0,66	0,69
Lu	0,183	0,128	0,067	0,179	0,252	0,142	0,122	0,122	0,121
Hf	0,246	0,147	0,083	0,296	0,47	0,57	0,148	0,151	0,09
Ta	3,8	4,28	2,99	0,79	0,92	0,77	2,67	2,75	2,42
Pb	1,86	2,08	1,52	2,2	2,68	2,95	1,55	1,32	1,26
Th	0,715	0,81	0,49	1,2	1,37	1,24	0,655	0,679	0,63
U	0,264	0,189	0,153	0,31	0,283	2,38	0,222	0,232	0,233

Element/ Sample Nr.	*G7BF-16a-24*	*G7BF-16b-25*	*G7BF-16c-24*	*G7BF-17a-31*	*G7BF-17b-32*	*G7BF-17c-18*	*G7BF-18a-9*	*G7BF-18b-10*	*G7BF-18c-26*
Sc	3,67	3,97	3,22	3,85	3,76	4,7	5,79	5,83	5,17
Ti	132,1	140,37	135,6	152,8	149,96	129,21	192,46	201,71	213,22
V	15,25	15,47	12,98	12,95	12,23	13,34	14,87	16,14	14,79
Cr	42,7	48,16	44,35	31,48	32,16	36,07	37,92	38,42	39,98
Mn	4789,71	5000,9	4765,36	5205,84	5141,33	5034,96	5939,75	6007,77	6207,84
Co			25,73			29,29			31,99
Ni			20,99			22,64			20,52
Cu	6,99	8,2	8,76	4,68	3,89	4,94	7,31	8,19	7,54
Zn	26,03	31,47	24,06	24,53	28,75	32,39	25,05	14,24	31,7
Ga	0,87	1,02	1,15	1,91	1,36	1,65	1,58	1,29	1,1
As	5,45	5,29	5,39	7,87	6,27	5,2	5,41	8,28	5,05
Rb	2,46	3,01	2,55	2,34	2,6	2,28	2,46	2,38	2,14
Sr	18,1	18,17	17,75	14,41	14,86	13,17	32,12	31,99	29,1
Y	11,32	13,09	12,09	9,35	9,37	7,53	9,52	9,9	8,49
Zr	7,07	8,64	8,31	17,15	16,67	14,62	14,56	14,82	12,89
Mo			0,722			1,75			1,09
Nb	0,744	0,883	0,79	1,76	1,85	0,72	1	1	0,87
Cs	0,947	1,06	1	1	1,18	0,891	0,971	0,888	0,803
Ba	13,63	10,54	11,98	17,79	17,18	15,38	12,54	16,27	14,89
La	4,78	5,18	5,05	3,29	3,34	2,98	4,34	4,36	4,02
Ce	7,88	7,64	7,98	4,29	4,61	3,88	6,34	6,72	5,71
Pr	0,92	0,95	0,98	0,546	0,63	0,493	0,791	0,827	0,77
Nd	3,81	4,27	3,98	1,97	1,81	1,82	3,49	3,45	3,15
Sm	0,94	1,06	0,88	0,42	0,62	0,58	0,603	0,86	0,72
Eu	0,181	0,2175	0,2385	0,133	0,0745	0,1475	0,215	0,273	0,1465
Gd	0,9	1,52	1,11	1,1	<0,49	0,65	0,78	1,14	0,82
Tb	0,168	0,188	0,183	0,151	0,196	0,051	0,143	0,125	0,146
Dy	1,26	1,29	0,93	1,09	1,19	0,91	1,16	1,25	1,08
Ho	0,278	0,306	0,283	0,223	0,22	0,208	0,294	0,258	0,208
Er	0,77	1,14	0,82	1,13	0,89	0,49	0,87	0,97	1,02
Yb	0,97	0,87	0,89	1,27	1,58	1,18	1,29	1,04	0,87
Lu	0,171	0,196	0,225	0,24	0,227	0,193	0,176	0,217	0,19
Hf	0,137	0,122	0,101	0,413	0,446	0,341	0,219	0,193	0,304
Ta	0,71	0,74	0,67	3,41	3,99	2,53	2,43	2,65	1,93
Pb	1,33	1,14	1,25	1,52	2,23	1,74	2,42	2,12	1,66
Th	0,487	0,6	0,536	1,6	1,69	1,38	1	1,59	1,23
U	0,305	0,481	0,165	0,419	0,459	0,334	0,343	0,39	0,303

Element/ Sample Nr.	G7BF-19a-41	G7BF-19b-42	G7BF-19c-31	G7BF-20a-18	G7BF-20b-19	G7BF-20c-10	G7BF-21a-11	G7BF-21b-12	G7BF-21c-27
Sc	6,06	6,12	6,42	3,64	3,65	4,39	7,25	7,14	6,14
Ti	282,5	280,2	300,82	151,98	133,93	141,19	394,51	400,39	386,88
V	22,28	21,63	20,77	11,8	11,65	12,09	22,04	21,57	21,2
Cr	47,98	41,76	48,88	45,57	33,05	37,66	47,57	53,07	50,99
Mn	5094,43	4865,88	5065,19	3841,27	3655,26	3629,02	9601,13	9233,46	9830,43
Co			22,4			23,76			33
Ni			20,39			20,31			36,19
Cu	5,76	7,08	7,9	7,94	4,3	6,07	16,36	17,34	16,79
Zn	23,16	24,29	27,17	21,74	26,35	27,02	32,75	30,86	31,17
Ga	1,47	1,43	2,06	1,18	<1,78	1,44	4,07	3,66	2,83
As	6,42	5,84	6,63	6,79	4,06	5,21	12,26	12,76	11,56
Rb	1,38	1	1,41	3,83	3,88	3,78	2,36	2,41	2,15
Sr	36,69	33,21	35,54	87,15	90,01	81,41	312,3	307,22	286,25
Y	14,95	13,58	13,71	16,09	15,25	13,8	14,14	13,99	11,53
Zr	14,9	13,54	14,58	7,58	7,66	6,65	16,45	15,98	14,74
Mo			1,36			0,789			1,71
Nb	1,33	1,37	1,54	0,663	0,795	0,66	2	2	0,83
Cs	1,08	0,941	0,985	1,45	1,4	1,24	1	1	1,13
Ba	13,74	14,84	15,08	14,25	15,4	13,55	56,4	56,06	46,56
La	10,94	10,22	10,52	10,34	10,9	9,96	10,47	10	9
Ce	17,92	17,02	17,99	17,49	17,69	15,14	16,11	15,67	14,33
Pr	2,2	2,1	2,11	1,9	2,07	1,77	2	2	1,74
Nd	9,89	8,47	8,41	8,32	8,63	7,75	7,87	7,68	6,79
Sm	1,75	1,52	2,25	1,86	1,61	1,31	1,25	1,43	1,38
Eu	0,346	0,3385	0,4375	0,3185	0,333	0,3515	0,393	0,316	0,264
Gd	2,01	1,78	1,98	2,39	2,5	1,72	1,54	1,92	1,11
Tb	0,293	0,222	0,308	0,243	0,205	0,19	0,225	0,228	0,263
Dy	1,96	1,48	1,99	1,35	1,47	1,63	1,65	1,79	1,07
Ho	0,49	0,37	0,45	0,433	0,407	0,287	0,35	0,369	0,26
Er	1,15	0,97	0,99	1,39	1,68	1,09	1,39	1,48	1,28
Yb	1,36	1,34	1,01	0,83	0,98	0,83	0,93	1,22	0,93
Lu	0,259	0,168	0,27	0,215	0,184	0,129	0,18	0,218	0,197
Hf	0,332	0,206	0,319	<0,170	0,248	0,167	0,405	0,413	0,317
Ta	0,94	0,87	0,84	2,81	3,01	2,19	3,27	3,11	2,51
Pb	1,86	1,4	1,18	1,04	1,45	0,99	5,02	4,9	4,46
Th	1,6	1,61	1,55	1,02	0,976	0,73	2,58	2,54	2,07
U	0,424	0,436	0,51	0,689	0,317	0,26	0,684	0,649	5,02

Element/ Sample Nr.	*G7BF-22a-43*	*G7BF-22b-44*	*G7BF-22c-32*	*Average StDev*
Sc	3,3	3,28	2,75	0,305045
Ti	106,6	116	116,77	5,837698
V	12,15	11,61	25,32	0,914887
Cr	30,25	27,96	27,39	2,108963
Mn	8515,07	8193,54	8394,73	98,76211
Co			25,36	
Ni			18,69	
Cu	4,94	4,11	4,71	0,928376
Zn	21,75	19,62	10,59	3,629138
Ga	<0,64	1,08	1,17	
As	7,58	7,12	5,96	1,313889
Rb	0,873	0,561	0,86	0,287429
Sr	16	15,73	17,65	2,42065
Y	9,26	8,41	8,16	0,596748
Zr	6,11	5,6	4,61	0,526125
Mo			0,616	
Nb	0,585	0,645	0,63	0,160909
Cs	0,593	0,598	0,541	0,130228
Ba	9,88	10,62	10,45	1,331739
La	5,02	4,4	4,41	0,29068
Ce	7,24	7,01	6,75	0,376494
Pr	0,87	0,84	0,84	0,060463
Nd	3,84	3,81	3,2	0,31882
Sm	0,79	0,81	0,87	0,099184
Eu	0,209	0,197	0,2455	0,034012
Gd	0,87	1,21	0,83	0,171859
Tb	0,123	0,16	0,186	0,020913
Dy	1,03	0,86	1,09	0,121988
Ho	0,253	0,241	0,192	0,029633
Er	0,77	0,69	0,47	0,107231
Yb	0,64	0,43	0,83	0,118154
Lu	0,127	0,128	0,081	0,019394
Hf	0,111	0,115	0,178	0,040909
Ta	0,73	0,66	0,62	0,232045
Pb	1,07	6,48	0,78	0,574221
Th	0,66	0,63	0,78	0,062105
U	0,215	0,218	0,263	0,492232

Element / Sample Nr.	*MP-BIF-01a-7*	*MP-BIF-01b-8*	*MP-BIF-01c-59*	*MP-BIF-02a-7*	*MP-BIF-02b-8*	*MP-BIF-02c-6*	*MP-BIF-03a-9*	*MP-BIF-03b-10*	*MP-BIF-03c-7*
Sc	1,46	1,65	1,11	1,77	1,44	2,03	1,5	2,28	1,52
Ti	26,68	18,71	217,16	39,94	45,83	43,34	46,11	51,76	33
V	7,72	7,22	5,51	6,54	6,95	7,19	7,32	7,07	5,5
Cr	27,44	24,1	24,46	25,44	26,3	25,42	27,96	28,59	23,75
Mn	10742,09	10294,98	11387,95	7463,09	7340,35	7397,89	10160,93	10207,74	7477,7
Co			41,52			23,75			16,03
Ni			35,56			12,85			11,48
Cu	7,46	2,98	<2,77	7,22	6,72	7,08	8,96	8,02	7,77
Zn	20,58	16,15	15,12	184,8	19,15	21,47	36,19	27,92	17,72
Ga	5,32	4,69	4,26	1	<0,86	0,26	<1,65	<1,15	0,68
As	6,58	4,11	<2,54	7,2	6,89	6,95	8,95	10,2	5,95
Rb	1,39	1,23	1,12	0,691	0,651	0,635	1,42	1,6	1,02
Sr	69,37	64,47	68,3	85	84,04	76,72	35,24	34,3	23,51
Y	9,61	9,06	9,43	10,54	10,37	9,42	10,88	10,93	7,37
Zr	1,84	2,74	1,99	3,64	3,44	3,28	3,3	3,57	2,29
Mo			0,252			0,15			0,133
Nb	<0,136	0,137	0,7	0,222	0,147	0,74	0,177	0,199	0,59
Cs	0,201	0,133	0,28	0,213	0,304	0,189	0,46	0,559	0,388
Ba	118,73	121,81	124,17	11,43	11,28	9,06	11,08	12,16	7,87
La	8,67	8,15	8,34	6,5	6,65	5,92	4,61	3,77	2,81
Ce	13,34	12,8	13,2	8,47	8,95	7,3	5,52	5,46	3,72
Pr	1,45	0,46	1,47	0,875	0,9	0,76	0,7	0,591	0,345
Nd	3,46	4,51	3,69	2,98	3,41	3	2,43	1,72	1,49
Sm	0,82	1,14	1,16	0,5	0,69	0,35	0,51	<0,25	0,47
Eu	0,2785	0,152	0,1205	0,26	0,1515	0,123	0,201	0,09	0,073
Gd	<0,61	1,07	0,58	0,87	0,99	0,36	<0,98	<0,75	0,44
Tb	0,093	0,115	0,117	0,151	0,084	0,104	<0,096	0,08	0,065
Dy	1,22	0,71	0,47	0,75	1,17	0,48	0,71	0,49	0,51
Ho	0,095	0,15	0,105	0,149	0,117	0,193	0,132	0,21	0,131
Er	0,22	0,39	0,6	0,62	0,49	0,68	0,31	0,54	0,34
Yb	0,1	0,31	0,45	0,86	1,79	0,63	0,8	0,45	0,52
Lu	0,099	0,092	0,083	0,071	0,134	0,06	<0,086	0,109	0,061
Hf	0,28	0,088	0,078	<0,049	<0,079	0,072	0,171	0,626	0,017
Ta	0,64	0,82	0,8	3,09	2,82	2,34	2,88	2,63	1,54
Pb	1,07	0,96	0,64	1,56	1,59	1,36	4,13	1,51	0,8
Th	0,065	0,189	0,178	0,191	0,169	0,123	0,107	0,183	0,064
U	0,61	0,524	0,63	0,056	0,048	0,051	0,07	<0,130	0,0273

Element / Sample Nr.	*MP-BIF-04a-35*	*MP-BIF-04b-36*	*MP-BIF-04c-39*	*MP-BIF-05a-9*	*MP-BIF-05b-10*	*MP-BIF-05c-60*	*MP-BIF-06a-5*	*MP-BIF-06b-6*	*MP-BIF-06c-5*
Sc	2,65	3,1	2,09	2,46	3,28	2,03	2,33	1,84	3,38
Ti	44,36	45	38,03	47,82	43,29	33,7	86,81	95,49	97,06
V	9,57	7,47	6,48	8,26	10,4	7,81	8,24	8,35	9,99
Cr	26,07	28,25	28,64	25,96	30,53	38,31	23,79	26,58	25,06
Mn	8247,94	8980,11	8600,49	6402,06	7247,65	7141,62	9559,18	9456,97	9805,17
Co			22,83			23			26,29
Ni			7,72			33,02			16,76
Cu	5,52	4,63	4,03	6,41	4,53	5,5	11,24	6,29	8,52
Zn	16,57	28,32	33,69	26,13	30,78	22,71	41,92	31,88	31,02
Ga	0,67	1,08	0,81	0,91	1,46	2,81	0,87	<0,72	1,07
As	8,69	9,8	7,76	6,11	8,98	9,09	7,3	7,85	6,3
Rb	2,45	2,18	2,04	1,11	1,59	1,05	1,63	1,83	1,66
Sr	38,91	40,86	36,15	27,39	30,78	29,11	33,67	35,2	32,66
Y	12,51	13,55	11,91	9,7	10,6	9,77	10,14	10,26	9,34
Zr	3,24	3,16	2,99	3,84	5,25	4,17	5,36	4,74	5,39
Mo			0,217			0,37			0,425
Nb	0,289	0,293	0,51	0,243	0,181	<0,41	0,364	0,271	0,86
Cs	0,718	0,831	0,644	0,391	0,461	0,3	0,583	0,502	0,387
Ba	5,32	9,13	8,7	9,49	9,45	6,52	10,83	11,8	13,5
La	4,93	5,19	4,73	4,12	4,13	4,66	3,75	4,18	3,83
Ce	5,79	5,84	5,08	4,56	4,85	4,53	4,53	4,31	3,93
Pr	0,732	0,697	0,498	0,535	0,589	0,66	0,415	0,504	0,448
Nd	2,67	2,53	2,24	2,78	2,3	2	1,31	2,16	1,9
Sm	0,49	0,71	0,42	0,26	0,45	<0,19	0,15	0,188	0,24
Eu	0,1375	0,0905	0,0965	0,089	0,129	0,129	0,1435	0,2825	0,134
Gd	0,85	<0,43	0,61	<0,32	<0,68	0,75	<0,28	0,8	0,42
Tb	0,089	0,12	0,094	0,067	0,16	<0,044	0,109	0,066	0,074
Dy	0,57	1,55	0,59	0,38	0,76	0,51	0,85	0,59	0,6
Ho	0,233	0,221	0,162	0,113	0,252	0,23	0,122	0,185	0,158
Er	0,75	0,75	0,7	0,49	0,3	0,61	0,52	0,66	0,56
Yb	0,64	0,84	0,47	0,7	0,49	0,57	0,59	0,35	0,66
Lu	0,14	0,161	0,128	0,067	0,085	0,092	0,163	0,118	0,116
Hf	<0,057	0,1	<0,028	0,061	0,131	0,22	0,033	0,681	0,054
Ta	3,16	3,03	2,59	0,75	1,03	0,84	2,92	3,04	2,53
Pb	1,62	1,7	1,71	1,12	1,34	4,27	2,32	1,99	1,59
Th	0,208	0,202	0,16	0,268	0,234	0,189	0,322	0,32	0,347
U	0,172	0,105	0,067	0,198	0,054	5,96	0,106	2,56	0,089

Element / Sample Nr.	*MP-BIF-07a-11*	*MP-BIF-07b-12*	*MP-BIF-07c-8*	*MP-BIF-08a-5*	*MP-BIF-08b-6*	*MP-BIF-08c-55*	*MP-BIF-09a-33*	*MP-BIF-09b-34*	*MP-BIF-09c-38*
Sc	2,29	1,62	1,5	2,19	2,61	2,02	1,81	2,24	1,61
Ti	49,38	52,31	44,61	33,58	34,56	29,59	37,42	35,72	42,85
V	7,72	7,84	7,95	8,15	7,17	9,01	7,44	6,99	7,69
Cr	28,04	29,83	30,22	25,41	29,08	34,06	22,32	24,28	25,47
Mn	5849,66	5690,88	5885,43	6282,26	6090,26	6517,17	4314,19	4275,27	4426,03
Co			23,76			22,83			19,63
Ni			21,42			17,8			16,51
Cu	6,57	7,13	7,53	5,46	6,07	5,23	4,93	4,83	5,23
Zn	27,29	22,55	18,57	28,8	15,77	19,62	31,79	26,96	25,83
Ga	<1,10	2,01	<0,67	1,1	<0,95	1,94	0,95	0,98	0,67
As	6,6	7,5	7,18	5,33	<2,10	8,74	3,96	5,61	2,64
Rb	2,16	2,01	1,81	1,47	0,8	1,25	3,31	3,53	3,06
Sr	24,91	25,61	22,58	25,46	23,97	25,03	23,67	23,37	21,71
Y	8,43	8,73	7,48	9	9,34	8,06	7,61	7,67	6,49
Zr	7,11	6,25	5,36	3,86	3,78	4,36	3,15	3,08	2,22
Mo			0,177			0,27			0,171
Nb	0,335	0,251	0,55	0,206	0,248	0,32	0,207	0,127	0,7
Cs	0,485	0,587	0,381	0,327	0,37	0,279	0,925	1	0,92
Ba	8,28	8,74	7,8	6,01	6,95	8,44	14,16	13,84	12,38
La	3,97	4,21	3,47	3,12	3,52	3,28	3,14	3,19	2,68
Ce	4,24	4,02	3,65	2,93	2,93	3,55	2,99	3,14	2,61
Pr	0,461	0,468	0,343	0,4	0,298	0,363	0,345	0,367	0,274
Nd	2,17	1,84	1,57	1,83	1,65	1,53	1,54	1,99	0,94
Sm	0,29	<0,42	0,366	0,211	0,178	0,32	0,357	0,268	0,231
Eu	0,088	0,1625	0,0635	0,062	0,084	0,1595	0,0915	0,0615	0,0495
Gd	<0,65	<0,83	<0,25	0,58	0,63	<0,43	<0,29	0,31	0,36
Tb	<0,048	0,083	<0,033	0,108	<0,054	0,093	0,096	0,039	0,043
Dy	0,46	<0,51	0,33	0,54	0,4	<0,22	0,44	0,52	0,32
Ho	0,222	0,164	0,114	0,113	0,151	0,2	0,095	0,124	0,075
Er	0,53	0,49	0,29	0,5	0,55	0,5	0,46	0,371	0,46
Yb	0,5	0,75	0,58	0,69	0,36	0,52	0,298	0,41	0,44
Lu	0,092	0,13	0,081	0,089	0,074	0,11	0,058	0,079	0,069
Hf	<0,088	0,12	0,124	0,042	<0,059	<0,062	<0,030	<0,061	0,041
Ta	2,44	2,68	1,98	0,74	0,87	0,81	3,49	3,58	2,85
Pb	2,43	2,74	1,74	0,66	2,98	1,21	1,45	0,68	0,77
Th	0,186	0,252	0,205	0,198	0,198	0,101	0,118	0,125	0,108
U	0,084	0,073	0,035	0,058	0,081	0,088	0,0373	0,0411	0,033

Element / Sample Nr.	*MP-BIF-10a-20*	*MP-BIF-10b-21*	*MP-BIF-10c-30*	*MP-BIF-11a-22*	*MP-BIF-11b-23*	*MP-BIF-11c-31*	*MP-BIF-12a-94*	*MP-BIF-12b-95*	*MP-BIF-12c-53*
Sc	2,53	2,13	2,07	2,48	2,35	2,06	1,89	2,39	1,73
Ti	34,05	32,56	28,22	51,07	48,25	43,64	31,42	36,28	35,7
V	7,37	6,77	7,13	7,29	3,58	8,4	7,89	8,81	6,64
Cr	23,48	23,08	22,89	23,72	24,07	24,26	32	36,36	24,58
Mn	9049,49	9159,88	9396,12	10230,63	10199,21	10490,91	5982,14	6567,29	5828,07
Co			17,76			21,24			22,43
Ni			8,2			9,28			18,94
Cu	5,18	4,47	4,48	5,88	6,48	5,26	5,61	5,43	6,42
Zn	25,93	28,77	22,75	23,53	21,25	20,05	29,86	32,9	22,7
Ga	0,51	<0,50	0,58	0,44	0,66	<0,51	<0,84	<0,99	1,24
As	5,15	5,5	3,64	4,95	5,2	2,51	4,12	5,27	3,87
Rb	2,04	1,95	1,88	1,6	1,87	1,52	2,9	4,16	3,04
Sr	71,52	73,96	64,18	104,48	106,25	97,81	50,1	56,78	46,14
Y	14,9	15,09	12,7	16,59	17,31	15,5	10,39	12,2	9,06
Zr	3,55	3,48	3,27	4,16	3,85	4,01	4,34	3,12	3,34
Mo			0,098			0,21			0,123
Nb	0,19	0,173	0,42	0,181	0,245	0,45	0,282	0,188	0,62
Cs	0,578	0,512	0,53	0,472	0,579	0,392	1,16	1,21	0,766
Ba	9,31	9,56	8,38	11,25	10,92	9,43	9,41	9,09	9,1
La	4,24	4,66	3,69	4,7	4,64	4,07	3,52	3,86	3,4
Ce	4,27	4,21	3,33	4,54	5,12	4,25	3,31	3,86	3,09
Pr	0,399	0,424	0,399	0,54	0,542	0,46	0,385	0,46	0,367
Nd	1,78	2,25	1,69	1,79	2,59	1,78	1,82	2,56	1,78
Sm	0,352	0,258	0,48	0,321	0,358	0,297	0,43	0,6	0,26
Eu	0,099	0,1125	0,0785	0,1215	0,1345	0,0895	0,1195	0,1375	0,069
Gd	0,51	0,43	0,49	0,65	0,61	0,39	0,49	0,4	0,48
Tb	0,081	0,089	0,051	0,141	0,082	0,091	0,088	0,071	0,096
Dy	0,85	0,44	0,73	1,05	0,85	0,84	0,68	0,61	1,04
Ho	0,277	0,263	0,185	0,254	0,224	0,24	0,17	0,23	0,105
Er	0,73	0,78	0,63	0,76	0,83	0,69	0,86	0,69	0,38
Yb	0,99	1,19	0,56	0,74	0,92	0,93	0,52	1,23	0,61
Lu	0,243	0,262	0,166	0,255	0,243	0,199	0,153	0,133	0,103
Hf	0,043	0,078	0,023	0,04	0,06	0,49	<0,071	<0,121	<0,00
Ta	2,72	2,94	2,27	2,8	2,8	2,41	0,88	0,95	0,78
Pb	1,1	0,85	0,97	0,9	1,18	0,83	0,86	1,87	0,85
Th	0,215	0,157	0,147	0,163	0,196	0,132	1,43	0,09	0,056
U	0,0354	0,0326	0,059	0,035	0,054	0,058	0,039	0,046	0,036

Element / Sample Nr.	*MP-BIF-13a-43*	*MP-BIF-13b-44*	*MP-BIF-13c-44*	*MP-BIF-14a-13*	*MP-BIF-14b-14*	*MP-BIF-14c-9*	*MP-BIF-15a-96*	*MP-BIF-15b-97*	*MP-BIF-15c-54*
Sc	2,53	1,32	1,68	1,96	1,95	2,4	1,94	2,2	2,62
Ti	45,72	54,59	46,58	27,45	23,97	37,19	29,57	29,53	33,85
V	6,1	7,38	6,78	5,58	7,23	8,35	8,12	10,11	6,98
Cr	33,4	26,38	24,95	25,68	29,29	28,98	26,34	27,56	24,54
Mn	4483,16	4496,64	4529,47	4047,17	4027,75	4077,04	5224,85	5971,74	5788,53
Co			18,67			21,09			21,77
Ni			13,54			14,85			23,37
Cu	5,52	4,35	4,85	3,34	3,52	6,32	5,54	4,23	5,92
Zn	25,88	19,81	17,64	13,81	21,62	17,76	31,45	28,07	18,47
Ga	<0,73	2,04	0,69	<1,20	<1,81	0,45	1,24	<0,63	1,36
As	3,87	5,39	3,37	3,47	<3,66	3,17	4,92	4,58	5,94
Rb	3,01	2,91	2,55	2,12	2,31	2,19	2,61	3,08	2,69
Sr	38,38	36,05	31,72	32,38	32,31	27,94	44,99	50,48	44,86
Y	9,27	9,08	7,59	8,68	8,22	7,26	11,86	12,57	10,47
Zr	3,61	3,22	3,1	6,44	5,83	5,23	3,22	6,12	3,52
Mo			0,194			0,171			0,195
Nb	0,238	0,216	0,42	0,103	0,173	0,88	0,154	0,225	0,93
Cs	0,727	0,787	0,607	0,451	0,679	0,494	0,671	0,98	0,82
Ba	8,88	7,32	7,43	8,42	7,25	6,11	8,42	7,92	7,41
La	3,42	3,39	3,02	3,55	3,47	2,84	4,31	4,6	4,08
Ce	2,44	3,76	2,96	3,16	3,25	2,71	4,39	4,96	4,37
Pr	0,353	0,377	0,343	0,437	0,366	0,319	0,57	0,57	0,61
Nd	1,52	2,06	1,63	1,78	1,86	1,3	2,46	2,76	2,45
Sm	0,187	0,442	0,27	<0,24	<0,58	0,41	0,38	0,35	0,24
Eu	0,0705	0,188	0,066	0,1495	0,1745	0,043	0,1685	0,155	0,189
Gd	<0,25	0,62	0,56	<0,70	<1,49	0,5	1,04	1,03	<0,57
Tb	0,072	0,074	0,056	0,107	<0,093	<0,0124	0,092	0,068	0,23
Dy	0,39	0,89	0,45	0,4	0,69	0,35	0,69	0,85	0,57
Ho	0,148	0,185	0,112	0,104	0,185	0,127	0,17	0,21	0,19
Er	0,49	0,55	0,46	0,34	0,61	0,39	0,6	0,56	0,6
Yb	0,42	0,42	0,32	0,62	<0,43	0,162	0,6	0,59	0,36
Lu	0,076	0,084	0,077	0,091	0,095	0,047	0,127	0,174	0,117
Hf	0,089	0,075	<0,030	0,18	<0,147	0,091	<0,075	0,089	0,194
Ta	2,66	2,7	2,12	3,21	3,49	2,65	0,75	0,88	0,82
Pb	0,91	0,93	0,72	1,94	2,3	1,66	1,18	1,02	0,75
Th	0,164	0,18	0,133	0,182	0,245	0,117	0,142	0,115	0,119
U	0,044	0,0513	0,053	0,096	0,062	0,073	0,05	0,061	0,048

Element / Sample Nr.	MP-BIF-16a-65	MP-BIF-16b-66	MP-BIF-16c-55	MP-BIF-17a-31	MP-BIF-17b-32	MP-BIF-17c-37	MP-BIF-18a-18	MP-BIF-18b-19	MP-BIF-18c-29
Sc	3,53	4,64	3,7	1,75	2,03	1,75	2,16	2,46	1,9
Ti	193,62	189,07	159,75	30,79	24,12	24,38	28,29	25,96	26,73
V	15,66	15,75	16,59	7,12	8,36	6,78	7,39	7,2	7,14
Cr	38,32	39,2	40,98	24	24,03	26,57	41,29	40,93	50,55
Mn	5552,78	5432,06	5746,82	5903	5901,32	6148,82	7734,62	7496,03	7803,18
Co			23,34			18,88			21,81
Ni			22,2			11,34			32,61
Cu	4,39	5,23	5,89	3,35	2,55	4,34	6,46	6,56	5,94
Zn	16,83	29,8	23,58	31,18	25,1	23,69	25,31	26,26	22,54
Ga	<1,39	1,52	1,89	<0,50	0,74	<0,62	0,53	<0,52	<0,54
As	12,17	12,95	9,48	4,1	4,18	4,11	4,97	6,84	3,16
Rb	1,21	0,71	1,61	3,47	3,81	3,01	3,25	2,97	2,64
Sr	10,28	10,06	8,89	38,69	39,67	36,44	52,76	53,19	48,8
Y	8,43	8,49	7,55	10,76	9,99	9,51	13,47	13,17	11,76
Zr	12,45	12,83	11,22	3,81	4,02	3,8	3,65	3,26	3,28
Mo			0,88			0,191			0,145
Nb	1	1	0,73	0,148	0,255	0,37	0,267	0,187	0,89
Cs	0,848	0,784	0,74	0,886	0,79	0,884	0,776	0,843	0,709
Ba	7,24	8,98	7,3	8,91	9,75	8,01	8,57	8,73	9,19
La	7,78	8,12	6,99	4,38	4,44	3,91	4	3,84	3,69
Ce	10,35	10,5	10,37	4,41	4,62	4,14	3,79	3,8	3,28
Pr	1	1	0,9	0,598	0,557	0,422	0,438	0,387	0,452
Nd	4,54	4,62	4,61	2,32	2,62	2,02	1,83	1,75	1,61
Sm	0,81	0,89	1,1	0,382	0,48	0,32	0,267	0,346	0,4
Eu	0,194	0,119	0,11	0,107	0,109	0,119	0,0795	0,09	0,0975
Gd	<0,85	0,85	0,9	0,71	0,31	0,26	0,58	0,57	0,49
Tb	0,207	0,128	0,168	0,083	0,092	0,07	0,194	0,116	0,089
Dy	1,21	0,6	0,89	0,68	0,55	0,56	0,8	0,69	0,36
Ho	0,235	0,231	0,21	0,185	0,126	0,169	0,185	0,245	0,164
Er	0,46	0,91	0,43	0,53	0,6	0,5	0,81	0,7	0,53
Yb	0,79	0,85	0,63	0,57	0,45	0,41	1,02	1,04	0,78
Lu	0,174	0,111	0,104	0,125	0,052	0,063	0,206	0,208	0,147
Hf	0,242	0,235	0,25	0,057	0,13	0,069	0,065	0,063	0,054
Ta	2,48	2,72	2,29	3,01	2,92	2,48	2,56	2,46	2,04
Pb	2,65	2,95	3,07	0,75	0,97	0,81	127,33	0,89	0,74
Th	1,2	1,31	1,2	0,146	0,121	0,11	0,12	0,155	0,098
U	0,367	0,285	0,26	0,0348	0,042	0,038	0,067	0,0498	0,047

Element / Sample Nr.	*MP-BIF-19a-79*	*MP-BIF-19b-80*	*MP-BIF-19c-47*	*MP-BIF-20a-106*	*MP-BIF-20b-107*	*MP-BIF-20c-9*	*MP-BIF-21a-5*	*MP-BIF-21b-6*	*MP-BIF-21c-12*
Sc	1,74	2,27	1,26	1,37	1,44	3,06	2,69	2,34	2,24
Ti	31,66	19,9	26,34	18,85	28,89	31,08	28,48	31,63	32,34
V	8,79	8,59	7,42	7,58	7,62	8,6	8,04	8,39	8,51
Cr	26,76	29,74	28,55	28,72	27,73	31,97	22,17	22,96	28,13
Mn	10485,69	10082,18	11139,45	5954,28	5929,48	5874,27	7668,36	7291,92	7715,81
Co			16,38			21,16			21,97
Ni			20,64			18,04			18,38
Cu	3,3	3,27	6,31	4,94	4,59	14,73	6,11	5,67	17,86
Zn	20,89	25,63	20,52	21,88	26,85	26,18	32,57	24,77	28
Ga	0,73	0,71	1,22	<0,79	<0,55	<0,38	0,651	0,63	0,89
As	3,47	4,74	3,01	4,23	7,7	3,58	3,32	4,71	2,54
Rb	2,35	2,64	2,29	0,84	2,52	1,59	2	2	2,07
Sr	35,02	35,42	33,56	27,99	28,89	25,33	23,12	22,6	23,03
Y	14,47	13,91	13,36	13,33	13,27	11,8	12,67	12,62	11,9
Zr	3,81	4,99	4,49	4,51	4,48	4,04	3,96	3,79	4,66
Mo			0,187			0,149			0,166
Nb	0,172	0,207	1,03	0,098	0,361	0,97	0,257	0,208	0,33
Cs	0,589	0,703	0,647	0,384	0,479	0,365	0,554	0,548	0,553
Ba	7,98	7,44	8,78	8,02	7,76	6,7	7,19	6,8	7,13
La	3,6	3,62	3,48	5,21	5,43	4,37	4	4,02	3,76
Ce	3,71	3,37	3,66	5,74	6,28	5,1	4,31	4,07	4,21
Pr	0,461	0,57	0,376	0,707	0,741	0,582	0,512	0,602	0,53
Nd	1,85	1,63	1,38	3,3	3,16	2,6	2,3	2,34	2,62
Sm	0,21	0,34	0,45	0,32	0,49	0,187	0,414	0,355	0,46
Eu	0,1025	0,131	0,1365	0,1545	0,151	0,244	0,1115	0,1275	0,281
Gd	0,43	1,02	0,28	0,95	0,77	0,62	0,715	0,451	1,03
Tb	0,085	0,117	0,12	0,132	0,125	0,078	0,094	0,113	0,082
Dy	0,87	0,64	0,79	1,29	0,98	0,58	0,84	0,84	0,93
Ho	0,21	0,25	0,28	0,231	0,5	0,154	0,181	0,21	0,174
Er	0,93	0,84	0,88	0,53	0,75	0,53	0,8	0,622	0,5
Yb	1,16	1,25	0,51	0,68	0,61	0,5	0,56	0,71	0,74
Lu	0,194	0,215	0,178	0,122	0,071	0,078	0,201	0,146	0,128
Hf	0,065	<0,056	0,092	0,096	0,066	<0,028	0,029	0,069	<0,037
Ta	0,84	1,1	0,64	3,01	2,97	2,35	2,7	2,84	2,9
Pb	0,63	0,62	0,36	0,84	0,94	0,66	0,78	0,706	0,64
Th	0,16	0,67	0,089	0,221	0,196	0,139	0,197	0,173	0,128
U	0,63	0,05	0,054	0,048	0,261	0,046	0,045	0,0568	0,047

Element / Sample Nr.	*MP-BIF-22a-90*	*MP-BIF-22b-91*	*MP-BIF-22c-51*	*MP-BIF-23a-80*	*MP-BIF-23b-81*	*MP-BIF-23c-63*	*MP-BIF-24a-71*	*MP-BIF-24b-72*	*MP-BIF-24c-58*
Sc	1,96	1,75	1,68	3,41	3,42	2,67	2,93	3,23	3,36
Ti	32,45	33,88	37,38	106,02	106,57	95,06	126,8	131,96	126,71
V	9,61	9,62	7,83	10,85	11,11	8,79	14,69	14,53	14,45
Cr	26,42	30,19	28,49	31,62	32,71	25,09	33,28	35,34	34,48
Mn	8301,23	8354,82	8920,03	8680,78	8542,2	7112,17	10246,47	9893,94	10302,23
Co			25,04			20,16			32,57
Ni			19,11			12,2			16,64
Cu	4,74	4,35	6,27	8,57	9,09	8,03	4,4	3,31	4,01
Zn	18,49	19,48	26,71	8,26	26,57	19,73	26,37	14,94	16,65
Ga	0,57	0,41	<1,13	1,46	<1,19	0,61	1,06	0,96	0,67
As	5,36	6,55	5,85	10,53	14,78	11,74	12,23	12,36	9,97
Rb	1,28	1,23	1,16	1,42	1,64	0,86	1,01	0,94	1,05
Sr	23,51	23,06	22,2	17,45	16,36	12,81	15,14	15,27	14,93
Y	16,4	15,99	14,38	11,24	11,49	8,83	18,56	18,41	17,25
Zr	5,06	4,4	3,18	8,35	7,57	5,65	9,36	9,52	8,53
Mo			0,156			0,505			0,88
Nb	0,192	0,229	1,15	0,644	0,59	0,73	0,857	0,93	0,78
Cs	0,325	0,374	0,273	0,482	0,433	0,395	0,594	0,546	0,575
Ba	8,1	7,4	7,94	8,53	8,39	6,13	9,75	10,28	9,08
La	4,68	4,75	3,97	5,09	5,01	3,87	10,11	9,81	9,14
Ce	5,06	5,29	4,73	7,34	7,15	5,08	16,24	15,75	15,05
Pr	0,61	0,7	0,62	0,785	0,815	0,68	2	1,79	1,74
Nd	2,86	2,58	2,4	4,41	4,6	2,61	7,51	8,25	6,92
Sm	0,73	0,39	0,7	<0,28	1,01	0,84	1,57	1,48	1,46
Eu	0,125	0,125	0,202	0,2445	0,158	0,1535	0,2965	0,298	0,345
Gd	0,79	0,85	0,62	1,23	1,51	0,37	2,15	1,27	2,13
Tb	0,104	0,157	0,116	0,154	0,167	0,138	0,284	0,265	0,27
Dy	1,01	1,02	0,62	0,84	1,27	0,84	2,39	2,09	2,22
Ho	0,24	0,31	0,138	0,269	0,233	0,24	0,58	0,48	0,47
Er	1,02	1,01	0,6	1,23	0,99	0,79	1,31	1,54	1,91
Yb	1,52	1,32	1,38	0,5	0,99	1,06	1,58	1,53	0,94
Lu	0,233	0,217	0,116	0,263	0,17	0,117	0,274	0,259	0,251
Hf	<0,029	0,048	<0,062	0,16	<0,156	0,173	0,195	0,263	0,131
Ta	0,88	0,94	0,81	3,28	2,96	2,27	3,08	3,33	2,83
Pb	1	0,92	1,18	2,69	3,07	1,92	2,33	2,09	1,95
Th	0,238	0,242	0,232	0,87	0,839	0,65	0,951	0,9	0,98
U	0,056	0,03	0,094	0,264	0,216	0,127	0,187	4,43	0,23

Element / Sample Nr.	*MP-BIF-25a-39*	*MP-BIF-25b-40*	*MP-BIF-25c-42*	*MP-BIF-26a-11*	*MP-BIF-26b-12*	*MP-BIF-26c-61*	*MP-BIF-27a-97*	*MP-BIF-27b-98*	*MP-BIF-27c-6*
Sc	1,58	1,84	1,61	2,1	2,59	2,23	1,71	1,54	2,01
Ti	33,28	39,29	34,57	22,27	26,74	29,38	22,82	24,13	29,9
V	8,38	12,6	8,37	7,87	<1,21	7,11	5,56	6,83	8,14
Cr	23,05	24,11	27,84	26,44	27,22	28,26	28,38	26,03	25,65
Mn	6827,64	6737,91	7251,03	8319,48	8614,88	9130,73	3768,92	3800,49	3911,07
Co			21,24			20,78			19,35
Ni			17,97			16,03			14,56
Cu	5,49	5,33	4,73	3,55	5,1	5,5	5,38	5,8	15,29
Zn	26,19	20,19	24,66	24,04	30,47	21,32	32,72	26,2	23,64
Ga	1,21	0,85	1,41	0,92	<0,95	1,18	<0,77	0,63	<0,53
As	4,36	5,99	4,73	6,13	3,6	3,63	6,47	3,15	4,43
Rb	1	1,4	1,51	1,57	2,04	2	2,9	4,04	3,32
Sr	27,99	28,2	27,22	18,06	20,26	20,51	14,16	12,71	11,7
Y	16,39	16,24	15,14	13,62	14,02	14,03	9,75	9,27	9,14
Zr	4,77	4,82	4,57	4,27	4,44	4,61	3,83	4,34	4,19
Mo			0,231			0,18			0,212
Nb	0,283	0,359	0,69	0,219	0,151	0,72	0,269	0,233	0,6
Cs	0,387	0,341	0,344	0,589	0,517	0,505	2,01	1,04	0,988
Ba	7,24	7,82	7,28	9,55	10,09	9,07	7,16	8,68	5,17
La	6,31	6,23	6,04	3,99	4,12	4,21	6,14	5,89	5,12
Ce	7,27	7,37	7,1	4,47	4,53	4,92	7,03	15,25	5,81
Pr	0,816	0,805	0,79	0,46	0,571	0,54	0,321	0,729	0,592
Nd	4,1	3,9	4,09	1,88	3,95	2,07	3,23	3,39	2,58
Sm	0,55	0,89	0,76	<0,15	0,57	0,47	0,47	0,34	0,43
Eu	0,2215	0,2905	0,1955	0,1175	0,1595	0,132	0,2415	0,227	0,117
Gd	1,15	1,3	1,23	0,72	0,75	0,78	0,84	1,13	0,8
Tb	0,164	0,09	0,132	0,09	0,151	0,09	0,134	0,074	0,09
Dy	1,26	1,12	0,89	0,7	0,96	0,92	0,89	0,63	0,58
Ho	0,244	0,271	0,28	0,176	0,282	0,35	0,246	0,18	0,092
Er	1,03	0,68	0,98	0,4	0,77	0,89	0,66	0,46	0,35
Yb	0,75	0,78	0,69	0,67	1,1	1,03	0,46	0,35	0,38
Lu	0,173	0,154	0,155	0,159	0,205	0,177	0,084	0,095	0,063
Hf	0,139	0,064	0,079	0,238	1,02	0,107	<0,068	0,089	0,044
Ta	2,48	2,64	2,32	0,91	0,84	0,95	3,54	3,29	2,57
Pb	0,93	0,96	0,97	0,76	0,97	0,96	0,57	0,63	0,54
Th	0,216	0,248	0,194	0,199	0,373	0,192	0,174	0,47	0,127
U	<0,16	0,061	0,053	0,055	<0,114	0,039	0,087	0,082	0,04

Element / Sample Nr.	MP-BIF-28a-69	MP-BIF-28b-70	MP-BIF-28c-57	MP-BIF-29a-63	MP-BIF-29b-64	MP-BIF-29c-37	MP-BIF-30a-76	MP-BIF-30b-77	MP-BIF-30c-61
Sc	2,4	1,99	1,82	2,17	2,58	2,68	2,46	2,54	1,94
Ti	28,58	36,82	26,51	49,19	41,67	48,95	57,63	52,94	55,43
V	7,61	7,11	7,88	9,56	9,97	9,12	8,56	8,64	9,04
Cr	27,83	28,95	27,36	24,66	27,28	26,79	26,12	24,63	23,6
Mn	8919,92	8769,49	8641,9	8388,09	8450,75	8518,94	12117,02	11890,81	11654,06
Co			19,22			25,24			17,13
Ni			9,35			13,88			24,76
Cu	5,95	5,89	5,85	6,71	7,02	2,27	5,72	6,3	5,16
Zn	26,2	29,52	17,16	19,73	25,39	21,23	22,54	28,65	22,47
Ga	<1,00	<0,92	<0,67	0,45	0,53	<0,88	1,4	<0,88	0,76
As	5,79	5,07	<1,89	6,28	7,26	5,62	5,82	6,64	7,62
Rb	2,41	2,22	2,18	1,97	2,11	2,31	1,97	1,97	2,03
Sr	18,09	18,67	16,29	15,61	12,4	16,62	16,87	17,04	15,97
Y	14,66	14,56	13,03	14,33	13,84	13,05	16,92	17,44	16,57
Zr	4,4	4,47	4,15	5,36	5,29	4,32	5,86	5,8	5,15
Mo			0,163			0,298			0,322
Nb	0,137	0,271	0,85	0,317	0,287	0,43	0,419	0,399	0,78
Cs	0,645	0,588	0,555	0,564	0,589	0,588	0,634	0,717	0,595
Ba	6,84	8,12	6,68	6,8	5,86	9,73	6,83	7,67	6,93
La	3,73	3,64	3,39	3,78	3,7	3,62	3,28	3,22	3,11
Ce	3,99	3,86	3,29	4,4	3,8	3,84	3,63	3,52	3,47
Pr	0,404	0,482	0,322	0,512	0,479	0,477	0,373	0,459	0,365
Nd	1,64	2,15	1,86	2,04	2,56	2,39	2,38	1,85	1,77
Sm	0,35	0,34	0,44	0,205	0,48	0,71	0,52	0,39	0,43
Eu	0,1525	0,132	0,173	0,1585	0,1095	0,3355	0,1505	0,16	0,0885
Gd	0,79	0,44	0,87	0,62	0,48	0,77	0,62	0,76	0,77
Tb	<0,071	0,207	0,075	0,117	0,102	0,108	0,085	0,108	0,15
Dy	1,12	0,72	0,79	0,94	0,77	0,98	1,45	0,92	1,64
Ho	0,232	0,233	0,25	0,22	0,214	0,184	0,226	0,35	0,29
Er	0,8	0,97	0,81	0,74	0,9	0,55	1,26	1,32	1,35
Yb	1,13	0,97	0,58	0,97	1,08	0,65	1,76	1,12	2,21
Lu	0,24	0,219	0,148	0,18	0,181	0,164	0,301	0,271	0,259
Hf	<0,122	0,093	<0,059	0,096	<0,040	0,051	0,062	<0,076	0,133
Ta	2,63	2,75	2,34	0,88	0,84	0,93	2,45	2,78	2,5
Pb	1,06	0,96	0,86	0,92	0,77	1,06	1,24	1,4	1,32
Th	0,218	0,224	0,207	0,247	0,208	0,223	0,368	0,343	0,32
U	0,078	0,054	0,033	0,088	0,059	0,127	0,099	0,111	0,073

Element / Sample Nr.	*MP-BIF-31a-26*	*MP-BIF-31b-27*	*MP-BIF-31c-33*	*MP-BIF-32a-58*	*MP-BIF-32b-59*	*MP-BIF-32c-50*	*MP-BIF-33a-65*	*MP-BIF-33b-66*	*MP-BIF-33c-38*
Sc	3,32	3,3	2,49	2,86	3,17	2,64	1,64	2,71	1,68
Ti	45,5	49,02	48,19	43,96	51,06	47,14	37,86	37,03	45,64
V	8,27	5,96	7,56	5,1	9,79	5,51	8,72	9,4	8,76
Cr	24,48	24,44	23,39	11,63	29,84	26,78	23,7	26,87	33,2
Mn	14535,05	14532,56	15170,1	6763,74	7870,93	7094,92	4410,25	4698,27	4932,04
Co			26,44			18,12			25,58
Ni			13,16			21,53			23,15
Cu	7,66	7,22	5,39	6,61	5,07	7,51	5,29	4,63	7,18
Zn	31,93	27,43	27,94	27,18	29,79	26,52	19,94	24,96	27,18
Ga	<0,91	<0,78	<0,57	1,93	<0,91	0,75	<0,29	<0,39	<1,16
As	7,49	6,77	6,62	6,94	7,55	10,06	5,17	5,87	5,79
Rb	1,75	1,74	1,52	<0,31	2,66	2,51	1,88	2,02	2,03
Sr	23,35	22,42	21,1	12,22	11,98	11,68	10,77	11,72	11
Y	25,03	24,49	22,33	8,88	10,13	8,29	8,25	8,53	8,71
Zr	5,64	4,78	5,56	6,13	6,51	4,32	4,15	5,65	4,64
Mo			0,379			0,402			0,3
Nb	0,258	0,334	0,73	0,278	0,558	0,74	0,203	0,415	0,83
Cs	0,291	1,9	0,467	0,449	0,913	0,83	0,604	0,51	0,456
Ba	8,1	8,29	6,33	8,3	9,68	5,71	6,78	7,83	7,04
La	5,05	5,07	4,59	4,78	6,28	4,25	3,87	4,14	4,35
Ce	5,95	0,76	5,05	5,21	6,45	4,89	4,74	4,69	5,97
Pr	0,826	0,673	0,58	0,53	0,63	0,45	0,64	0,6	0,513
Nd	3,05	3,06	2,57	2,41	2,86	1,87	2,94	2,98	2,72
Sm	0,38	0,61	0,42	0,69	0,67	0,3	0,33	0,75	<0,29
Eu	0,212	0,2805	0,1455	0,157	0,153	0,107	0,116	0,1165	0,095
Gd	1,01	1,2	0,7	0,91	0,87	0,36	0,47	0,54	0,51
Tb	0,33	0,152	0,166	0,048	0,134	0,062	0,074	0,115	0,189
Dy	1,55	1,33	1,15	0,82	0,82	0,44	0,65	0,53	0,6
Ho	0,45	0,48	0,34	0,203	0,258	0,146	0,145	0,189	0,23
Er	1,63	1,65	1,45	0,73	0,61	0,57	0,56	0,32	0,47
Yb	1,78	2,12	1,9	0,69	1,12	0,49	0,42	0,43	0,45
Lu	0,441	0,382	0,259	0,136	0,241	0,151	0,081	0,129	<0,048
Hf	<0,081	0,139	0,109	<0,060	0,193	0,12	<0,031	0,146	0,097
Ta	2,49	2,21	1,94	2,92	3,19	2,71	0,72	1	0,92
Pb	1,4	3,04	1,03	1,34	1,98	1,32	0,96	1,07	0,98
Th	0,372	0,393	0,296	0,391	0,316	0,3	0,29	0,197	0,238
U	0,102	0,107	0,087	<0,16	<0,26	0,073	0,073	0,078	0,06

Element / Sample Nr.	*MP-BIF-34a-24*	*MP-BIF-34b-25*	*MP-BIF-34c-32*	*MP-BIF-35a-95*	*MP-BIF-35b-96*	*MP-BIF-35c-5*	*MP-BIF-36a-92*	*MP-BIF-36b-93*	*MP-BIF-36c-52*
Sc	3,15	2,8	3,33	2,99	2,45	4,41	2,44	3,28	2,56
Ti	44,51	42,97	50,18	56,96	65,6	46,89	52,84	52,99	53,1
V	8,35	8,64	4,73	9,59	9,45	10,34	9,91	9,64	8,92
Cr	23,71	22,53	25,7	21,37	24,79	27,05	31,48	32,62	27,56
Mn	8093,16	8199	8388,22	12130,65	11839,33	13066,93	8360,89	8959,17	8578,7
Co			30,02			18,29			43,94
Ni			12,08			21,4			29,76
Cu	5,11	6,75	6,37	7,44	6,49	32,74	13,65	14,18	13,68
Zn	31,61	32,69	35,38	18,7	11,68	29,33	34,15	32,48	18,73
Ga	<0,77	1,14	1,22	<0,46	<0,53	0,85	<0,62	<0,59	<1,28
As	7,32	7,21	7,43	7,55	6,83	5,87	6,7	6,33	9
Rb	2,31	2,74	2,21	1,44	1,11	1,2	1,8	1,78	1,64
Sr	14,74	15,43	12,85	21,1	20,57	19,48	13,97	15,18	14,72
Y	14,11	14,81	12,07	20,69	20,64	18,97	13,02	12,91	12,21
Zr	4,47	5,11	4,26	7,18	6,19	6,62	5	5,33	4,61
Mo			0,235			0,329			0,388
Nb	0,314	0,317	0,54	0,369	0,201	0,79	0,293	0,319	0,76
Cs	0,739	0,787	0,716	<0,067	0,404	0,273	0,508	0,52	4,41
Ba	8,11	8,4	5,87	6,65	8,95	7,67	6,63	7,57	5,89
La	4,51	4,52	4,6	5,56	5,77	4,8	4,12	4,18	4,15
Ce	5,59	5,57	5,28	6,88	6,4	5,65	5,04	5,03	4,65
Pr	0,608	0,608	0,59	0,709	0,739	0,727	0,52	0,6	0,57
Nd	2,54	2,58	2,42	3,23	3,71	3,06	2,15	2,5	1,91
Sm	0,483	0,59	0,37	0,71	0,45	0,21	0,53	0,38	0,74
Eu	0,0985	0,163	0,1605	0,18	0,154	0,1405	0,163	0,1215	0,1125
Gd	0,46	1,23	0,73	0,97	0,95	0,98	0,57	0,56	0,88
Tb	0,154	0,128	0,092	0,148	0,114	0,15	0,146	0,116	0,165
Dy	0,83	1,32	1,22	1,45	1,7	1,22	1,01	0,9	0,5
Ho	0,259	0,311	0,25	0,57	0,52	0,315	0,23	0,26	0,21
Er	0,89	0,83	0,75	1,47	1,65	1,11	0,81	1,24	0,64
Yb	0,97	1,07	0,6	1,5	1,81	1,72	1,24	1,37	1,19
Lu	0,191	0,284	0,154	0,36	0,311	0,282	0,224	0,3	0,174
Hf	0,084	0,158	<0,038	0,05	0,159	0,14	<0,073	0,174	0,146
Ta	2,81	2,86	2,34	3,27	2,9	2,79	0,95	1,03	0,71
Pb	0,62	1,31	0,83	1,6	5,45	1,55	1,28	1,01	1,29
Th	0,259	0,326	0,22	0,582	0,485	0,455	0,35	0,33	0,305
U	0,077	0,078	0,107	0,411	<0,17	0,11	0,081	0,111	0,099

Element / Sample Nr.	*MP-BIF-37a-60*	*MP-BIF-37b-61*	*MP-BIF-37c-51*	*MP-BIF-38a-82*	*MP-BIF-38b-83*	*MP-BIF-38c-64*	*MP-BIF-39a-13*	*MP-BIF-39b-14*	*MP-BIF-39c-28*
Sc	2,08	2,48	2,05	2,62	3,07	2,52	3,06	3,31	2,53
Ti	26,31	30,9	27,39	72,85	88,99	79,11	58,33	55,86	58,75
V	3,36	6,7	6,57	10,42	9,79	9,68	9,27	8,55	8,63
Cr	25,74	25,96	26,55	32,17	25,76	31,35	31,21	30,21	31,18
Mn	8009,14	8025,89	8186,81	8320,85	8238,98	8247,15	5412,34	5027,04	5225,26
Co			20,3			21,41			21,58
Ni			11,34			19,03			17,95
Cu	4,48	6,62	4,82	16,3	16,99	17,11	4,72	5,07	5,57
Zn	36,56	37,68	24,51	19,24	19,86	19,83	23,81	23,93	21,72
Ga	<1,12	6,35	0,81	0,76	<0,62	<0,67	1,02	0,67	0,73
As	6,23	5,15	4,37	7,64	8,48	6,21	7,45	9,83	7,03
Rb	4,01	4,04	3,65	0,87	0,86	0,88	1,8	1,48	1,47
Sr	86,79	88,32	80,16	18,84	18,86	18,51	21,06	19,43	18,21
Y	13,92	15,06	12,87	13,55	13,53	12,3	12,66	12,06	10,7
Zr	3,68	2,73	3,23	6,67	6,23	5,95	5,21	4,76	4,19
Mo			0,1			0,256			0,313
Nb	0,109	0,21	0,57	0,325	0,36	0,77	0,269	0,256	0,442
Cs	1	1,22	1	0,232	0,276	0,305	0,607	0,482	0,437
Ba	12,5	13,09	10,89	7,29	7,59	7,6	8,97	8,45	7,42
La	5,01	5,01	4,52	5,63	5,41	5,01	7,82	7,32	6,17
Ce	4,76	4,95	4,68	6,54	6,71	6,54	9,35	8,71	7,86
Pr	0,482	0,636	0,5	0,698	0,844	0,81	1	1	0,98
Nd	2,54	2,61	1,87	3,87	3,67	3,67	4,78	4,47	4,11
Sm	0,34	0,43	0,38	0,9	0,24	0,44	0,99	0,97	0,7
Eu	0,1395	0,1065	0,1145	0,1805	0,2305	0,1675	0,191	0,206	0,182
Gd	<0,69	0,88	0,53	1,3	1,06	0,99	0,8	1,32	1,11
Tb	0,119	0,075	0,095	0,219	0,081	0,144	0,219	0,158	0,145
Dy	0,83	0,82	0,54	0,91	0,83	0,93	0,9	1,09	1,17
Ho	0,19	0,274	0,2	0,33	0,175	0,3	0,28	0,191	0,175
Er	0,8	0,78	0,5	0,85	0,89	0,74	0,7	0,66	0,59
Yb	1,17	0,31	0,51	1	0,65	0,62	0,61	0,62	0,58
Lu	0,178	0,1	0,15	0,241	0,216	0,224	0,131	0,124	0,088
Hf	0,146	<0,081	0,081	0,177	0,055	<0,089	0,079	0,155	0,071
Ta	3,26	3,54	2,89	4,11	3,92	3,73	2,75	2,79	2,36
Pb	0,79	1	0,83	1,28	1,41	1,53	0,96	0,78	0,76
Th	0,136	0,128	0,145	0,505	0,668	0,48	0,368	0,376	0,221
U	0,074	0,074	0,066	0,102	0,089	0,13	0,081	0,108	0,1

Element / Sample Nr.	*MP-BIF-40a-69*	*MP-BIF-40b-70*	*MP-BIF-40c-43*	*MP-BIF-41a-7*	*MP-BIF-41b-8*	*MP-BIF-41c-13*	*MP-BIF-42a-102*	*MP-BIF-42b-103*	*MP-BIF-42c-7*
Sc	3,53	2,53	2,2	2,89	3,12	2,24	2,61	2,77	4,41
Ti	72,87	69,75	67,52	73,67	67,19	60,78	83,08	79,65	102,31
V	11,34	11,18	15,48	10,48	10,2	9,62	10,28	9,94	10,75
Cr	34,17	30,77	33,36	23,75	26,44	26,83	29,96	32,09	31,57
Mn	7786,27	7491,14	7653,13	5658,21	5700,37	5914,98	7511,62	7362,56	7330,73
Co			23,04			48,24			48,23
Ni			30,22			13,52			22,88
Cu	3,8	3,33	4,99	70,83	70,11	76,14	58,82	63,2	68,59
Zn	32,63	27,62	19,93	20,87	24,72	21,07	26,24	16,35	26,27
Ga	1,17	1,34	1,4	0,6	0,69	0,86	1,05	<1,26	0,81
As	11,46	10,73	11,75	10,01	10,14	10,86	10,93	13,41	11,7
Rb	1,13	0,96	1,18	1	0,866	0,846	0,91	0,88	0,91
Sr	18,03	18,04	17,3	17,64	17,85	18,08	21,26	13,26	18,32
Y	12,75	11,8	11,84	10,86	10,51	10,55	11,98	12,04	11,03
Zr	7,84	7,59	6,82	5,42	5,4	5,41	1,59	6,7	7,12
Mo			0,457			0,366			0,38
Nb	0,356	0,549	0,75	0,341	0,349	0,53	0,504	0,413	0,66
Cs	0,393	0,374	0,193	0,31	0,28	0,429	0,4	0,355	0,378
Ba	8,93	10,93	9,03	6,92	7,08	6,5	8,51	8,32	7,85
La	4,77	4,56	4,66	6,12	6,29	5,92	5,26	5,22	4,57
Ce	5,87	5,78	5,34	7,92	7,48	7,68	6,88	7,09	6,88
Pr	0,61	0,72	0,72	0,854	0,84	0,849	0,823	1,8	0,657
Nd	3,3	2,88	3,13	3,88	3,75	3,25	4,32	4,36	3,61
Sm	0,49	0,69	0,51	0,744	0,749	0,63	0,81	0,97	0,83
Eu	0,206	0,1025	0,261	0,173	0,1735	0,1735	0,195	0,158	0,231
Gd	0,44	0,65	0,75	0,91	0,93	0,95	1,11	0,75	0,94
Tb	0,161	0,095	0,08	0,121	0,139	0,132	0,115	0,121	0,144
Dy	1,05	0,98	1,09	0,76	0,9	0,75	1,4	0,78	0,84
Ho	0,24	0,2	0,22	0,192	0,201	0,237	0,272	0,31	0,216
Er	0,9	0,56	0,95	0,69	0,62	0,48	0,72	1,11	0,7
Yb	1,02	0,96	0,75	0,66	0,68	0,89	0,79	0,89	0,73
Lu	0,206	0,159	0,152	0,098	0,155	0,101	0,145	0,145	0,111
Hf	0,122	0,045	0,106	0,065	0,083	0,053	0,085	0,21	0,107
Ta	0,79	0,75	0,73	2,38	2,45	2,35	3,02	2,88	2,24
Pb	1,1	0,76	1,75	1,4	1,24	1,17	1,79	2	1,21
Th	0,48	0,45	0,57	0,381	0,423	0,358	0,618	0,626	0,477
U	0,111	0,091	0,99	<0,023	<0,10	0,1	2,8	0,17	0,191

Element / Sample Nr.	*MP-BIF-43a-67*	*MP-BIF-43b-68*	*MP-BIF-43c-42*	*MP-BIF-44a-41*	*MP-BIF-44b-42*	*MP-BIF-44c-43*	*MP-BIF-45a-78*	*MP-BIF-45b-79*	*MP-BIF-45c-62*
Sc	3,84	3,48	3,08	5,29	5,26	5,23	1,49	1,98	2
Ti	107,95	113,09	109,97	192,59	196,59	209,66	18,6	12,1	18,66
V	12,78	13,58	11,94	12,47	17,03	17,13	7,02	7	8,44
Cr	27,82	27,75	31,44	31,09	33,73	37,54	24,39	30,19	29,48
Mn	9173,07	9792,01	9695,24	14732,91	14720,7	15809,3	4935,57	4823,87	6071,95
Co			20,18			17,01			23,7
Ni			16,82			16,38			15,42
Cu	6,81	8,06	6,7	5,16	5,49	6,02	4,15	4,87	5,46
Zn	18,8	23,78	24,6	23,42	28,5	23,76	23,13	25,13	27,67
Ga	0,58	0,65	0,75	1,96	1,84	1	<1,05	<1,17	0,99
As	9,57	10,82	7,58	10,35	13,75	9,4	4,34	7,33	6,15
Rb	0,834	0,551	0,66	8,33	1,83	1,67	3,33	3,04	3,48
Sr	21,85	23,15	20,65	29,67	29,67	28,56	19,29	21,35	25,72
Y	11,6	13	11,28	12,53	12,7	11,78	11,62	11,41	13,6
Zr	8,11	8,37	7,64	11,92	12,89	10,83	4,08	3,97	4,78
Mo			0,68			1,05			0,179
Nb	0,583	0,667	1,1	0,974	1	1	0,105	0,165	1,08
Cs	0,34	0,383	0,34	1	1	1,26	0,961	0,812	0,89
Ba	7,35	7,72	4,63	7,42	7,82	7,13	8,6	8,86	9,37
La	7,99	8,55	7,6	7,55	7,29	6,83	4,36	4,87	5,09
Ce	10,49	10,34	9,75	11,2	12,17	10,48	5,19	5,28	6,16
Pr	1,01	1,11	1,14	1	1	1,3	0,662	0,625	0,7
Nd	4,25	4,52	4,26	6,09	6,3	6,07	2,91	2,81	2,82
Sm	0,85	0,96	0,8	0,96	1,25	1,13	0,55	0,81	0,88
Eu	0,1995	0,2045	0,2345	0,364	0,3615	0,265	0,1275	0,3825	0,189
Gd	0,82	0,9	1,15	1,28	1,48	0,93	1,2	0,91	1,2
Tb	0,146	0,155	0,108	0,171	0,218	0,158	0,101	0,109	0,128
Dy	1,26	1,31	0,99	1,19	1,55	1,33	0,93	0,88	0,91
Ho	0,29	0,29	0,24	0,328	0,312	0,23	0,211	0,26	0,22
Er	0,86	0,75	0,38	0,77	1	0,97	0,7	0,5	0,78
Yb	1,17	0,97	0,87	0,53	0,78	0,75	0,6	0,32	0,75
Lu	0,169	0,198	0,153	0,328	0,176	0,168	0,086	0,111	0,113
Hf	0,169	0,135	0,099	0,202	0,212	0,201	0,124	0,024	0,142
Ta	0,75	0,81	0,68	2,76	2,71	2,31	3,39	3,25	3,83
Pb	1,98	2,16	1,39	2,16	2,5	2,03	1,19	1,02	1,32
Th	0,73	0,81	0,65	1,65	1,73	1,6	0,139	0,149	0,146
U	0,184	0,144	0,116	0,428	0,744	0,4	0,0344	0,457	0,102

Element / Sample Nr.	*MP-BIF-46a-67*	*MP-BIF-46b-68*	*MP-BIF-46c-56*	*MP-BIF-47a-83*	*MP-BIF-47b-84*	*MP-BIF-47c-49*	*MP-BIF-48a-54*	*MP-BIF-48b-55*	*MP-BIF-48c-48*
Sc	1,93	2,3	2,29	3,73	3,52	2,96	3,95	3,78	3,99
Ti	40,55	37,25	41,13	101,84	115,38	117,84	108,06	109,51	105,53
V	8,4	8,17	8,93	18,94	14,92	12,76	11,15	10,82	11,33
Cr	25,65	31,14	35,36	43,95	35,43	38,72	28,97	27,87	36,55
Mn	13024,64	13363,57	13821,3	5972,07	5753,58	6185,34	6242,55	6362,02	6745,24
Co			18,71			24,84			34,94
Ni			31,72			23,42			<13,35
Cu	6,93	4,17	4,54	12,2	10,86	12,33	6,88	6,2	6,9
Zn	18,7	21,38	23,25	29,94	19,79	20,98	26,99	24,76	26,45
Ga	<0,77	<1,02	<0,69	1,1	0,89	0,96	1,16	1,38	1,75
As	7,98	6,64	6,33	13,84	10,27	10,6	6,99	7,86	11,84
Rb	1,32	1,4	1,51	1,21	0,62	1	1,29	1,31	1,33
Sr	30,58	30,52	30,56	9,68	9,17	33,9	5,89	6,54	5,95
Y	27,26	26,92	25,73	10,97	11,24	10,92	5,99	6,22	5,55
Zr	5,97	6,11	6,85	8,53	8,24	8,39	8,11	9,11	7,38
Mo			0,322			0,724			0,551
Nb	0,269	0,358	0,93	0,586	0,539	0,69	0,717	0,769	0,69
Cs	0,345	0,399	0,414	1,35	0,404	0,336	0,826	0,755	0,86
Ba	9,36	10,21	9,93	7,9	8,14	7,92	8,9	10,79	8,68
La	6,35	5,95	5,79	7,92	8,3	7,61	1,82	1,85	1,69
Ce	7,2	7,39	7,32	10,88	10,95	11,05	1,75	1,83	1,7
Pr	0,534	0,731	0,98	0,93	1,16	1,1	0,243	0,237	0,214
Nd	4,27	5,4	3,29	5,69	4,48	4,26	1,09	1,04	1,18
Sm	0,91	1,05	0,5	0,85	0,74	1,19	0,284	<0,33	0,34
Eu	0,352	0,524	0,26	0,136	0,1785	0,185	0,0995	0,07	0,105
Gd	0,96	0,98	1,14	0,84	1,4	0,89	<0,23	0,45	<0,58
Tb	0,189	0,244	0,166	0,117	0,109	0,156	0,08	<0,067	0,085
Dy	1,88	2,27	1,85	1,25	1,53	1,31	0,53	0,77	0,62
Ho	0,51	0,52	0,49	0,31	0,24	0,28	0,177	0,179	0,123
Er	1,75	1,53	1,65	0,69	1,45	0,81	0,53	0,44	0,55
Yb	1,69	2,02	2,93	1,04	1,14	0,87	0,85	0,61	0,73
Lu	0,476	0,339	0,39	0,171	0,255	0,247	0,177	0,109	0,097
Hf	0,127	0,096	0,062	0,27	0,137	<0,082	0,21	0,267	0,138
Ta	2,92	2,92	2,73	1,58	1,38	1,28	2,67	2,7	2,39
Pb	1,69	1,14	0,88	2,51	3,68	2,11	1,55	2,01	1,77
Th	0,335	0,316	0,29	0,62	0,72	0,61	0,627	0,744	0,6
U	0,069	0,053	0,156	0,158	0,132	0,96	0,207	0,223	0,188

Element / Sample Nr.	*MP-BIF-49a-56*	*MP-BIF-49b-57*	*MP-BIF-49c-49*	*MP-BIF-50a-88*	*MP-BIF-50b-89*	*MP-BIF-50c-50*	*MP-BIF-51a-104*	*MP-BIF-51b-105*	*MP-BIF-51c-8*
Sc	2,62	2,79	2,44	2,43	3,16	2,42	3,16	3,2	3,91
Ti	43,16	49,99	52,23	76,37	80,1	74,41	98,56	95,56	99,73
V	9,27	8,85	8,92	11,5	11,82	9,88	11,75	12,12	13,17
Cr	27,7	32,53	28,69	37,22	29,65	27,77	34,4	32,13	35,07
Mn	8406,33	8436,68	8919,31	7297,79	7214,78	7610,33	3855,89	3932,04	4049,61
Co			26,67			23,37			22,41
Ni			11,48			21,72			16,9
Cu	3,79	3,53	5,19	4,79	4,92	6,56	<1,39	5,75	12,61
Zn	30,04	21,23	25,13	20,86	10,96	18,88	21,35	16,67	24,81
Ga	1,63	<1,77	<0,54	<0,51	0,67	1,69	1,34	3,5	0,51
As	7,68	<4,86	6,72	12,32	11,6	9,89	7,82	8,62	8,4
Rb	1,11	1,08	0,903	0,893	1	1,2	1,29	1,39	1,34
Sr	20,95	21,22	19,67	10,04	10,05	9,83	4,52	4,96	4,23
Y	18,59	18,69	17,01	13,65	14,57	12,82	5,63	5,61	5,36
Zr	6,69	7,02	6,27	6,48	6,85	5,79	8,34	9,04	7,4
Mo			0,276			0,528			0,676
Nb	0,298	0,333	1,05	0,588	0,535	0,83	0,728	0,518	0,89
Cs	0,297	0,291	0,295	0,604	0,666	0,669	0,93	5,65	0,649
Ba	7,5	7,51	8,1	7,84	6,86	8,1	8,06	15,83	7,25
La	5,9	7,18	5,6	5,65	5,6	5,42	1,79	1,8	1,53
Ce	7,62	7,82	6,86	8,52	8,61	8,18	1,81	1,93	1,65
Pr	0,836	0,897	0,98	0,96	1,18	1,02	0,264	0,256	0,179
Nd	4,12	4,18	3,71	4,89	5,27	5,04	1,16	2,3	0,85
Sm	0,95	0,77	0,68	1,08	1	1,31	0,373	<0,169	0,175
Eu	0,209	0,213	0,193	0,325	0,2875	0,2305	0,084	0,0885	0,0495
Gd	1,25	<1,40	0,68	1,39	1,39	1,45	0,45	<0,50	0,158
Tb	0,177	0,122	0,22	0,26	0,23	0,152	0,097	0,11	0,047
Dy	1,84	1,5	1,34	1,76	1,4	2,42	0,59	0,73	0,61
Ho	0,45	0,38	0,33	0,48	0,43	0,32	0,195	0,179	0,161
Er	1,09	1,55	1,09	1,26	1,44	1,48	0,47	0,69	0,35
Yb	1,01	1,49	0,94	1,22	1,46	1,28	0,78	1,12	0,7
Lu	0,218	0,288	0,239	0,233	0,196	0,157	0,15	0,144	0,111
Hf	0,096	0,037	0,114	0,11	0,138	0,062	<0,094	0,114	0,088
Ta	3,08	2,83	2,6	0,73	0,82	0,77	2,5	2,43	2,05
Pb	1,09	1,39	0,8	1,17	1,26	1,34	8,78	1,76	1,14
Th	0,416	0,427	0,271	0,61	0,58	0,48	0,65	0,709	0,629
U	0,115	0,097	0,057	0,145	0,168	<0,33	1,08	0,191	0,164

Element / Sample Nr.	*MP-BIF-52a-47*	*MP-BIF-52b-48*	*MP-BIF-52c-46*	*MP-BIF-53a-81*	*MP-BIF-53b-102*	*MP-BIF-53c-48*	*Average StDev*
Sc	4,62	4,48	3,68	2,73	2,24	1,66	0,319341
Ti	159,73	160,8	161,34	75,46	73,21	73,4	5,308537
V	14,94	14,81	14,69	13,2	13,26	12,91	0,766812
Cr	37,63	34,94	44,17	37,25	34,81	36,85	2,083578
Mn	5031,52	4953,3	5172,56	9337,17	9354,7	9980,58	234,8529
Co			27,21			32,29	
Ni			24,17			23,7	
Cu	7,74	7,54	6,55	3,61	3,85	45,1	1,6706
Zn	27,71	21,73	13,15	19,31	21,16	19,55	4,960246
Ga	0,91	<0,47	1,56	0,46	0,79	1,85	
As	7,54	7,55	4,3	9,28	8,09	5,95	0,957743
Rb	1,64	1,51	1,44	0,548	0,552	0,32	0,216245
Sr	53,15	53,55	49,84	24,2	24,93	24,91	1,594954
Y	16,6	16,28	14,62	35,28	35,8	34,35	0,630434
Zr	11,55	11,09	10,35	7,35	6,8	6,71	0,454048
Mo			0,575			0,49	
Nb	0,78	0,606	0,9	0,494	0,559	0,85	0,187067
Cs	0,826	0,764	0,772	0,246	0,21	0,274	0,160617
Ba	13,88	15,76	13,85	11,51	12,72	11,04	0,81735
La	8,2	8,17	7,36	14,57	14,42	14,07	0,272971
Ce	11,2	11,38	10,35	22,31	22,72	23,05	0,421463
Pr	1	1	1,05	2,81	2,95	2,61	0,076777
Nd	5,2	5,32	5,67	11,68	12,93	12,35	0,289946
Sm	1,05	0,35	1,13	2,38	2,59	2,23	0,107583
Eu	0,243	0,3085	0,2345	0,58	0,595	0,59	0,034912
Gd	0,74	1,23	1,14	4,01	3,04	3,11	0,139427
Tb	0,216	0,194	0,22	0,47	0,52	0,53	0,024698
Dy	1,53	1,12	1,15	3,88	4,07	4,14	0,158735
Ho	0,339	0,289	0,32	0,85	1,15	0,82	0,039529
Er	0,99	1,22	1,12	3,74	3,23	2,98	0,122052
Yb	0,85	0,72	1,14	3,28	3,48	2,6	0,168562
Lu	0,238	0,225	0,184	0,43	0,51	0,54	0,027763
Hf	0,256	0,33	0,172	0,095	0,04	0,072	
Ta	2,73	3,63	2,32	0,83	0,84	0,69	0,194029
Pb	1,27	<0,28	1,51	2,02	1,9	2,13	1,477437
Th	0,928	1,09	0,74	0,49	0,35	0,368	0,057917
U	0,24	0,131	0,169	0,091	0,103	0,094	0,187185

Table 3: LA-ICP-MS determined trace element abundance (ppm) of BCR2G reference material. The GeoRem accepted values, average BCR2G and their respective agreement with one another are presented as well. The agreement of the measured BCR2G usually lies within 10 % of the accepted values.

Element	*BCR2G-4*	*BCR2G-17*	*BCR2G-30*	*BCR2G-39*	*BCR2G-4*	*BCR2G-30*	*BCR2G-51*	*BCR2G-64*	*BCR2G-75*
Sc	33,39	35,85	34,7	35,11	33,94	35,78	35,4	36,52	33,35
Ti	16288,18	17182,71	16951,71	17273,12	16807,21	17577,39	16736,28	16963,56	16670,46
V	461,12	466,34	458,98	463,7	460,72	475,55	454,48	463,81	463,95
Cr	17,7	17,9	17,81	17,57	18,55	18,2	17,4	17,28	17,86
Mn	1616,86	1604,07	1580,23	1571,12	1573,17	1500,93	1457,13	1455,25	1532,69
Co									
Ni									
Cu	16,19	16,31	16,02	16,62	16,26	16,45	16,95	16,1	15,48
Zn	149,88	149,89	149,3	158,96	166,26	166,86	142,61	143	144,91
Ga	47,13	46,58	46,38	46,51	46,38	45,91	45,48	46,37	46,01
Rb	49,55	49,98	49,73	51,48	48,56	51,36	50,46	50,72	47,35
Sr	329,53	350,38	340,3	355,23	321,44	349	339,83	350,2	325,16
Y	31,24	34,48	32,66	33,18	32,47	32,65	34	34,68	31,08
Zr	161,34	175,79	166,87	170,68	166,22	169,4	170,39	178,46	160,24
Nb	11,38	11,95	11,82	12,14	11,42	11,87	11,32	11,83	11,24
Mo									
Cs	1,201	1,180	1,218	1,230	1,174	1,177	1,169	1,192	1,092
Ba	645,77	690,77	673,93	709,42	666,9	691,88	668,66	688,78	636,69
La	23,53	25,66	24,7	25,98	23,93	24,53	24,61	25,28	23,54
Ce	51,25	55,01	53,62	55,52	51,87	53,48	52,04	53,36	51,01
Pr	6,24	6,78	6,44	6,82	6,34	6,37	6,38	6,53	6,18
Nd	26,46	29,11	27,87	29,35	27,28	27,07	26,85	27,74	26,67
Sm	6,02	6,74	6,22	6,52	6,35	5,9	5,88	6,33	6,12
Eu	1,78	1,87	1,78	1,98	1,78	1,71	1,86	1,82	1,79
Gd	6,02	6,5	6,04	6,42	6,12	5,88	6,16	6,62	6,33
Tb	0,918	0,939	0,914	0,961	0,95	0,87	0,86	0,92	0,96
Dy	5,98	6,38	6,19	6,32	6,1	5,74	5,96	6,22	6,28
Ho	1,18	1,27	1,23	1,22	1,25	1,13	1,21	1,25	1,18
Er	3,42	3,47	3,31	3,3	3,45	3,29	3,39	3,47	3,49
Yb	3,23	3,59	3,4	3,11	3,41	3,14	3,19	3,34	3,62
Lu	0,444	0,515	0,481	0,521	0,484	0,483	0,483	0,523	0,435
Hf	4,26	4,69	4,34	4,48	4,3	4,43	4,54	4,68	4,21
Ta	0,702	0,804	0,721	0,802	0,74	0,738	0,766	0,78	0,717
Pb	10,99	10,75	10,93	11,71	11,03	10,6	10,65	10,47	11,24
Th	5,3	6,03	5,58	5,99	5,45	5,6	5,62	5,93	5,29
U	1,66	1,83	1,72	1,84	1,63	1,67	1,62	1,68	1,6

Element	*BCR2G-88*	*BCR2G-101*	*BCR2G-4*	*BCR2G-17*	*BCR2G-26*	*BCR2G-4*	*BCR2G-17*	*BCR2G-30*	*BCR2G-49*
Sc	35,72	34,47	36,86	34,4	34,99	31,74	35,25	33,88	35,35
Ti	17175,42	16901,72	17679,25	17140,5	16393,86	17115,23	17596,56	17736,8	17825,87
V	465,97	459,32	473,05	470,66	469,6	470,71	470,23	475,15	476,81
Cr	17,82	18,1	18,84	18	18,14	18,95	18,34	18,51	17,98
Mn	1495,19	1475,07	1568,22	1565,56	1659,12	1675,59	1595,83	1561,89	1526,73
Co									
Ni									
Cu	15,56	15,98	16,31	16,35	16,41	15,46	16,33	16,62	16,21
Zn	138,47	137,16	200,16	185,91	159,52	166,42	140,75	172,47	162,56
Ga	45,24	45,43	46,2	46,42	46,68	38,17	37,56	37,62	37,88
Rb	48,8	48,31	49,95	50,93	52,69	50,14	48,45	50,32	49,58
Sr	339,64	336,36	330,05	329,92	339,97	328,93	331,35	334,42	347,69
Y	33,49	32,77	34,34	31,51	32,96	30,78	32,36	30,65	32,1
Zr	170,85	168,77	178,2	163,41	169,01	156,67	168,48	158,42	166,41
Nb	11,53	11,65	11,6	11,58	11,73	11,8	11,5	11,72	11,58
Mo									
Cs	1,111	1,200	1,118	1,169	1,178	1,143	1,129	1,158	1,137
Ba	664,94	670,46	677,7	669,47	682,02	705,43	657,07	665,27	665,07
La	24,52	24,79	24,99	23,87	24,75	23,85	24,29	23,46	24,01
Ce	52,57	53,57	52,68	52,54	54,79	55,83	51,27	51,85	52,07
Pr	6,41	6,48	6,4	6,36	6,65	6,55	6,24	6,18	6,22
Nd	27,89	28,02	28,29	26,91	28,85	28,64	27,09	25,94	26,99
Sm	6,41	6,22	6,54	6,22	6,44	6,42	6,2	5,85	5,86
Eu	1,92	1,94	1,86	1,79	1,84	1,92	1,79	1,72	1,76
Gd	6,5	6,53	6,21	5,84	6,79	6,48	6,05	5,55	5,77
Tb	1,02	0,96	0,934	0,89	1,03	0,97	0,91	0,84	0,84
Dy	6,64	6,78	6,29	5,68	7,03	6,52	5,8	5,36	5,54
Ho	1,31	1,32	1,18	1,11	1,41	1,25	1,15	1,07	1,08
Er	3,68	3,61	3,34	3,11	4,05	3,64	3,18	2,91	3,01
Yb	3,66	3,7	3,21	3,04	4,11	3,63	3,11	2,93	2,94
Lu	0,513	0,508	0,495	0,45	0,491	0,479	0,468	0,431	0,465
Hf	4,52	4,6	4,56	4,09	4,71	4,34	4,14	3,96	4,21
Ta	0,725	0,747	0,758	0,716	0,77	0,78	0,71	0,68	0,7
Pb	10,71	11,15	10,69	11,14	12,58	12,48	10,21	10,4	9,99
Th	5,71	5,73	5,61	5,36	5,8	5,66	5,34	5,06	5,27
U	1,68	1,7	1,64	1,63	1,76	1,93	1,53	1,58	1,61

Element	*BCR2G-62*	*BCR2G-73*	*BCR2G-87*	*BCR2G-100*	*BCR2G-4*	*BCR2G-15*	*BCR2G-4*	*BCR2G-17*	*BCR2G-36*
Sc	35,51	36,12	37,23	35,89	37,08	34,16	35,52	35,35	34,59
Ti	17353,42	18182,55	17899,95	18277,37	17053,7	17186,56	17080,46	17321,86	16851,08
V	460,71	489,66	480,46	489,57	461,81	468,78	471,95	466,47	462,78
Cr	18	19,33	18,91	18,28	17,75	18,44	18,82	18,14	17,98
Mn	1491,81	1566,25	1567,13	1622,27	1565,47	1616,64	1633,31	1558,8	1519,62
Co							40,01	39,14	38,32
Ni							11,73	11,74	11,68
Cu	17,53	15,95	16,05	15,12	18,99	17,15	18,08	17,53	17,39
Zn	151,41	159,62	152,08	159,8	152,73	159,58	142,34	155,04	144,48
Ga	38,04	38,97	39,11	40,03	41,86	42	43,08	42,18	41,05
Rb	50,5	50,51	50,14	50,6	48,62	47,91	49,66	48,81	48,54
Sr	337,94	358,61	357,64	366,69	344,74	341,46	347,17	334,73	335,75
Y	32,43	33,68	35,61	33,72	34,37	31,04	33,79	31,75	31,13
Zr	167,14	174,97	182,77	175,63	179,89	162,74	173,59	161,23	159,41
Nb	11,58	12,29	12,15	12,62	11,64	11,81	11,62	11,32	11,22
Mo							272,65	266,79	261,94
Cs	1,100	1,170	1,180	1,170	1,113	1,023	1,125	1,135	1,130
Ba	657,2	705,41	707,69	722,63	667,16	669,13	675,18	648,91	658,85
La	24,36	25,75	26,74	26,44	24,65	24,4	25,26	23,73	23,69
Ce	51,63	55,72	56,2	57,06	52,23	53,18	53,02	51,24	51,15
Pr	6,32	6,7	6,91	6,99	6,41	6,3	6,45	6,17	6,22
Nd	27,42	29,14	30,84	30,4	27,75	27,13	28,32	26,53	26,11
Sm	6,2	6,54	6,99	7,02	6,19	6,25	6,29	5,79	5,78
Eu	1,82	1,92	2,07	2,04	1,8	1,87	1,83	1,7	1,75
Gd	6	6,57	6,88	6,95	6,35	6,18	6,37	5,83	5,62
Tb	0,89	0,98	1,11	1,09	0,9	0,94	0,91	0,87	0,85
Dy	5,79	6,35	7,16	6,97	6,12	6,03	6,22	5,34	5,5
Ho	1,12	1,26	1,43	1,39	1,19	1,21	1,23	1,09	1,09
Er	3,21	3,49	4,06	4,06	3,41	3,45	3,42	3,09	2,97
Yb	3	3,5	4,12	4,05	3,21	3,19	3,41	2,94	2,98
Lu	0,46	0,5	0,55	0,53	0,522	0,451	0,496	0,453	0,45
Hf	4,28	4,61	5,11	4,89	4,67	4,23	4,54	4,08	4,13
Ta	0,71	0,8	0,85	0,85	0,775	0,72	0,75	0,69	0,68
Pb	10,02	11,36	12,23	12,86	9,72	11,02	11,14	9,84	9,71
Th	5,36	5,88	6,49	6,35	5,77	5,43	5,65	5,24	5,26
U	1,62	1,71	1,84	1,92	1,73	1,66	1,69	1,57	1,62

Element	*BCR2G-54*	*BCR2G-67*	*BCR2G-4*	*BCR2G-16*	*BCR2G-28*	*BCR2G-41*	*BCR2G-58*	*BCR2G-76*
Sc	34,25	34,26	36,57	34,89	34,93	34,39	35,06	34,36
Ti	16971,9	16946,52	17460,75	17214,7	17293,83	17160,31	17277,64	17062,63
V	464,45	463,3	475,4	475,52	470,87	458,39	466,19	460,15
Cr	18,13	19,3	18,24	17,46	17,88	17,82	17,85	18,1
Mn	1564,89	1609,74	1532,35	1553,76	1556,86	1504,67	1583,4	1647,34
Co	38,24	38,37	38,8	47,12	38,21	38,23	39,24	37,9
Ni	12,13	11,91	11,68	12,49	11,31	12,53	13,64	12,89
Cu	17,58	16,73	17,42	16,81	16,23	16,93	17,28	16,64
Zn	137,94	126,22	153,48	154,64	145,21	142,71	135,56	133,31
Ga	41,44	42,79	43,76	44,63	44,15	43,48	45,25	45,8
Rb	49,07	48,87	48,88	49,38	47,99	48,55	50,07	50,57
Sr	338,85	343,73	348,58	338,82	338,19	330,95	350,58	350,02
Y	31,92	32,53	34,22	32,62	32,05	31,04	33,43	33,53
Zr	163,34	166,11	182,67	171,73	167	163,66	172,03	166,1
Nb	11,5	11,79	11,8	11,58	11,64	11,53	11,9	12,04
Mo	269,84	278,01	269,97	271,77	262,8	260,48	277,97	284,21
Cs	1,150	1,190	1,117	1,169	1,147	1,103	1,160	1,220
Ba	671,59	677,78	665,44	668,21	661,93	658,22	698,22	706,11
La	24,33	25,28	24,88	24,49	24,22	24,02	25,64	26
Ce	53,29	54,09	52,22	52,42	51,85	52,06	55,07	57,09
Pr	6,37	6,64	6,48	6,38	6,44	6,32	6,77	6,83
Nd	27,57	28,71	28,35	27,37	27,28	25,94	29,03	30,73
Sm	6,42	6,48	6,25	6,18	5,98	5,99	6,31	7,11
Eu	1,82	1,97	1,79	1,77	1,75	1,74	1,87	1,99
Gd	6,02	6,39	6,3	6,32	6,15	5,65	6,62	7,11
Tb	0,9	1,01	0,93	0,91	0,91	0,85	0,94	1,05
Dy	5,9	6,57	6,06	5,94	6,15	5,33	6,47	7,09
Ho	1,18	1,3	1,18	1,24	1,2	1,09	1,26	1,39
Er	3,16	3,66	3,37	3,38	3,25	2,95	3,45	3,9
Yb	3,25	3,51	3,16	3,16	3,22	2,91	3,49	3,96
Lu	0,47	0,51	0,486	0,494	0,453	0,463	0,51	0,53
Hf	4,48	4,57	4,49	4,35	4,23	4,11	4,58	4,61
Ta	0,72	0,81	0,76	0,75	0,72	0,68	0,77	0,82
Pb	10,4	11,64	10,21	10,46	10,46	9,41	10,8	12,41
Th	5,6	5,92	5,56	5,46	5,37	5,24	5,88	6,06
U	1,65	1,8	1,55	1,66	1,58	1,6	1,72	1,84

Element	*GEORem value*	*Average BCR2G*	*Agreement*
Sc	33	35,05314	1,1
Ti	14100	17217,46	1,2
V	425	468,1889	1,1
Cr	17	18,15371	1,1
Mn	1550	1563,113	1,0
Co	38	39,41636	1,0
Ni	13	12,15727	0,9
Cu	21	16,60057	0,8
Zn	125	152,6069	1,2
Ga	23	43,302	1,9
Rb	47	49,62943	1,1
Sr	342	341,2529	1,0
Y	35	32,75029	0,9
Zr	184	168,8463	0,9
Nb	12,5	11,70543	0,9
Mo	270	270,5845	1,0
Cs	1,16	1,153657	1,0
Ba	683	675,7111	1,0
La	24,7	24,69057	1,0
Ce	53,3	53,25286	1,0
Pr	6,7	6,464857	1,0
Nd	28,9	27,87543	1,0
Sm	6,59	6,286	1,0
Eu	1,97	1,840286	0,9
Gd	6,71	6,260571	0,9
Tb	1,02	0,935029	0,9
Dy	6,44	6,165714	1,0
Ho	1,27	1,2186	1,0
Er	3,7	3,411429	0,9
Yb	3,39	3,354857	1,0
Lu	0,503	0,485629	1,0
Hf	4,84	4,429143	0,9
Ta	0,78	0,748886	1,0
Pb	11	10,89743	1,0
Th	5,9	5,624286	1,0
U	1,69	1,6878	1,0

Table 4: LA-ICP-MS measurements for the Iron powder glass beads (all in ppm). Note that apart from La and Ce nearly all measurements are below the detection limits (values starting with <) and thus are not reliable measurements.

Element	*Fe1-1-5*	*Fe1-2-6*	*Fe1-3-7*	*Fe1-4-8*	*Fe1-5-9*	*Fe1-6-10*	*Fe1-7-11*	*Fe1-8-12*	*Fe1-9-13*
La139	0,721	0,782	0,853	0,681	0,685	0,586	0,712	0,655	0,637
Ce140	0,088	0,052	0,083	0,078	0,112	0,114	0,053	0,121	0,076
Pr141	<0,0169	0,033	0,143	0,058	0,0144	0,0235	0,055	<0,024	<0,0174
Nd146	0,115	0,128	0,069	<0,093	0,17	<0,053	<0,090	<0,096	0,164
Sm147	<0,138	<0,217	<0,151	<0,116	<0,143	<0,091	<0,137	<0,124	<0,119
Eu151	<0,024	<0,037	<0,040	<0,027	<0,030	<0,020	<0,044	<0,042	0,343
Eu153	<0,041	<0,048	<0,024	<0,0172	<0,041	<0,034	<0,047	<0,035	<0,022
Gd157	<0,179	<0,215	<0,236	<0,151	<0,157	<0,182	<0,220	<0,245	<0,229
Tb159	<0,0126	<0,0244	<0,0155	0,0122	<0,024	<0,0179	<0,023	<0,028	<0,0144
Dy163	0,02	<0,103	<0,070	<0,055	<0,071	<0,081	<0,100	<0,085	<0,058
Ho165	0,0103	<0,0220	<0,0178	<0,0160	0,0071	<0,0137	<0,024	<0,0201	0,04
Er166	<0,030	0,051	<0,034	<0,024	0,03	0,031	<0,061	0,121	0,023
Yb172	0,018	<0,051	<0,041	<0,029	<0,061	0,054	<0,067	<0,086	<0,067
Lu175	0,018	<0,035	<0,0179	<0,0135	0,0112	<0,0153	<0,0212	<0,0231	<0,0163

Element	*Fe1-10-14*	*Fe2-1-18*	*Fe2-2-19*	*Fe2-3-20*	*Fe2-4-21*	*Fe2-5-22*	*Fe2-6-23*	*Fe2-7-24*	*Fe2-8-25*
La139	0,83	0,673	0,614	0,748	0,742	0,721	0,694	0,767	0,582
Ce140	0,102	0,074	0,062	0,052	0,059	0,066	0,034	0,032	0,045
Pr141	<0,021	<0,0176	0,137	<0,0212	<0,0179	<0,033	0,219	<0,0182	<0,0181
Nd146	<0,41	<0,078	<0,072	<0,124	<0,092	<0,066	<0,120	0,089	0,058
Sm147	0,241	<0,138	<0,176	<0,151	<0,164	<0,139	0,134	<0,162	<0,085
Eu151	0,043	<0,029	<0,046	<0,025	<0,031	<0,048	<0,074	<0,038	0,06
Eu153	<0,033	<0,046	<0,049	<0,032	<0,036	<0,048	<0,048	<0,035	<0,034
Gd157	<0,207	<0,174	<0,23	<0,197	<0,239	<0,233	<0,212	<0,26	<0,153
Tb159	<0,0072	<0,0123	<0,025	<0,0242	<0,0252	0,0117	<0,0256	<0,021	<0,0176
Dy163	<0,092	<0,056	<0,115	0,102	<0,092	<0,069	<0,083	0,131	<0,054
Ho165	<0,0204	<0,0192	<0,029	0,0238	<0,0199	<0,0111	<0,0151	<0,023	<0,0139
Er166	0,011	<0,027	<0,114	<0,047	<0,038	0,019	<0,059	0,023	<0,021
Yb172	<0,044	<0,059	0,082	<0,042	<0,095	<0,059	<0,046	0,04	<0,053
Lu175	<0,0158	<0,0189	0,0147	<0,0168	<0,0201	<0,0144	<0,0260	<0,0181	<0,0162

Element	Fe2-9-26	Fe2-10-27	Fe3-1-31	Fe3-2-32	Fe3-3-33	Fe3-4-34	Fe3-5-35	Fe3-6-36	Fe3-7-37
La139	0,689	0,662	0,629	0,714	0,799	0,776	0,567	0,988	0,647
Ce140	0,085	0,078	0,114	0,207	0,152	0,144	0,07	0,08	0,137
Pr141	<0,0171	<0,0204	<0,0128	<0,064	<0,024	<0,027	<0,056	<0,027	0,0159
Nd146	<0,088	0,042	<0,060	<0,060	<0,113	<0,130	<0,068	<0,105	<0,099
Sm147	<0,197	<0,151	<0,137	<0,129	<0,166	<0,175	<0,23	<0,174	<0,198
Eu151	<0,051	<0,031	<0,034	<0,054	<0,049	<0,022	<0,061	<0,044	<0,054
Eu153	<0,037	<0,053	<0,030	<0,151	0,197	<0,071	<0,048	<0,050	<0,047
Gd157	<0,206	<0,195	0,155	<0,25	<0,228	<0,213	<0,30	<0,27	<0,21
Tb159	<0,027	<0,033	<0,0128	0,059	<0,027	0,023	0,02	<0,041	<0,022
Dy163	<0,084	0,039	<0,065	0,144	<0,112	<0,082	<0,145	0,119	0,073
Ho165	<0,0233	<0,0225	<0,015	<0,019	<0,035	0,027	<0,031	<0,018	<0,031
Er166	<0,076	<0,056	0,027	<0,058	<0,075	<0,046	<0,077	<0,053	<0,072
Yb172	<0,047	<0,049	<0,053	<0,146	0,064	<0,00	<0,098	<0,118	<0,092
Lu175	<0,0145	0,0109	0,082	<0,0206	<0,0191	<0,0259	<0,033	<0,032	<0,023

Element	Fe3-8-38	Fe3-9-39	Fe3-10-40	Average
La139	0,706	0,773	0,616	0,7083
Ce140	0,086	0,112	0,113	0,089367
Pr141	<0,030	<0,0223	<0,027	0,023293
Nd146	<0,098	<0,096	<0,105	0,027833
Sm147	<0,149	<0,160	<0,183	0,0125
Eu151	<0,060	<0,047	<0,036	0,014867
Eu153	<0,046	<0,044	<0,069	0,006567
Gd157	<0,27	<0,30	<0,34	0,005167
Tb159	<0,0216	<0,029	<0,034	0,004197
Dy163	<0,124	<0,100	<0,169	0,020933
Ho165	<0,030	0,019	<0,070	0,00424
Er166	0,095	<0,080	<0,039	0,014367
Yb172	<0,073	<0,112	<0,142	0,0086
Lu175	<0,027	<0,025	<0,024	0,00456

4. Carbon Isotope values

Table 5: The carbon isotope values (in ‰) for each individual sample.

Sample	*δ13C*
G7BF - 01	-11,35
G7BF - 02	-11,93
G7BF - 03	-12,91
G7BF - 04	-12,60
G7BF - 05	-12,85
G7BF - 06	-12,52
G7BF - 07	-12,22
G7BF - 08	-12,56
G7BF - 09	-12,39
G7BF - 10	-12,65
G7BF - 11	-11,69
G7BF - 12	-14,33
G7BF - 13	-15,35
G7BF - 14	-17,97
G7BF - 15	-18,32
G7BF - 16	-18,01
G7BF - 17	-18,39
G7BF - 18	-17,80
G7BF - 19	-17,45
G7BF - 20	-15,01
G7BF - 21	-14,75
G7BF - 22	-15,70

Sample	*δ13C*
MP-BIF-01	-14,18
MP-BIF-02	-13,74
MP-BIF-03	-14,61
MP-BIF-04	-14,59
MP-BIF-05	-15,22
MP-BIF-06	-15,25
MP-BIF-07	-15,57
MP-BIF-08	-15,98
MP-BIF-09	-16,36
MP-BIF-10	-16,60
MP-BIF-11	-16,65
MP-BIF-12	-16,92
MP-BIF-13	-17,15
MP-BIF-14	-17,28
MP-BIF-15	-17,41
MP-BIF-16	-17,41
MP-BIF-17	-17,52
MP-BIF-18	-17,63
MP-BIF-19	-17,79
MP-BIF-20	-17,91
MP-BIF-21	-17,69
MP-BIF-22	-17,94
MP-BIF-23	-17,14
MP-BIF-24	-17,81
MP-BIF-25	-17,79
MP-BIF-26	-17,26
MP-BIF-27	-17,91
MP-BIF-28	-17,82
MP-BIF-29	-17,62
MP-BIF-30	-17,66
MP-BIF-31	-17,73
MP-BIF-32	-17,21
MP-BIF-33	-18,11
MP-BIF-34	-17,75
MP-BIF-35	-17,72
MP-BIF-36	-18,53
MP-BIF-37	-17,76
MP-BIF-38	-17,53
MP-BIF-39	-17,66
MP-BIF-40	-17,62
MP-BIF-41	-17,03
MP-BIF-42	-16,90
MP-BIF-43	-17,45

MP-BIF-44	-17,31
MP-BIF-45	-17,07
MP-BIF-46	-17,69
MP-BIF-47	-17,64
MP-BIF-48	-19,20
MP-BIF-49	-20,66
MP-BIF-50	-19,00
MP-BIF-51	-19,40
MP-BIF-52	-17,83
MP-BIF-53	-18,43

5. XRD

2θ Background subtracted plots from the XRD results for the selected number of samples. The coloured bars represent the mineral peak position selected from the database.

G7BF-01

(Coupled TwoTheta/Theta)

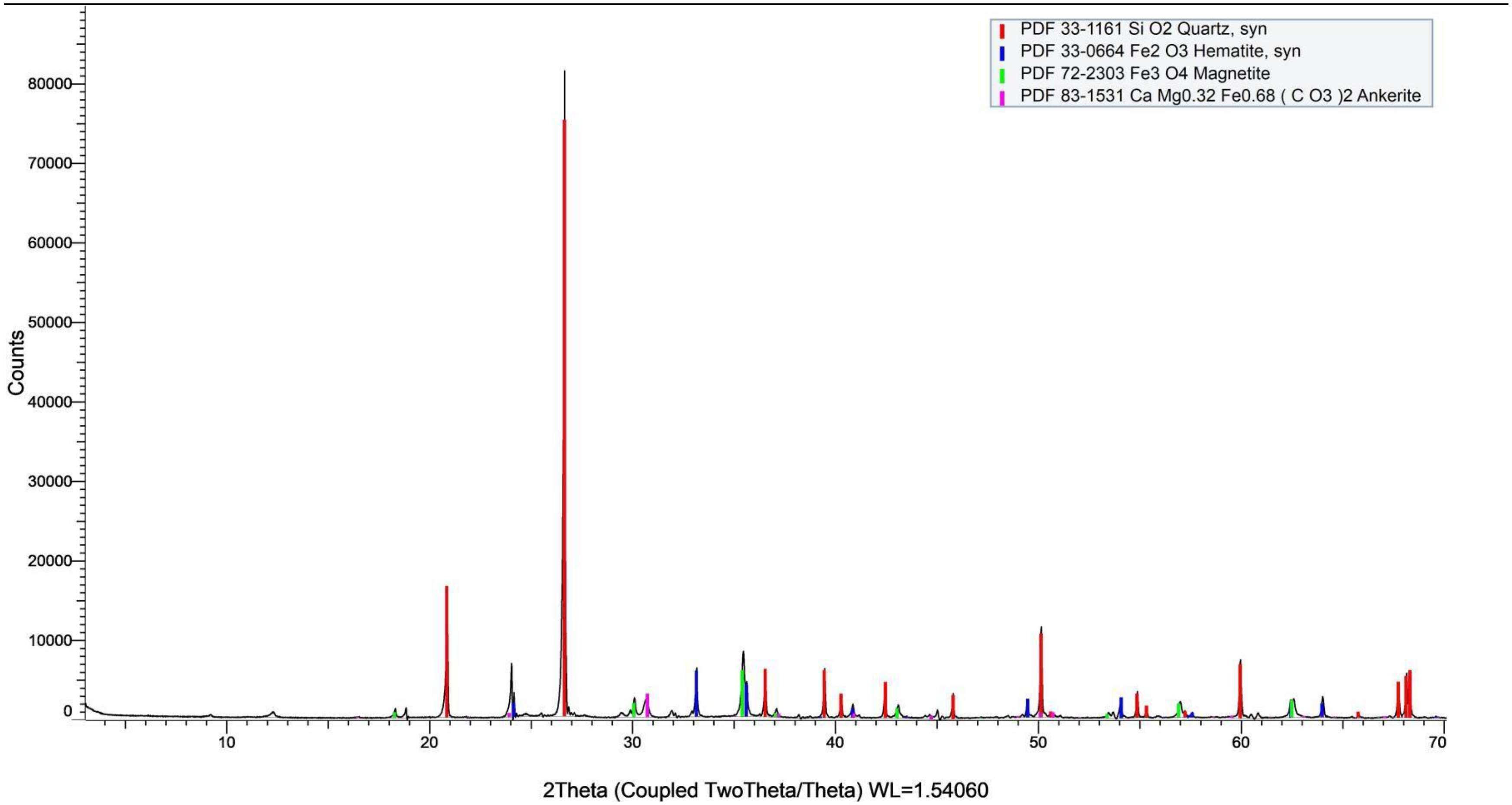

G7BF-06

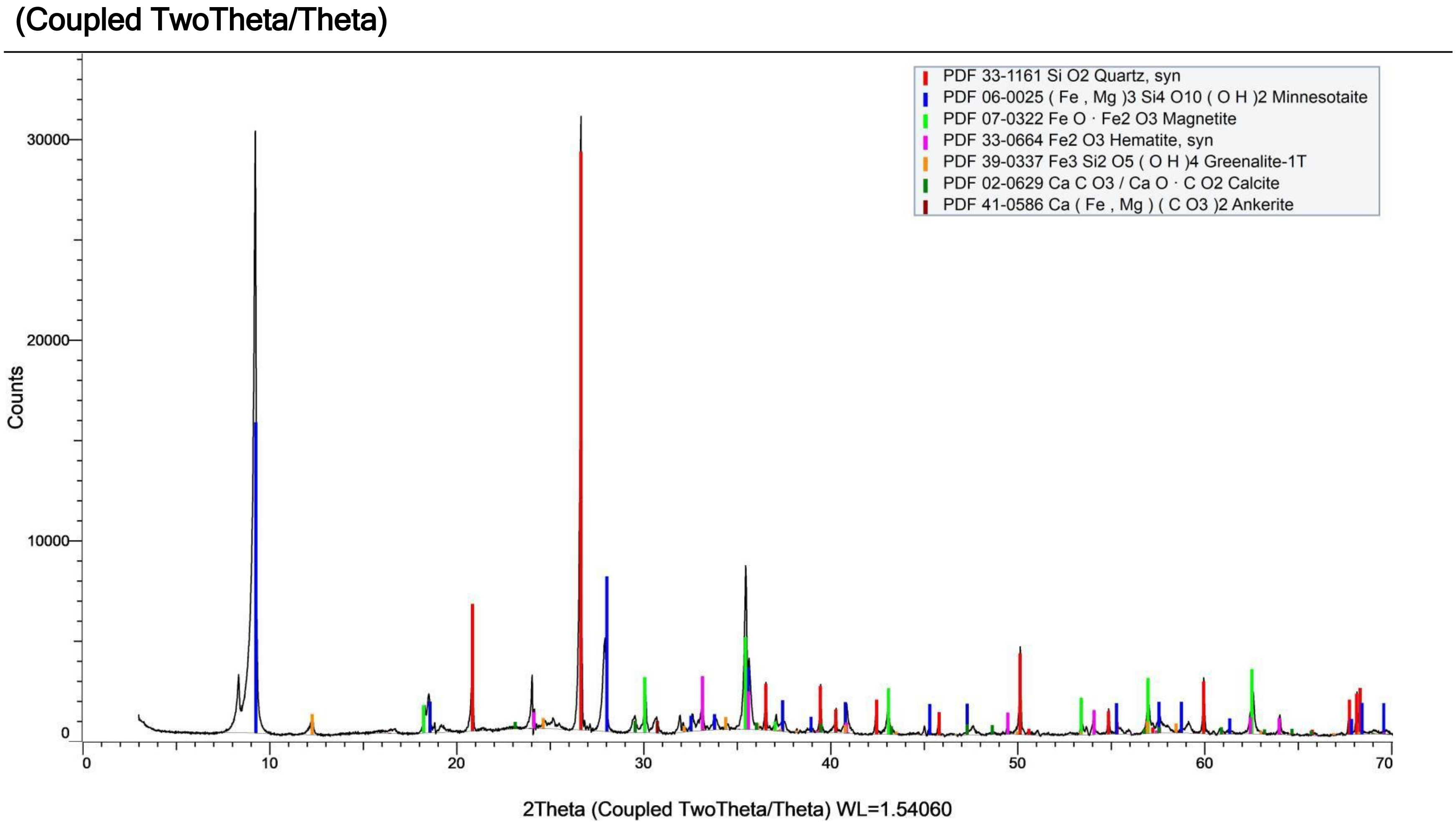
(Coupled TwoTheta/Theta)
PDF 33-1161 Si O2 Quartz, syn
PDF 06-0025 (Fe , Mg)3 Si4 O10 (O H)2 Minnesotaite
PDF 07-0322 Fe O · Fe2 O3 Magnetite
PDF 33-0664 Fe2 O3 Hematite, syn
PDF 39-0337 Fe3 Si2 O5 (O H)4 Greenalite-1T
PDF 02-0629 Ca C O3 / Ca O · C O2 Calcite
PDF 41-0586 Ca (Fe , Mg) (C O3)2 Ankerite
Counts
30000
20000
10000
0
0
10
20
30
40
50
60
70
2Theta (Coupled TwoTheta/Theta) WL=1.54060

G7BF-09

(Coupled TwoTheta/Theta)

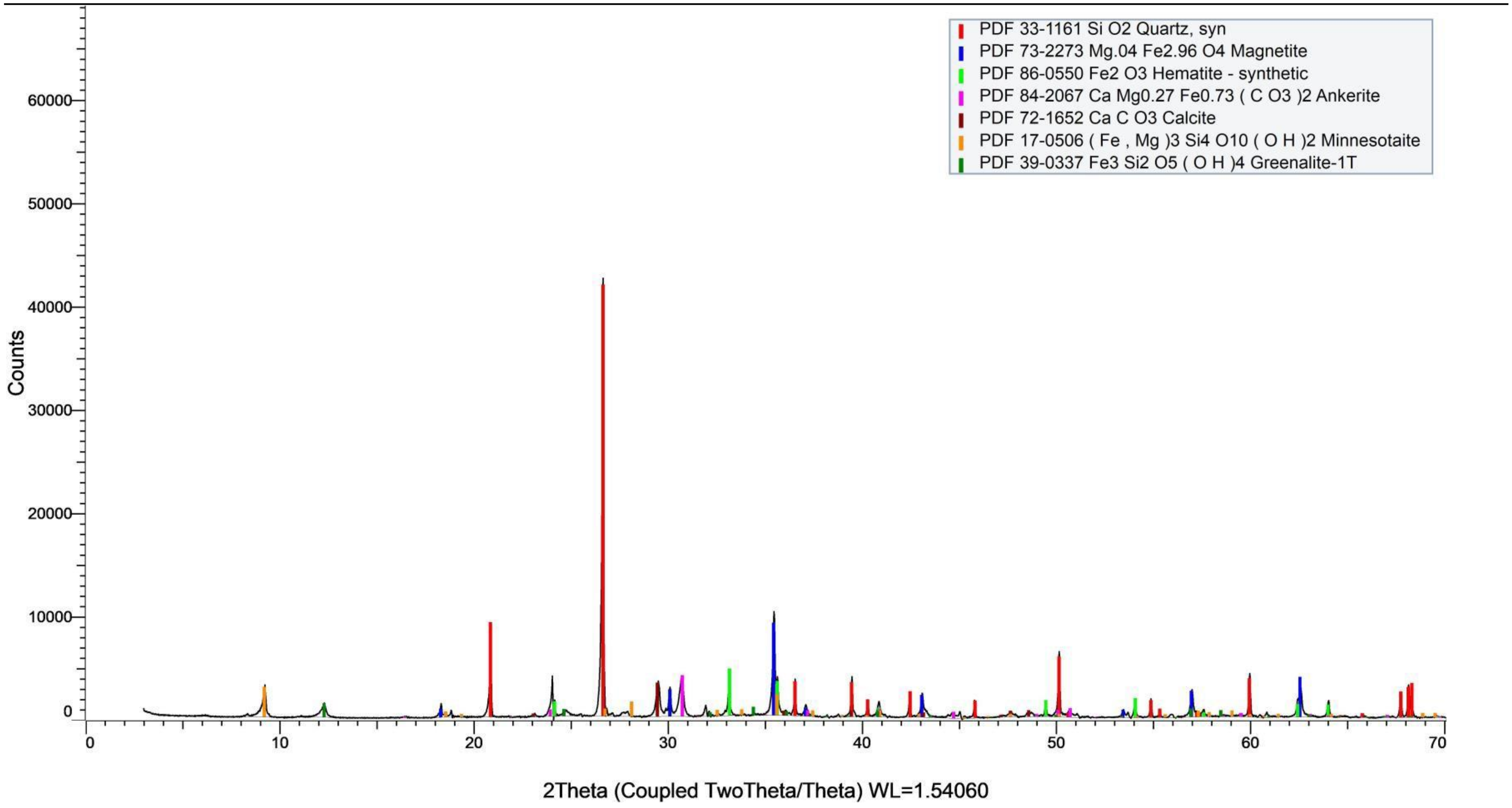

G7BF-11

(Coupled TwoTheta/Theta)

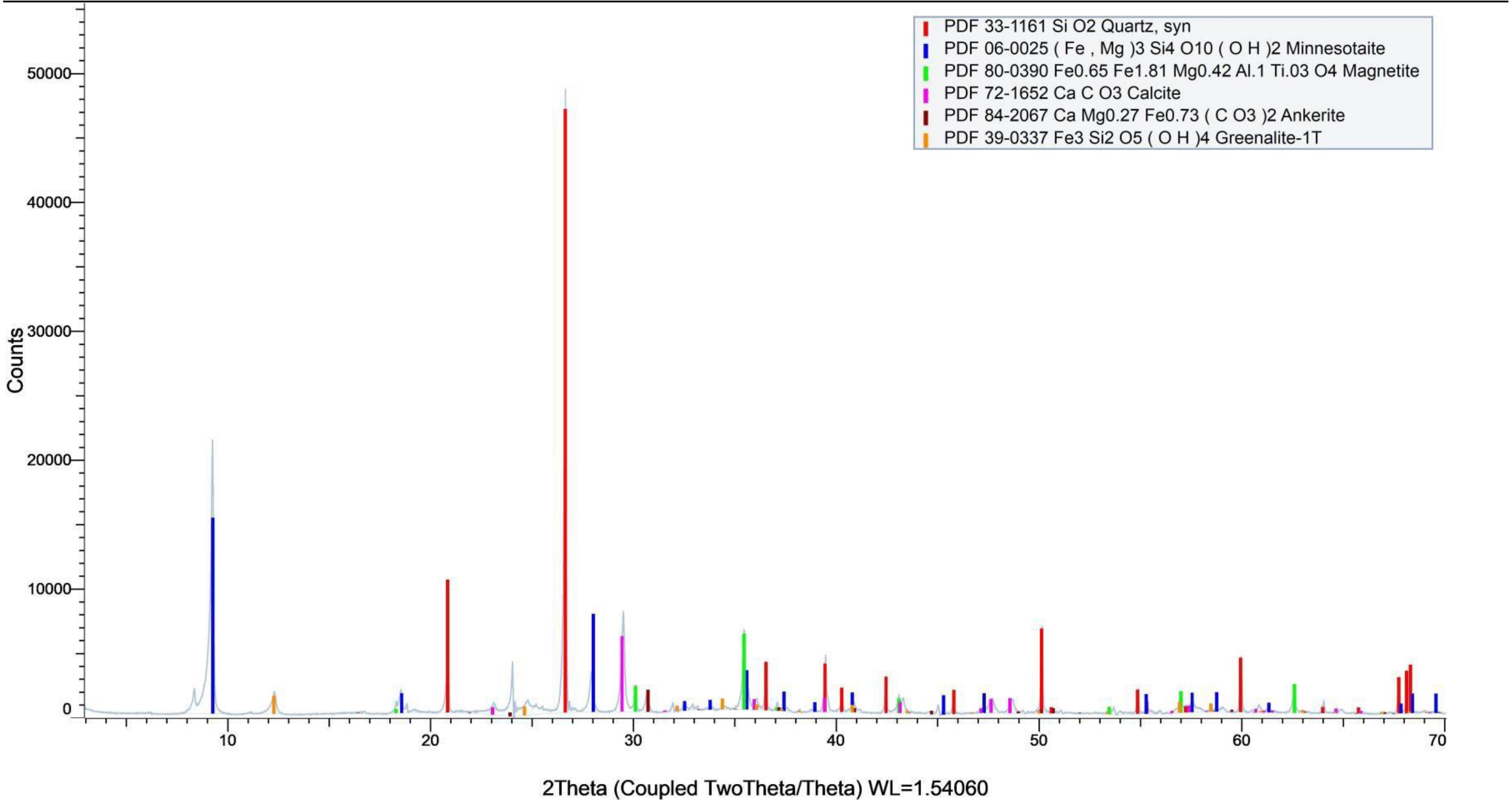

G7BF-13

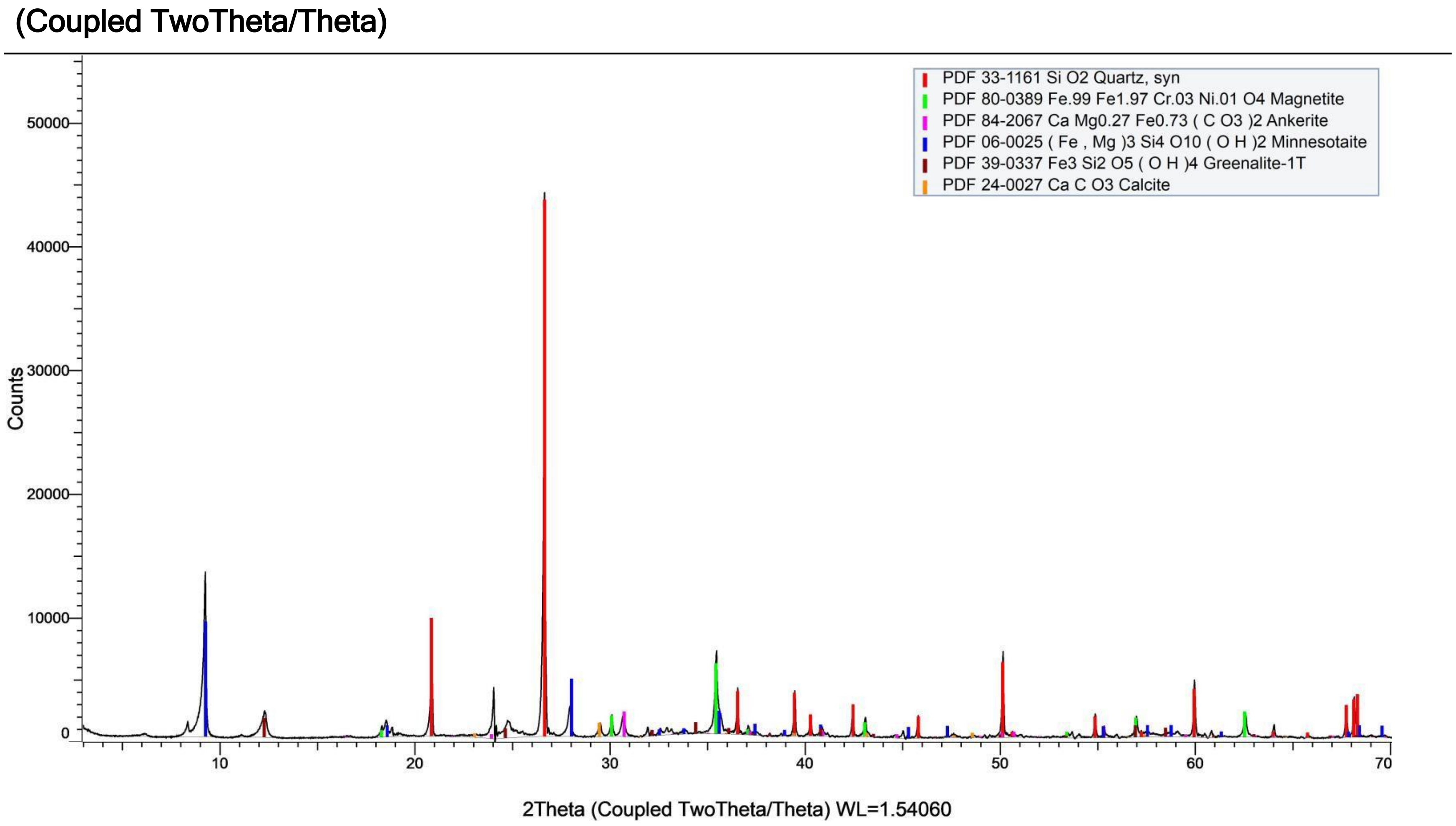
(Coupled TwoTheta/Theta)
PDF 33-1161 Si O2 Quartz, syn
PDF 80-0389 Fe.99 Fe1.97 Cr.03 Ni.01 O4 Magnetite
PDF 84-2067 Ca Mg0.27 Fe0.73 (C O3)2 Ankerite
PDF 06-0025 (Fe , Mg)3 Si4 O10 (O H)2 Minnesotaite
PDF 39-0337 Fe3 Si2 O5 (O H)4 Greenalite-1T
PDF 24-0027 Ca C O3 Calcite
Counts
50000
40000
30000
20000
10000
0
10
20
30
40
50
60
70
2Theta (Coupled TwoTheta/Theta) WL=1.54060

G7BF-14

(Coupled TwoTheta/Theta)

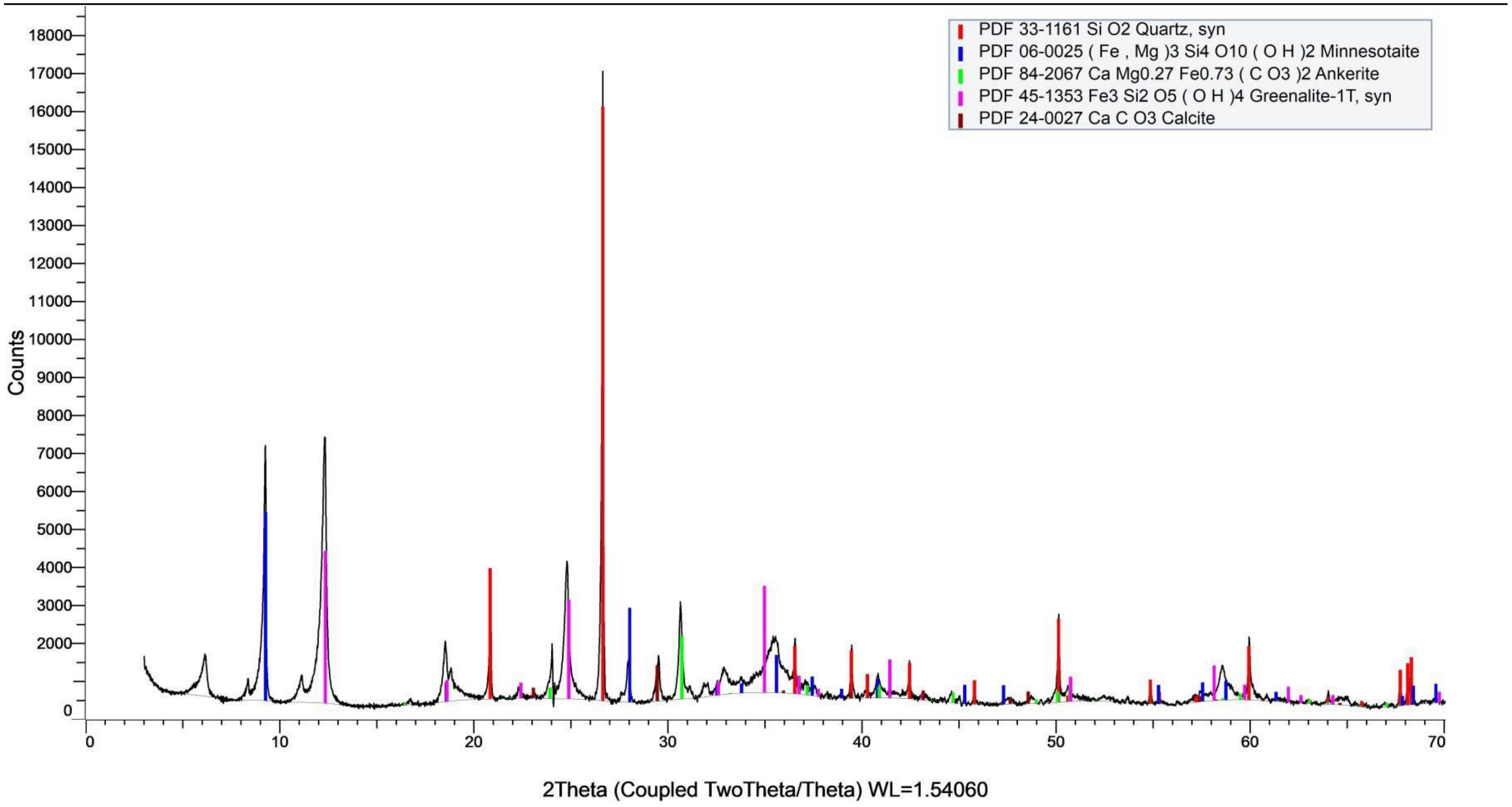

G7BF-19

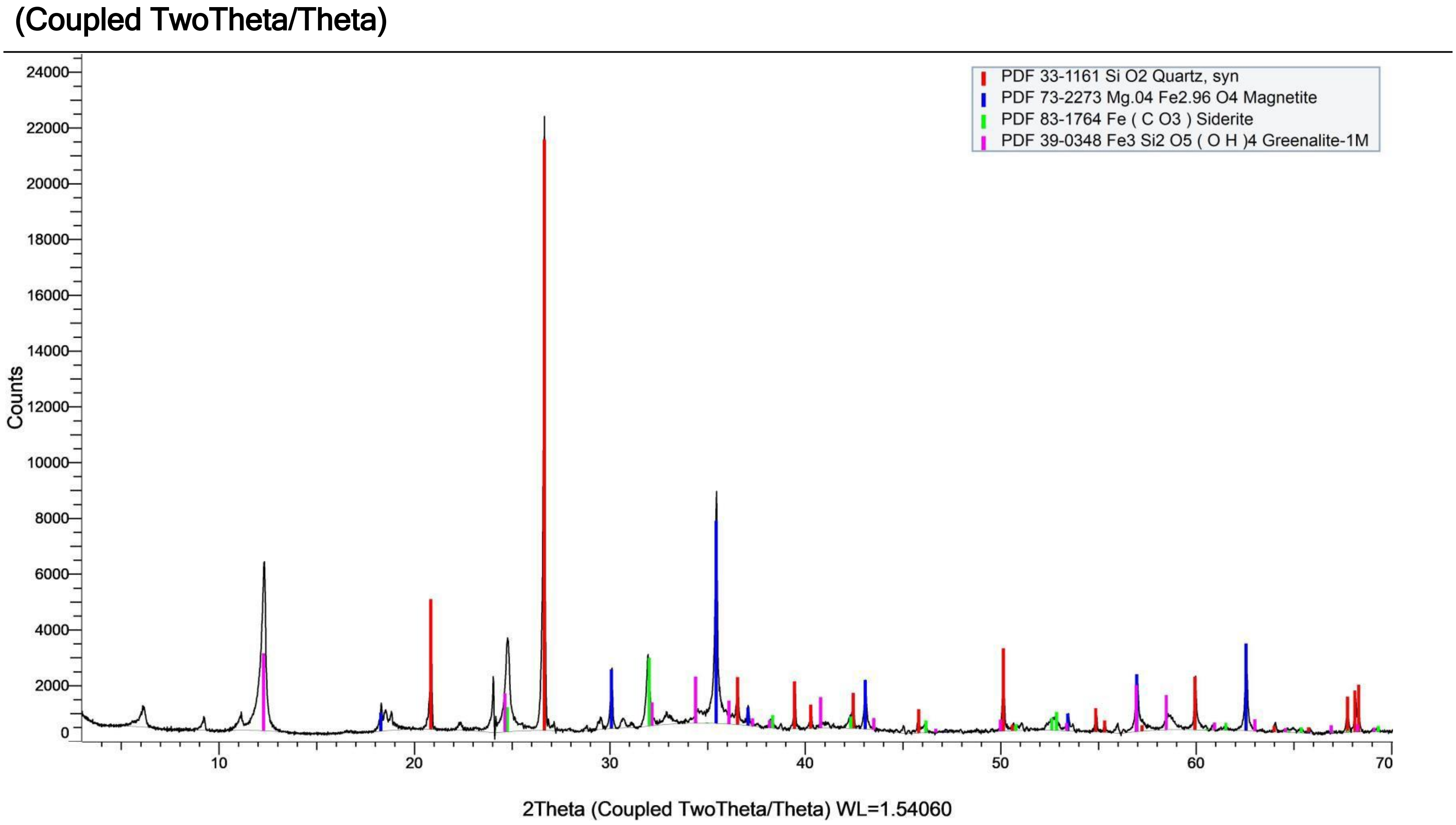
(Coupled TwoTheta/Theta)
PDF 33-1161 Si O2 Quartz, syn
PDF 73-2273 Mg.04 Fe2.96 O4 Magnetite
PDF 83-1764 Fe (C O3) Siderite
PDF 39-0348 Fe3 Si2 O5 (O H)4 Greenalite-1M
Counts
24000
22000
20000
18000
16000
14000
12000
10000
8000
6000
4000
2000
0
10
20
30
40
50
60
70
2Theta (Coupled TwoTheta/Theta) WL=1.54060

G7BF-21

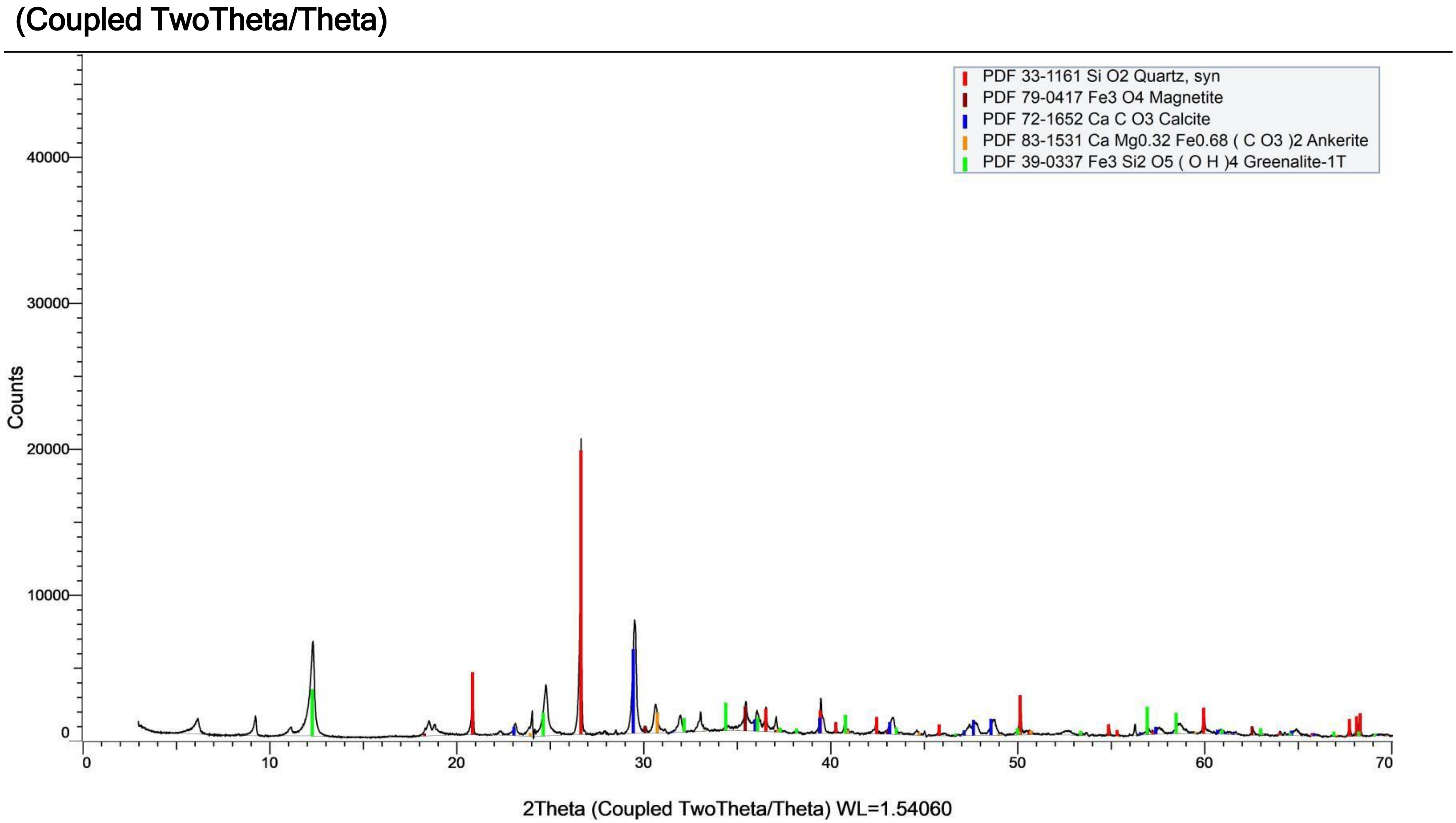
(Coupled TwoTheta/Theta)
PDF 33-1161 Si O2 Quartz, syn
PDF 79-0417 Fe3 O4 Magnetite
PDF 72-1652 Ca C O3 Calcite
PDF 83-1531 Ca Mg0.32 Fe0.68 (C O3)2 Ankerite
PDF 39-0337 Fe3 Si2 O5 (O H)4 Greenalite-1T
Counts
40000
30000
20000
10000
0
0
10
20
30
40
50
60
70
2Theta (Coupled TwoTheta/Theta) WL=1.54060

G7BF-22

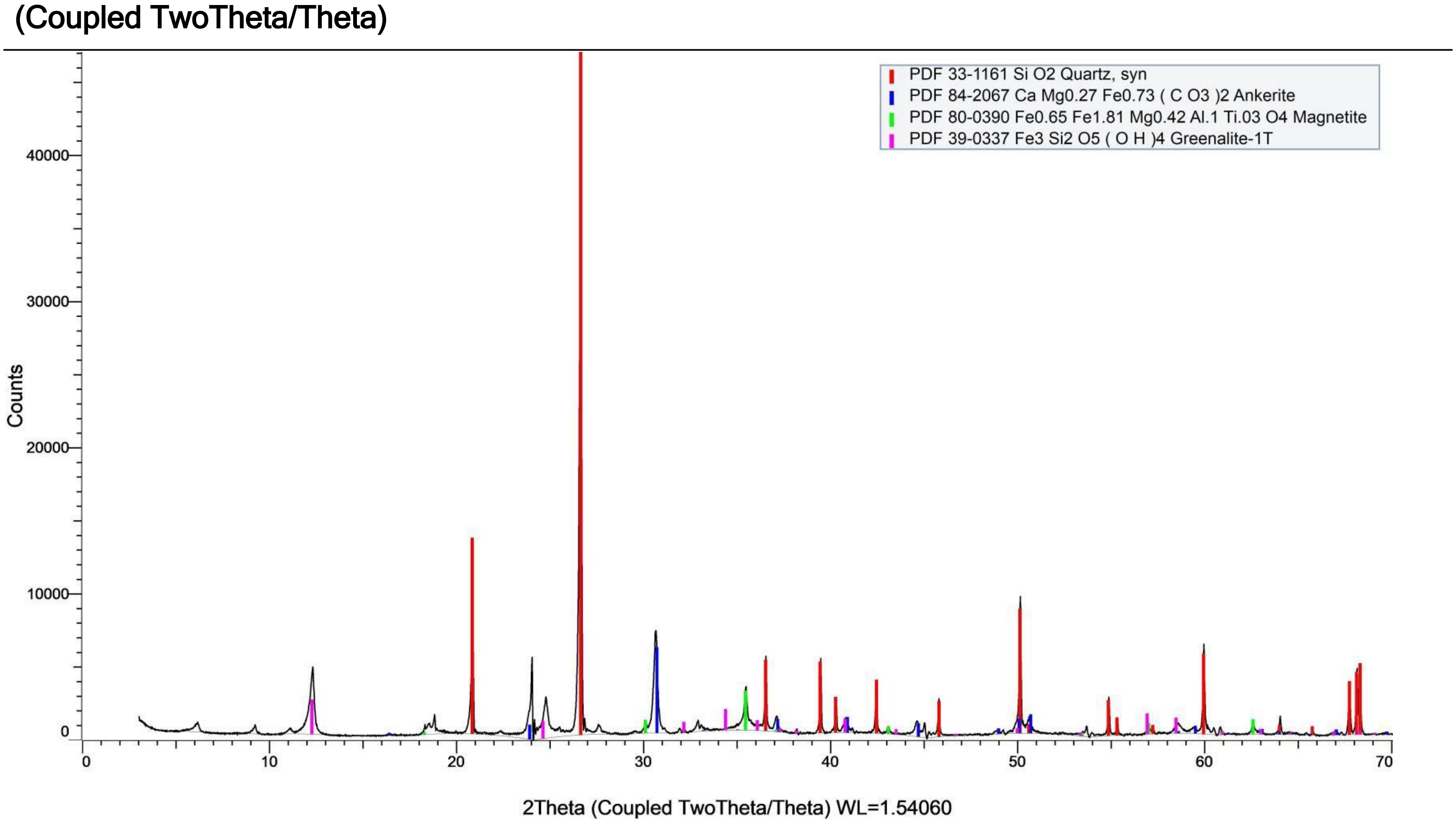
(Coupled TwoTheta/Theta)
PDF 33-1161 Si O2 Quartz, syn
PDF 84-2067 Ca Mg0.27 Fe0.73 (C O3)2 Ankerite
PDF 80-0390 Fe0.65 Fe1.81 Mg0.42 Al.1 Ti.03 O4 Magnetite
PDF 39-0337 Fe3 Si2 O5 (O H)4 Greenalite-1T
Counts
40000
30000
20000
10000
0
0
10
20
30
40
50
60
70
2Theta (Coupled TwoTheta/Theta) WL=1.54060

MP-BIF-02

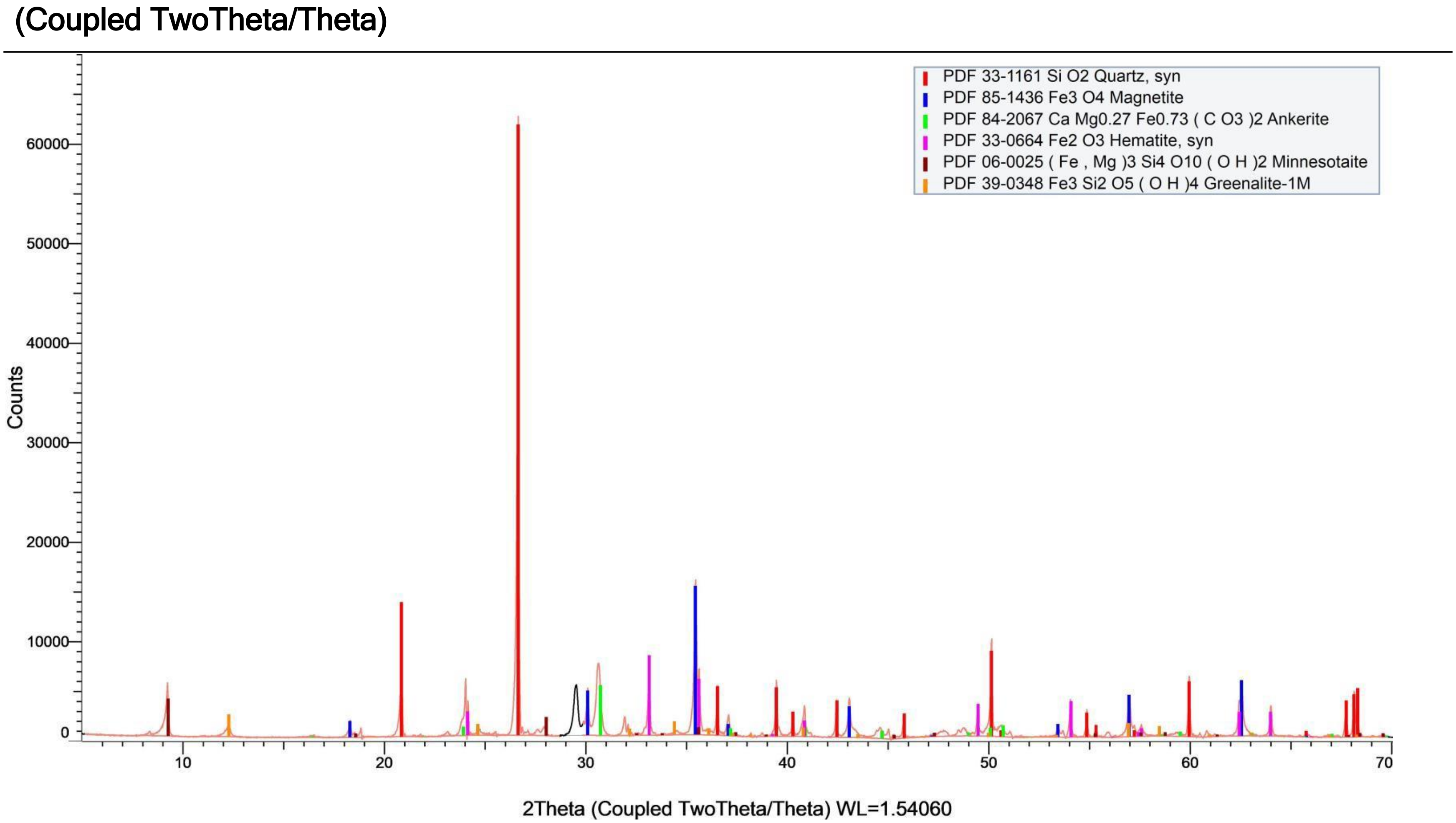
(Coupled TwoTheta/Theta)
PDF 33-1161 Si O2 Quartz, syn
PDF 85-1436 Fe3 O4 Magnetite
PDF 84-2067 Ca Mg0.27 Fe0.73 (C O3)2 Ankerite
PDF 33-0664 Fe2 O3 Hematite, syn
PDF 06-0025 (Fe , Mg)3 Si4 O10 (O H)2 Minnesotaite
PDF 39-0348 Fe3 Si2 O5 (O H)4 Greenalite-1M
Counts
60000
50000
40000
30000
20000
10000
0
10
20
30
40
50
60
70
2Theta (Coupled TwoTheta/Theta) WL=1.54060

MP-BIF-08

(Coupled TwoTheta/Theta)

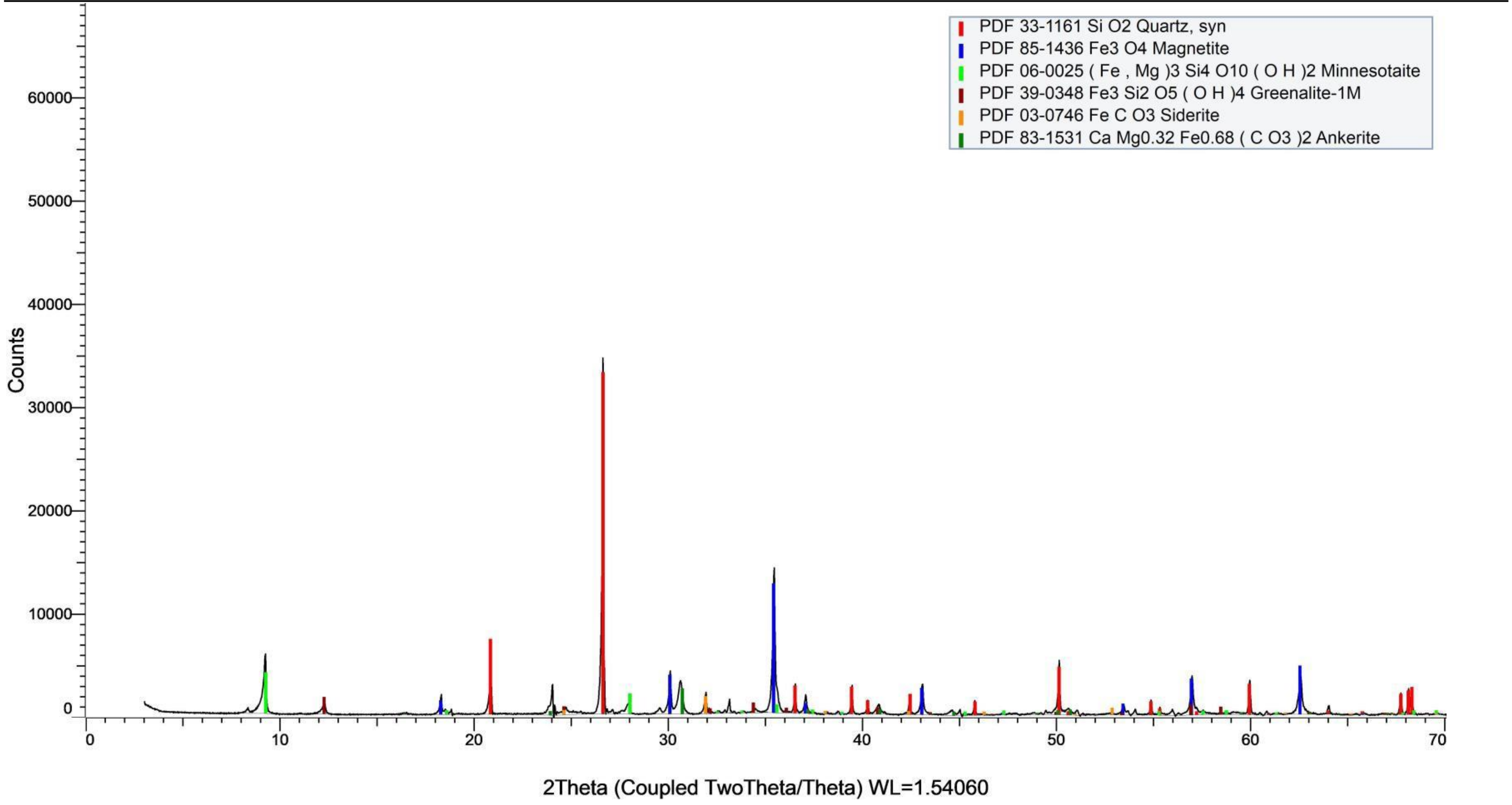

MP-BIF-15

(Coupled TwoTheta/Theta)

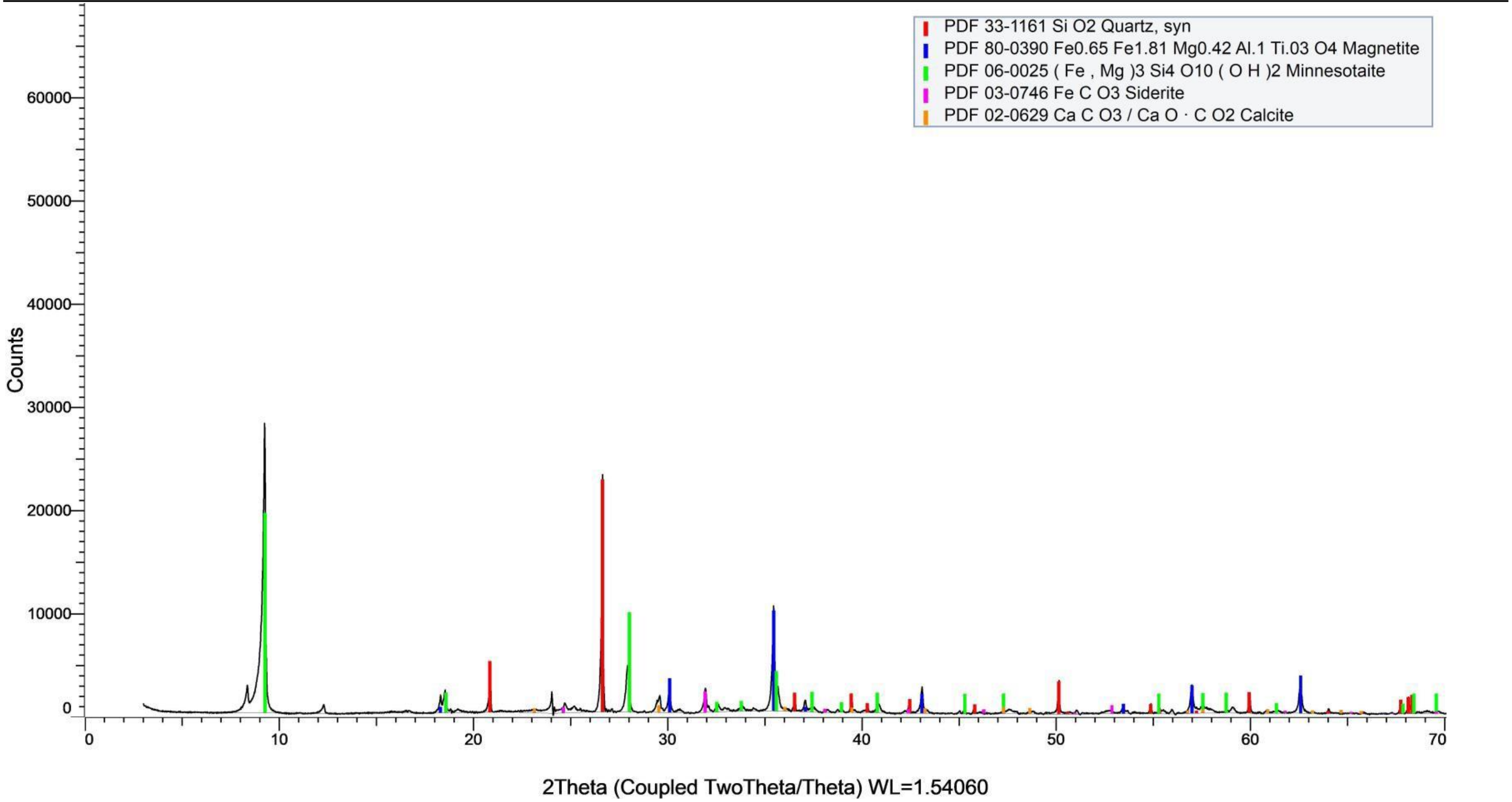

MP-BIF-22

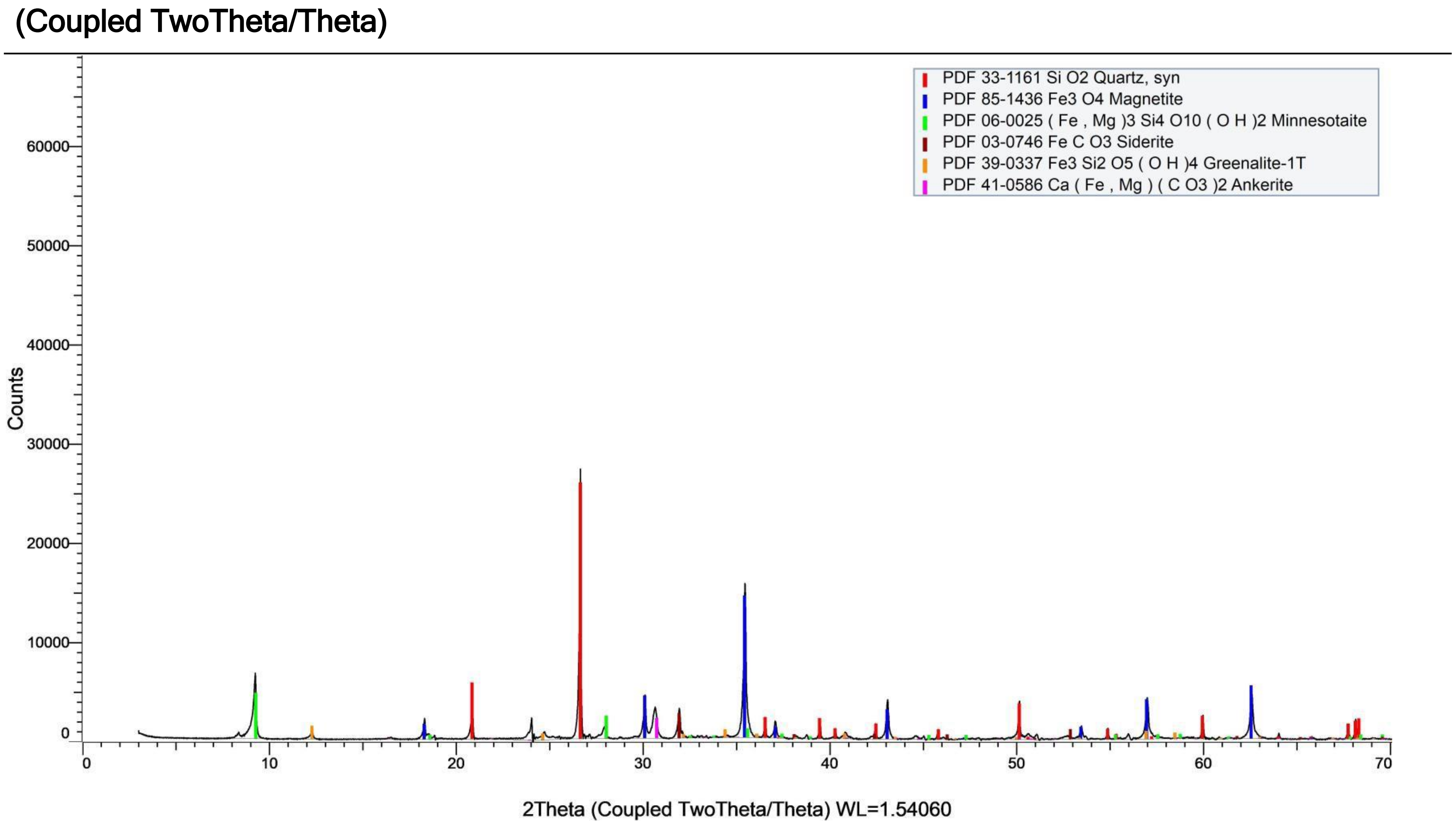
(Coupled TwoTheta/Theta)
🟥 PDF 33-1161 Si O2 Quartz, syn
🟦 PDF 85-1436 Fe3 O4 Magnetite
🟩 PDF 06-0025 (Fe , Mg)3 Si4 O10 (O H)2 Minnesotaite
🟫 PDF 03-0746 Fe C O3 Siderite
🟧 PDF 39-0337 Fe3 Si2 O5 (O H)4 Greenalite-1T
🟪 PDF 41-0586 Ca (Fe , Mg) (C O3)2 Ankerite
Counts
60000
50000
40000
30000
20000
10000
0
0
10
20
30
40
50
60
70
2Theta (Coupled TwoTheta/Theta) WL=1.54060

MP-BIF-33

(Coupled TwoTheta/Theta)

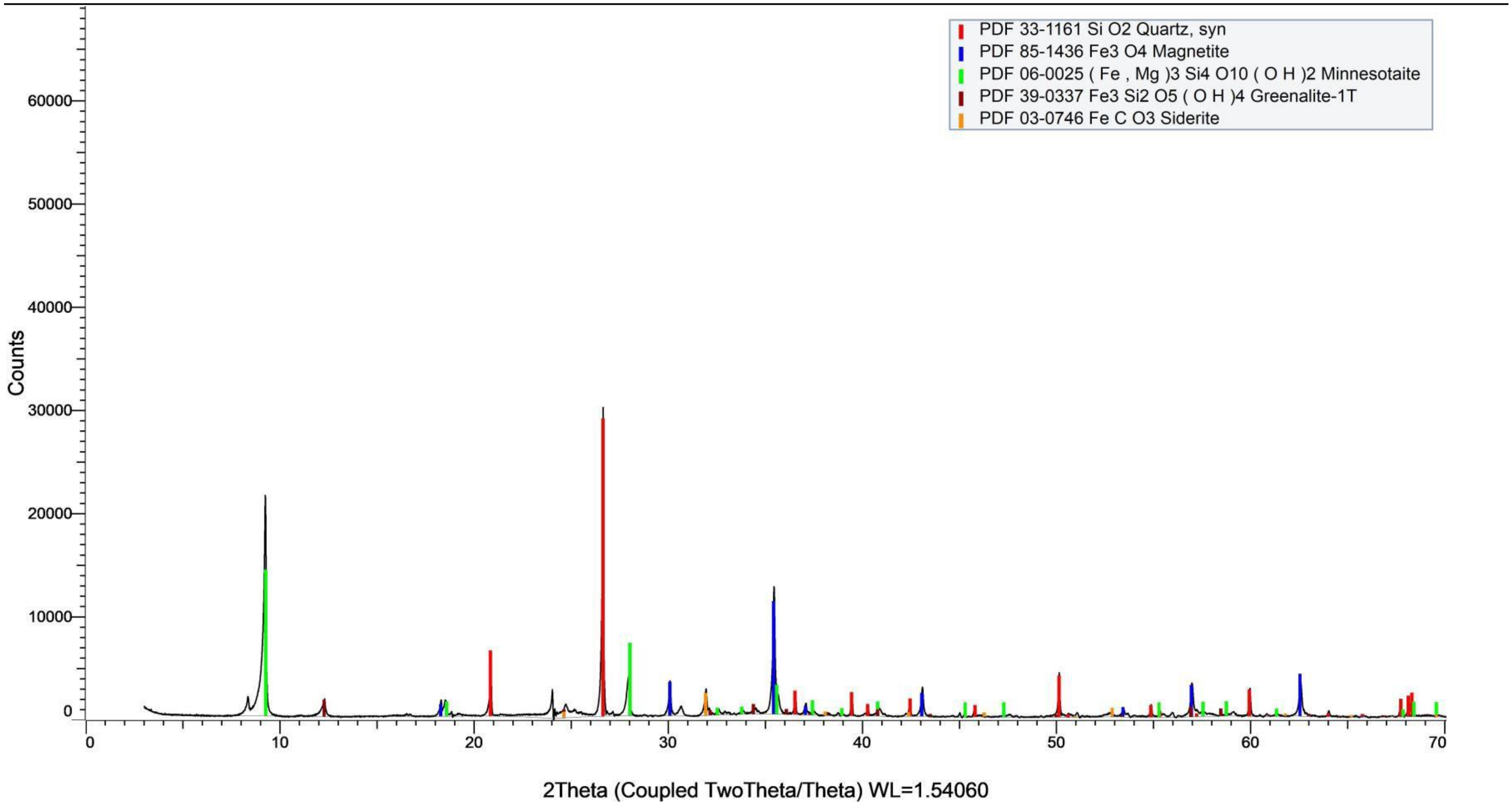

MP-BIF-40

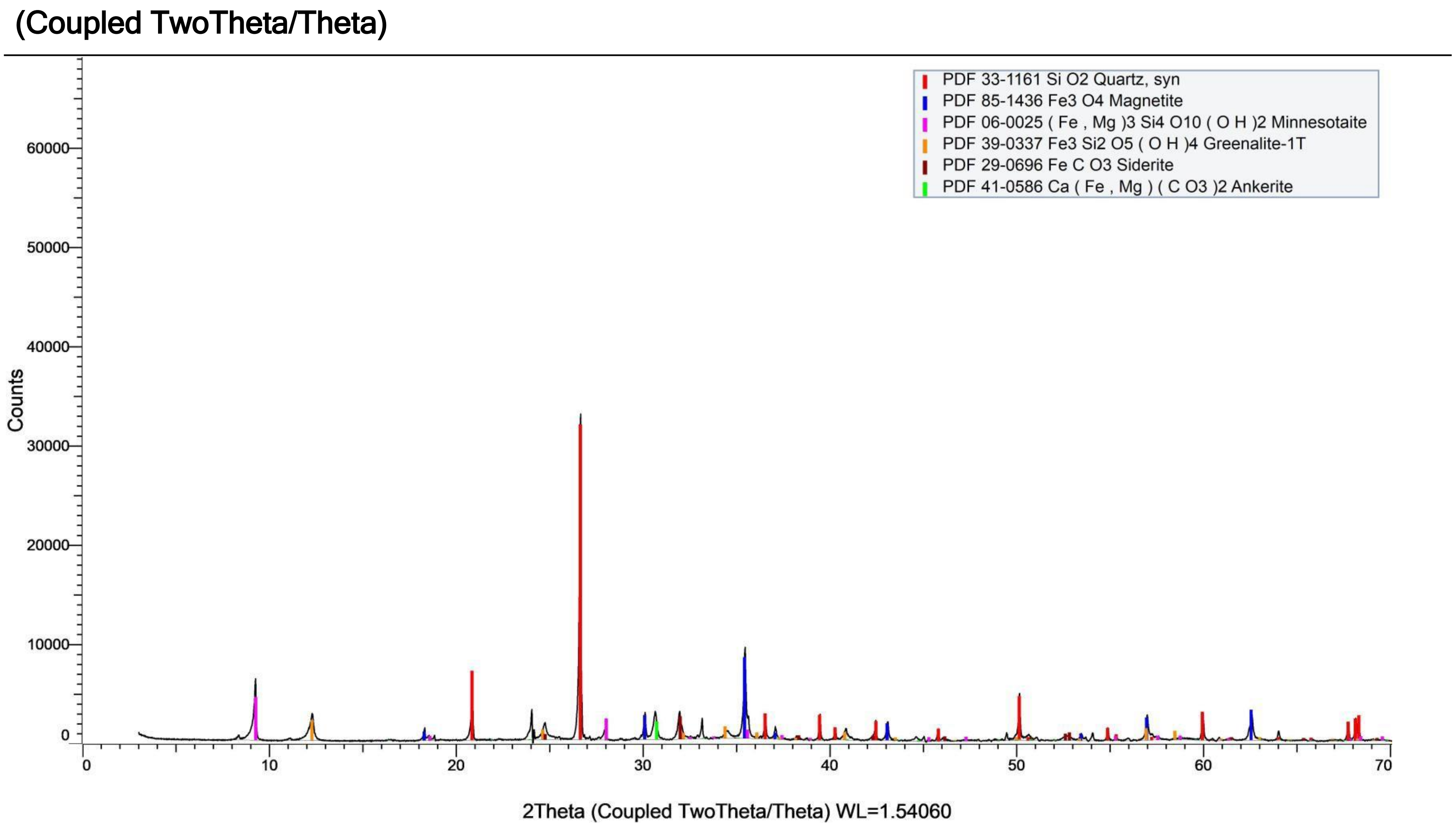
(Coupled TwoTheta/Theta)
PDF 33-1161 Si O2 Quartz, syn
PDF 85-1436 Fe3 O4 Magnetite
PDF 06-0025 (Fe , Mg)3 Si4 O10 (O H)2 Minnesotaite
PDF 39-0337 Fe3 Si2 O5 (O H)4 Greenalite-1T
PDF 29-0696 Fe C O3 Siderite
PDF 41-0586 Ca (Fe , Mg) (C O3)2 Ankerite
Counts
60000
50000
40000
30000
20000
10000
0
0
10
20
30
40
50
60
70
2Theta (Coupled TwoTheta/Theta) WL=1.54060

MP-BIF-42

(Coupled TwoTheta/Theta)

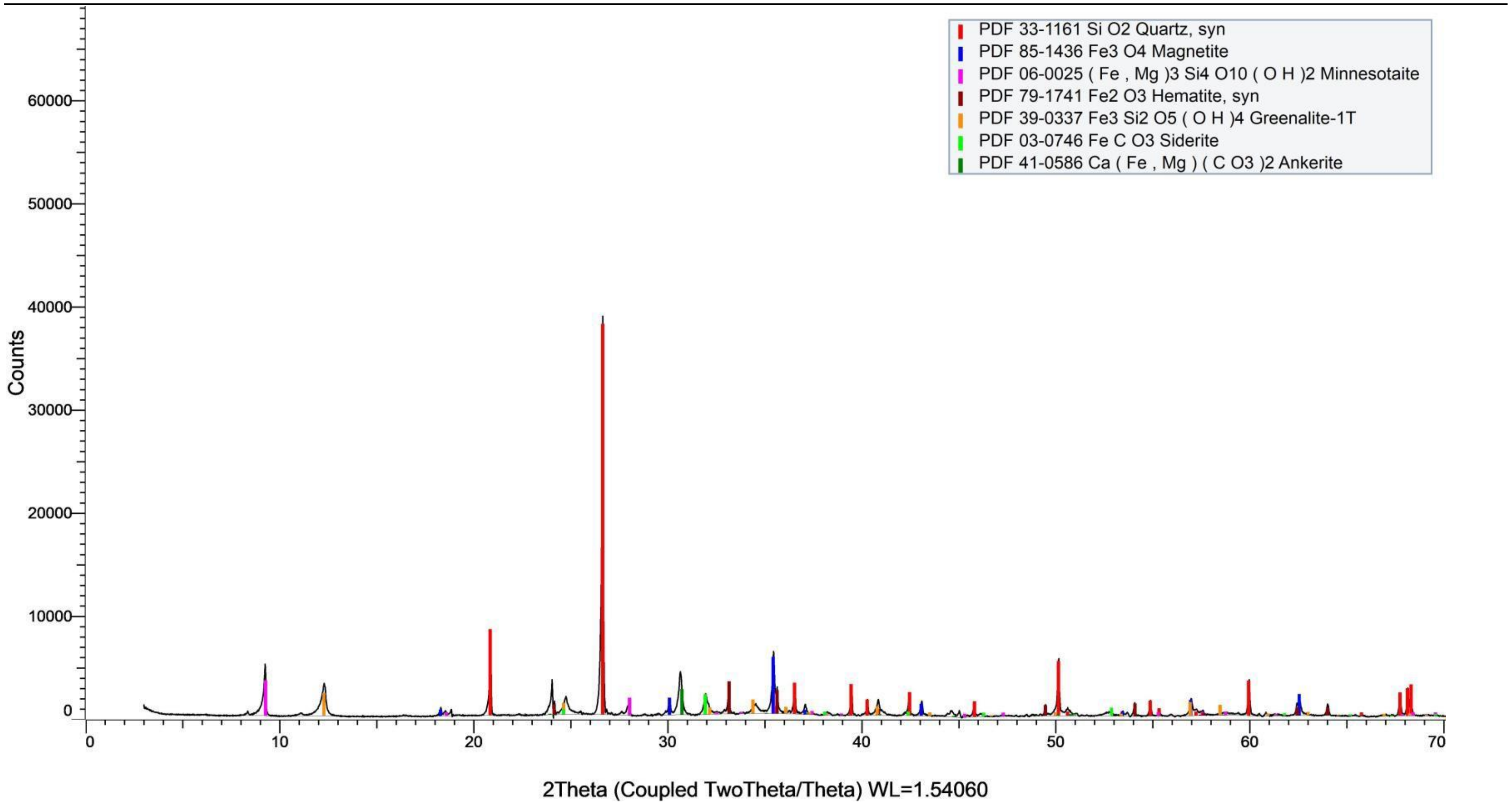

MP-BIF-46

(Coupled TwoTheta/Theta)

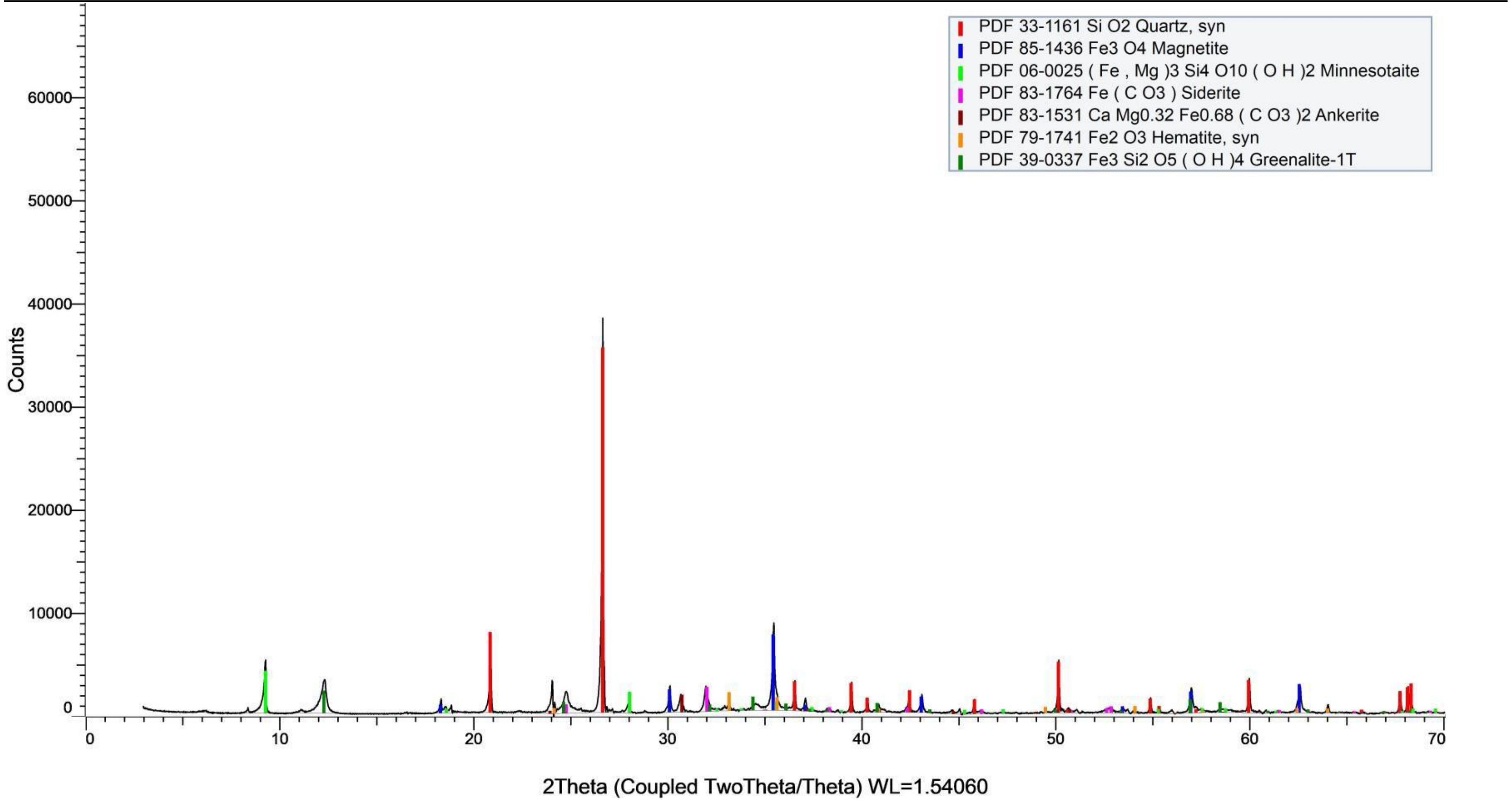

MP-BIF-49

(Coupled TwoTheta/Theta)

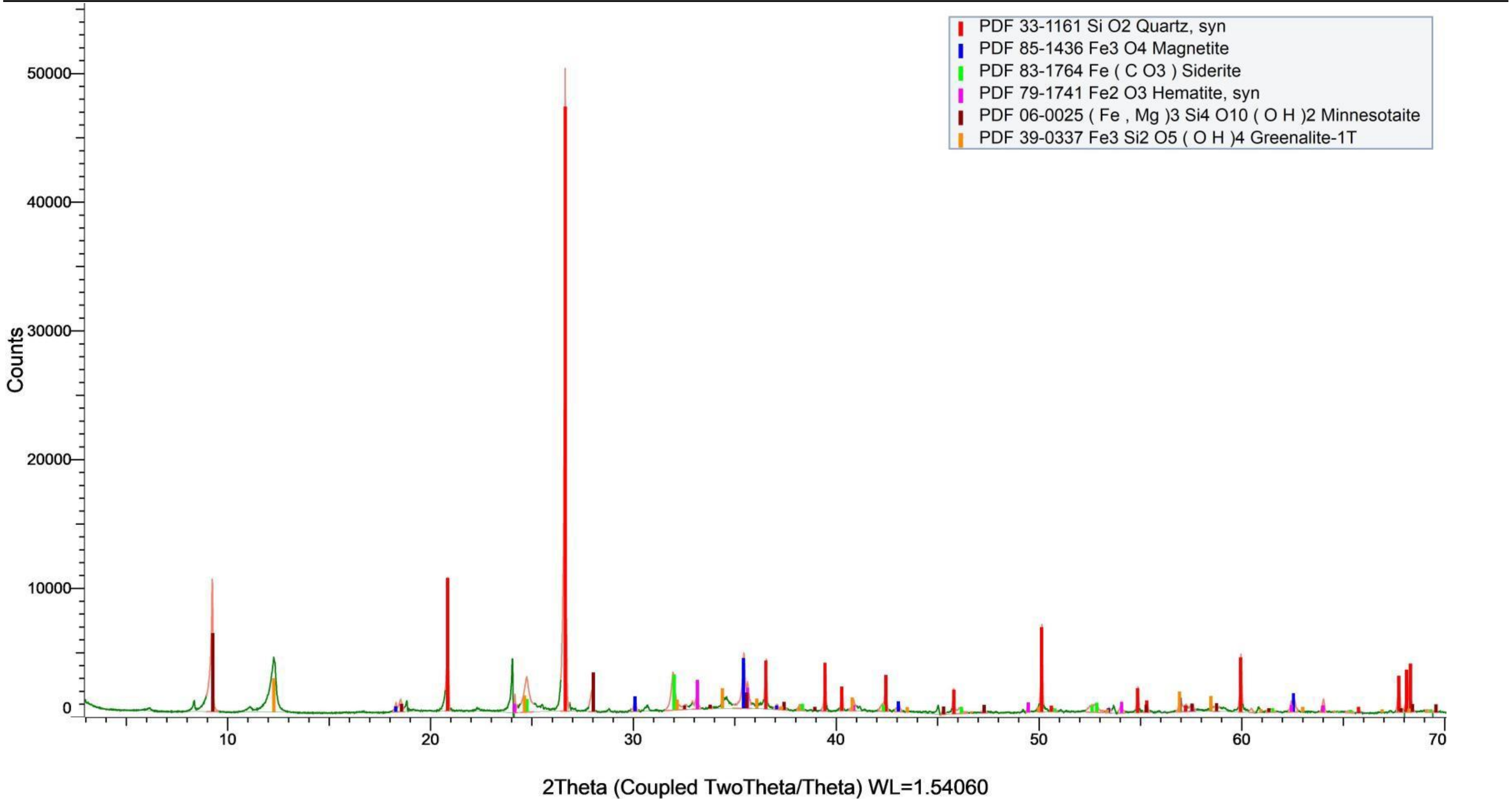

MP-BIF-52

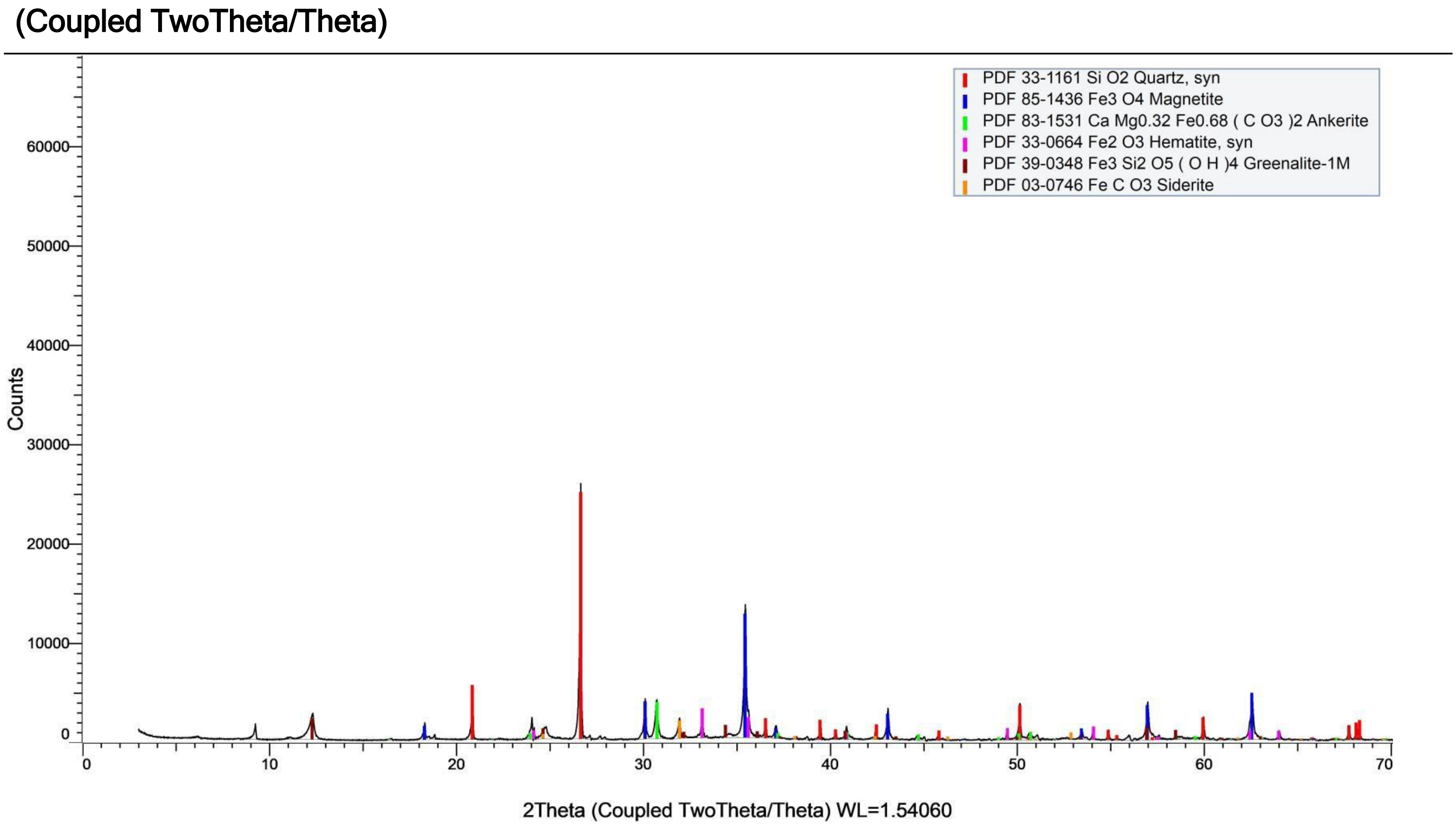
(Coupled TwoTheta/Theta)
PDF 33-1161 Si O2 Quartz, syn
PDF 85-1436 Fe3 O4 Magnetite
PDF 83-1531 Ca Mg0.32 Fe0.68 (C O3)2 Ankerite
PDF 33-0664 Fe2 O3 Hematite, syn
PDF 39-0348 Fe3 Si2 O5 (O H)4 Greenalite-1M
PDF 03-0746 Fe C O3 Siderite
Counts
60000
50000
40000
30000
20000
10000
0
0
10
20
30
40
50
60
70
2Theta (Coupled TwoTheta/Theta) WL=1.54060

Statement of originality of the MSc thesis

I declare that:

1. this is an original report, which is entirely my own work,

2. where I have made use of the ideas of other writers, I have acknowledged the source in all instances,

3. where I have used any diagram or visuals I have acknowledged the source in all instances,

4. this report has not and will not be submitted elsewhere for academic assessment in any other academic course.

Student data:

Name: Sten Jacobs

Registration number: 5496772

Date:

11-03-2019

Signature:

Jacobs